

MAGDALENA RUCKA

GUIDED WAVE PROPAGATION IN STRUCTURES

MODELLING, EXPERIMENTAL STUDIES
AND APPLICATION TO DAMAGE DETECTION

POLITECHNIKA GDAŃSKA

monografie

106

GDANSK UNIVERSITY OF TECHNOLOGY

MAGDALENA RUCKA

GUIDED WAVE PROPAGATION IN STRUCTURES

MODELLING, EXPERIMENTAL STUDIES
AND APPLICATION TO DAMAGE DETECTION



GDAŃSK 2011

PRZEWODNICZĄCY KOMITETU REDAKCYJNEGO
WYDAWNICTWA POLITECHNIKI GDAŃSKIEJ

Romuald Szymkiewicz

REDAKTOR PUBLIKACJI NAUKOWYCH

Janusz T. Cieśliński

REDAKTOR SERII

Jerzy M. Sawicki

RECENZENCI

Wojciech Gilewski

Tomasz Mikulski

PROJEKT OKŁADKI

Jolanta Cieślawska

Wydano za zgodą
Rektora Politechniki Gdańskiej

Oferta wydawnicza Politechniki Gdańskiej jest dostępna na stronach
www.pg.gda.pl/WydawnictwoPG

© Copyright by Wydawnictwo Politechniki Gdańskiej
Gdańsk 2011

Utwór nie może być powielany i rozpowszechniany, w jakiegokolwiek formie
i w jakiegokolwiek sposób, bez pisemnej zgody wydawcy

ISBN 978-83-7348-346-0

CONTENTS

LIST OF SYMBOLS AND ABBREVIATIONS.....	5
1. INTRODUCTION	9
1.1. Damage detection in engineering structures	9
1.2. Guided wave application in damage detection	10
1.3. Aim and scope of study	11
2. ELASTIC WAVES IN STRUCTURAL ELEMENTS	13
2.1. Outline of bulk and guided waves	13
2.2. Axial waves in rods	17
2.2.1. Elementary rod theory	17
2.2.2. Love rod theory	20
2.2.3. Mindlin-Herrmann rod theory	21
2.3. Flexural waves in beams	22
2.3.1. Euler-Bernoulli beam theory	22
2.3.2. Timoshenko beam theory	23
2.4. In-plane waves in plates	25
2.4.1. Plane stress theory	25
2.4.2. Kane-Mindlin plate theory	27
2.5. Flexural waves in plates	30
2.5.1. Kirchhoff plate theory	30
2.5.2. Mindlin plate theory	31
2.6. Summary and conclusions	34
3. SPECTRAL ELEMENT METHOD	36
3.1. General formulation of the spectral element method	38
3.1.1. Definition of element nodes	39
3.1.2. Definition of shape functions	41
3.1.3. Integration quadratures	44
3.1.4. Time integration	44
3.1.4.1. The central difference method	45
3.1.4.2. The Newmark method	46
3.2. Formulation of one-dimensional spectral finite elements	47
3.2.1. Elementary rod element	49
3.2.2. Love rod element	49
3.2.3. Mindlin-Herrmann rod element	49
3.2.4. Timoshenko beam element	50
3.2.5. Frame element based on Mindlin-Herrmann and Timoshenko theories	51
3.3. Formulation of two-dimensional spectral finite elements	52
3.3.1. Plane stress element	53
3.3.2. Kane-Mindlin extensional plate element	54
3.3.3. Mindlin bending plate element	55
3.4. Summary and conclusions	56

4. WAVE PROPAGATION IN BARS	57
4.1. Experimental setup	58
4.1.1. Excitation signal	59
4.1.2. Dispersion curves	62
4.2. Experimental investigations on bars with discontinuities	65
4.3. Spectral element analysis of wave propagation in an intact bar	71
4.3.1. Guidelines for spectral element models on the example of longitudinal waves	71
4.3.2. Simulations of longitudinal waves	75
4.3.3. Simulations of flexural waves	75
4.4. Spectral element analysis of wave propagation in bars with structural discontinuities	77
4.5. Summary and conclusions	81
5. WAVE PROPAGATION IN FRAME STRUCTURES	83
5.1. Experimental setup	84
5.2. Damage detection in L-frame by guided waves	88
5.2.1. Spectral element method model of L-frame	88
5.2.2. Longitudinal wave propagation in L-frame	89
5.2.3. Flexural wave propagation in L-frame	94
5.3. Damage detection in T-frame by guided waves	98
5.3.1. Longitudinal wave propagation in T-frame	98
5.3.2. Flexural wave propagation in T-frame	103
5.4. Damage detection in portal frame by guided waves	107
5.4.1. Longitudinal wave propagation in portal frame	107
5.4.2. Flexural wave propagation in portal frame	111
5.5. Summary and conclusions	115
6. WAVE PROPAGATION IN PLATES	117
6.1. In-plane wave propagation in plate	118
6.1.1. Experimental setup	118
6.1.2. Dispersion curves	121
6.1.3. Numerical model	124
6.1.4. Damage detection in plate by in-plane waves	124
6.2. Flexural wave propagation in plate	138
6.2.1. Experimental setup	138
6.2.2. Dispersion curves	140
6.2.3. Numerical model	142
6.2.4. Damage detection in plate by flexural waves	142
6.3. Summary and conclusions	157
7. FINAL REMARKS	158
ACKNOWLEDGEMENTS	160
REFERENCES	161
SUMMARY IN ENGLISH	169
SUMMARY IN POLISH	170
APPENDIX A	172

LIST OF SYMBOLS AND ABBREVIATIONS

Symbols

A	– cross-sectional area
A_0, A_1, A_2, \dots	– antisymmetric Lamb modes
\mathbf{b}	– vector of inertia forces
b	– width of a structure
B	– surface area
\mathbf{B}	– strain-displacement matrix
c_g	– group velocity
c_L	– longitudinal wave speed in a plate
c_o	– thin-rod velocity
c_p	– phase velocity (wave speed)
c_P	– speed of P wave
c_R	– speed of R wave
c_S	– speed of S wave
\mathbf{c}	– vector of damping forces
\mathbf{C}	– structure damping matrix
$\mathbf{C}_{(e)}$	– element damping matrix in local element coordinates
$\bar{\mathbf{C}}_{(e)}$	– element damping matrix in global element coordinates
d	– half of plate thickness
D	– plate flexural rigidity
\mathbf{D}	– differential operator matrix
E	– modulus of elasticity
\mathbf{E}	– stress-strain matrix
f	– frequency
f_x, f_y, f_z	– distributed loads
\mathbf{f}	– vector of distributed loads
\mathbf{f}_b	– vector of body forces
\mathbf{f}_s	– vector of surface forces
G	– shear modulus
h	– thickness of a plate
\mathbf{H}	– shape function matrix
i	– imaginary unit
I	– moment of inertia
J	– Jacobian
\mathbf{J}	– Jacobian matrix
J_o	– polar moment of inertia
k	– wavenumber
\mathbf{K}	– structure stiffness matrix
$\mathbf{K}_{(e)}$	– element stiffness matrix in local element coordinates
$\bar{\mathbf{K}}_{(e)}$	– element stiffness matrix in global element coordinates
K_L	– adjustable parameter in the Love theory

K_1^{M-H} , K_2^{M-H}	– adjustable parameters in the Mindlin-Herrmann theory
K_1^{Tim} , K_2^{Tim}	– adjustable parameters in the Timoshenko theory
L	– length of a structure
L_e	– effective length of finite element
L_N	– Lobatto polynomial of order N
\mathbf{M}	– structure mass matrix
$\mathbf{M}_{(e)}$	– element mass matrix in local element coordinates
$\bar{\mathbf{M}}_{(e)}$	– element mass matrix in global element coordinates
n	– number of element interpolation nodes
n_{el}	– number of elements
n_r, n_s	– number of integration points
N	– degree of interpolation polynomial
p	– excitation force signal (external force)
p_V	– excitation voltage signal
\mathbf{p}	– vector of external forces
$\mathbf{p}_{(e)}$	– vector of element external forces in local element coordinates
$\bar{\mathbf{p}}_{(e)}$	– vector of element external forces in global element coordinates
P_N	– Legendre polynomial of order N
\mathbf{q}	– vector of nodal displacements
$\mathbf{q}_{(e)}$	– vector of element nodal displacements
\mathbf{r}	– vector of internal forces
$\mathbf{r}_{(e)}$	– vector of element internal forces
S_0, S_1, S_2, \dots	– symmetric Lamb modes
t	– time
T	– kinetic energy
\mathbf{T}	– transformation matrix from local to global coordinates
u_x, u_y, u_z	– translational displacements
\mathbf{u}	– vector of displacements
U	– potential energy
v	– velocity of vibrations
W_{ext}	– work of external forces
x, y, z	– Cartesian coordinates
β, γ	– parameters in the Newmark method
$\gamma_{xy}, \gamma_{xz}, \gamma_{yz}$	– shear strains
δ_{ij}	– Kronecker delta
$\delta\mathbf{u}$	– vector of virtual displacements
δW	– virtual work
δW_{ext}	– virtual external work
δW_{damp}	– virtual damping work
δW_{int}	– virtual internal work
δW_{kin}	– virtual kinetic work
$\delta\boldsymbol{\varepsilon}$	– vector of virtual strains
Δt	– time step
Δt_{cr}	– critical time step
$\varepsilon_{xx}, \varepsilon_{yy}, \varepsilon_{zz}$	– normal strains
ε_t	– transverse strain

$\boldsymbol{\varepsilon}$	– vector of strains
η_d	– damping property parameter
κ	– adjustable parameter in the Mindlin theory
κ_{KM}	– adjustable parameter in the Kane-Mindlin theory
λ	– wavelength
Λ, G	– Lamé constants of elasticity
$\boldsymbol{\mu}$	– mass density matrix
ν	– Poisson's ratio
ξ, η	– natural (parent) coordinate system
ρ	– mass density
$\sigma_{xx}, \sigma_{yy}, \sigma_{zz}$	– normal stresses
$\sigma_{xy}, \sigma_{xz}, \sigma_{yz}$	– shear stresses
φ, ψ_x, ψ_y	– rotations
ψ	– lateral contraction
ω	– circular frequency
ω_c	– cut-off frequency

Abbreviations

1-D	– one-dimensional
2-D	– two-dimensional
3-D	– three-dimensional
FEM	– finite element method
FFT	– fast Fourier transform
GLL	– Gauss-Lobatto-Legendre
NDE	– nondestructive evaluation
NDT	– nondestructive testing
PZT	– lead zirconate titanate
P wave	– primary, pressure, compressional, extensional, dilatational, irrotational, axial, longitudinal wave
R wave	– Rayleigh wave
SEM	– spectral element method
SFEM	– spectral finite element method
SHM	– structural health monitoring
S wave	– secondary, shear, distortional, rotational, transverse wave
SH wave	– shear horizontal wave
SV wave	– shear vertical wave

Chapter 1

INTRODUCTION

1.1. Damage detection in engineering structures

Engineering structures undergo gradual destruction in the course of time as a result of static and dynamic loading, temperature, humidity, wind or corrosive factors. Under the influence of these environmental and operating conditions, structures are subjected to fatigue, corrosion, creep and wear. Damage in structural elements may lead to improper operation of any engineering object and it can be a potential threat of financial burden, environmental contamination as well as human lives. After Adams (2007), *damage* is defined here as a permanent change in the mechanical state of a structural material or component that could potentially affect its performance. *Damage detection* is termed as identification of defects and their locations. Damage detection can extend the service life of structures, improve reliability and safety, reduce maintenance costs or even prevent a catastrophic failure. Therefore, the ability to detect structural damage at the earliest possible stage has been of great interest to civil, mechanical and aerospace engineering communities.

The process of assessing the current damage state of a structural material or component without accelerating the damage is termed as nondestructive evaluation (NDE) (Adams 2007). The most common method of a nondestructive assessment of the structure integrity is a periodic visual inspection, mandatory for important structures, for example bridges, which are regularly controlled by experienced engineers. Damage detection can be facilitated by nondestructive testing (NDT) which is the offline implementation of NDE methodologies (e.g. Brunarski and Runkiewicz 1983, Runkiewicz 1999). There are many methods for NDT including radiography (e.g. Lashkia 2001, Ghose and Kankane 2008), acoustic emission (e.g. Rogers 2005, Rahman et al. 2009), infrared thermography (e.g. Clark et al. 2003), ultrasonic testing (e.g. Yeih and Huang 1998, Hoła and Schabowicz 2005), impact-echo techniques (e.g. Lin et al. 2004, Hoła et al. 2009, Rucka and Wilde 2010) or eddy current methods (e.g. Gros 1995). Such diagnostic methods can be effectively applied to damage detection in a few known a priori areas in a structure; however, they can be laborious in searching of potential damage in the whole engineering object.

Further development in local NDT methods leads to so-called structural health monitoring (SHM), which is the online implementation of NDE. Vibration-based and wave propagation methods play a significant role in SHM strategies of dynamics-based global damage detection techniques, where the location of damage is not known. Vibration-based damage detection methods make use of dynamic characteristics of structures (e.g. Dimarogonas 1996, Salawu 1997, Doebling et al. 1998, Ren and Roeck 2002a, 2002b, Uhl 2005, Wilde 2008, Kawecki and Stypuła 2009, Tomaszewska 2010). Recently, many damage detection methods based on structural vibrations, especially combined with genetic algorithms (Kokot and Zembaty 2008, 2009), artificial neural networks (Waszczyszyn and Ziemiański 2001, Kuźniar and Waszczyszyn 2002), modal filters (Mendrok and Uhl 2010), virtual distortion methods (Świercz et al. 2008) or wavelet analysis (Knitter-Piątkowska et al. 2006, Ziopaja et al. 2006, Rucka and Wilde 2006, 2007) have been developed. The

second group of damage detection methods based on dynamics are guided wave propagation techniques, which are the subject of this study. Wave propagation is an extension of the NDT wave testing from the local to global approach of sending and sensing waves. The passage of waves through material thickness is extended to methods based on the long-range guided wave propagation along the structure to inspect large areas rapidly.

1.2. Guided wave application in damage detection

Guided wave-based damage detection methods have been dynamically developed over last years. The term *guided wave propagation* refers to wave propagation in bounded media. In the guided wave propagation approach, a structure can be perceived as a waveguide, which directs the wave energy along its length. This technique utilizes excitation of high frequencies (of order a few dozen kHz to a few hundred kHz) in the form of an impulse or a wave packet. Ultrasonic excitation causes that waves are reflected and modes are converted inside a structure, and after some travel superposition causes formation of guided wave modes (Rose 1999).

Since guided waves have the ability of propagation over long distances with a little amplitude loss, they are very suitable for inspecting large structures. Guided Lamb and Rayleigh waves, named after their investigators, are frequently used for damage detection purposes. The Rayleigh waves, discovered by Lord Rayleigh (1885), can propagate in solids containing a free surface. The Rayleigh waves, called also guided-surface waves, travel close to the free surface with very little penetration in the depth, therefore these waves are particularly suitable for detection of surface defects. The Lamb waves, described by Lamb (1917), are guided waves propagating in solid plates with free boundaries. The Lamb wave technique enables to find internal, as well as surface defects, because Lamb waves produce stresses throughout the plate thickness and the entire thickness of the plate is interrogated (Giurgiutiu 2008). Guided waves can also exist in other types of thin-walled structures such as bars, shells and tubes. Other types of guided waves are Love waves travelling in layered materials and Stonley waves occurring at the interface between two media.

Techniques of using Lamb waves for ultrasonic inspection were patented by Firestone and Ling (1951). Their invention was devoted to the method and means for generating and utilizing Lamb waves. Intensive experimental investigations with the use of Lamb waves were undertaken from the early 1960s. Worlton (1961) presented an experimental study on Lamb waves excited in a plate submerged in water. He discussed characteristics of the various modes in the light of potential nondestructive testing applications. In the same year, Grigsby and Tajchman (1961) described properties of Lamb wave propagation which are relevant to possible nondestructive testing application. An experiment was conducted on a steel plate with an artificial flaw using transmitting and receiving ultrasonic transducers. Thompson et al. (1972) developed and fabricated non-contact electromagnetic transducers that enabled to launch and detect ultrasonic flexural Lamb waves of frequency 130 kHz in gas pipelines. Victorov (1976) in his book described experimental research with the use of Rayleigh and Lamb waves for damage detection. He discussed methods for generating and detecting guided waves. Alleyne and Cawley (1992) presented a study of the interaction of Lamb waves with a variety of defects simulated by notches. The finite element results were checked experimentally on a steel 3 mm plate using two conventional wideband ultrasonic immersion transducers and the excitation was in the form of a tone burst modified by a

Hanning window function. Since the 1990s the idea of application of guided waves to damage detection has been followed by many research groups, and it successfully is used in a lot of practical applications, especially in plates (e.g. Giurgiutiu and Bao 2004, Yu and Giurgiutiu 2008), pipes (e.g. Cawley and Alleyne 1996, Lowe et al. 1998, Demma et al. 2004, Rose et al. 2009), rails (e.g. Rose et al. 2004, Lee et al. 2009), composites (e.g. Su et al. 2002, 2009) or aircraft structures (e.g. Dalton et al. 2001, Giurgiutiu et al. 2004).

1.3. Aim and scope of study

The purpose of this research is to conduct detailed experimental and numerical investigations on ultrasonic guided wave propagation in steel structures. The particular aims of the present study are:

- modelling of wave propagation phenomenon in structural elements undergoing dispersion effects,
- developing of numerical models for wave propagation,
- systematic experimental verification of the developed numerical models,
- application of the guided wave-based technique to damage detection.

The numerical simulations of wave propagation are performed by the time domain Legendre spectral element method. To model longitudinal, as well as flexural wave propagation taking lateral deformations, shear deformations and rotational inertia effects into consideration, special spectral elements based on higher order theories are formulated, in particular the frame spectral element based on the Mindlin-Herrmann rod theory and the Timoshenko beam theory, as well as the extensional plate element based on the Kane-Mindlin theory and the bending plate element based on the Mindlin theory.

An essential part of the study is devoted to experimental investigations of wave propagation. Longitudinal and flexural waves are excited by means of a piezoelectric actuator and propagating Lamb waves are sensed by a scanning laser vibrometer. A special emphasis is focused on damage detection aspects. Steel structures with discontinuity of material and cross-section are analysed and tested. As a result, this study discusses in detail the possibility of damage detection in bars, frames and plates and it compares the usefulness of longitudinal and flexural waves in nondestructive damage detection.

The content is organized as follows. **Chapter 1** reviews structural health monitoring methods and describes previous researches on the application of guided waves in damage detection. The aim and scope of the study are also presented.

Chapter 2 describes elastic wave propagation in structural elements. Several models of rods, beams and plates providing approximated description of wave motion have been derived. The necessity of using higher order theories when analysing waves of ultrasonic frequencies is demonstrated.

The formulation of the spectral element method is introduced in **Chapter 3**. The development of time domain spectral elements for a rod, beam, frame, as well as extensional and bending plates is carried out.

In **Chapter 4**, longitudinal, as well as flexural wave propagation in a bar is investigated both experimentally and numerically. In particular, detection of damage in various forms of discontinuity of cross-section and material is considered by analysing wave speeds and time of reflections in guided wave response signals.

Chapter 5 deals with the mode conversion occurring during longitudinal and flexural wave propagation in planar frames. Three types of frames, namely an L-frame, a T-frame and a portal frame are analysed. Guidelines for SHM systems dedicated for the considered frames concerning the required number of actuators and measurement points are formulated.

In **Chapter 6**, the numerical and experimental studies of Lamb wave propagation in a steel plate are presented. Detection of damage in the form of rectangular surface notch is considered by analysing surface vibration data in the form of A-scans (waveform data plotted as a function of time), B-scans (time-position scans) and C-scans (two-dimensional plane views at selected time instants).

Final remarks and plans for future research are presented in **Chapter 7**.

The idea of the work was initiated by the studies performed by prof. dr hab. K. Wilde, prof. dr hab. J. Chróścielewski, dr W. Witkowski and the author of the work within the confines of the project of Polish Ministry of Science and Higher Education: *Multilevel damage detection system in engineering structures*, no. N506 065 31/3149 (Wilde et al. 2009) and some related papers (see References). The research on guided wave propagation in structures was continued by the author of the work resulting in some journal papers (Rucka 2010a, 2010b, 2011) and finally in this monograph.

The original elements – the results of the author’s scientific research – which have not been published in the joint papers are:

- the experimental and numerical analyses of possibility of damage detection in frame structures indicating the minimum number of actuators and measurement points required to monitor a whole frame,
- the experimental and numerical analyses of possibility of damage detection in plates using B-scans and C-scans,
- the systematic construction of spectral element method models for wave propagation analysis with a special emphasis on dispersion effects and the systematic experimental verification of effectiveness of the proposed spectral element method models,
- the development of the time domain spectral elements for longitudinal waves in rods based on the refined Love and Mindlin-Herrmann theories, as well as the frame spectral element based on the Mindlin-Herrmann rod and Timoshenko beam theories,
- the development of the time domain spectral element for in-plane waves in plates based on the higher order Kane-Mindlin theory.

Chapter 2

ELASTIC WAVES IN STRUCTURAL ELEMENTS

Waves are disturbances travelling from one part of a medium to another and they are characterized by the transport of energy through motions of particles about a state of equilibrium. Energy, in the forms of kinetic and potential energies, can be transmitted over long distances by mechanical wave motion. This chapter focuses on elastic wave propagation in basic structural elements of rods, beams and plates. The governing equations are derived and then the spectrum relations are obtained for longitudinal and flexural modes. For more details see books by Achenbach (1975), Doyle (1997), Giurgiutiu (2008), Graff (1975), Hagedorn and DasGupta (2007), Kaliski (1986), Kolsky (1953), Kosiński (1981), Love (1920), Nowacki (1972), Rose (1999), Victorov (1967).

2.1. Outline of bulk and guided waves

Mechanical waves can exist as *bulk waves* or *guided waves*. Bulk wave propagation occurs in infinite media, away from boundaries in the bulk of material. In contrast, guided waves require a boundary for their existence. The bulk waves and the guided waves are physically different, but they are governed by the same set of partial differential equations. For the bulk waves, there are no boundary conditions to be satisfied, whereas the solution to a guided wave problem must satisfy governing equations, as well as physical boundary conditions (Rose 1999). In this section, guided and bulk waves are outlined. Detailed wave solutions in isotropic elastic continua using the theory of elasticity are derived in Appendix A.

Two types of waves can propagate in an unbounded isotropic solid, namely P waves (also known as primary, pressure, compressional, extensional, dilatational, irrotational, axial, longitudinal waves) and S waves (a.k.a. secondary, shear, distortional, rotational, transverse waves). These wave types are not coupled and they can exist independently of each other. Figure 2.1 visualizes the wave motion of a section of unbounded solid. For the P wave, the particle motion is parallel to the direction of wave propagation, i.e. along the x axis (Fig. 2.1a). For the S wave, particle motion occurs perpendicular to the direction of wave propagation. The shear wave can occur with particle motion along the y axis as the shear vertical wave (SV wave) or with particle motion along the z axis as the shear horizontal wave (SH wave), as it is shown in Fig. 2.1b and Fig. 2.1c, respectively. For isotropic medium, the P wave speed c_p and the S wave speed c_s are given by the following equations (cf. Appendix A.1):

$$c_p = \sqrt{\frac{E(1-\nu)}{\rho(1+\nu)(1-2\nu)}}, \quad (2.1)$$

$$c_s = \sqrt{\frac{E}{2\rho(1+\nu)}} = \sqrt{\frac{G}{\rho}}, \quad (2.2)$$

where E is the modulus of elasticity, ρ is the mass density, ν denotes the Poisson's ratio and G is the shear modulus.

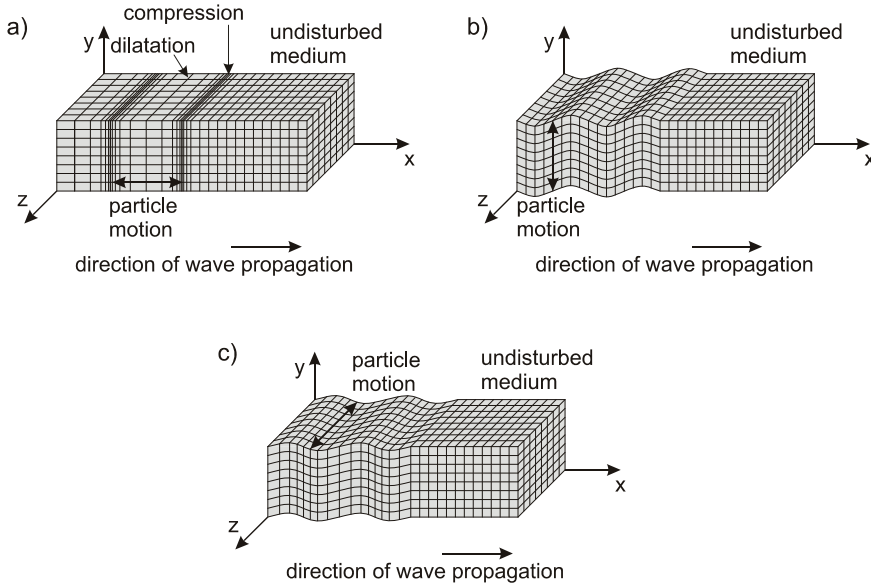


Fig. 2.1. Propagation of bulk waves in a section of continuum: a) P wave; b) SV wave; c) SH wave

Another type of waves, an R wave (a.k.a. Rayleigh wave, surface guided wave), appears in semi-infinite media. For practical purposes, a structure can be perceived as semi-infinite if the wavelength of an excitation is small with respect to its thickness. The motion amplitude of R waves rapidly decreases with depth. The particle motion is elliptical and retrograde with respect to the direction of propagation (Fig. 2.2). The R wave propagates along a free surface of a solid with the speed c_R approximated by the following relation (cf. Appendix A.3):

$$c_R \approx c_S \frac{0.87 + 1.12\nu}{1 + \nu}. \quad (2.3)$$

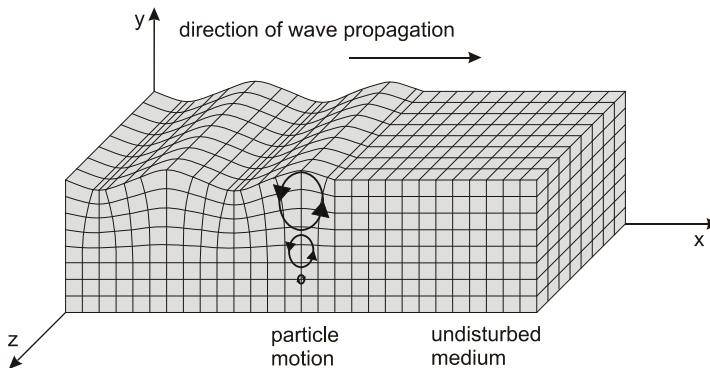


Fig. 2.2. Propagation of Rayleigh wave in a section of continuum containing free surface

Guided Lamb waves refer to wave propagation between two parallel free surfaces. The P waves and the SV waves, simultaneously existed in a plate, through multiple reflections on plate surfaces and through constructive and destructive interference give rise to the Lamb waves. The guided Lamb waves can exist in two types: symmetric (S_0, S_1, S_2, \dots) and antisymmetric (A_0, A_1, A_2, \dots) modes, as it is illustrated in Fig. 2.3. The symmetric modes are termed as longitudinal, because the average displacement over a plate thickness is in the longitudinal direction. For the antisymmetric modes, the average displacement is in the transverse direction; hence these modes are termed as the flexural modes (Achenbach 1975). At the lowest frequencies, two basic modes S_0 and A_0 simultaneously exist. The higher frequency, the larger number of Lamb modes can simultaneously exist and in general, infinite number of modes is associated with a guided Lamb wave problem. Interaction of waves with boundaries causes, that the Lamb waves are dispersive, i.e. their velocity is frequency dependent. The Rayleigh-Lamb frequency equations can be used to determine dispersion relation, i.e. the velocities at which wave of particular frequency f propagates within a plate of thickness $h = 2d$ (see Appendix A.5):

$$\frac{\tan(q_L d)}{q_L} + \frac{4k^2 p_L \tan(p_L d)}{(q_L^2 - k^2)^2} = 0, \quad (2.4)$$

$$q_L \tan(q_L d) + \frac{(q_L^2 - k^2)^2 \tan(p_L d)}{4k^2 p_L} = 0. \quad (2.5)$$

Equation (2.4) is related to symmetric modes, whereas Eq. (2.5) describes antisymmetric modes, and parameters p_L, q_L are given by:

$$p_L^2 = \left(\frac{\omega}{c_P}\right)^2 - k^2, \quad q_L^2 = \left(\frac{\omega}{c_S}\right)^2 - k^2. \quad (2.6)$$

The wavenumber k is equal to:

$$k = \frac{\omega}{c_p}, \quad (2.7)$$

where c_p is the phase velocity (a.k.a. wave speed) of the wave mode and ω denotes the circular frequency. The phase velocity c_p is related to the wavelength λ by the relation:

$$c_p = \frac{\omega}{k} = \frac{\omega}{2\pi} \lambda = \lambda f, \quad f = \frac{\omega}{2\pi}, \quad (2.8)$$

where f denotes frequency. For Lamb waves, the phase speed, i.e. speed at which individual waves in a packet move, is not constant with respect to frequency, therefore the Lamb waves are dispersive. The group velocity c_g is the velocity at which the wave packet propagates and it is defined as:

$$c_g = \frac{d\omega}{dk}. \quad (2.9)$$

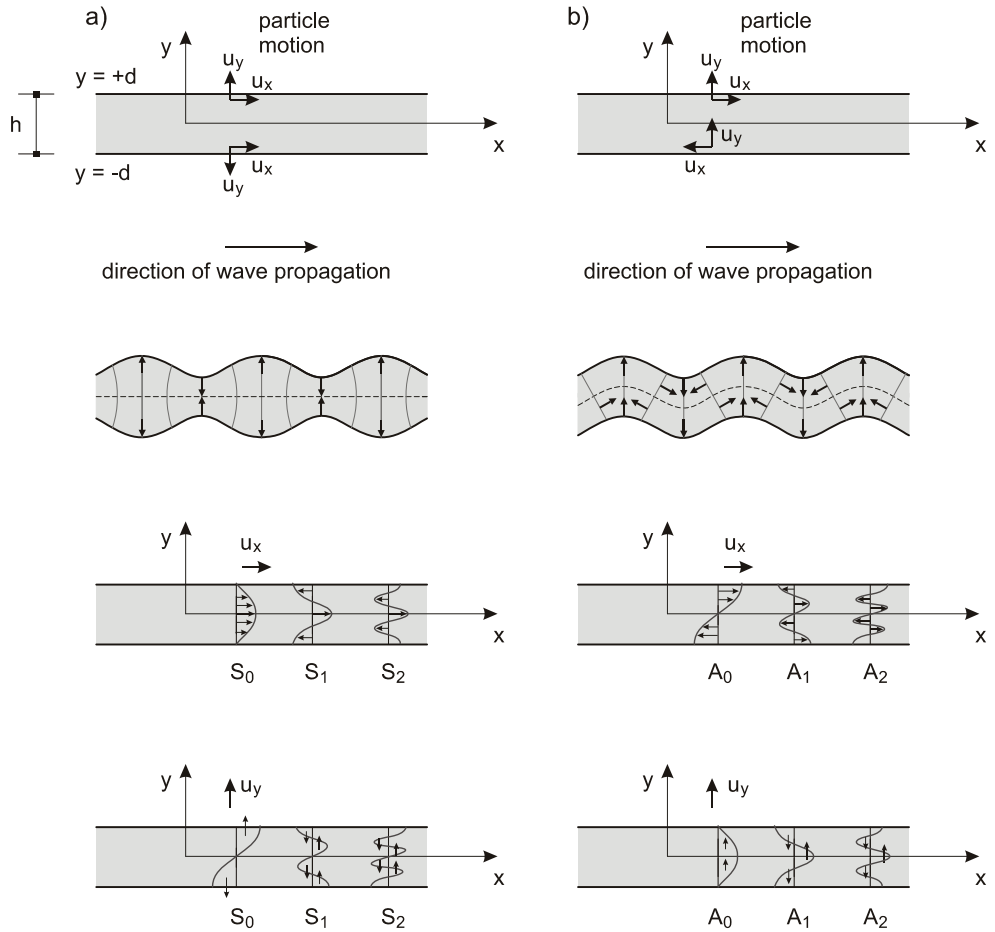


Fig. 2.3. Propagation of plate Lamb waves: a) symmetric form of motion; b) antisymmetric form of motion

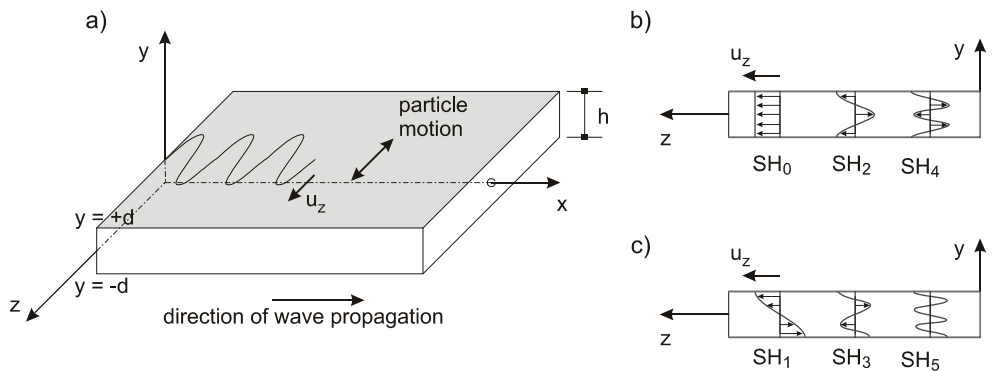


Fig. 2.4. Propagation of shear horizontal wave in the plate: a) coordinate system and particle motion; b) symmetric modes; c) antisymmetric modes

Another type of waves occurring in plates are SH waves (shear horizontal waves). The particle motion of SH waves is polarized parallel to the plate surface and perpendicular to the direction of wave propagation (Giurgiutiu 2008). As it is shown in Fig. 2.4, the particle wave motion occurs along the z axis while the wave propagation occurs along the x axis. The SH waves can exist as symmetric (SH_0, SH_2, \dots) and antisymmetric (SH_1, SH_3, \dots) modes. The dispersion relation for the SH waves is given by (see Appendix A.4):

$$c_g(\omega) = c_s \sqrt{1 - (\eta h)^2 \left(\frac{c_s}{\omega h} \right)^2}, \quad (2.10)$$

where $\eta h = n\pi/2$ and $n = 0, 2, 4, 6, \dots$ for symmetric modes and $n = 1, 3, 5, 7, \dots$ for antisymmetric modes. The examples of group velocity dispersion curves for Lamb modes as well as shear horizontal modes in a 5-mm steel plate (investigated next in Chapter 6) are given in Fig. 2.5.

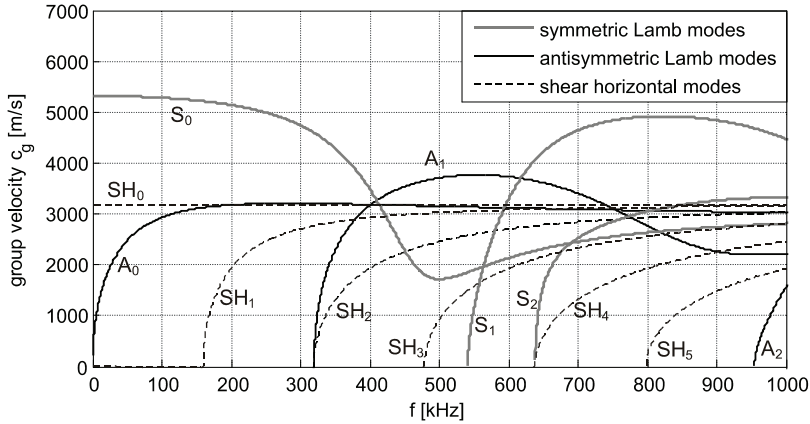


Fig. 2.5. Group velocity dispersion curves for symmetric and antisymmetric Lamb modes and shear horizontal modes for a plate of thickness $h = 5$ mm, $E = 205.35$ GPa, $\rho = 7872$ kg/m³, $\nu = 0.28$

Since the exact treatment of Lamb wave motion in structural elements is rather complicated, several models of rods, beams and plates are derived in the following sections. These models provide approximated description of wave motion. However, application of higher order theories ensures that obtained results cover with the exact guided Lamb modes.

2.2. Axial waves in rods

2.2.1. Elementary rod theory

The elementary wave theory for a thin rod assumes the presence of 1-D (one-dimensional) uniform axial stress only and neglects the lateral contraction (Doyle 1997). Consider a rod of length L , axial stiffness EA and mass per unit length ρA , where A denotes the cross-sectional area. The time-varying axial displacement of the rod is denoted as $u_x(x, t)$, where x is the spatial variable and t denotes the temporal variable. The axial strain corresponding to the deformation $u_x(x, t)$ is given by:

$$\varepsilon_{xx} = \frac{\partial u_x}{\partial x}. \quad (2.11)$$

The kinetic energy T and the strain energy U are formulated as follows:

$$T = \frac{1}{2} \int_L \rho A \dot{u}_x^2 dx, \quad (2.12)$$

$$U = \frac{1}{2} \int_L EA \left(\frac{\partial u_x}{\partial x} \right)^2 dx. \quad (2.13)$$

The governing equation can be derived using the Hamilton's principle (cf. Achenbach 1975, Doyle 1977, Nowacki 1970):

$$\delta \int_{t_1}^{t_2} (T - U + W_{\text{ext}}) dt = 0, \quad (2.14)$$

where W_{ext} is the work done by external forces $f_x(x, t)$:

$$W_{\text{ext}} = \int_L f_x u_x dx. \quad (2.15)$$

By substituting the energies (2.12) and (2.13), as well as the work of external forces (2.15) into the Hamilton's principle (2.14), the governing equation can be written as:

$$EA \frac{\partial^2 u_x}{\partial x^2} = \rho A \ddot{u}_x - f_x. \quad (2.16)$$

To obtain the spectrum relation, the displacement is assumed to have the solution in the form:

$$u_x(x, t) = \sum \hat{u}_x e^{-i(kx - \omega t)}, \quad (2.17)$$

where the summation is over the angular frequency ω , k denotes the wavenumber, $i = \sqrt{-1}$, and the amplitude spectrum \hat{u}_x is frequency dependent. Substitution of Eq. (2.17) into the homogeneous differential equation of motion (2.16) yields the characteristic equation for determining k :

$$k^2 = \frac{\rho}{E} \omega^2. \quad (2.18)$$

Therefore, the spectrum relation for the elementary rod is given by the expression:

$$k = \frac{\omega}{c_o}, \quad (2.19)$$

where the velocity $c_o = \sqrt{E/\rho}$ is called the thin-rod velocity. The dispersion relation for the elementary rod theory is:

$$c_p = \frac{\omega}{k} = \sqrt{\frac{E}{\rho}} = c_o, \quad c_g = \frac{d\omega}{dk} = \sqrt{\frac{E}{\rho}} = c_o, \quad (2.20)$$

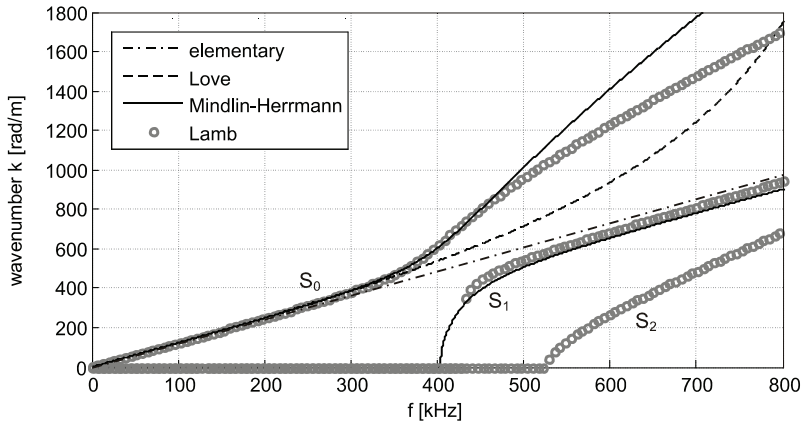


Fig. 2.6. Spectrum relation for the elementary, Love and Mindlin-Herrmann rod theories (for a steel rod of cross-section $A = 6 \times 6$ mm, $E = 200.11$ GPa, $\rho = 7556$ kg/m³, $\nu = 0.33$)

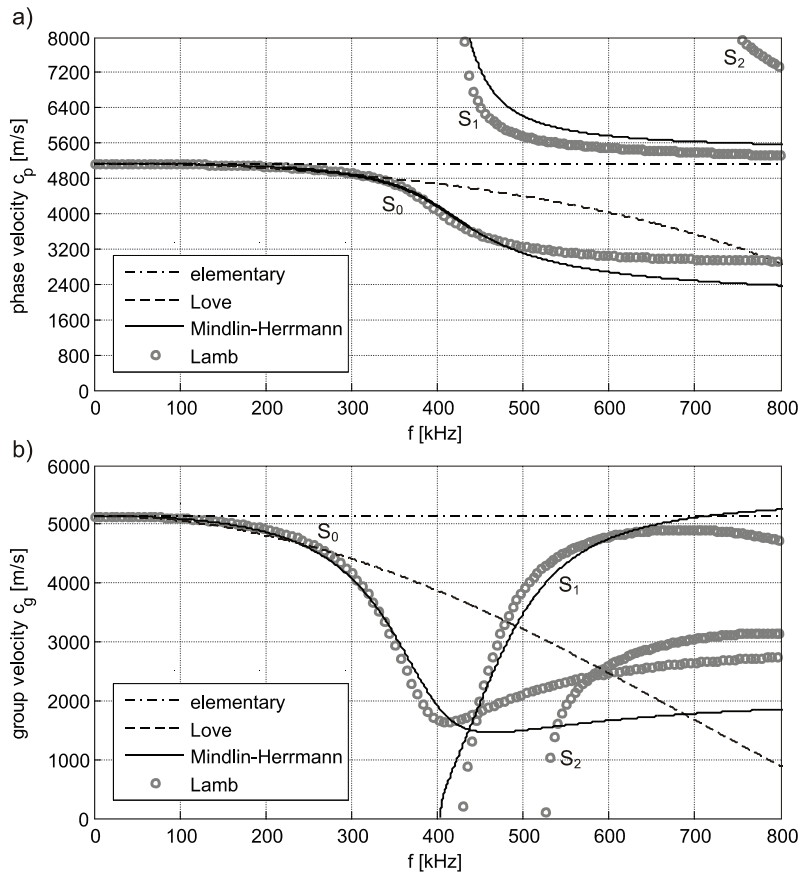


Fig. 2.7. Dispersion relation for the elementary, Love and Mindlin-Herrmann rod theories (for a steel rod of cross-section $A = 6 \times 6$ mm, $E = 200.11$ GPa, $\rho = 7556$ kg/m³, $\nu = 0.33$): a) in terms of phase velocity; b) in terms of group velocity

where the phase velocity c_p and the group velocity c_g are constant with respect to the frequency and equal to the thin-rod velocity c_o . Therefore, the result of the wave equation (2.16) is a non-dispersive signal, i.e. the signal that does not change shape as it propagates. The plot of the wavenumber variation with the frequency, called the *spectrum relation*, is shown in Fig. 2.6. The *dispersion relation*, i.e. the plot of the wave velocity against the frequency, is presented in Fig. 2.7. The spectrum and dispersion relations are calculated for a rod investigated in Chapter 4. The results of the elementary rod theory are compared with the exact Lamb modes calculated from Eq. (2.4). In the frequency range 0–800 kHz, presented in Fig. 2.6 and Fig. 2.7, there exist three Lamb symmetric modes (S_0, S_1, S_2), while the elementary rod reveals only one propagating mode S_0 . Moreover, the elementary theory coincides with the Lamb S_0 mode only at low frequencies.

2.2.2. Love rod theory

An improvement of the elementary one mode rod theory can be achieved by taking into consideration the effects of the lateral inertia. The rod not only deforms in longitudinal direction, but it also contracts due to the Poisson's ratio effect. The transverse strain ε_t and the axial strain ε_{xx} are connected through the relation $\varepsilon_t = -\nu\varepsilon_{xx}$, where ν denotes the Poisson's ratio. Such modified theory is called the Love theory after its investigator (Love 1920). In the Love theory, the strain energy is the same as for the elementary theory, given by Eq. (2.13), whereas the kinetic energy takes into account the component related with the lateral deformation (see Love 1920, Nowacki 1972, Doyle 1997):

$$T = \frac{1}{2} \int_L \left(\rho A \dot{u}_x^2 + \nu^2 \rho J_o K_L^2 \left(\frac{\partial \dot{u}_x}{\partial x} \right)^2 \right) dx, \quad (2.21)$$

where J_o is the polar moment of inertia of the rod cross-section and K_L is the adjustable parameter, introduced after Doyle (1997). Reasoning that the lateral deformation is represented not sufficiently accurately in the Love theory, the kinetic energy term associated with transverse motion is modified by the parameter K_L . Thus the governing differential equation becomes:

$$EA \frac{\partial^2 u_x}{\partial x^2} + \nu^2 \rho J_o K_L^2 \frac{\partial^2 \dot{u}_x}{\partial x^2} = \rho A \ddot{u}_x - f_x. \quad (2.22)$$

The spectrum relation for the Love theory is given by:

$$k = \pm \omega \sqrt{\frac{\rho A}{EA - \nu^2 \rho J_o K_L^2 \omega^2}}, \quad (2.23)$$

and it is nonlinear to the frequency ω , therefore, the Love theory is characterized by dispersive waves, i.e. waves for which the wave speed changes with frequency, what is illustrated in Fig. 2.6 and Fig. 2.7. The adjustable parameter K_L was set as 1.05 in this example. It was determined by the method of the least squares to give the best fit with the exact S_0 Lamb mode in the frequency range 50–300 kHz. The one mode Love model can give a reasonable approximation for the S_0 Lamb mode; however, it should be noted, that the Love theory is unable to coincide exactly with the first symmetric Lamb mode in such wide frequency range.

2.2.3. Mindlin-Herrmann rod theory

The one mode Love rod theory takes into account contraction of a rod, but it retains the Poisson's ratio relation between the axial and transverse strains. A more general approach introduces the Mindlin-Herrmann theory (Mindlin and Herrmann 1952), in which the lateral contraction $\psi(x,t)$ is assumed to be independent of the axial deformation $u_x(x,t)$. The 2-D deformations \bar{u}_x, \bar{u}_y in this theory can be approximated by (Mindlin and Herrmann 1952, Doyle 1997):

$$\begin{aligned}\bar{u}_x(x, y, t) &\approx u_x(x, t), \\ \bar{u}_y(x, y, t) &\approx \psi(x, t) y.\end{aligned}\quad (2.24)$$

The strains corresponding to the above deformations are:

$$\varepsilon_{xx} = \frac{\partial u_x}{\partial x}, \quad \varepsilon_{yy} = \psi, \quad \gamma_{xy} = \frac{\partial \psi}{\partial x} y. \quad (2.25)$$

The kinetic and strain energies are, respectively:

$$T = \frac{1}{2} \int_L \left(\rho A \dot{u}_x^2 + K_2^{M-H} \rho I \dot{\psi}^2 \right) dx, \quad (2.26)$$

$$U = \frac{1}{2} \int_L \left\{ \frac{EA}{1-\nu^2} \left[\left(\frac{\partial u_x}{\partial x} \right)^2 + \psi^2 + 2\nu \frac{\partial u_x}{\partial x} \psi \right] + K_1^{M-H} GI \left(\frac{\partial \psi}{\partial x} \right)^2 \right\} dx, \quad (2.27)$$

where I is the moment of inertia and G denotes the shear modulus. The constants K_1^{M-H} and K_2^{M-H} are adjustable parameters set to compensate the approximate form of the displacement field (2.24) and they are associated with the lateral contraction energies. Different rules to establish the correction factors K_1^{M-H} and K_2^{M-H} were considered by Doyle (1997) and Martin et al. (1994), nevertheless due to approximate character of the considered theory, neither approach can be judged more right than the other. Marin et al. (1994) proposed to select K_1^{M-H} and K_2^{M-H} based upon comparison with the 2-D finite element results. In studies, in which experimental investigations are performed, the parameters K_1^{M-H} and K_2^{M-H} can be chosen to give the best correspondence with the experimental results in the considered frequency range (Rucka 2010a, 2010b).

The governing equations for the Mindlin-Herrmann rod theory follow from the Hamilton's principle as:

$$\begin{aligned}\frac{EA}{1-\nu^2} \left(\frac{\partial^2 u_x}{\partial x^2} + \nu \frac{\partial \psi}{\partial x} \right) &= \rho A \ddot{u}_x - f_x, \\ K_1^{M-H} GI \frac{\partial^2 \psi}{\partial x^2} - \frac{EA}{1-\nu^2} \left(\nu \frac{\partial u_x}{\partial x} + \psi \right) &= K_2^{M-H} \rho I \ddot{\psi}.\end{aligned}\quad (2.28)$$

Spectral analysis represents the solutions $u_x(x,t)$ and $\psi(x,t)$ in the form:

$$u_x(x, t) = \sum \hat{u}_x e^{-i(kx - \omega t)}, \quad \psi(x, t) = \sum \hat{\psi} e^{-i(kx - \omega t)}. \quad (2.29)$$

Substitution of Eqs. (2.29) into the homogeneous differential equations of motion (2.28) results in the characteristic equation for determining the wavenumber k :

$$\begin{aligned} & \left(\frac{EA}{1-\nu^2} K_1^{M-H} GI \right) k^4 + \left(K_2^{M-H} \rho I \omega^2 - \frac{EA}{1-\nu^2} \right) \rho A \omega^2 + \\ & + \left(\frac{EA}{1-\nu^2} 2GA(1+\nu) - \frac{EA}{1-\nu^2} K_2^{M-H} \rho I \omega^2 - K_1^{M-H} GI \rho A \omega^2 \right) k^2 = 0. \end{aligned} \quad (2.30)$$

The equation (2.30) is quadratic in respect of k^2 , and therefore there are two propagating modes in the Mindlin-Herrmann rod theory. The first mode is characterized by decreasing speed with the frequency. The second mode appears above the cut-off frequency ω_c :

$$\omega_c = \sqrt{\frac{2GA}{\rho I K_2^{M-H} (1-\nu)}}. \quad (2.31)$$

The spectrum and dispersion relations for the Mindlin-Herrmann theory, given in Fig. 2.6 and Fig. 2.7, were obtained using the parameters $K_1^{M-H} = 0.68$ and $K_2^{M-H} = 1.54$. The parameters, determined by the method of least squares, were chosen to give the best fit with the first and second symmetric Lamb modes in the frequency range from 50 kHz to 500 kHz. Both modes of the Mindlin-Herrmann rod theory reveal good agreement with the exact Lamb modes.

2.3. Flexural waves in beams

2.3.1. Euler-Bernoulli beam theory

A beam is a slender member undergoing transverse displacements, and the dynamic behaviour of beams is called flexural motion. The Euler-Bernoulli theory considers only the effects of bending moments on the dynamics of a beam and neglects any shear deformation as well as rotary inertia effects. In the Euler-Bernoulli theory of bending it is assumed that plane cross-sections initially perpendicular to the beam axis remain plane and perpendicular to the neutral axis during bending. The vertical deflection \bar{u}_y is assumed to be constant through a beam thickness whereas the horizontal displacement \bar{u}_x follows the assumption of plane sections (cf. Doyle 1997):

$$\begin{aligned} \bar{u}_x(x, y, t) &\approx -y \frac{\partial u_y(x, t)}{\partial x}, \\ \bar{u}_y(x, y, t) &\approx u_y(x, t), \end{aligned} \quad (2.32)$$

where $u_y(x, t)$ is the vertical deflection of the centre line. The only non-zero strain is:

$$\epsilon_{xx} = -y \frac{\partial^2 u_y}{\partial x^2}. \quad (2.33)$$

The kinetic energy for the Euler-Bernoulli beam is defined as:

$$T = \frac{1}{2} \int_L (\rho A \dot{u}_y^2) dx, \quad (2.34)$$

and the strain energy is:

$$U = \frac{1}{2} \int_L EI \left(\frac{\partial^2 u_y}{\partial x^2} \right)^2 dx. \quad (2.35)$$

The equation of motion for the Euler-Bernoulli beam under the transverse load $f_y(x, t)$ becomes:

$$EI \frac{\partial^4 u_y}{\partial x^4} + \rho A \ddot{u}_y = f_y. \quad (2.36)$$

Spectral analysis represents the solution $u_y(x, t)$ in the form:

$$u_y(x, t) = \sum \hat{u}_y e^{-i(kx - \omega t)}, \quad (2.37)$$

which leads to the characteristic equation for determining the wavenumber k :

$$EI k^4 - \rho A \omega^2 = 0. \quad (2.38)$$

There is a one propagating mode in the Euler-Bernoulli beam and the spectrum relation is given by:

$$k = \sqrt{\omega} \left(\frac{\rho A}{EI} \right)^{1/4}, \quad (2.39)$$

which results in a dispersive solution.

2.3.2. Timoshenko beam theory

The Timoshenko beam theory takes into account the effects of the shear deformation, as well as the rotational inertia. The 2-D displacement field \bar{u}_x and \bar{u}_y is approximated by two independent functions, namely rotation $\varphi(x, t)$ and vertical displacement $u_y(x, t)$:

$$\begin{aligned} \bar{u}_x(x, y, t) &\approx -y\varphi(x, t), \\ \bar{u}_y(x, y, t) &\approx u_y(x, t). \end{aligned} \quad (2.40)$$

The axial and shear strains corresponding to the deformations (2.40) are:

$$\varepsilon_{xx} = -y \frac{\partial \varphi}{\partial x}, \quad \gamma_{xy} = -\varphi + \frac{\partial u_y}{\partial x}. \quad (2.41)$$

The kinetic energy T and the strain energy U can be stated as:

$$T = \frac{1}{2} \int_L \left(\rho A \dot{u}_y^2 + K_2^{Tim} \rho I \dot{\varphi}^2 \right) dx, \quad (2.42)$$

$$U = \frac{1}{2} \int_L \left[EI \left(\frac{\partial \varphi}{\partial x} \right)^2 + K_1^{Tim} GA \left(\frac{\partial u_y}{\partial x} - \varphi \right)^2 \right] dx. \quad (2.43)$$

By employing the Hamilton's principle, the following set of governing equations for a beam flexural motion can be obtained:

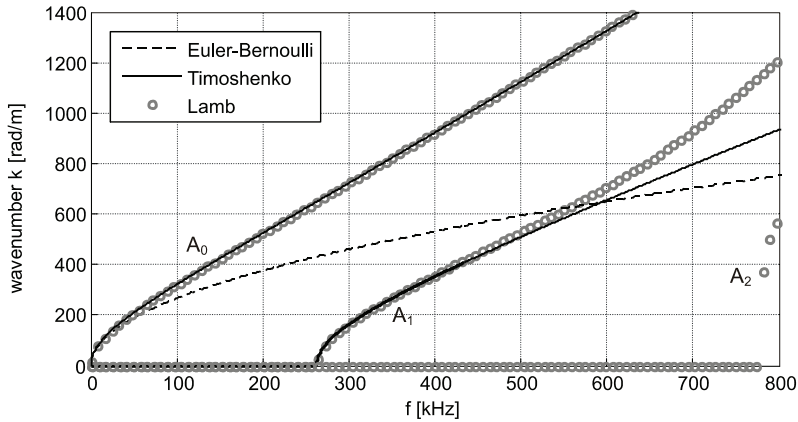


Fig. 2.8. Spectrum relation for the Euler-Bernoulli and Timoshenko beam theories (for a steel beam of cross-section $A = 6 \times 6$ mm, $E = 200.11$ GPa, $\rho = 7556$ kg/m³, $\nu = 0.33$)

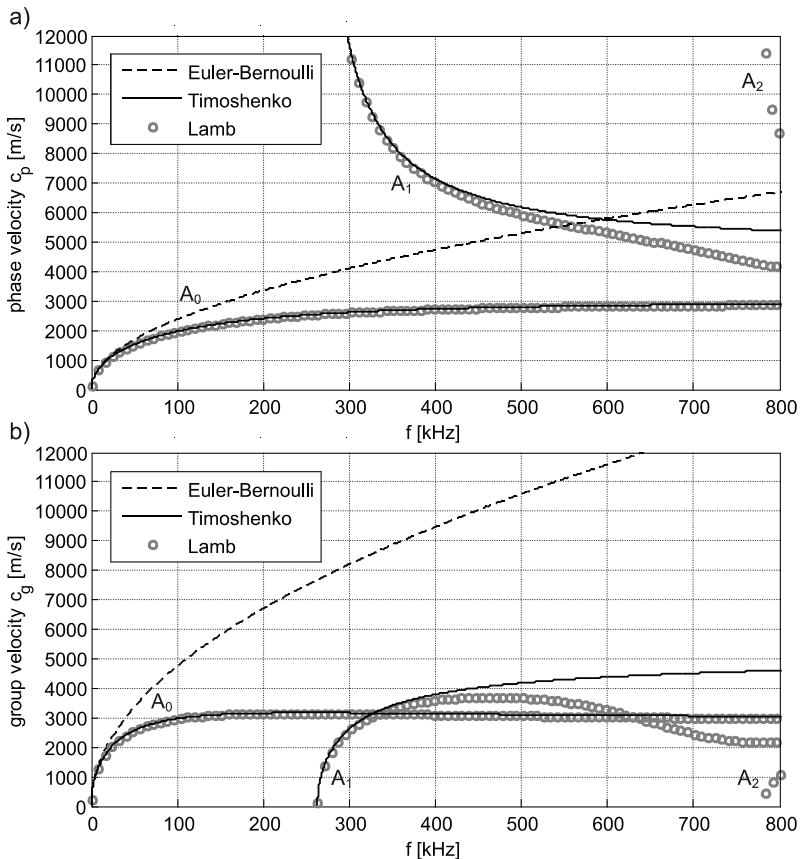


Fig. 2.9. Dispersion relation for the Euler-Bernoulli and Timoshenko beam theories (for a steel beam of cross-section $A = 6 \times 6$ mm, $E = 200.11$ GPa, $\rho = 7556$ kg/m³, $\nu = 0.33$):
a) in terms of phase velocity; b) in terms of group velocity

$$\begin{aligned}
K_1^{Tim} GA \frac{\partial}{\partial x} \left(\frac{\partial u_y}{\partial x} - \varphi \right) &= \rho A \ddot{u}_y - f_y, \\
EI \frac{\partial^2 \varphi}{\partial x^2} + K_1^{Tim} GA \left(\frac{\partial u_y}{\partial x} - \varphi \right) &= K_2^{Tim} \rho I \ddot{\varphi}.
\end{aligned} \tag{2.44}$$

The constants K_1^{Tim} and K_2^{Tim} are adjustable parameters. There are different rules to establish these parameters (see Gopalakrishnan et al. 1992, Doyle 1997). Values of the parameters K_1^{Tim} and K_2^{Tim} can be chosen based upon comparison with the 2-D finite element results or based on the comparison with the experimental results within the frequency range of interest.

Spectral analysis represents solutions in the form:

$$u_y(x, t) = \sum \hat{u}_y e^{-i(kx - \omega t)}, \quad \varphi(x, t) = \sum \hat{\varphi} e^{-i(kx - \omega t)}. \tag{2.45}$$

The dispersion relation for the Timoshenko beam can be found from the equation:

$$\begin{aligned}
(GAK_1^{Tim} EI) k^4 - (GAK_1^{Tim} \rho IK_2^{Tim} \omega^2 + EI \rho A \omega^2) k^2 + \\
+ (\rho IK_2^{Tim} \omega^2 - GAK_1^{Tim}) \rho A \omega^2 = 0.
\end{aligned} \tag{2.46}$$

Thus, the Timoshenko theory is characterized by two propagating antisymmetric modes. The first mode has increasing speed with the frequency, while the second mode appears above the cut-off frequency ω_c :

$$\omega_c = \sqrt{\frac{GAK_1^{Tim}}{\rho IK_2^{Tim}}}. \tag{2.47}$$

Figures 2.8 and 2.9 illustrate the spectrum and dispersion relations for both the Euler-Bernoulli and Timoshenko beam theories and their comparisons with the exact antisymmetric A_0 and A_1 Lamb modes calculated from Eq. (2.5). The dispersion and spectrum relations for the Timoshenko theory were obtained using the parameters $K_1^{Tim} = 0.89$, $K_2^{Tim} = 12K_1^{Tim} / \pi^2$. These parameters were chosen to ensure the best fit with the exact A_0 and A_1 Lamb modes in the frequency range 50–300 kHz. It can be seen that both modes of the Timoshenko beam theory reveal good agreement with the exact Lamb modes, whereas the Euler theory does not show the presence of the second mode and the velocity of the first mode differs considerably from the velocity obtained by the Timoshenko theory.

2.4. In-plane waves in plates

2.4.1. Plane stress theory

Force applied normal to a plate edge results in propagation of both in-plane waves, namely a longitudinal wave and a shear horizontal wave, which propagate with different speeds. Consider a plate of surface area B and thickness h . The plate lies in the xy plane bounded by planes $z = \pm h/2$ and is subjected to in-plane loads $f_x(x, y, t)$ and $f_y(x, y, t)$. In-plane displacements \bar{u}_x and \bar{u}_y are assumed to be uniform across the plate thickness:

$$\begin{aligned}\bar{u}_x(x, y, z, t) &\approx u_x(x, y, t), \\ \bar{u}_y(x, y, z, t) &\approx u_y(x, y, t).\end{aligned}\quad (2.48)$$

The normal and shear strains are:

$$\varepsilon_{xx} = \frac{\partial u_x}{\partial x}, \quad \varepsilon_{yy} = \frac{\partial u_y}{\partial y}, \quad \gamma_{xy} = \frac{\partial u_x}{\partial y} + \frac{\partial u_y}{\partial x}.$$
 (2.49)

The kinetic and strain energies associated with the in-plane behaviour are:

$$T = \frac{1}{2} \int_B (\rho h \dot{u}_x^2 + \rho h \dot{u}_y^2) dx dy, \quad (2.50)$$

$$\begin{aligned}U &= \frac{1}{2} \int_B \frac{Eh}{1-\nu^2} \left[\left(\frac{\partial u_x}{\partial x} \right)^2 + \left(\frac{\partial u_y}{\partial y} \right)^2 + 2\nu \frac{\partial u_x}{\partial x} \frac{\partial u_y}{\partial y} \right] dx dy + \\ &+ \frac{1}{2} \int_B Gh \left[\left(\frac{\partial u_x}{\partial y} \right)^2 + \left(\frac{\partial u_y}{\partial x} \right)^2 + 2 \frac{\partial u_x}{\partial y} \frac{\partial u_y}{\partial x} \right] dx dy.\end{aligned}\quad (2.51)$$

The governing equations for a plate in-plane motion are formulated as:

$$\begin{aligned}\frac{Eh}{1-\nu^2} \left(\frac{\partial^2 u_x}{\partial x^2} + \nu \frac{\partial^2 u_y}{\partial x \partial y} \right) + Gh \left(\frac{\partial^2 u_x}{\partial y^2} + \frac{\partial^2 u_y}{\partial x \partial y} \right) &= \rho h \ddot{u}_x - f_x, \\ \frac{Eh}{1-\nu^2} \left(\frac{\partial^2 u_y}{\partial y^2} + \nu \frac{\partial^2 u_x}{\partial x \partial y} \right) + Gh \left(\frac{\partial^2 u_y}{\partial x^2} + \frac{\partial^2 u_x}{\partial x \partial y} \right) &= \rho h \ddot{u}_y - f_y,\end{aligned}\quad (2.52)$$

where f_x and f_y are the external forces in the x and y directions, respectively.

To determine velocities of waves moving simultaneously in the x and y direction, the straight-crested waves are analysed. First straight-crested axial waves are considered which have particle motion in the direction of wave propagation. Taking the y -axis along the wave crest yields a y -invariant problem that depends on x variable only (cf. Giurgiutiu 2008):

$$\begin{aligned}u_x(x, y, t) &\rightarrow u_x(x, t), \\ u_y(x, y, t) &\equiv 0,\end{aligned}\quad (2.53)$$

where the particle motion is assumed to be parallel to the x -axis. Substitution of Eqs. (2.53) into homogeneous part of Eqs. (2.52) yields:

$$\frac{Eh}{1-\nu^2} \frac{\partial^2 u_x}{\partial x^2} = \rho h \ddot{u}_x. \quad (2.54)$$

The spectrum relation for the plane stress is given by:

$$k = \omega \sqrt{\frac{\rho(1-\nu^2)}{E}} = \frac{\omega}{c_L}, \quad c_L = \sqrt{\frac{E}{\rho(1-\nu^2)}}, \quad (2.55)$$

where c_L is the longitudinal wave speed in a plate. As in the case of the elementary rod, the phase velocity c_p and the group velocity c_g are constant with respect to the frequency and equal to the longitudinal wave velocity c_L , therefore the resulting waves are non-dispersive. The second considered type of waves are straight-crested shear waves. In this case particle motion is perpendicular to the direction of wave propagation. Taking the y -axis along the wave crest yields a y -invariant problem that depends on x only:

$$\begin{aligned} u_x(x, y, t) &\equiv 0, \\ u_y(x, y, t) &\rightarrow u_y(x, t), \end{aligned} \quad (2.56)$$

where the particle motion is assumed to be parallel to the y -axis. Substitution of Eqs. (2.56) into homogeneous part of Eqs. (2.52) yields:

$$Gh \frac{\partial^2 u_y}{\partial x^2} = \rho h \ddot{u}_y. \quad (2.57)$$

The spectrum relation for the plane stress theory can be expressed as:

$$k = \omega \sqrt{\rho/G} = \omega/c_S, \quad c_S = \sqrt{G/\rho}, \quad (2.58)$$

where c_S is the shear wave speed. The phase velocity c_p and the group velocity c_g are constant with respect to the frequency and equal to the shear wave velocity c_S , thus the resulting waves are non-dispersive.

2.4.2. Kane-Mindlin plate theory

In-plane waves in plates described by the equations of the plane stress theory provide non-dispersive signals. An improvement of the plane stress theory can be achieved by including the thickness-stretch effect. Kane and Mindlin (1956) developed a higher order plate theory, which takes into account coupling between extensional motion and the first mode of thickness vibration. The 3-D components of displacements (in-plane displacements \bar{u}_x , \bar{u}_y and out-of-plane displacement \bar{u}_z) in the Kane-Mindlin theory are approximated by the relations:

$$\begin{aligned} \bar{u}_x(x, y, z, t) &\approx u_x(x, y, t), \\ \bar{u}_y(x, y, z, t) &\approx u_y(x, y, t), \\ \bar{u}_z(x, y, z, t) &\approx u_z(x, y, t) 2z/h. \end{aligned} \quad (2.59)$$

The strains corresponding to the above deformations are:

$$\begin{aligned} \varepsilon_{xx} &= \frac{\partial u_x}{\partial x}, & \varepsilon_{yy} &= \frac{\partial u_y}{\partial y}, & \varepsilon_{zz} &= \frac{2}{h} u_z, \\ \gamma_{xy} &= \frac{\partial u_x}{\partial y} + \frac{\partial u_y}{\partial x}, & \gamma_{xz} &= \frac{2z}{h} \frac{\partial u_z}{\partial x}, & \gamma_{yz} &= \frac{2z}{h} \frac{\partial u_z}{\partial y}. \end{aligned} \quad (2.60)$$

The formulae for the kinetic and strain energies become:

$$T = \frac{1}{2} \int_B \left(h \rho \dot{u}_x^2 + h \rho \dot{u}_y^2 + h \rho \dot{u}_z^2 / 3 \right) dx dy, \quad (2.61)$$

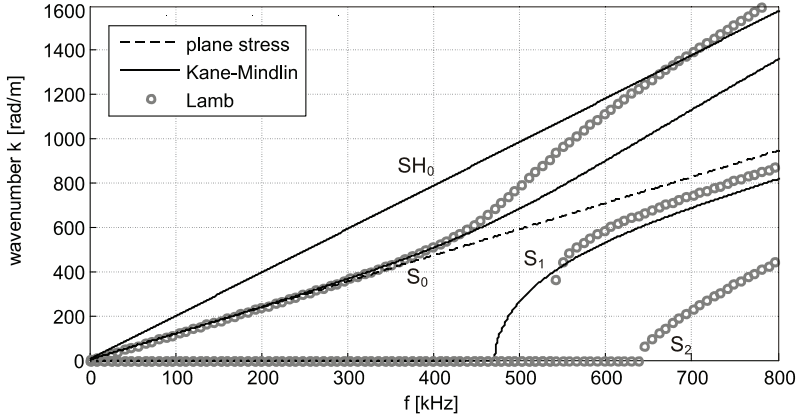


Fig. 2.10. Spectrum relation for the plane stress and Kane-Mindlin plate theories (for a steel plate of thickness $h = 5$ mm, $E = 205.35$ GPa, $\rho = 7872$ kg/m³, $\nu = 0.28$)

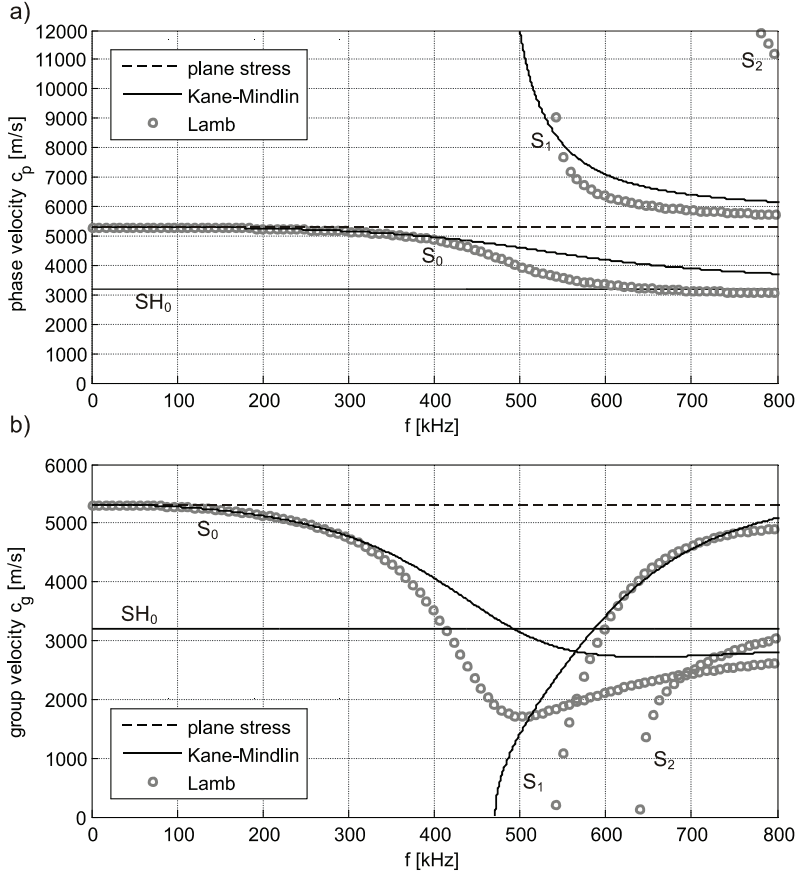


Fig. 2.11. Dispersion relation for the plane stress and Kane-Mindlin plate theories (for a steel plate of thickness $h = 5$ mm, $E = 205.35$ GPa, $\rho = 7872$ kg/m³, $\nu = 0.28$): a) in terms of phase velocity; b) in terms of group velocity

$$\begin{aligned}
U = & \frac{1}{2} \int_B (\Lambda + 2G) \left[h \left(\frac{\partial u_x}{\partial x} \right)^2 + h \left(\frac{\partial u_y}{\partial y} \right)^2 + \frac{4\kappa_{KM}^2}{h} u_z^2 \right] dx dy + \\
& + \frac{1}{2} \int_B \Lambda \left[2h \frac{\partial u_x}{\partial x} \frac{\partial u_y}{\partial y} + 4\kappa_{KM} \frac{\partial u_x}{\partial x} u_z + 4\kappa_{KM} \frac{\partial u_y}{\partial y} u_z \right] dx dy + \\
& + \frac{1}{2} \int_B G \left[h \left(\frac{\partial u_x}{\partial y} \right)^2 + h \left(\frac{\partial u_y}{\partial x} \right)^2 + 2h \frac{\partial u_x}{\partial y} \frac{\partial u_y}{\partial x} + \frac{h}{3} \left(\frac{\partial u_z}{\partial x} \right)^2 + \frac{h}{3} \left(\frac{\partial u_z}{\partial y} \right)^2 \right] dx dy,
\end{aligned} \tag{2.62}$$

where Λ , G are the Lamé constants. Substituting these energies into the Hamilton's principle, the governing equations for the Kane-Mindlin theory can be derived:

$$\begin{aligned}
(\Lambda + 2G)h \frac{\partial^2 u_x}{\partial x^2} + \Lambda h \frac{\partial^2 u_y}{\partial x \partial y} + 2\Lambda \kappa_{KM} \frac{\partial u_z}{\partial x} + Gh \frac{\partial^2 u_y}{\partial x \partial y} + Gh \frac{\partial^2 u_x}{\partial y^2} &= \rho h \ddot{u}_x - f_x, \\
(\Lambda + 2G)h \frac{\partial^2 u_y}{\partial y^2} + \Lambda h \frac{\partial^2 u_x}{\partial x \partial y} + 2\Lambda \kappa_{KM} \frac{\partial u_z}{\partial y} + Gh \frac{\partial^2 u_x}{\partial x \partial y} + Gh \frac{\partial^2 u_y}{\partial x^2} &= \rho h \ddot{u}_y - f_y, \\
\frac{Gh}{3} \frac{\partial^2 u_z}{\partial x^2} + \frac{Gh}{3} \frac{\partial^2 u_z}{\partial y^2} - \frac{4\kappa_{KM}^2}{h} (\Lambda + 2G)u_z - 2\Lambda \kappa_{KM} \frac{\partial u_x}{\partial x} - 2\Lambda \kappa_{KM} \frac{\partial u_y}{\partial y} &= \frac{\rho h \ddot{u}_z}{3},
\end{aligned} \tag{2.63}$$

where f_x and f_y are the external forces in the x and y directions, respectively. The constant κ_{KM} was inserted in the expression for the strain energy to compensate for the approximation of displacement field given by Eq. (2.59). Kane and Mindlin (1956) chose the value of κ_{KM} as $\pi/\sqrt{12}$ by equating the frequency of pure thickness vibration obtained from the plate equation of motion with the corresponding frequency obtained from three-dimensional equations.

Analysis of the straight-crested axial waves:

$$\begin{aligned}
u_x(x, y, t) &\rightarrow u_x(x, t), \\
u_y(x, y, t) &\equiv 0, \\
u_z(x, y, t) &\rightarrow u_z(x, t),
\end{aligned} \tag{2.64}$$

gives the dispersion relation in the form of the following equation:

$$\begin{aligned}
k^4 [(\Lambda + 2G)G] + \left[\rho^2 \omega^4 - \rho \omega^2 \frac{12\kappa_{KM}^2}{h^2} (\Lambda + 2G) \right] + \\
+k^2 \left[(\Lambda + 2G)^2 \frac{12\kappa_{KM}^2}{h^2} - \rho \omega^2 G - \rho \omega^2 (\Lambda + 2G) - \frac{12\Lambda^2 \kappa_{KM}^2}{h^2} \right] = 0.
\end{aligned} \tag{2.65}$$

The equation (2.65) is quadratic in k^2 , thus the Kane-Mindlin theory is characterized by two axial propagating modes S_0 and S_1 . Both modes are dispersive. The first mode reveals decreasing speed with frequency, while the second mode appears above at the cut-off frequency ω_c given by the relation:

$$\omega_c = \frac{\kappa_{KM}}{h} \sqrt{\frac{12}{\rho} (\Lambda + 2G)} \quad (2.66)$$

Analysis of the straight-crested shear waves:

$$\begin{aligned} u_x(x, y, t) &\equiv 0, \\ u_y(x, y, t) &\rightarrow u_y(x, t), \\ u_z(x, y, t) &\equiv 0, \end{aligned} \quad (2.67)$$

gives the dispersion relation for the non-dispersive shear wave:

$$k^2 = \frac{\rho}{G} \omega^2, \quad c_s = \sqrt{\frac{G}{\rho}}. \quad (2.68)$$

The spectrum and dispersion relations for the plane stress and the Kane Mindlin theories are compared with the Lamb modes in Fig. 2.10 and Fig. 2.11 (for a steel 5 mm thick plate investigated next in Chapter 6). The plane stress theory models two modes: the fundamental extensional mode and the fundamental shear horizontal mode. The shear horizontal mode is the SH_0 mode but the extensional mode only approximates the exact S_0 mode at low frequencies, because it reveals a non-dispersive character. For the Kane-Mindlin theory three modes exist, namely the first and second extensional modes and the fundamental SH_0 mode. Two extensional modes of the Kane-Mindlin theory correctly approximate the dispersion behaviour of the S_0 and S_1 Lamb modes. In Figs. 2.10 and 2.11, the parameter κ_{KM} in the Kane-Mindlin theory was chosen as 0.73 to give the best compatibility with the exact Lamb mode for the frequency range 50–300 kHz.

2.5. Flexural waves in plates

2.5.1. Kirchhoff plate theory

Flexural waves in a plate appear as a result of bending action. The plate lying in the xy plane is subjected to the transverse load $f_z(x, y, t)$ in the z direction. The Kirchhoff theory assumes that the transverse shear deformation is negligible. It is also assumed, that plane sections remain plane and perpendicular to the mid-plane after deformation. For flexural motion, the 3-D in-plane displacements \bar{u}_x , \bar{u}_y and out-of-plane displacement \bar{u}_z are approximated by the following relations:

$$\begin{aligned} \bar{u}_x(x, y, z, t) &\approx -z \frac{\partial u_z(x, y, t)}{\partial x}, \\ \bar{u}_y(x, y, z, t) &\approx -z \frac{\partial u_z(x, y, t)}{\partial y}, \\ \bar{u}_z(x, y, z, t) &\approx u_z(x, y, t). \end{aligned} \quad (2.69)$$

The normal and shear strains corresponding to the deformations (2.69) are:

$$\varepsilon_{xx} = -z \frac{\partial^2 u_z}{\partial x^2}, \quad \varepsilon_{yy} = -z \frac{\partial^2 u_z}{\partial y^2}, \quad \gamma_{xy} = -2z \frac{\partial^2 u_z}{\partial x \partial y}. \quad (2.70)$$

The kinetic energy and the strain energy for the out-of-plane flexural behaviour become:

$$T = \frac{1}{2} \int_B (\rho h \dot{u}_z^2) dx dy, \quad (2.71)$$

$$U = \frac{1}{2} \int_B \left[D \left(\frac{\partial^2 u_z}{\partial x^2} \right)^2 + 2D\nu \frac{\partial^2 u_z}{\partial x^2} \frac{\partial^2 u_z}{\partial y^2} + D \left(\frac{\partial^2 u_z}{\partial y^2} \right)^2 + \frac{Gh^3}{3} \left(\frac{\partial^2 u_z}{\partial x \partial y} \right)^2 \right] dx dy, \quad (2.72)$$

where D denotes the plate flexural rigidity:

$$D = \frac{Eh^3}{12(1-\nu^2)}. \quad (2.73)$$

The governing equation for plate flexural motion is formulated as:

$$D \left(\frac{\partial^4 u_z}{\partial x^4} + 2 \frac{\partial^4 u_z}{\partial x^2 \partial y^2} + \frac{\partial^4 u_z}{\partial y^4} \right) + \rho h \ddot{u}_z = f_z. \quad (2.74)$$

For determination of the spectrum relation, the straight-crested flexural plate waves are considered. Taking the y -axis along the wave crest yields a y -invariant problem depending on x only (Giurgiutiu 2008):

$$u_z(x, y, t) \rightarrow u_z(x, t). \quad (2.75)$$

The dispersion relation can be found from the following equation:

$$Dk^4 - \rho h \omega^2 = 0. \quad (2.76)$$

There is one propagating mode in the Kirchhoff plate theory and the spectrum relation is obtained as:

$$k = \sqrt{\omega} \left(\frac{\rho h}{D} \right)^{1/4}, \quad (2.77)$$

which results in dispersive solution.

2.5.2. Mindlin plate theory

The Mindlin plate theory (Mindlin 1951) takes the shear deformation and the effects of rotatory inertia into account. The 3-D displacements \bar{u}_x , \bar{u}_y and \bar{u}_z at any location z in the plate thickness can be approximated by:

$$\begin{aligned} \bar{u}_x(x, y, z, t) &\approx -z\psi_x(x, y, t), \\ \bar{u}_y(x, y, z, t) &\approx -z\psi_y(x, y, t), \\ \bar{u}_z(x, y, z, t) &\approx u_z(x, y, t). \end{aligned} \quad (2.78)$$

where ψ_x and ψ_y are the rotations of the mid-plane and u_z is the transverse (out-of-plane) displacement of the plate mid-plane. The normal and shear strains corresponding to above deformations become:

$$\begin{aligned}\varepsilon_{xx} &= -z \frac{\partial \psi_x}{\partial x}, & \varepsilon_{yy} &= -z \frac{\partial \psi_y}{\partial y}, \\ \gamma_{xy} &= -z \left(\frac{\partial \psi_x}{\partial y} + \frac{\partial \psi_y}{\partial x} \right), & \gamma_{xz} &= \frac{\partial u_z}{\partial x} - \psi_x, & \gamma_{yz} &= \frac{\partial u_z}{\partial y} - \psi_y.\end{aligned}\quad (2.79)$$

The kinetic and strain energies are:

$$T = \frac{1}{2} \int_B \left(\frac{\rho h^3}{12} \dot{\psi}_x^2 + \frac{\rho h^3}{12} \dot{\psi}_y^2 + \rho h \dot{u}_z^2 \right), \quad (2.80)$$

$$\begin{aligned}U &= \frac{1}{2} \int_B \left[D \left(\left(\frac{\partial \psi_x}{\partial x} \right)^2 + 2\nu \frac{\partial \psi_x}{\partial x} \frac{\partial \psi_y}{\partial y} + \left(\frac{\partial \psi_y}{\partial y} \right)^2 \right) \right] dx dy + \\ &+ \frac{1}{2} \int_B \left[\frac{Gh^3}{12} \left(\left(\frac{\partial \psi_x}{\partial y} \right)^2 + 2 \frac{\partial \psi_x}{\partial y} \frac{\partial \psi_y}{\partial x} + \left(\frac{\partial \psi_y}{\partial x} \right)^2 \right) \right] dx dy + \\ &+ \frac{1}{2} \int_B \left[\kappa^2 Gh \left(\left(\frac{\partial u_z}{\partial x} \right)^2 - 2 \frac{\partial u_z}{\partial x} \psi_x + (\psi_x)^2 + \left(\frac{\partial u_z}{\partial y} \right)^2 - 2 \frac{\partial u_z}{\partial y} \psi_y + (\psi_y)^2 \right) \right] dx dy.\end{aligned}\quad (2.81)$$

The flexural motion of a Mindlin plate is governed by the following three equations:

$$\begin{aligned}\kappa^2 Gh \frac{\partial}{\partial x} \left(\frac{\partial u_z}{\partial x} - \psi_x \right) + \kappa^2 Gh \frac{\partial}{\partial y} \left(\frac{\partial u_z}{\partial y} - \psi_y \right) &= \rho h \ddot{u}_z - f_z, \\ D \left(\frac{\partial^2 \psi_x}{\partial x^2} + \nu \frac{\partial^2 \psi_y}{\partial x \partial y} \right) + \frac{Gh^3}{12} \left(\frac{\partial^2 \psi_x}{\partial y^2} + \frac{\partial^2 \psi_y}{\partial x \partial y} \right) + \kappa^2 Gh \left(\frac{\partial u_z}{\partial x} - \psi_x \right) &= \frac{\rho h^3}{12} \ddot{\psi}_x, \\ D \left(\frac{\partial^2 \psi_y}{\partial y^2} + \nu \frac{\partial^2 \psi_x}{\partial x \partial y} \right) + \frac{Gh^3}{12} \left(\frac{\partial^2 \psi_y}{\partial x^2} + \frac{\partial^2 \psi_x}{\partial x \partial y} \right) + \kappa^2 Gh \left(\frac{\partial u_z}{\partial y} - \psi_y \right) &= \frac{\rho h^3}{12} \ddot{\psi}_y,\end{aligned}\quad (2.82)$$

where κ is a shear correction factor set by Mindlin (1951) as $\kappa = \pi / \sqrt{12}$ by matching the cut-off frequency of the plate flexural mode with the second antisymmetric mode of 3-D elastic theory.

Analysis of straight-crested flexural plate waves:

$$\begin{aligned}u_z(x, y, t) &\rightarrow u_z(x, t), \\ \psi_x(x, y, t) &\rightarrow \psi_x(x, t), \\ \psi_y(x, y, t) &\equiv 0,\end{aligned}\quad (2.83)$$

gives the spectrum relation in the form of the following equation:

$$k^4 \left(D \kappa^2 Gh \right) + k^2 \left(-\rho h D \omega^2 - \kappa^2 \frac{Gh^4}{12} \rho \omega^2 \right) + \left(\frac{\rho^2 h^4}{12} \omega^4 - \kappa^2 \rho h^2 G \omega^2 \right) = 0. \quad (2.84)$$

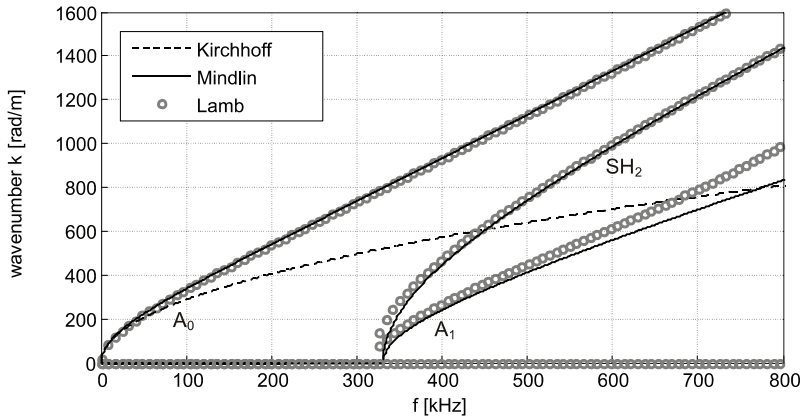


Fig. 2.12. Spectrum relation for the Kirchhoff and Mindlin plate theories (for a steel plate of thickness $h = 5$ mm, $E = 205.35$ GPa, $\rho = 7872$ kg/m³, $\nu = 0.28$)

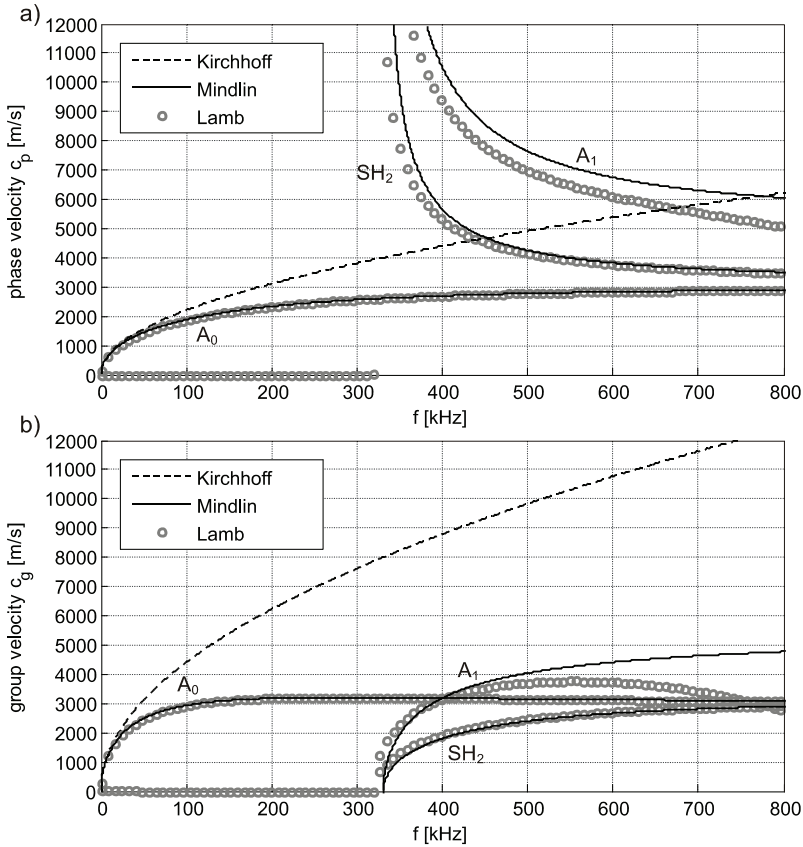


Fig. 2.13. Dispersion relation for the Kirchhoff and Mindlin plate theories (for a steel plate of thickness $h = 5$ mm, $E = 205.35$ GPa, $\rho = 7872$ kg/m³, $\nu = 0.28$): a) in terms of phase velocity; b) in terms of group velocity

There exist two propagating flexural modes. The second mode appears above cut-off frequency ω_c :

$$\omega_c = \sqrt{\frac{12G\kappa^2}{\rho h^2}} . \quad (2.85)$$

Analysis of straight-crested shear waves:

$$\begin{aligned} u_z(x, y, t) &\equiv 0, \\ \psi_x(x, y, t) &\equiv 0, \\ \psi_y(x, y, t) &\rightarrow \psi_y(x, t), \end{aligned} \quad (2.86)$$

gives the spectrum relation for the dispersive shear wave (SH₂ mode):

$$k^2 = \frac{\rho\omega^2}{G} - \frac{12\kappa^2}{h^2}, \quad (2.87)$$

which appears above the cut-off frequency ω_c :

$$\omega_c = \sqrt{\frac{12G\kappa^2}{\rho h^2}} . \quad (2.88)$$

Spectrum and dispersion relations for the Kirchhoff and Mindlin plate theories are presented in Fig. 2.12 and Fig. 2.13, respectively. For the Kirchhoff plate theory, only one propagating flexural mode exists. The dispersion relation shows that only for low frequencies the Kirchhoff theory agrees with the first antisymmetric Lamb mode (A₀ mode). For the higher frequencies, velocity of the first mode based on the Kirchhoff theory differs considerably from the velocity of the Lamb A₀ mode. The Mindlin theory provides three modes: two antisymmetric modes (A₀ and A₁) and one shear mode (SH₂). These three modes reveal good agreement with the exact Lamb modes. The parameter κ for the Mindlin plate theory was determined by the method of least squares and its value was set to 0.94. This value ensures the best compatibility to the exact Lamb modes for the frequency range 50–300 kHz.

2.6. Summary and conclusions

In this chapter, a review of elastic wave propagation in structural elements has been conducted. Several models of rods, beams and plates, providing approximated description of wave motion, have been derived. The necessity of using higher order theories when analysing ultrasonic frequency ranges has been demonstrated. It was found that approximated higher order theories can adequately account for dispersive behaviour of the lowest symmetric and antisymmetric modes over the substantial range of frequencies in bars and plates.

Damage detection should be based on single wave propagation mode, if possible, because existence of a few modes complicates localization of defects. Therefore, an effort should be made on the development of an approximate description of wave motions that provides the first mode behaviour compatible with the exact Lamb mode.

The elementary rod theory gives non-dispersive wave results, thus it coincides with the first symmetric Lamb-wave mode only at low frequencies. The Love model provides a reasonable approximation for the first symmetric mode (S_0 mode), however this theory reveals a drawback, when the spectral element method is used, which will be discussed in Chapter 3. Therefore, the Mindlin-Herrmann theory is suggested to be used in damage detection systems, because it has excellent the S_0 mode behaviour. When analysing flexural waves in beams, the Timoshenko beam theory should be used instead of the Euler-Bernoulli theory. In the case of in-plane wave propagation in plates, the plane stress theory cannot describe dispersion. Similarly, for flexural motion in plates the Kirchhoff theory is applicable only for low frequencies. Higher order theories: the Kane-Mindlin theory for in-plane waves and the Mindlin theory for flexural waves yield very good convergence with the exact Lamb modes over a substantial range of frequencies.

Chapter 3

SPECTRAL ELEMENT METHOD

Modelling of wave propagation in structural elements and structures has been the subject of intensive investigations over the years. Many analytical techniques have been developed for treating wave motion. However, wave propagation in engineering objects with aspects of complex geometry, connection of members, boundaries and discontinuities is still an open area of research.

It is possible to model wave propagation phenomena in both time and frequency domains. One of efficient frequency-based methods is the spectral finite element method (SFEM) developed by Doyle (1988) for longitudinal wave propagation in an elementary rod. Doyle and Farris presented spectral element formulation of flexural waves in an Euler-Bernoulli beam (Doyle and Farris 1990a) and 3-D frame structures (Doyle and Farris 1990b). Spectral elements in the frequency domain for higher order Mindlin-Herrmann rod and Timoshenko beam theories were developed by Martin et al. (1994) and Gopalakrishnan et al (1992). The book of Doyle (1997) gives a broad reference on spectral analysis of wave propagation in structures. The SFEM technique is based on a Fourier spectral analysis. Here the *spectral analysis* denotes working in terms of the spectrum (Doyle 1997). In this method, the assembled system of equations is solved in the frequency domain and the inverse fast Fourier transform is utilized to convert the frequency domain results back to the time domain. The SFEM utilizes the exact solution of differential equations governing a problem, therefore the distribution of mass and rotational inertia of a structural element is exact. Very few elements are required to model the system, because only one spectral element needs to be placed between any two joints, which substantially reduces the total number of degrees of freedom in a system. To handle local regions of non-uniformity, the spectral finite element method can be extended by the introduction of a super-element (Gopalakrishnan and Doyle 1995). Numerical analyses of wave propagation by the SFEM in an isotropic cracked rod, a cracked beam and a plate with a crack can be found in papers by Krawczuk et al. (2003, 2004, 2006a, 2006b), Ostachowicz (2008), Palacz and Krawczuk (2002). The SFEM were extended by Gopalakrishnan et al. (2008) to anisotropic media. Other papers concerning wave propagation in composite media are directed to analysis of laminated composite beams (e.g. Mahapatra et al. 2000, Mahapatra and Gopalakrishnan 2003, Palacz et al. 2005b), composite beams with delaminations and inclusions (e.g. Chakraborty et al. 2002, Mahapatra and Gopalakrishnan 2004, Palacz et al. 2005c) or laminated composite plates (e.g. Chakraborty and Gopalakrishnan 2005, 2006). The main disadvantage of the SFEM is the fact that the method is effective only to a few cases where the exact solutions can be found to the governing equations. In 2-D and 3-D domains of arbitrary geometries, the solution of wave equations is almost impossible and therefore the method cannot be used in the general sense (Gopalakrishnan 2000). Moreover, in the SFEM mainly infinite and semi-infinite elements are considered, because the use of the fast Fourier transform (FFT) always provides periodicity. To overcome these drawbacks of the conventional Fourier-based SFEM, Mitra and Gopalakrishnan (2005, 2006) proposed the use of the wavelet transform instead of the Fourier transform. Igawa et al. (2004) applied

the Laplace transform to avoid the problem of periodicity, which made the analysis of 3-D frame structures with finite-length beams based on the Euler-Bernoulli theory possible.

Modelling of wave propagation can also be performed in the time domain by the finite element method (FEM), see e.g. papers by Moser et al. (1999), Kishore et al. (2000), Hill et al. (2004), Bartoli et al. (2005) or Gao et al. (2006). The advantage of this approach is the availability of numerous commercial FEM codes, e.g. ANSYS (Gao et al. 2006, Moser et al. 1999), ABAQUS EXPLICIT (Bartoli et al. 2005), PAFEC-FE (Hill et al. 2004) and its great ability to analyse structures with complicated geometry. However, the application of the FEM to model wave propagation requires very fine mesh, i.e. it is recommended to use more than 20 nodes per the shortest wavelength (Moser et al. 1999). The improvement of the finite element method accuracy may follow two main strategies, either by decreasing the element size h remaining the polynomial order fixed (h -refinement) or by increasing the degree p of the polynomial remaining the element size fixed (p -refinement), cf. Bathe (1996), Boyd (2000), Campion and Jarvis (1996), Stein et al. (2004), Zienkiewicz and Taylor (2000a). The combination of both above refinement approaches is classified as h - p -refinement (see Zienkiewicz et al. 1989, Babuška and Suri 1990, Szabó 1990). Low order ($p = 1, 2$) h -type elements exhibit an algebraic convergence to the exact solution, i.e. the error is proportional to $1/N^p$, where N is the number of degrees of freedom in the model. Finite elements of h -type are preferred for their computational efficiency; however, in structural dynamics they have a serious deficiency in that they propagate elastic waves poorly (Sprague and Geers 2008). Standard p -elements have Lagrange shape functions defined over equispaced nodes and they show higher convergence rate than the h -type version. The p - and h - p methods can yield a highly desirable exponential rate of convergence with the error proportional to $1/\exp(\alpha N^\theta)$, where α and θ are positive constants (Stein et al. 2004). The exponential convergence is also referred to as spectral convergence or infinite-order accuracy.

An expansion of the FEM is the time domain spectral element method (SEM) introduced by Patera (1984) in computational fluid mechanics. The SEM has the same viewpoint, as the p -version of the FEM, i.e. the main idea of the SEM is to use an interpolating polynomial of high degree. The term *spectral* means here that the numerical error decreases faster than any power of $1/p$, where p is the order of the polynomial expansion (Pozrikidis 2005). The SEM combines the accuracy of the global spectral methods with the ability of the FEM to solve problems involving complicated geometries. The essential difference between the p -version of the FEM and the SEM lies in the choice of interpolation nodes (cf. Canuto et al. 1998). In the spectral element method, the element interpolation nodes are placed at the zeros of an appropriate family of orthogonal polynomials (Pozrikidis 2005). There are two main approaches in the SEM. The first approach, called the *Legendre spectral element method*, employs Lagrange polynomials as shape functions applied at the Gauss-Legendre-Lobatto (GLL) nodes (e.g. Komatitsch and Vilotte 1998, Komatitsch et al. 1999, 2001, Kudela et al. 2007a, 2007b, Tromp et al. 2008, Chróscielewski et al. 2009, Rucka 2010a). As a consequence of the choice of the Lagrange interpolants at the GLL points in conjunction with the GLL integration rule, the element mass matrix is exactly diagonal by construction (Komatitsch et al. 2001). In the second approach, called the *Chebyshev spectral element method*, element shape functions are based on the Chebyshev polynomials and they pass through the Chebyshev-Gauss-Lobatto nodes (e.g. Dauksher and Emery 1997, 1999, 2000, Patera 1984, Sridhar et al. 2006). The element matrices are evaluated using the Gauss-Legendre integration, which provides a non-

diagonal mass matrix. To obtain diagonal mass matrix, the diagonalization scheme based on a row-summing procedure can be applied, as proposed by Dauksher and Emery (1997).

Spectral elements in the time domain are available for structural elements: elementary rods and beams (Kudela et al. 2007a), bending plates (Kudela et al. 2007b, Chróścielewski et al. 2010) or plane stress problems (Sridhar et al. 2006, Žak et al. 2006a, 2006b, Chróścielewski et al. 2011). An analysis of wave propagation in 3-D truss and 3-D frame structures is given in papers by Chróścielewski et al. (2009) and Witkowski et al. (2009). Peng et al. (2009) developed a 3-D spectral element and they used it to analysis of wave propagation in plates. A spectral element formulation for wave propagation in rods, beams and frames based on higher order theories was presented by Rucka (2010a, 2010b). Rucka (2011) developed a spectral plate element based on a higher order extensional plate theory.

The aim of the present chapter is to develop a numerical tool in the form of the Legendre spectral element method. Novel spectral elements based on higher order rod theories (the Love rod theory and the Mindlin-Herrmann rod theory), as well as on the higher order Kane-Mindlin extensional plate theory are formulated. A family of computer programs incorporating the developed spectral element method formulation for wave propagation problems has been written in MATLAB[®] (for bars and frames) and in FORTRAN (for plates). In comparison with the classical FEM, beside the aforementioned fact that the mass matrix is diagonal, which allows to reduce significantly the algorithm cost, the very important advantage of the SEM is the possibility of reduction in grid points, i.e. in the SEM the required number of nodes per the shortest wavelength is of order of 10 or less.

3.1. General formulation of the spectral element method

The spectral element method formulation discussed in this study is based upon a weak formulation of equations of motion. Following classical steps the weak formulation (here: the principle of virtual work) is obtained in the form (cf. Fung 1965, Reddy 2002):

$$\delta W = \delta W_{\text{kin}} + \delta W_{\text{damp}} + \delta W_{\text{int}} - \delta W_{\text{ext}} = 0, \quad (3.1)$$

$$\delta W = \int_{\Omega} \delta \mathbf{u}^T \rho \ddot{\mathbf{u}} d\Omega + \int_{\Omega} \delta \mathbf{u}^T \eta_d \dot{\mathbf{u}} d\Omega + \int_{\Omega} \delta \boldsymbol{\varepsilon}^T \mathbf{E} \boldsymbol{\varepsilon} d\Omega - \int_{\Omega} \delta \mathbf{u}^T \mathbf{f}_b d\Omega - \int_{\partial\Omega_f} \delta \mathbf{u}^T \mathbf{f}_s d\partial\Omega = 0, \quad (3.2)$$

where \mathbf{u} and $\boldsymbol{\varepsilon}$ are displacements and strains, $\delta \mathbf{u}$ and $\delta \boldsymbol{\varepsilon}$ are corresponding virtual displacements and virtual strains, \mathbf{f}_b are body forces, \mathbf{f}_s are surface tractions, \mathbf{E} denotes the stress-strain matrix of the material, ρ is the mass density and η_d is a damping property parameter. The solution domain is denoted as Ω and its part of the boundary on which the surface forces are prescribed is denoted as $\partial\Omega_f$. In the SEM, the domain Ω can be approximated as a sum of n_{el} nonoverlapping elements $\Omega_{(e)}$, i.e. $\Omega \approx \bigcup_{e=1}^{n_{el}} \Omega_{(e)}$ and $\Omega_{(i)} \cap \Omega_{(j)} = \emptyset$ for $i \neq j$. Finite element approximations to displacements, virtual displacements, strains and virtual strains are denoted by (cf. Bathe 1996, Hughes 2000, Liu and Quek 2003, Zienkiewicz and Taylor 2000a, 2000b):

$$\mathbf{u}(\mathbf{x}, t) = \mathbf{H}(\mathbf{x}) \mathbf{q}_{(e)}(t), \quad \delta \mathbf{u}(\mathbf{x}) = \mathbf{H}(\mathbf{x}) \delta \mathbf{q}_{(e)}, \quad (3.3)$$

$$\boldsymbol{\varepsilon}(\mathbf{x}, t) = \mathbf{B}(\mathbf{x}) \mathbf{q}_{(e)}(t), \quad \delta \boldsymbol{\varepsilon}(\mathbf{x}) = \mathbf{B}(\mathbf{x}) \delta \mathbf{q}_{(e)}. \quad (3.4)$$

In the above, $\mathbf{q}_{(e)}(t)$ is the vector of element nodal displacements, $\mathbf{H}(\mathbf{x})$ is the matrix of interpolation functions (a.k.a. shape function matrix) of an element and $\mathbf{B}(\mathbf{x})$ is the strain-displacement transformation matrix given by the following relation:

$$\mathbf{B}(\mathbf{x}) = \mathbf{D}\mathbf{H}(\mathbf{x}), \quad (3.5)$$

where \mathbf{D} is the differential operator matrix. Substitution of Eqs. (3.3) and (3.4) into Eq. (3.2) provides the following set of equations on the local element level:

$$\mathbf{M}_{(e)}\ddot{\mathbf{q}}_{(e)} + \mathbf{C}_{(e)}\dot{\mathbf{q}}_{(e)} + \mathbf{K}_{(e)}\mathbf{q}_{(e)} = \mathbf{p}_{(e)}, \quad (3.6)$$

where $\mathbf{K}_{(e)}$, $\mathbf{C}_{(e)}$ and $\mathbf{M}_{(e)}$ are the stiffness, damping and mass element matrices, and $\mathbf{p}_{(e)}$ is the vector of external forces acting on nodes of an element:

$$\mathbf{M}_{(e)} = \int_{\Omega_{(e)}} \mathbf{H}^T \rho \mathbf{H} d\Omega, \quad (3.7)$$

$$\mathbf{C}_{(e)} = \int_{\Omega_{(e)}} \mathbf{H}^T \eta_d \mathbf{H} d\Omega, \quad (3.8)$$

$$\mathbf{K}_{(e)} = \int_{\Omega_{(e)}} \mathbf{B}^T \mathbf{E} \mathbf{B} d\Omega, \quad (3.9)$$

$$\mathbf{p}_{(e)} = \int_{\Omega_{(e)}} \mathbf{H}^T \mathbf{f}_b d\Omega + \int_{\partial\Omega_{f(e)}} \mathbf{H}^T \mathbf{f}_s d\partial\Omega. \quad (3.10)$$

Then the system of equations of motion is built in the course of standard aggregation of element matrices and vectors referred to the structural coordinate system:

$$\mathbf{M} = \mathbf{A}_{e=1}^{n_{el}} \mathbf{M}_{(e)}, \quad \mathbf{C} = \mathbf{A}_{e=1}^{n_{el}} \mathbf{C}_{(e)}, \quad \mathbf{K} = \mathbf{A}_{e=1}^{n_{el}} \mathbf{K}_{(e)}, \quad \mathbf{p} = \mathbf{A}_{e=1}^{n_{el}} \mathbf{p}_{(e)}, \quad (3.11)$$

giving the global equations of equilibrium:

$$\mathbf{M}\ddot{\mathbf{q}} + \mathbf{C}\dot{\mathbf{q}} + \mathbf{K}\mathbf{q} = \mathbf{p}. \quad (3.12)$$

3.1.1. Definition of element nodes

In the spectral element method approach, the choice of the coordinates of the element nodes plays a crucial role. As it will be shown in this chapter, the appropriate distribution of element nodes can provide a diagonal mass matrix and avoid the Runge effect that occurs for high-order elements in the case of evenly distributed nodes. In this work, Legendre type spectral elements are studied, for which the $n = N + 1$ element interpolation nodes are defined in the parent (natural) coordinate system $\zeta \in [-1, +1]$ as the roots of the following equation (see Hilderbrand 1956, Canuto et al. 1998):

$$(1 - \zeta^2) \frac{dP_N(\zeta)}{d\zeta} = 0, \quad (3.13)$$

where P_N denotes the orthogonal Legendre polynomial of degree N . The first few members of the family of Legendre polynomials are (cf. Hilderbrand 1956, Pozrikidis 2005):

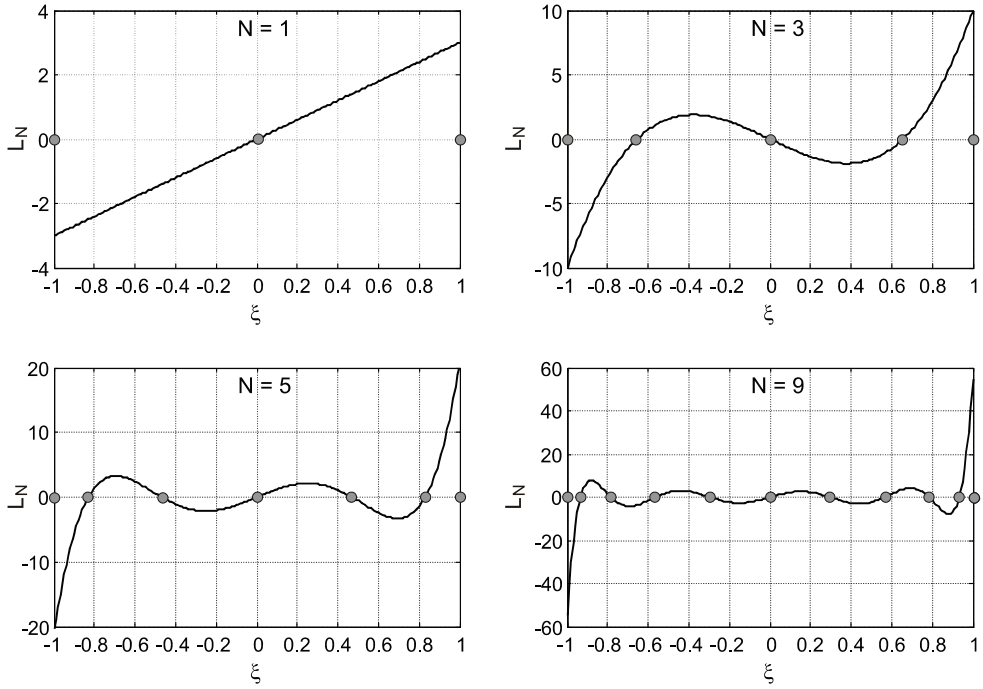


Fig. 3.1. Graphs of Lobatto polynomials L_N for $N = 1, 3, 5, 9$ in the parent domain

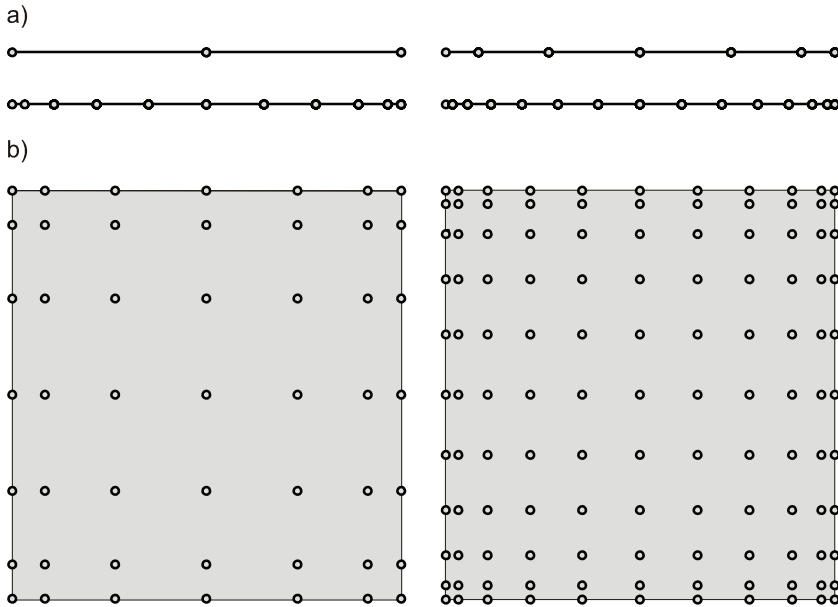


Fig. 3.2. Distribution of Gauss-Lobatto-Legendre element interpolation nodes: a) in one-dimensional elements with 3, 7, 11, 15 nodes; b) in two-dimensional elements with 7×7 nodes and 11×11 nodes

$$\begin{aligned}
P_0(\xi) &= 1, & P_1(\xi) &= \xi, \\
P_2(\xi) &= \frac{1}{2}(-1 + 3\xi^2), & P_3(\xi) &= \frac{1}{2}(-3\xi + 5\xi^3), \\
P_4(\xi) &= \frac{1}{8}(3 - 30\xi^2 + 35\xi^4), & P_5(\xi) &= \frac{1}{8}(15\xi - 70\xi^3 + 63\xi^5), \\
P_N(\xi) &= \frac{1}{2^N N!} \left[\frac{d^N}{d\xi^N} (\xi^2 - 1)^N \right].
\end{aligned} \tag{3.14}$$

The derivatives of Legendre polynomials P_N define the Lobatto polynomials L_N :

$$\begin{aligned}
L_{N-1}(\xi) &= dP_N(\xi)/d\xi, \\
L_0(\xi) &= 1, & L_1(\xi) &= 3\xi, \\
L_2(\xi) &= \frac{1}{2}(-3 + 15\xi^2), & L_3(\xi) &= \frac{1}{8}(-60\xi + 140\xi^3), \\
L_4(\xi) &= \frac{1}{8}(15 - 210\xi^2 + 315\xi^4), & L_5(\xi) &= \frac{1}{8}(210\xi - 1260\xi^3 + 1386\xi^5), \\
L_N(\xi) &= \frac{1}{2^{N+1}(N+1)!} \frac{d^{N+2}}{d\xi^{N+2}} (\xi^2 - 1)^{N+1},
\end{aligned} \tag{3.16}$$

which explains why this approach is also known as the Lobatto SEM. Therefore, the Eq. (3.13) can be rewritten for the one-dimensional problem in the parent domain with variable $\xi \in [-1, +1]$ as:

$$(1 - \xi^2)L_{N-1}(\xi) = 0, \tag{3.17}$$

or in the two-dimensional problem in the natural coordinate system with variables $\xi, \eta \in [-1, +1]$ as:

$$(1 - \xi^2)L_{N-1}(\xi) = 0, \quad (1 - \eta^2)L_{N-1}(\eta) = 0. \tag{3.18}$$

Figure 3.1 presents the Lobatto polynomials of degree $N = 1, 3, 5, 9$. Zeros of the Lobatto polynomials determine the localization of $n - 2$ intermediate element interpolation nodes. The location of the first and the last node is fixed as $\xi_1 = -1$ and $\xi_n = 1$. Distribution of the GLL element interpolation nodes in one- and two-dimensional elements is illustrated in Fig. 3.2. Note that the GLL nodes are non-uniformly distributed, and the concentration of nodes reveals at the element ends.

3.1.2. Definition of shape functions

In the presented Legendre SEM formulation, all vector variables are interpolated using Lagrange interpolation. The Lagrange polynomial of degree N is defined by:

$$H_a(\xi) = \prod_{k=1, k \neq a}^{N+1} \frac{\xi - \xi_k}{\xi_a - \xi_k}, \quad a = 1, 2, \dots, N+1, \tag{3.19}$$

and satisfies the properties (cf. Hilderbrand 1956):

$$H_a(\xi_k) = \delta_{ak}, \quad \sum_{a=1}^{N+1} H_a(\xi) = 1, \tag{3.20}$$

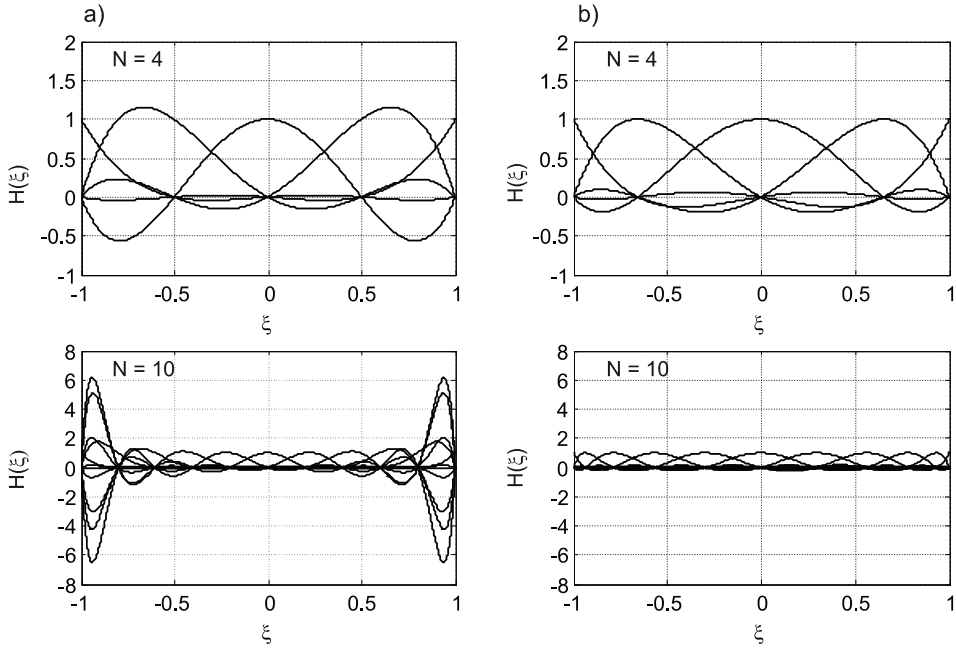


Fig. 3.3. Graphs of Lagrange interpolation functions of degree $N = 4$ and degree $N = 10$:
a) evenly spaced nodes; b) GLL nodes

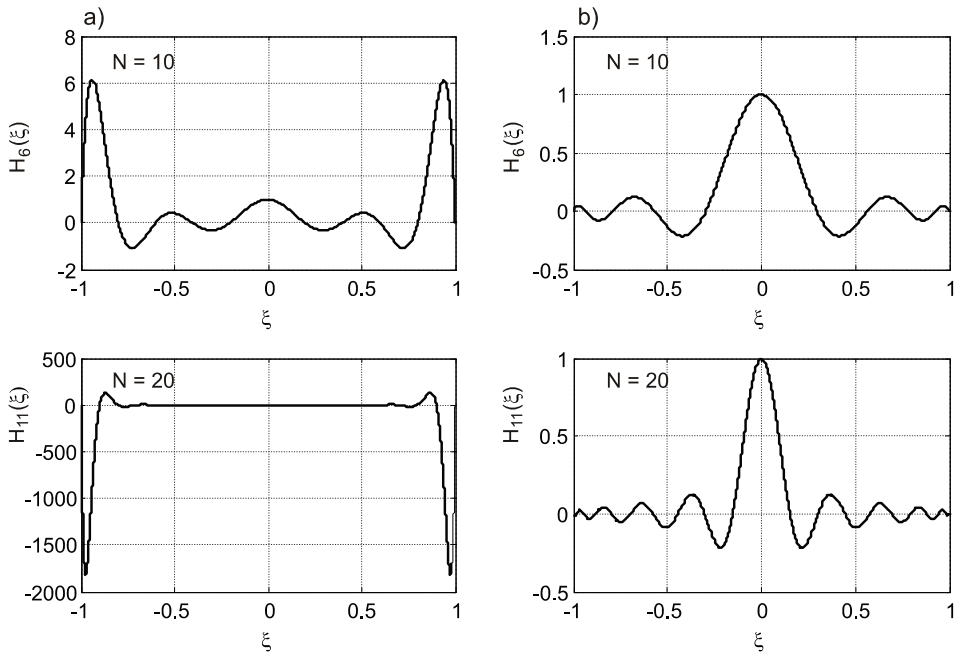


Fig. 3.4. Graphs of selected Lagrange interpolation functions of degree $N = 10$ and degree $N = 20$:
a) evenly spaced nodes; b) GLL nodes

where δ_{ak} is the Kronecker delta. In the case of the two-dimensional problem, the shape function can be expressed by:

$$H_a(\xi, \eta) = H_r(\xi)H_s(\eta), \quad (3.21)$$

where $H_r(\xi)$ and $H_s(\eta)$ are the one-dimensional shape functions described by Eq. (3.19).

A function of interest, can be approximated with the N th degree interpolating polynomial. It can be constructed in terms of specified unknown nodal values and the Lagrange polynomials as (cf. Hilderbrand 1956, Liu and Quek 2003):

$$z(\xi) = \sum_{a=1}^{N+1} H_a(\xi)z_a, \quad z(\xi, \eta) = \sum_{a=1}^{N+1} H_a(\xi, \eta)z_a. \quad (3.22)$$

Figure 3.3 presents the Lagrange interpolation functions over the parent domain for data sets of $n = 5$ and $n = 11$ evenly distributed and GLL nodes. For low-order polynomials (here of order $N = 4$), the evenly spaced nodes can ensure the accurate interpolation. However, as the number of nodes is raised (for example to $n = 11$, as it is shown in Fig. 3.3a), the oscillation near the ends occurs if evenly spaced nodes are used. This phenomenon is called the *Runge effect* and it may lead to an unreliable solution because the mass matrix for the evenly distributed nodes is significantly worse conditioned for polynomial orders higher than 5 (Pozrikidis 2005). This effect does not appear when the GLL nodes are used. The application of the GLL nodes guarantees that the values of Lagrange polynomials of any order N spanned over n GLL nodes do not exceed one (see Fig. 3.3b), which ensures the reliability of the spectral element results.

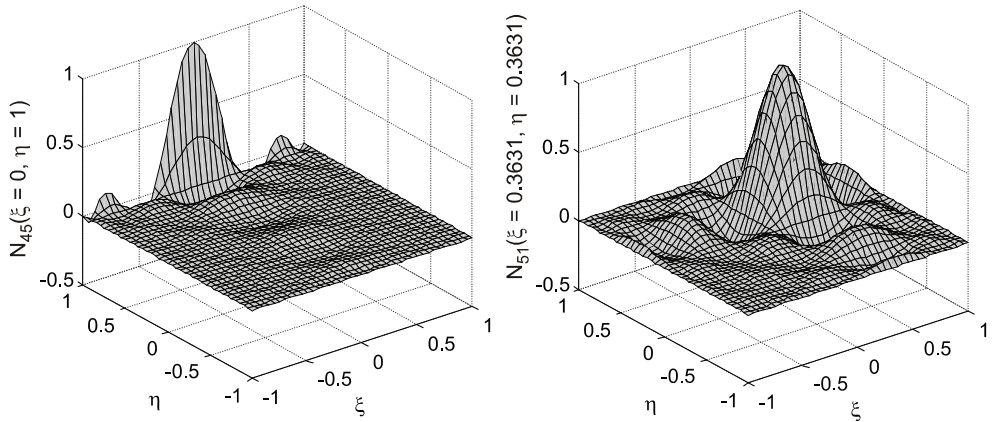


Fig. 3.5. An 81-node spectral finite element in the parent domain and selected shape functions $N_{45}(\xi, \eta)$ and $N_{51}(\xi, \eta)$

Selected Lagrange interpolants $H_a(\xi)$ associated with the a th abscissa are shown in Fig. 3.4 for the one-dimensional case. The abscissa was chosen as $\xi = 0$. It can be seen, that the Lagrange polynomial spanned over evenly spaced nodes achieves the largest values at the element ends, while the Lagrange polynomial spanned over the Gauss-Lobatto-Legendre nodes coincides to zeros at the element ends and achieves the largest values for the middle node. Figure 3.5 presents selected Lagrange interpolants $H_{45}(\xi, \eta)$ and $H_{51}(\xi, \eta)$ for a two-dimensional element having 9×9 GLL nodes.

3.1.3. Integration quadratures

To evaluate element matrices (3.7) to (3.10), numerical integration is employed. In the classical finite element method, the Gauss-Legendre quadrature is usually used. The distribution of $n = N + 1$ integration points in the Gauss-Legendre integration quadrature is determined as the roots of the Legendre polynomial of order n (e.g. Hilderbrand 1956):

$$P_n(\xi) = 0, \quad (3.23)$$

while the corresponding weights are found from the equation:

$$w_r = \frac{2(1 - \xi_r^2)}{(n+1)^2 [P_{n+1}(\xi_r)]^2}. \quad (3.24)$$

In this quadrature, n points enable to integrate exactly a polynomial of order $(2n-1)$, thus the mass and stiffness matrices are integrated exactly if the number of interpolation nodes equals the number of integration points.

As an alternative, the Gauss-Legendre-Lobatto quadrature (also known as the Lobatto quadrature) may be used. The coordinates of the Gauss-Lobatto-Legendre integration points ξ_r are obtained as the roots of the Legendre polynomial according to Eq. (3.13) and the associated weights w_r are found from:

$$w_r = \frac{2}{N(N+1)[P_N(\xi_r)]^2}, \quad r = 1, 2, \dots, n_r \equiv n. \quad (3.25)$$

In the GLL integration quadrature, the integration points are the same as the element interpolation nodes. Due to the Gauss-Lobatto-Legendre rule, interpolation carried out over the GLL nodes leads to a diagonal local mass matrix. In both stiffness and mass matrices the same shape functions are used for displacement field interpolation, therefore the resulting matrices are called consistent (Cook et al. 1989). However, in the GLL quadrature, n points enable to integrate exactly a polynomial of order $(2n-3)$. Thus the stiffness matrix is integrated exactly while the mass matrix is integrated non-exactly, and the mass lumping present in this approach arises from the inexact integration of the element mass matrix (Pozrikidis 2005). Diagonal mass matrix integrated in such a way is said to be optimally lumped (Cook et al. 1989).

3.1.4. Time integration

Time integration is performed in the standard form (e.g. Weaver and Johnston 1987, Bathe 1996, Hughes 2000, Chopra 2001). The initial-value problem for the system of ordinary differential equations (3.12) consists of finding a displacement $\mathbf{q} = \mathbf{q}(t)$ satisfying (3.12) and the given initial conditions:

$$\mathbf{q}(t=0) = \mathbf{q}_0, \quad \dot{\mathbf{q}}(t=0) = \dot{\mathbf{q}}_0. \quad (3.26)$$

It is assumed, that the solution of the equation of motion (3.12) is satisfied only at discrete time intervals $\Delta t = t_{i+1} - t_i$ apart as $\mathbf{q}_i \equiv \mathbf{q}(t_i)$.

3.1.4.1. The central difference method

The central difference method is based on a finite difference approximation of the time derivatives of the displacement:

$$\dot{\mathbf{q}}_i = \frac{\mathbf{q}_{i+1} - \mathbf{q}_{i-1}}{2\Delta t}, \quad \ddot{\mathbf{q}}_i = \frac{\mathbf{q}_{i+1} - 2\mathbf{q}_i + \mathbf{q}_{i-1}}{\Delta t^2}. \quad (3.27)$$

The displacement solution for time $i+1$ is obtained by considering Eq. (3.12) at time i :

$$\mathbf{M}\ddot{\mathbf{q}}_i + \mathbf{C}\dot{\mathbf{q}}_i + \mathbf{K}\mathbf{q}_i = \mathbf{p}_i. \quad (3.28)$$

Substituting the velocity and acceleration expansions (3.27) into (3.28) yields the following equation for solution \mathbf{q}_{i+1} :

$$\left(\frac{1}{\Delta t^2} \mathbf{M} + \frac{1}{2\Delta t} \mathbf{C} \right) \mathbf{q}_{i+1} = \mathbf{p}_i - \left(\mathbf{K} - \frac{2}{\Delta t^2} \mathbf{M} \right) \mathbf{q}_i - \left(\frac{1}{\Delta t^2} \mathbf{M} - \mathbf{C} \frac{1}{2\Delta t} \right) \mathbf{q}_{i-1}. \quad (3.29)$$

The above procedure is called an explicit integration method, because the solution \mathbf{q}_{i+1} is based on the equilibrium conditions at time i . The central difference method is conditionally stable and it requires the time step Δt to be smaller than the critical value Δt_{cr} :

$$\Delta t \leq \Delta t_{cr} = \frac{2}{\omega_n}, \quad (3.30)$$

where the ω_n is the largest frequency of an assembled finite element mesh with n degrees of freedom. Therefore, for solutions of wave propagation problems, a relatively small time step must be used. In this study a damping matrix is assumed, after Kudela et al. (2007a), as proportional with respect to the mass matrix $\mathbf{C} = \eta_d \mathbf{M}$, with a damping parameter η_d . Hence, if the mass matrix is diagonal, as a result of using the GLL quadrature, time integration can be efficiently conducted. In such case, Eq. (3.29) reduces to

$$\left(\frac{1}{\Delta t^2} + \frac{\eta_d}{2\Delta t} \right) \mathbf{M}\mathbf{q}_{i+1} = \hat{\mathbf{p}}_i, \quad (3.31)$$

where $\hat{\mathbf{p}}_i$ is the effective load vector:

$$\hat{\mathbf{p}}_i = \mathbf{p}_i - \left(\mathbf{K} - \frac{2}{\Delta t^2} \mathbf{M} \right) \mathbf{q}_i - \left(\frac{1}{\Delta t^2} - \frac{\eta_d}{2\Delta t} \right) \mathbf{M}\mathbf{q}_{i-1}. \quad (3.32)$$

To solve displacements \mathbf{q}_{i+1} , the inverse of the mass matrix is not required and only matrix multiplications are used to obtain the vector $\hat{\mathbf{p}}_i$. The displacement components are obtained as:

$$q_{i+1}^k = \frac{p_i^k}{M^{kk}} \left(\frac{2\Delta t^2}{2 + \eta_d \Delta t} \right), \quad (3.33)$$

where q_{i+1}^k and p_i^k are the k th components of the vectors \mathbf{q}_i and $\hat{\mathbf{p}}_i$, respectively, and M^{kk} denotes the k th diagonal element of the mass matrix \mathbf{M} .

3.1.4.2. The Newmark method

In the Newmark method (Newmark 1959) the solution at the time instant t_{i+1} consists of the following approximations:

$$\dot{\mathbf{q}}_{i+1} = \dot{\mathbf{q}}_i + \Delta t(1-\gamma)\ddot{\mathbf{q}}_i + \Delta t\gamma\ddot{\mathbf{q}}_{i+1} = \tilde{\mathbf{v}}_{i+1} + \Delta t\gamma\ddot{\mathbf{q}}_{i+1}, \quad (3.34)$$

$$\mathbf{q}_{i+1} = \mathbf{q}_i + \Delta t\dot{\mathbf{q}}_i + \frac{1}{2}(\Delta t)^2(1-2\beta)\ddot{\mathbf{q}}_i + (\Delta t)^2\beta\ddot{\mathbf{q}}_{i+1} = \tilde{\mathbf{d}}_{i+1} + (\Delta t)^2\beta\ddot{\mathbf{q}}_{i+1}, \quad (3.35)$$

where γ and β are parameters specifying various integration schemes. These parameters are responsible for the stability and the accuracy of the integration scheme. In this study two methods are considered. The first one is the implicit average acceleration rule with the following values $\beta=1/4$, $\gamma=1/2$ that guarantee unconditional stability. The second method is the central difference scheme with $\beta=0$, $\gamma=1/2$. This method is explicit, when matrices \mathbf{M} and \mathbf{C} are diagonal. To obtain a solution for the displacements, velocities and accelerations at time t_{i+1} , the equilibrium equation (3.12) at time $i+1$ is considered:

$$\mathbf{M}\ddot{\mathbf{q}}_{i+1} + \mathbf{C}\dot{\mathbf{q}}_{i+1} + \mathbf{K}\mathbf{q}_{i+1} = \mathbf{p}_{i+1}. \quad (3.36)$$

Substituting (3.34) and (3.35) to (3.36) leads to the following equation with respect to accelerations $\ddot{\mathbf{q}}_{i+1}$ as the unknowns:

$$\left[\mathbf{M} + \Delta t\gamma\mathbf{C} + (\Delta t)^2\beta\mathbf{K} \right] \ddot{\mathbf{q}}_{i+1} = \mathbf{p}_{i+1} - \mathbf{C}\tilde{\mathbf{v}}_{i+1} - \mathbf{K}\tilde{\mathbf{d}}_{i+1}, \quad (3.37)$$

$$\tilde{\mathbf{M}}\ddot{\mathbf{q}}_{i+1} = \mathbf{p}_{i+1} - \tilde{\mathbf{j}}_{i+1}, \quad \tilde{\mathbf{j}}_{i+1} = \tilde{\mathbf{j}}_{i+1}(\mathbf{q}_i, \dot{\mathbf{q}}_i, \ddot{\mathbf{q}}_i) = \mathbf{C}\tilde{\mathbf{v}}_{i+1} + \mathbf{K}\tilde{\mathbf{d}}_{i+1}. \quad (3.38)$$

It is known as the a-form. To obtain $\ddot{\mathbf{q}}_{i+1}$ it is necessary to compute:

$$\tilde{\mathbf{M}}^{-1} = \left[\mathbf{M} + \Delta t\gamma\mathbf{C} + (\Delta t)^2\beta\mathbf{K} \right]^{-1}. \quad (3.39)$$

The mass and damping matrices are diagonal in the Legendre SEM, but the problem remains with the stiffness matrix \mathbf{K} due to the fact that it is of full structure by definition. In order to devise fast and efficient time integration scheme with diagonal matrices \mathbf{M} and \mathbf{C} , useful in practical analysis of wave propagation analysis, it is reasonable to rephrase (3.36) in terms of vectors of internal forces \mathbf{r} (cf. Chróścielewski et al. 2009):

$$\mathbf{M}\ddot{\mathbf{q}}_{i+1} + \mathbf{C}\dot{\mathbf{q}}_{i+1} = \mathbf{p}_{i+1} - \mathbf{r}(\mathbf{q}_{i+1}). \quad (3.40)$$

Here $\mathbf{r}(\mathbf{q}_{i+1})$ is found directly from the equation:

$$\mathbf{r}_{(e)} = \int_{\Omega} \mathbf{B}^T \mathbf{E} \boldsymbol{\varepsilon} d\Omega, \quad (3.41)$$

$$\mathbf{r} = \mathbf{A} \begin{matrix} n_{el} \\ e=1 \end{matrix} \mathbf{r}_{(e)}, \quad (3.42)$$

and therefore, the stiffness matrix \mathbf{K} is not necessary in the time integration scheme. Due to the presence of \mathbf{q}_{i+1} on the right hand side of (3.40) the scheme is implicit, and therefore requires iteration. Substitution of iterative notation i.e.

$$\ddot{\mathbf{q}}_{i+1}^{(j+1)} = \ddot{\mathbf{q}}_{i+1}^{(j)} + \delta\ddot{\mathbf{q}}, \quad (3.43)$$

$$\dot{\mathbf{q}}_{i+1}^{(j+1)} = \dot{\mathbf{q}}_i + \Delta t[(1-\gamma)\dot{\mathbf{q}}_i + \gamma\dot{\mathbf{q}}_{i+1}^{(j)}] + \Delta t\gamma\delta\ddot{\mathbf{q}} = \dot{\mathbf{q}}_{i+1}^{(j)} + \Delta t\gamma\delta\ddot{\mathbf{q}}, \quad (3.44)$$

$$\mathbf{q}_{i+1}^{(j+1)} = \mathbf{q}_i + \Delta t\dot{\mathbf{q}}_i + \frac{1}{2}(\Delta t)^2[(1-2\beta)\ddot{\mathbf{q}}_i + 2\beta\ddot{\mathbf{q}}_{i+1}^{(j)}] + (\Delta t)^2\beta\delta\ddot{\mathbf{q}} = \mathbf{q}_{i+1}^{(j)} + (\Delta t)^2\beta\delta\ddot{\mathbf{q}}, \quad (3.45)$$

into (3.40) and rearranging terms yields implicit equation with respect to $\delta\ddot{\mathbf{q}}$:

$$[\mathbf{M} + \Delta t\gamma\mathbf{C}]\delta\ddot{\mathbf{q}} = \mathbf{p}_{i+1} - \mathbf{b}_{i+1}^{(j)} - \mathbf{c}_{i+1}^{(j)} - \mathbf{r}(\mathbf{q}_{i+1}^{(j)} + (\Delta t)^2\beta\delta\ddot{\mathbf{q}}), \quad (3.46)$$

Where vectors of inertia forces and damping forces are given by:

$$\mathbf{b}_{i+1}^{(j)} = \mathbf{M}\ddot{\mathbf{q}}_{i+1}^{(j)}, \quad \mathbf{c}_{i+1}^{(j)} = \mathbf{C}\dot{\mathbf{q}}_{i+1}^{(j)}. \quad (3.47)$$

To obtain correction of $\delta\ddot{\mathbf{q}}$, the method of simple iteration is used:

$$\delta\ddot{\mathbf{q}} = [\mathbf{M} + \Delta t\gamma\mathbf{C}]^{-1} (\mathbf{p}_{i+1} - \mathbf{b}_{i+1}^{(j)} - \mathbf{c}_{i+1}^{(j)} - \mathbf{r}(\mathbf{q}_{i+1}^{(j)})). \quad (3.48)$$

It is clear that if \mathbf{M} and $\mathbf{C} = \eta_d \mathbf{M}$ are by assumption diagonal, substantial efficiency of computation is gained. Once (3.48) is solved, the remaining state variables are updated through relations (3.43)–(3.45). The equation (3.48) is solved in the iterative way until the equilibrium condition becomes satisfied:

$$\mathbf{j}_{i+1}^{(j+1)} = \mathbf{p}_{i+1} - \mathbf{b}_{i+1}^{(j+1)} - \mathbf{c}_{i+1}^{(j+1)} - \mathbf{r}(\mathbf{q}_{i+1}^{(j+1)}) \rightarrow \mathbf{0}. \quad (3.49)$$

The iterations are terminated if the convergence is achieved. Since in view of (3.48), the equation (3.49) is equivalent to $\delta\ddot{\mathbf{q}} \rightarrow \mathbf{0}$, the convergence is assessed using the relative criteria (cf. Chróścielewski et al. 2009):

$$\frac{\|\delta\ddot{\mathbf{q}}\|}{\|\ddot{\mathbf{q}}_{i+1}^{(j+1)} - \ddot{\mathbf{q}}_i\|} < \varepsilon_1, \quad \max_k \frac{|\delta\ddot{q}_k|}{|\ddot{q}_{k\ i+1}^{(j+1)} - \ddot{q}_{k\ i}|} < \varepsilon_2, \quad (3.50)$$

where $\|\cdot\|$ is the Euclidean norm of a vector, ε_1 and ε_2 are a-priori assumed. In wave propagation problems the resulting time step is very short. Then it is possible to exploit the condition if $\Delta t \rightarrow 0$, which leads to $\tilde{\mathbf{M}} = \mathbf{M} + \Delta t\gamma\mathbf{C} + (\Delta t)^2\beta\mathbf{K} \rightarrow \mathbf{M}$. The explicit central-difference method follows directly from (3.48) and update rules (3.43)–(3.45) assuming $\beta=0$, $\gamma=1/2$ and replacing iterative values by their incremental counterparts $\delta\ddot{\mathbf{q}} \rightarrow \Delta\ddot{\mathbf{q}}$, $(\ddot{\mathbf{q}}_{i+1}^{(j+1)}, \dot{\mathbf{q}}_{i+1}^{(j+1)}, \mathbf{q}_{i+1}^{(j+1)}) \rightarrow (\ddot{\mathbf{q}}_{i+1}, \dot{\mathbf{q}}_{i+1}, \mathbf{q}_{i+1})$ and $(\ddot{\mathbf{q}}_{i+1}^{(j)}, \dot{\mathbf{q}}_{i+1}^{(j)}, \mathbf{q}_{i+1}^{(j)}) \rightarrow (\ddot{\mathbf{q}}_i, \dot{\mathbf{q}}_i, \mathbf{q}_i)$. As a result the iterative correction is omitted.

3.2. Formulation of one-dimensional spectral finite elements

Formulation of spectral elements is analogous to that of classical finite elements (e.g. Bathe 1996, Hughes 2000). For standard C^0 elements, interpolation of the displacement field $\mathbf{u}(x, t)$ for a finite element of length $L_{(e)}$ is:

$$\mathbf{u}(x, t) = \mathbf{H}(x)\mathbf{q}_{(e)}(t), \quad \mathbf{H}(x) = [\mathbf{H}_1(x) \ \mathbf{H}_2(x) \ \dots \ \mathbf{H}_n(x)], \quad \mathbf{q}_{(e)}(t) = \begin{Bmatrix} \mathbf{q}_1(t) \\ \mathbf{q}_2(t) \\ \vdots \\ \mathbf{q}_n(t) \end{Bmatrix}, \quad (3.51)$$

where n is the number of element nodes, $\mathbf{q}_{(e)}(t)$ is the element displacement vector, \mathbf{q}_a is the vector of displacement for the node a ($a = 1, 2, \dots, n$), $\mathbf{H}(x)$ denotes the element shape function matrix, $\mathbf{H}_a(x)$ is the shape function matrix for the node a containing interpolation polynomials H_a of order $N = n - 1$. The strains are interpolated through the relation:

$$\boldsymbol{\varepsilon}(x, t) = \mathbf{B}(x)\mathbf{q}_{(e)}(t), \quad \mathbf{B}(x) = \mathbf{D}\mathbf{H}(x), \quad (3.52)$$

where $\mathbf{B}(x)$ is the strain-displacement matrix and \mathbf{D} is the differential operator matrix.

To perform numerical integration, an element is mapped from the x -axis to the parent domain $\xi \in [-1, +1]$, so that the formulae for the element stiffness and mass matrices, as well as for the element load vector become:

$$\mathbf{K}_{(e)} = \int_{L_{(e)}} \mathbf{B}^T(x)\mathbf{E}\mathbf{B}(x)dx = \int_{-1}^1 \mathbf{B}^T(\xi)\mathbf{E}\mathbf{B}(\xi)J(\xi)d\xi, \quad (3.53)$$

$$\mathbf{M}_{(e)} = \int_{L_{(e)}} \mathbf{H}^T(x)\boldsymbol{\mu}\mathbf{H}(x)dx = \int_{-1}^1 \mathbf{H}^T(\xi)\boldsymbol{\mu}\mathbf{H}(\xi)J(\xi)d\xi, \quad (3.54)$$

$$\mathbf{p}_{(e)} = \int_{L_{(e)}} \mathbf{H}^T(x)\mathbf{f}(x)dx = \int_{-1}^1 \mathbf{H}^T(\xi)\mathbf{f}(\xi)J(\xi)d\xi, \quad (3.55)$$

where $\mathbf{f}(x)$ is the vector of distributed loads and J is the Jacobian given by the following relation:

$$J = \frac{\partial x}{\partial \xi}. \quad (3.56)$$

To evaluate the element matrices, the numerical integration is employed. The element matrices are integrated using the Gauss-Lobatto-Legendre (GLL) quadrature. The formulae for the stiffness matrix $\mathbf{K}_{(e)}$, the mass matrix $\mathbf{M}_{(e)}$ and the external force vector $\mathbf{p}_{(e)}$ become:

$$\mathbf{K}_{(e)} = \sum_{r=1}^{n_r} w_r \mathbf{B}^T(\xi_r)\mathbf{E}\mathbf{B}(\xi_r)J(\xi_r), \quad (3.57)$$

$$\mathbf{M}_{(e)} = \sum_{r=1}^{n_r} w_r \mathbf{H}^T(\xi_r)\boldsymbol{\mu}\mathbf{H}(\xi_r)J(\xi_r), \quad (3.58)$$

$$\mathbf{p}_{(e)} = \sum_{r=1}^{n_r} w_r \mathbf{H}^T(\xi_r)\mathbf{f}(\xi_r)J(\xi_r). \quad (3.59)$$

where n_r is the number of integration points, r ($r = 1, 2, \dots, n_r \equiv n$) is the label of ξ_r i.e. the abscissa and w_r is the corresponding weight. The generalized stress-strain matrix and the mass density matrix are denoted as \mathbf{E} and $\boldsymbol{\mu}$, respectively.

Below the spectral elements for the elementary, Love and Mindlin-Herrmann rod theories, as well as for the Timoshenko beam theory are formulated. Then the spectral frame element based on the Timoshenko beam and the Mindlin-Herrmann rod is developed.

3.2.1. Elementary rod element

The strains within a rod based on the elementary rod theory are:

$$\boldsymbol{\varepsilon}(x,t) = \left\{ \frac{\partial u_x(x,t)}{\partial x} \right\} = \mathbf{D}\mathbf{u}(x,t), \quad (3.60)$$

where the displacement vector $\mathbf{u}(x,t)$ and the differential operator \mathbf{D} are given by:

$$\mathbf{u}(x,t) = u_x(x,t), \quad \mathbf{D} = \left[\frac{\partial}{\partial x} \right]. \quad (3.61)$$

The shape function matrix and the vector of displacements for the node a ($a = 1, 2, \dots, n$) become:

$$\mathbf{H}_a(x) = [H_a(x)], \quad \mathbf{q}_a(t) = \{u_x^a(t)\}. \quad (3.62)$$

The stress-strain matrix \mathbf{E} appearing in Eq. (3.57) and the mass density matrix $\boldsymbol{\mu}$ appearing in Eq. (3.58) are defined through relations:

$$\mathbf{E} = [EA], \quad \boldsymbol{\mu} = [\rho A]. \quad (3.63)$$

3.2.2. Love rod element

In the formulation of the spectral element method for the Love theory, the stiffness matrix is the same as for the elementary theory, while the mass matrix takes the following form:

$$\begin{aligned} \mathbf{M}_{(e)} \approx & \rho A \sum_{r=1}^{n_r} w_r \mathbf{H}^T(\xi_r) \mathbf{H}(\xi_r) J(\xi_r) + \\ & + \rho v^2 J_o K_L^2 \sum_{r=1}^{n_r} w_r \mathbf{B}^T(\xi_r) \mathbf{B}(\xi_r) J(\xi_r). \end{aligned} \quad (3.64)$$

Due to the additional component related with the lateral deformation, the mass matrix loses its diagonal form after application of the numerical GLL integration. Therefore, the Love theory cannot be used efficiently in the spectral element method formulation even though it gives reasonable approximation for the first symmetric Lamb mode.

3.2.3. Mindlin-Herrmann rod element

The strains in the Mindlin-Herrmann rod can be written as:

$$\boldsymbol{\varepsilon}(x,t) = \left\{ \begin{array}{c} \frac{\partial u_x(x,t)}{\partial x} \\ \psi(x,t) \\ \frac{\partial \psi(x,t)}{\partial x} \end{array} \right\} = \mathbf{D}\mathbf{u}(x,t), \quad (3.65)$$

where the displacement vector $\mathbf{u}(x,t)$ and the matrix of differential operators \mathbf{D} are:

$$\mathbf{u}(x,t) = \begin{Bmatrix} u_x(x,t) \\ \psi(x,t) \end{Bmatrix}, \quad \mathbf{D} = \begin{bmatrix} \frac{\partial}{\partial x} & 0 \\ 0 & 1 \\ 0 & \frac{\partial}{\partial x} \end{bmatrix}. \quad (3.66)$$

The same Lagrange polynomials are used to interpolate the axial displacement and the lateral contraction. The shape function matrix and the vector of displacements for the node a have the following form:

$$\mathbf{H}_a(x) = \begin{bmatrix} H_a(x) & 0 \\ 0 & H_a(x) \end{bmatrix}, \quad \mathbf{q}_a(t) = \begin{Bmatrix} u_x^a(t) \\ \psi_a(t) \end{Bmatrix}. \quad (3.67)$$

The stress-strain matrix \mathbf{E} and the mass density matrix $\boldsymbol{\mu}$ are:

$$\mathbf{E} = \begin{bmatrix} \frac{EA}{1-\nu^2} & \frac{\nu EA}{1-\nu^2} & 0 \\ \frac{\nu EA}{1-\nu^2} & \frac{EA}{1-\nu^2} & 0 \\ 0 & 0 & K_1^{M-H} GI \end{bmatrix}, \quad \boldsymbol{\mu} = \begin{bmatrix} \rho A & 0 \\ 0 & K_2^{M-H} \rho I \end{bmatrix}. \quad (3.68)$$

3.2.4. Timoshenko beam element

The strains in the beam based on the Timoshenko theory can be expressed by:

$$\boldsymbol{\varepsilon}(x,t) = \begin{Bmatrix} \frac{\partial \varphi(x,t)}{\partial x} \\ \frac{\partial u_y(x,t)}{\partial x} - \varphi(x,t) \end{Bmatrix} = \mathbf{D} \mathbf{u}(x,t), \quad (3.69)$$

where the displacement vector $\mathbf{u}(x,t)$ and the differential operator matrix \mathbf{D} become:

$$\mathbf{u}(x,t) = \begin{Bmatrix} u_y(x,t) \\ \varphi(x,t) \end{Bmatrix}, \quad \mathbf{D} = \begin{bmatrix} 0 & -\frac{\partial}{\partial x} \\ \frac{\partial}{\partial x} & -1 \end{bmatrix}. \quad (3.70)$$

The vertical displacement and the rotation are interpolated by the same Lagrange polynomials. The shape function matrix and the vector of displacements for the node a are:

$$\mathbf{H}_a(x) = \begin{bmatrix} H_a(x) & 0 \\ 0 & H_a(x) \end{bmatrix}, \quad \mathbf{q}_a(t) = \begin{Bmatrix} u_y^a(t) \\ \varphi_a(t) \end{Bmatrix}. \quad (3.71)$$

The stress-strain matrix \mathbf{E} and the mass density matrix $\boldsymbol{\mu}$ have the form:

$$\mathbf{E} = \begin{bmatrix} EI & 0 \\ 0 & K_1^{Tim} GA \end{bmatrix}, \quad \boldsymbol{\mu} = \begin{bmatrix} \rho A & 0 \\ 0 & K_2^{Tim} \rho I \end{bmatrix}. \quad (3.72)$$

3.2.5. Frame element based on Mindlin-Herrmann and Timoshenko theories

The *M-H-Tim* frame element consists of the Mindlin-Herrmann rod (*M-H*) combined with the Timoshenko beam (*Tim*). The strains in the frame element can be written as:

$$\boldsymbol{\varepsilon}(x, t) = \begin{Bmatrix} \boldsymbol{\varepsilon}^{M-H} \\ \boldsymbol{\varepsilon}^{Tim} \end{Bmatrix} = \begin{bmatrix} \mathbf{D}^{M-H} & \mathbf{0} \\ \mathbf{0} & \mathbf{D}^{Tim} \end{bmatrix} \begin{Bmatrix} \mathbf{u}^{M-H} \\ \mathbf{u}^{Tim} \end{Bmatrix} = \mathbf{D}\mathbf{u}(x, t), \quad (3.73)$$

where strains $\boldsymbol{\varepsilon}^{M-H}$ and $\boldsymbol{\varepsilon}^{Tim}$ are given by Eqs. (3.65) and (3.69), respectively and displacements \mathbf{u}^{M-H} and \mathbf{u}^{Tim} are given by Eqs. (3.66)₁ and (3.70)₁, respectively. The differential operator matrices \mathbf{D}^{M-H} , \mathbf{D}^{Tim} are expressed by Eqs. (3.66)₂ and (3.70)₂. The stress-strain matrix \mathbf{E} and the mass density matrix $\boldsymbol{\mu}$ are defined as follows:

$$\mathbf{E} = \begin{bmatrix} \mathbf{E}^{M-H} & \mathbf{0} \\ \mathbf{0} & \mathbf{E}^{Tim} \end{bmatrix}, \quad \boldsymbol{\mu} = \begin{bmatrix} \boldsymbol{\mu}^{M-H} & \mathbf{0} \\ \mathbf{0} & \boldsymbol{\mu}^{Tim} \end{bmatrix}, \quad (3.74)$$

where \mathbf{E}^{M-H} and $\boldsymbol{\mu}^{M-H}$ are the stress-strain matrix and the mass density matrix for the Mindlin-Herrmann theory given by Eqs. (3.68), while \mathbf{E}^{Tim} and $\boldsymbol{\mu}^{Tim}$ are the stress-strain matrix and the mass density matrix for the Timoshenko theory given by Eqs. (3.72). The shape function matrix and the vector of displacements for the node a have the following form:

$$\mathbf{H}_a(x) = \begin{bmatrix} H_a(x) & 0 & 0 & 0 \\ 0 & H_a(x) & 0 & 0 \\ 0 & 0 & H_a(x) & 0 \\ 0 & 0 & 0 & H_a(x) \end{bmatrix}, \quad \mathbf{q}_a(t) = \begin{Bmatrix} u_x^a(t) \\ \psi_a(t) \\ u_y^a(t) \\ \varphi_a(t) \end{Bmatrix}. \quad (3.75)$$

The above-developed element is then transformed to the global coordinate system. The element transformation matrix \mathbf{T} enables rotation of the local axes to the structural axes by the angle α :

$$\mathbf{T} = \begin{bmatrix} \mathbf{T}_1 & \mathbf{0} & \mathbf{0} & \mathbf{0} \\ \mathbf{0} & \mathbf{T}_2 & \mathbf{0} & \mathbf{0} \\ \mathbf{0} & \mathbf{0} & \dots & \mathbf{0} \\ \mathbf{0} & \mathbf{0} & \mathbf{0} & \mathbf{T}_n \end{bmatrix}, \quad \mathbf{T}_a = \begin{bmatrix} \cos \alpha & 0 & \sin \alpha & 0 \\ 0 & 1 & 0 & 0 \\ -\sin \alpha & 0 & \cos \alpha & 0 \\ 0 & 0 & 0 & 1 \end{bmatrix}. \quad (3.76)$$

Transformation of the local element matrices to the global matrices is given by:

$$\bar{\mathbf{K}}_{(e)} = \mathbf{T}^T \mathbf{K}_{(e)} \mathbf{T}, \quad \bar{\mathbf{M}}_{(e)} = \mathbf{T}^T \mathbf{M}_{(e)} \mathbf{T}, \quad \bar{\mathbf{p}}_{(e)} = \mathbf{T}^T \mathbf{p}_{(e)}. \quad (3.77)$$

Then the system of equations of motion is built in the course of the standard aggregation of the element matrices and vectors referred to the structural coordinate system.

3.3. Formulation of two-dimensional spectral finite elements

Interpolation of the displacement field $\mathbf{u}(x, y, t)$ in a typical finite element of surface area $B_{(e)}$ becomes:

$$\mathbf{u}(x, y, t) = \mathbf{H}(x, y) \mathbf{q}_{(e)}(t), \quad \mathbf{q}_{(e)}(t) = \begin{Bmatrix} \mathbf{q}_1(t) \\ \mathbf{q}_2(t) \\ \vdots \\ \mathbf{q}_n(t) \end{Bmatrix}, \quad (3.78)$$

where the matrix of interpolation functions $\mathbf{H}(x, y)$ for an element is:

$$\mathbf{H}(x, y) = [\mathbf{H}_1(x, y) \quad \mathbf{H}_2(x, y) \quad \dots \quad \mathbf{H}_n(x, y)], \quad (3.79)$$

$$\mathbf{H}_a(x, y) = \text{diag}[H_a(x, y)] = \text{diag}[H_r(x)H_s(y)]. \quad (3.80)$$

In the above, $H_a(x, y)$ are Lagrange type interpolation polynomials, the label a denotes nodal values ($a = 1, 2, \dots, n$) and $n = n_r \cdot n_s$ is the number of element nodes, where n_r denotes the number of nodes in x direction, whereas n_s in y direction.

Strains can be interpolated through the relation:

$$\boldsymbol{\varepsilon}(x, y, t) = \mathbf{B}(x, y) \mathbf{q}_{(e)}(t). \quad (3.81)$$

The strain-displacement matrix $\mathbf{B}(x, y)$ is defined as:

$$\mathbf{B}(x, y) = \mathbf{D}\mathbf{H}(x, y), \quad (3.82)$$

where \mathbf{D} denotes the differential operator matrix.

To perform numerical integration, an element is mapped from the xy -axes to the parent domain $\xi, \eta \in [-1, +1]$, so that the formulae for the element stiffness and mass matrices, as well as the element load vector become:

$$\begin{aligned} \mathbf{K}_{(e)} &= \int_{B_{(e)}} \mathbf{B}^T(x, y) \mathbf{E} \mathbf{B}(x, y) dx dy = \\ &= \int_{-1}^1 \int_{-1}^1 \mathbf{B}^T(\xi, \eta) \mathbf{E} \mathbf{B}(\xi, \eta) \det(\mathbf{J}(\xi, \eta)) d\xi d\eta, \end{aligned} \quad (3.83)$$

$$\begin{aligned} \mathbf{M}_{(e)} &= \int_{B_{(e)}} \mathbf{H}^T(x, y) \boldsymbol{\mu} \mathbf{H}(x, y) dx dy = \\ &= \int_{-1}^1 \int_{-1}^1 \mathbf{H}^T(\xi, \eta) \boldsymbol{\mu} \mathbf{H}(\xi, \eta) \det(\mathbf{J}(\xi, \eta)) d\xi d\eta, \end{aligned} \quad (3.84)$$

$$\begin{aligned} \mathbf{p}_{(e)} &= \int_{B_{(e)}} \mathbf{H}^T(x, y) \mathbf{f}(x, y) dx dy = \\ &= \int_{-1}^1 \int_{-1}^1 \mathbf{H}^T(\xi, \eta) \mathbf{f}(\xi, \eta) \det(\mathbf{J}(\xi, \eta)) d\xi d\eta, \end{aligned} \quad (3.85)$$

where \mathbf{J} is the Jacobian matrix defined by:

$$\mathbf{J} = \begin{bmatrix} \frac{\partial x}{\partial \xi} & \frac{\partial y}{\partial \xi} \\ \frac{\partial x}{\partial \eta} & \frac{\partial y}{\partial \eta} \end{bmatrix}. \quad (3.86)$$

Then, the element stiffness matrix $\mathbf{K}_{(e)}$, the element mass matrix $\mathbf{M}_{(e)}$ and the element load vector $\mathbf{p}_{(e)}$ are integrated using the Gauss-Lobatto-Legendre quadrature:

$$\mathbf{K}_{(e)} = \sum_{r=1}^{n_r} \sum_{s=1}^{n_s} w_r w_s \mathbf{B}^T(\xi_r, \eta_s) \mathbf{E} \mathbf{B}(\xi_r, \eta_s) \det(\mathbf{J}(\xi_r, \eta_s)), \quad (3.87)$$

$$\mathbf{M}_{(e)} = \sum_{r=1}^{n_r} \sum_{s=1}^{n_s} w_r w_s \mathbf{H}^T(\xi_r, \eta_s) \boldsymbol{\mu} \mathbf{H}(\xi_r, \eta_s) \det(\mathbf{J}(\xi_r, \eta_s)), \quad (3.88)$$

$$\mathbf{p}_{(e)} = \sum_{r=1}^{n_r} \sum_{s=1}^{n_s} w_r w_s \mathbf{H}^T(\xi_r, \eta_s) \mathbf{f}(\xi_r, \eta_s) \det(\mathbf{J}(\xi_r, \eta_s)). \quad (3.89)$$

3.3.1. Plane stress element

The strains in the plane stress can be expressed as:

$$\boldsymbol{\varepsilon}(x, y, t) = \left\{ \begin{array}{c} \frac{\partial u_x(x, y, t)}{\partial x} \\ \frac{\partial u_y(x, y, t)}{\partial y} \\ \frac{\partial u_x(x, y, t)}{\partial y} + \frac{\partial u_y(x, y, t)}{\partial x} \end{array} \right\} = \mathbf{D} \mathbf{u}(x, y, t), \quad (3.90)$$

where the displacement vector $\mathbf{u}(x, y, t)$ and the matrix of differential operators \mathbf{D} are given by:

$$\mathbf{u}(x, y, t) = \begin{Bmatrix} u_x(x, y, t) \\ u_y(x, y, t) \end{Bmatrix}, \quad \mathbf{D} = \begin{bmatrix} \frac{\partial}{\partial x} & 0 \\ 0 & \frac{\partial}{\partial y} \\ \frac{\partial}{\partial y} & \frac{\partial}{\partial x} \end{bmatrix}. \quad (3.91)$$

The shape function matrix and the vector of displacements for the node a have the following form:

$$\mathbf{H}_a(x, y) = \begin{bmatrix} H_r(x)H_s(y) & 0 \\ 0 & H_r(x)H_s(y) \end{bmatrix}, \quad \mathbf{q}_a(t) = \begin{Bmatrix} u_x^a(t) \\ u_y^a(t) \end{Bmatrix}. \quad (3.92)$$

The generalized stress-strain matrix \mathbf{E} appearing in Eq. (3.87) and the mass density matrix $\boldsymbol{\mu}$ appearing in Eq. (3.88) become:

$$\mathbf{E} = \begin{bmatrix} \frac{Eh}{1-\nu^2} & \frac{Eh\nu}{1-\nu^2} & 0 \\ \frac{Eh\nu}{1-\nu^2} & \frac{Eh}{1-\nu^2} & 0 \\ 0 & 0 & Gh \end{bmatrix}, \quad \boldsymbol{\mu} = \begin{bmatrix} \rho h & 0 \\ 0 & \rho h \end{bmatrix}. \quad (3.93)$$

3.3.2. Kane-Mindlin extensional plate element

The strains within the plate based on the Kane-Mindlin theory are expressed through the equation:

$$\boldsymbol{\varepsilon}(x, y, t) = \left\{ \begin{array}{c} \frac{\partial u_x(x, y, t)}{\partial x} \\ \frac{\partial u_y(x, y, t)}{\partial y} \\ \frac{2u_z(x, y, t)}{h} \\ \frac{\partial u_x(x, y, t)}{\partial y} + \frac{\partial u_y(x, y, t)}{\partial x} \\ \frac{\partial u_z(x, y, t)}{\partial x} \frac{2}{h} \\ \frac{\partial u_z(x, y, t)}{\partial y} \frac{2}{h} \end{array} \right\} = \mathbf{D}\mathbf{u}(x, y, t). \quad (3.94)$$

The displacement vector $\mathbf{u}(x, y, t)$ and the matrix of differential operators \mathbf{D} are given by the relations:

$$\mathbf{u}(x, y, t) = \begin{Bmatrix} u_x(x, y, t) \\ u_y(x, y, t) \\ u_z(x, y, t) \end{Bmatrix}, \quad \mathbf{D} = \begin{bmatrix} \frac{\partial}{\partial x} & 0 & 0 \\ 0 & \frac{\partial}{\partial y} & 0 \\ 0 & 0 & \frac{2}{h} \\ \frac{\partial}{\partial y} & \frac{\partial}{\partial x} & 0 \\ 0 & 0 & \frac{\partial}{\partial x} \frac{2}{h} \\ 0 & 0 & \frac{\partial}{\partial y} \frac{2}{h} \end{bmatrix}. \quad (3.95)$$

The shape function matrix $\mathbf{H}_a(x, y)$ and the vector of displacements $\mathbf{q}_a(t)$ for the node a have the following form:

$$\mathbf{H}_a(x, y) = \begin{bmatrix} H_r(x)H_s(y) & 0 & 0 \\ 0 & H_r(x)H_s(y) & 0 \\ 0 & 0 & H_r(x)H_s(y) \end{bmatrix}, \quad \mathbf{q}_a(t) = \begin{Bmatrix} u_x^a(t) \\ u_y^a(t) \\ u_z^a(t) \end{Bmatrix} \quad (3.96)$$

The stress-strain matrix \mathbf{E} appearing in Eq. (3.87) and the mass density matrix $\boldsymbol{\mu}$ appearing in Eq. (3.88) are:

$$\mathbf{E} = \begin{bmatrix} h(\Lambda + 2G) & \Lambda h & 2\Lambda\kappa_{KM} & 0 & 0 & 0 \\ \Lambda h & h(\Lambda + 2G) & 2\Lambda\kappa_{KM} & 0 & 0 & 0 \\ 2\Lambda\kappa_{KM} & 2\Lambda\kappa_{KM} & \frac{4\kappa_{KM}^2(\Lambda + 2G)}{h} & 0 & 0 & 0 \\ 0 & 0 & 0 & Gh & 0 & 0 \\ 0 & 0 & 0 & 0 & \frac{Gh}{3} & 0 \\ 0 & 0 & 0 & 0 & 0 & \frac{Gh}{3} \end{bmatrix}, \quad (3.97)$$

$$\boldsymbol{\mu} = \begin{bmatrix} \rho h & 0 & 0 \\ 0 & \rho h & 0 \\ 0 & 0 & \rho h/3 \end{bmatrix}. \quad (3.98)$$

3.3.3. Mindlin bending plate element

The strains within the plate based on the Mindlin theory become:

$$\boldsymbol{\varepsilon}(x, y, t) = \begin{Bmatrix} -\frac{\partial\psi_x(x, y, t)}{\partial x} \\ -\frac{\partial\psi_y(x, y, t)}{\partial y} \\ \frac{\partial\psi_x(x, y, t)}{\partial y} - \frac{\partial\psi_y(x, y, t)}{\partial x} \\ \frac{\partial u_z(x, y, t)}{\partial x} - \psi_x(x, y, t) \\ \frac{\partial u_z(x, y, t)}{\partial y} - \psi_y(x, y, t) \end{Bmatrix} = \mathbf{D}\mathbf{u}(x, y, t), \quad (3.99)$$

where the displacement vector $\mathbf{u}(x, y, t)$ and the matrix of differential operators \mathbf{D} are:

$$\mathbf{u}(x, y, t) = \begin{Bmatrix} \psi_x(x, y, t) \\ \psi_y(x, y, t) \\ u_z(x, y, t) \end{Bmatrix}, \quad \mathbf{D} = \begin{bmatrix} -\frac{\partial}{\partial x} & 0 & 0 \\ 0 & -\frac{\partial}{\partial y} & 0 \\ -\frac{\partial}{\partial y} & -\frac{\partial}{\partial x} & 0 \\ -1 & 0 & \frac{\partial}{\partial x} \\ 0 & -1 & \frac{\partial}{\partial y} \end{bmatrix}. \quad (3.100)$$

The shape function matrix $\mathbf{H}_a(x, y)$ and the vector of displacements $\mathbf{q}_a(t)$ for the node a are expressed by the relations:

$$\mathbf{H}_a(x, y) = \begin{bmatrix} H_r(x)H_s(y) & 0 & 0 \\ 0 & H_r(x)H_s(y) & 0 \\ 0 & 0 & H_r(x)H_s(y) \end{bmatrix}, \quad \mathbf{q}_a(t) = \begin{Bmatrix} \psi_x^a(t) \\ \psi_y^a(t) \\ u_z^a(t) \end{Bmatrix}. \quad (3.101)$$

The stress-strain matrix \mathbf{E} and mass density matrix $\boldsymbol{\mu}$ are defined as:

$$\mathbf{E} = \begin{bmatrix} D & D\nu & 0 & 0 & 0 \\ D\nu & D & 0 & 0 & 0 \\ 0 & 0 & Gh^3/12 & 0 & 0 \\ 0 & 0 & 0 & Gh & 0 \\ 0 & 0 & 0 & 0 & Gh \end{bmatrix}, \quad \boldsymbol{\mu} = \begin{bmatrix} \rho h^3/12 & 0 & 0 \\ 0 & \rho h^3/12 & 0 \\ 0 & 0 & \rho h \end{bmatrix}. \quad (3.102)$$

3.4. Summary and conclusions

In this chapter, the spectral element method has been outlined. The development of time domain spectral finite elements for a rod, beam and frame, as well as extensional and bending plates has been carried out.

The spectral element method is based upon high-order piecewise polynomial approximation of the weak formulation of the wave equation and combines high accuracy of spectral methods with the flexibility of the finite element method to handle complex geometries. The wavefield of elements is discretized using Lagrange polynomials and integration of element matrices is performed by the Gauss-Legendre-Lobatto quadrature. The inexact integration effectively diagonalizes the mass matrix, so that the time integration can be efficiently conducted.

Doyle (1997) suggested that for axial waves in a rod, a simple Love rod theory is sufficient in structural analysis. However, the Love theory in the time domain SEM leads to a non-diagonal mass matrix. Derived in this chapter spectral elements based on the higher order theories (the Mindlin-Herrmann rod, the Timoshenko beam, the Kane-Mindlin extensional plate and the Mindlin bending plate theories) provide optimally lumped mass matrix.

Chapter 4

WAVE PROPAGATION IN BARS

Bars are the simplest components of many mechanical systems and civil engineering structures. In this chapter, wave propagation in steel bars with discontinuity of material and cross-section is analysed. Two forms of elastic wave propagation, namely longitudinal and flexural waves are investigated in detail.

Earlier studies were related to numerical simulations in the SFEM formulation of longitudinal wave propagation based on the elementary theory on the examples of a rod with a crack of depth 5% of the rod height (Palacz and Krawczuk 2002) and 20% of the rod height (Krawczuk et al. 2006b). Experimental works were conducted on a rod with an additional mass equal to 4% and 12% of the total specimen mass (Palacz et al. 2005a). To take into account dispersion, modified rod theories were formulated in the frequency domain approach (e.g. Martin et al. 1994, Doyle 1997, Krawczuk et al. 2006a). Analytical and experimental study of compressional waves in a dispersive elastic rod was presented by Miklowitz and Calif (1957a) and Miklowitz et al. (1957b). They applied the Mindlin-Herrmann theory and compared it with experimental results. In the experiment, a step pressure was applied to the end of an aluminium rod by means of a shock tube. Radial displacement measurements were made with a radial condenser microphone, while axial strain measurements were performed using strain gauges. In the time domain approach, a spectral element for a rod based on the elementary theory can be found in the paper by Kudela et al. 2007a. To model longitudinal wave propagation taking lateral deformations into consideration, time domain spectral elements for the Love and Mindlin-Herrmann rod theories were developed by Rucka (2010a). In the paper by Rucka (2010a) experimental investigations on wave propagation in rods with structural discontinuities were performed applying a piezoactuator and a modern laser vibrometer.

In the case of flexural waves, earlier research concerned numerical, as well as experimental investigations. Doyle and Kamle (1985) performed an experimental study of the reflection of flexural waves at structural discontinuities. In their experiment, strain gages were attached to a beam and an incident pulse was created using a steel ball. Numerical simulations of flexural wave propagation in beams using the SFEM were initiated by Doyle and Farris (1990a). They developed a spectrally formulated element based on the Euler-Bernoulli beam theory. To take into account shear deformation, the spectral element based on the Timoshenko beam theory was formulated in the frequency domain approach by Gopalakrishnan et al. (1992). Numerical simulations of wave propagation in a cracked Timoshenko beam were presented by Krawczuk et al. (2003). They considered a crack with depth equal to 20% of the beam height and numerical simulations were performed by the SFEM in the frequency domain. Kudela et al. (2007a) presented a numerical study on the Timoshenko spectral element formulated in the time domain. However, they did not consider adjustable parameters for the Timoshenko beam theory and numerical results have not been compared with any experimental results. Experimental and numerical analyses of flexural wave propagation in beams with structural discontinuities were presented by Rucka (2010a).

The purpose of the present chapter is to conduct comprehensive experimental and numerical studies of the influence of different types of discontinuity on wave propagation, as well as the comparison of longitudinal and flexural waves and their usefulness for damage detection. Beside the results published by Rucka (2010a), this chapter contains measurements of experimental dispersion curves to update the SEM models and experimental Lamb-wave tuning to find frequencies at which waves are strongly excited and frequencies at which waves practically cannot be excited. Results of additional calculations concerning numerical dispersion, some guidelines for spectral element models and specifications concerning the shape of the excitation signals are also presented.

4.1. Experimental setup

A steel bar with dimensions $6 \text{ mm} \times 6 \text{ mm} \times 1000 \text{ mm}$ was considered as the testing structure. The experimentally determined mass density ρ was equal to 7556 kg/m^3 . The modulus of elasticity was also determined experimentally in a force-displacement test (tensile test) using a strain gauge attached to the bar in the longitudinal direction and a testing machine to register a force level, and its value was identified as $E = 200.11 \text{ GPa}$. The Poisson's ratio ν was set as 0.33. The bar was placed on a flat surface. It had free boundary conditions and there was no fixture, which could affect wave propagation. Since the excited waves had very low amplitudes, no rigid movement has occurred.

The photo of the experimental setup is given in Fig. 4.1a. The bar was excited by means of a plate actuator Noliac CMAP11 of dimensions $5 \text{ mm} \times 5 \text{ mm} \times 2 \text{ mm}$ bonded at the end of the bar using beeswax. The actuator was made with piezoelectric ceramics based on lead zirconate titanate (PZT). In piezoelectric materials, an applied electric field generates proportional strain. The Tektronix function generator AFG 3022 with the high voltage amplifier EC Electronics PPA 2000 created an excitation voltage signal $p_V(t)$ applied next to the actuator, which converted it into a mechanical force $p(t)$.

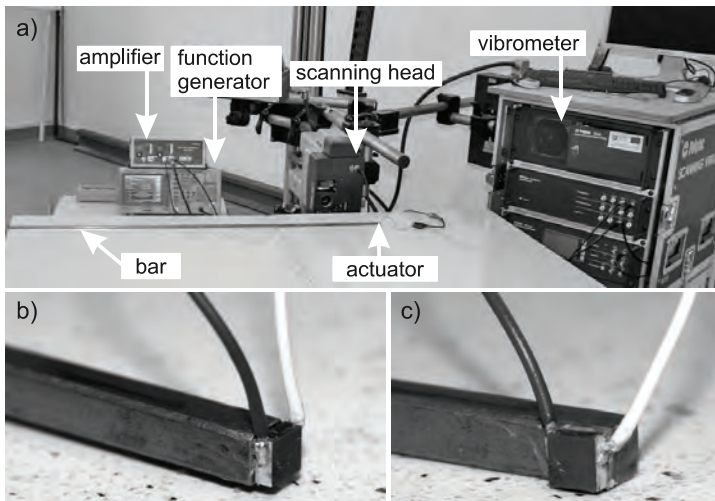


Fig. 4.1. Experimental setup for wave propagation: a) hardware and bar specimen; b) detail showing actuator in the case of longitudinal waves; c) detail showing actuator in the case of flexural waves

Non-contact sensing of propagating waves was achieved by a vibrometer. The Polytec Scanning Laser Vibrometer PSV-3D-400-M measured the velocity of the surface vibration $v(t)$. Velocity signals were averaged 100 times to improve the signal-to-noise ratio. In the experimental investigations, both longitudinal and flexural waves were measured. The specimen was called the rod, when longitudinal waves were excited and the beam, when flexural waves were excited. The details showing actuators are presented in Fig. 4.1b and Fig. 4.1c. The locations of the actuators and the measurement points are shown in Fig. 4.2.

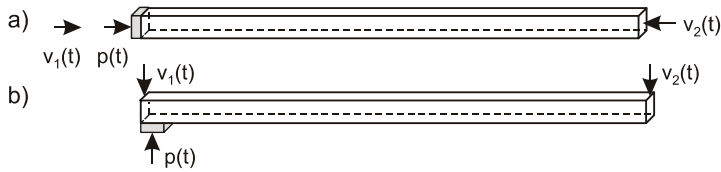


Fig. 4.2. Locations of actuators and velocity measurement points in the bar:
a) for longitudinal wave propagation; b) for flexural wave propagation

4.1.1. Excitation signal

The excitation signal $p(t)$ considered in this study was chosen as a single-frequency smoothed tone burst (a.k.a. wave packet) obtained from the multiplication of a sinusoidal function of frequency f and a window function $w(t)$:

$$p(t) = \begin{cases} p_o \sin(2\pi ft) \cdot w(t) & t \in [0, T_w], \\ 0 & t > T_w, \end{cases} \quad (4.1)$$

where T_w denotes the length of a window and p_o is an amplitude of a sinusoidal function. As $w(t)$, the Hanning window was applied (cf. Maia et al. 1997, Giurgitiu 2008):

$$w(t) = 0.5(1 - \cos(2\pi ft / n_w)), \quad t \in [0, T_w], \quad (4.2)$$

where n_w is the number of counts in the tone burst.

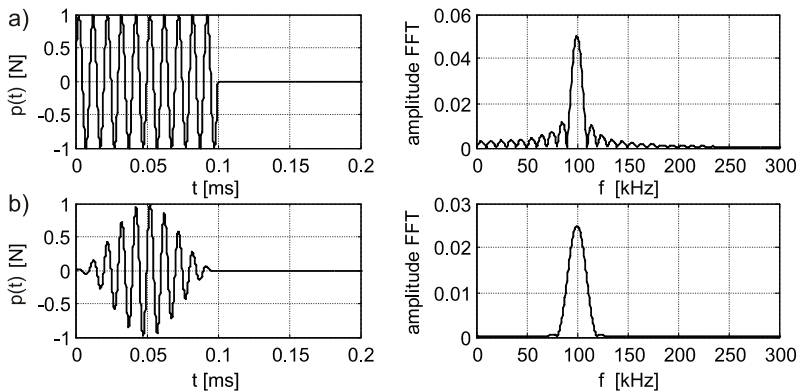


Fig. 4.3. Example of ten-count tone burst excitation signal of frequency 100 kHz in time and frequency domains: a) raw tone burst; b) tone burst smoothed with the Hanning window

The Hanning window provides smoothed tone burst in order to reduce the excitation of side frequencies (Giurgiutiu 2008). Figure 4.3 shows a comparison of raw and smoothed 10-count tone bursts and their FFT transforms. Both signals have the same central frequency 100 kHz. The raw signal results in excitation of both the main beam and significant number of side lobes, while in the case of smoothed burst side lobes are not excited and only the main beam exists. This aspect of excitation coherent single-frequency waves is important, especially when dealing with dispersive Lamb waves. The effect of dispersion can be minimized by using narrow bandwidth input signals to concentrate input energy at a point on the dispersion curves in which dispersion is low (Wilcox et al. 2001, Wilcox 2003).

The influence of the number of cycles in the tone burst, as well as the signal frequency and the window width is illustrated in Figs. 4.4 to 4.6. The excitation signals of frequency 100 kHz and different number of cycles (2, 5, and 12 cycles) are presented in Fig. 4.4. The width of the main beam in the frequency domain changes depending on the number of cycles. For the established frequency of the sine wave, the narrowest main beam is for the largest length T_w of the window function $w(t)$ (Fig. 4.4c). On the other hand, for the shortest window in the time domain, the main beam is the widest in the frequency domain (Fig. 4.4a). The comparison of the smoothed tone bursts for the established number of cycles is given in Fig. 4.5. The frequency of the applied sine wave influences the width of the main beam in the frequency domain. The smaller the frequency of the time signal, the narrower the main beam in the frequency domain. The last example concerns the signal with the established length of the window function in the time domain $T_w = 0.1$ ms. In such case, independently of the sine frequency, the width of the main beam is the same (Fig. 4.6). As can be seen from the above examples, the intensity of dispersion depends on the length of a wave packet. Moreover, according to the Heisenberg uncertainty principle, the product of the time-domain duration and the frequency spread is constant (Giurgiutiu 2008).

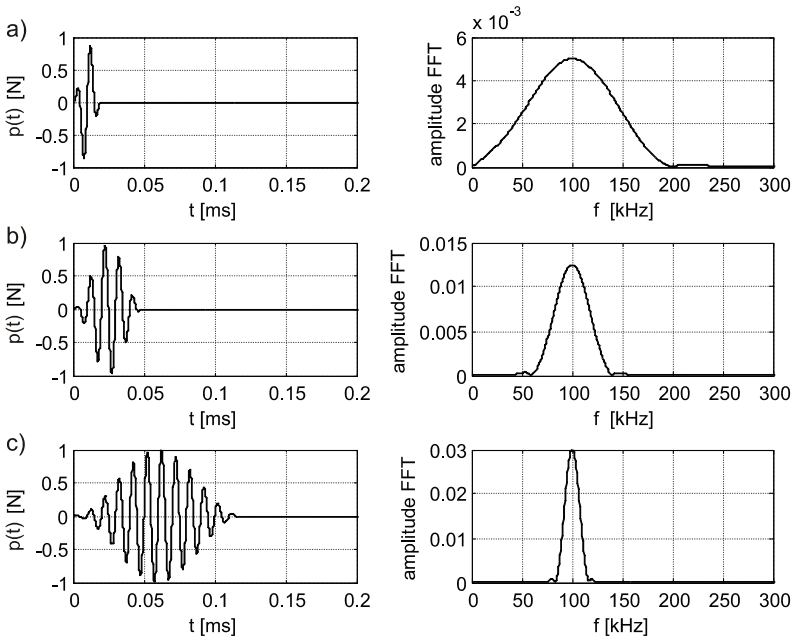


Fig. 4.4. Example of smoothed tone burst of frequency 100 kHz: a) 2 cycles; b) 5 cycles; c) 12 cycles

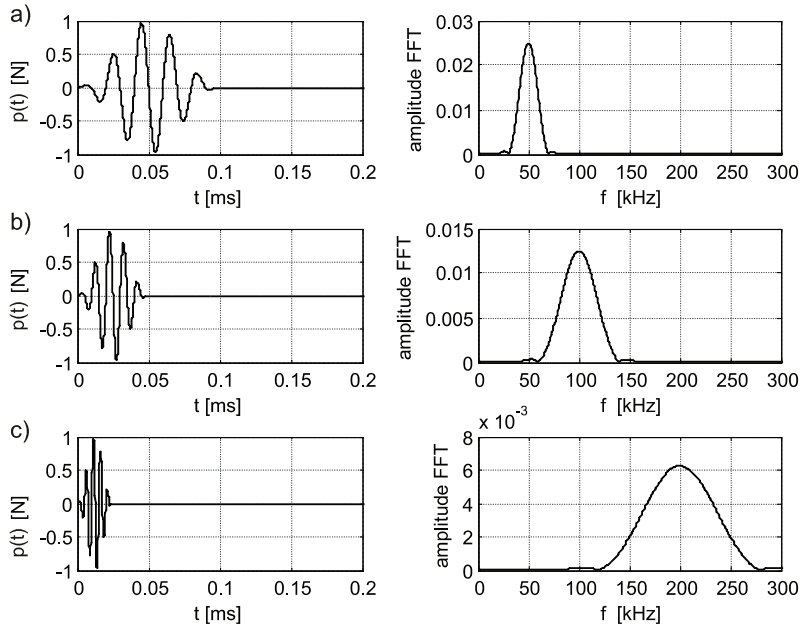


Fig. 4.5. Example of 5-count smoothed tone burst: a) signal of frequency 50 kHz; b) signal of frequency 100 kHz; c) signal of frequency 200 kHz

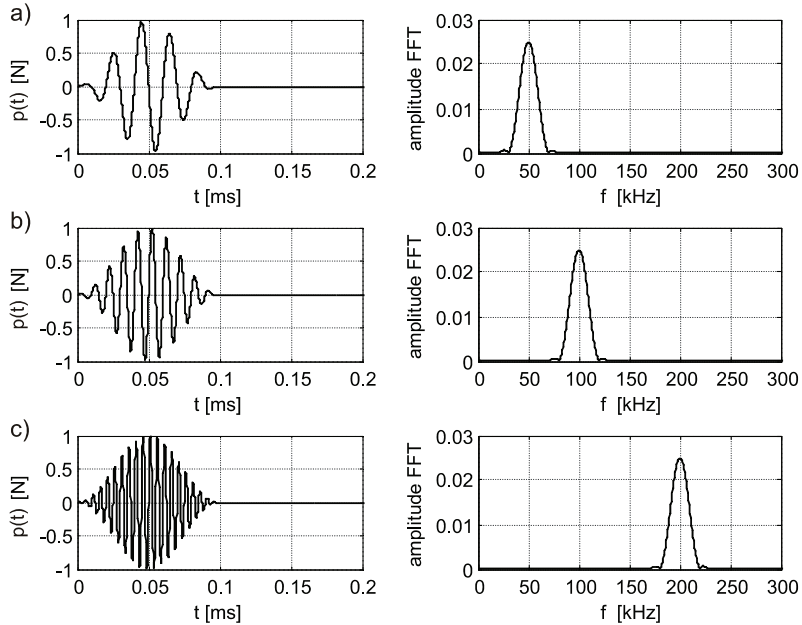


Fig. 4.6. Example of smoothed tone burst with window length $T_w = 0.1$ ms: a) 5-cycle signal of frequency 50 kHz; b) 10-cycle signal of frequency 100 kHz; c) 20-cycle signal of frequency 200 kHz

4.1.2. Dispersion curves

Group velocity dispersion curves were experimentally determined for the considered intact bar. The signal $v_1(t)$ was measured on the bar left end, in the position indicated in Fig. 4.2. The frequency of the excitation signal in the form of twelve-count burst was swept from 50 to 300 kHz in steps of 10 kHz. Figures 4.7 and 4.8 present examples of registered signals for frequencies 60, 100 and 250 kHz, in the case of longitudinal and flexural waves, respectively. In both cases, the influence of dispersion is visible. For longitudinal waves, time-of-flight increases with the increase of frequency, which can be clearly observed on the example of the third reflection in the signals shown in Fig. 4.7. On the other hand, for flexural waves, with the increase of frequency, time-of-flight decreases (Fig. 4.8).

During the above tests, the measurements for all frequencies were made with the same gain level set on the amplifier. However, it can be noted in Fig. 4.7 and Fig. 4.8 that the amplitude of the excitation signal $p_V(t)$ decreases with the increase of frequency. Consequently, the tuning test for the amplifier was performed to establish the amplifier characteristics. At first, signals on the amplifier output were collected. During this test, the actuator was disconnected from the amplifier. Figure 4.9 shows amplitudes of the excitation signal versus frequency. The obtained plot reveals small linear decay with the increase of frequency (Fig. 4.9a). As the second, similar test was performed, but with the actuator connected to the amplifier. This time, the amplifier revealed non-linear behaviour. The plot of amplitudes of the excitation signal versus frequency shows large exponential decay with the increase of frequency (Fig. 4.9b).

Experimental longitudinal and flexural wave tuning in the considered bar in the frequency range 50–300 kHz is shown in Figs. 4.10 and 4.11. The tuning test allows to find frequencies at which waves are strongly excited and frequencies at which waves practically cannot be excited in the considered bar. For each frequency, amplitudes of the incident wave, as well as the first reflection in $v_1(t)$ signal were collected and plotted in Fig. 4.10 (for longitudinal waves) and in Fig. 4.11 (for flexural waves). In spite of the exponential decay of the excitation force, visible in Fig. 4.9b, the maximum value of the registered velocity signal does not occur for frequency of 50 kHz, where the excitation signal has the largest amplitude. The strongest excitation frequencies were identified at around 120 kHz.

Experimental dispersion curves were obtained by dividing two lengths of the bar by the time-of-flight between incident wave and the first reflection in the $v_1(t)$ velocity signal. Figure 4.12 shows experimental and analytical dispersion curves for the longitudinal waves propagating in the considered rod. In the frequency range 50–300 kHz only one longitudinal mode exists (S_0 mode). The adjustable parameters for the Love and Mindlin-Herrmann theories were determined by the method of least squares to give the best fit with the experimental first mode in the frequency range 50–300 kHz and their values are: $K_L = 1.08$, $K_1^{M-H} = 1.93$, $K_2^{M-H} = 2.0$. It can be noted, that the experimental group velocity reveals dispersive character and it covers very well with the first exact S_0 Lamb mode, as well as the first S_0 Mindlin-Herrmann mode. Dispersion curves for the flexural waves are shown in Fig. 4.13. In the range 50–300 kHz two flexural modes exist (A_0 and A_1) but identification of the second flexural mode was impossible due to excessive noise present at higher frequencies (cf. Fig. 4.8c). The experimental dispersion curve agrees with the exact A_0 Lamb mode, as well as the first flexural mode of the Timoshenko theory. The adjustable parameters were determined as $K_1^{Tim} = 0.95$, $K_2^{Tim} = 12K_1^{Tim} / \pi^2$, based upon the comparison with the experimental results within the frequency range of interests.

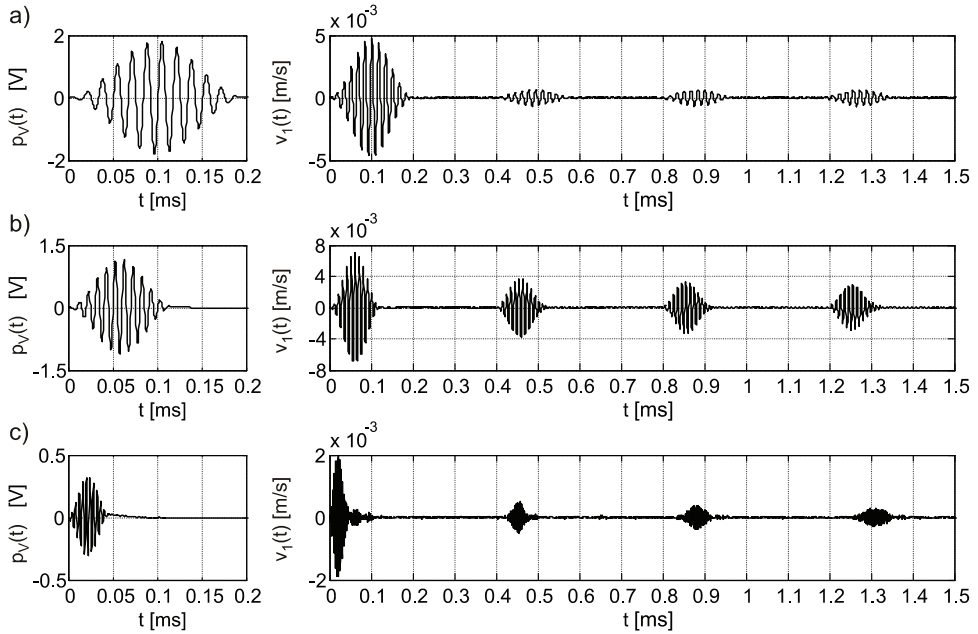


Fig. 4.7. Time history of experimentally measured longitudinal waves for determination of dispersion curves: a) 60 kHz; b) 100 kHz; c) 250 kHz

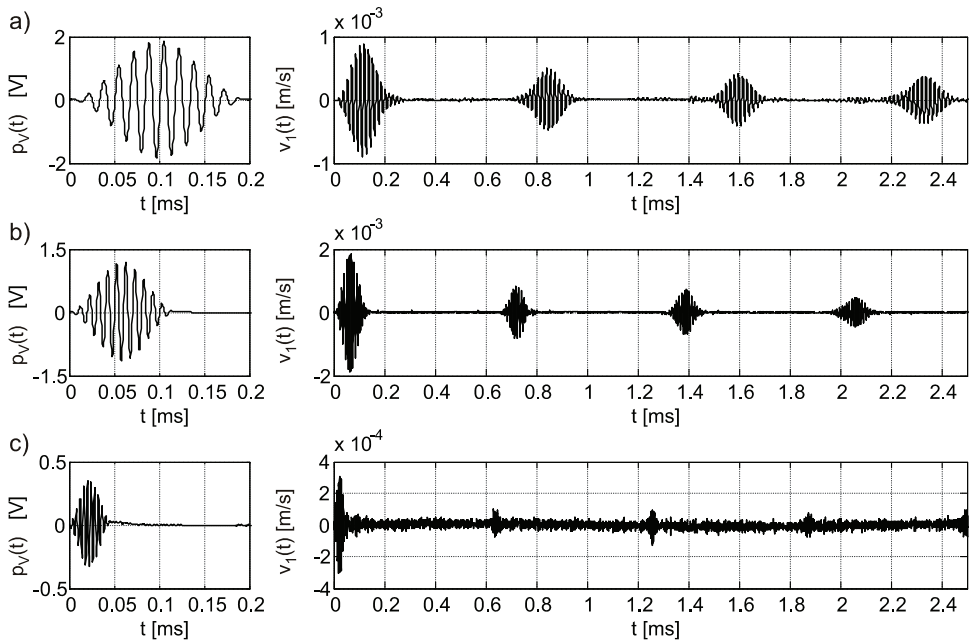


Fig. 4.8. Time history of experimentally measured flexural waves for determination of dispersion curves: a) 60 kHz; b) 100 kHz; c) 250 kHz

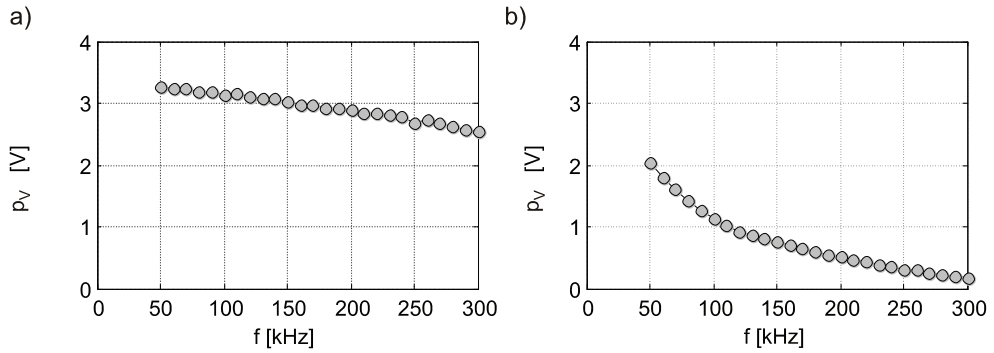


Fig. 4.9. Tuning test of the amplifier for frequency range 50–300 kHz: a) maximum value of the excitation signal $p_V(t)$ measured on the amplifier output in the case of actuator disconnected from the amplifier; b) maximum value of the excitation signal $p_V(t)$ measured on the amplifier output in the case of actuator connected to the amplifier

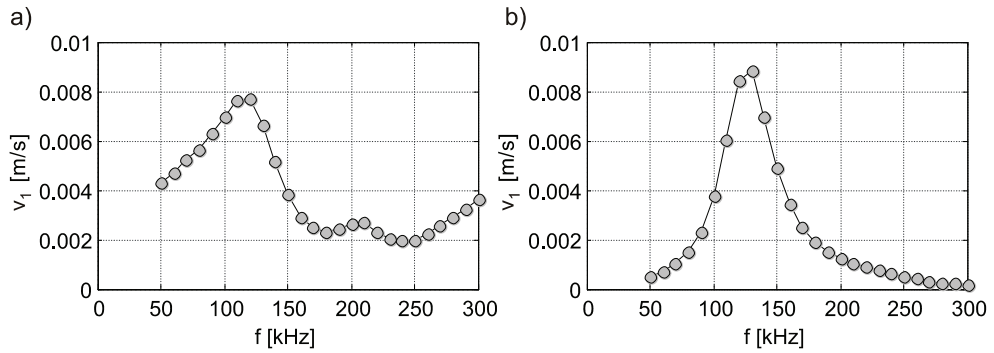


Fig. 4.10. Experimental longitudinal wave tuning in the intact rod for frequency range 50–300 kHz: a) maximum value of incident wave in the velocity signal $v_1(t)$; b) maximum value of first reflection signal in the velocity signal $v_1(t)$

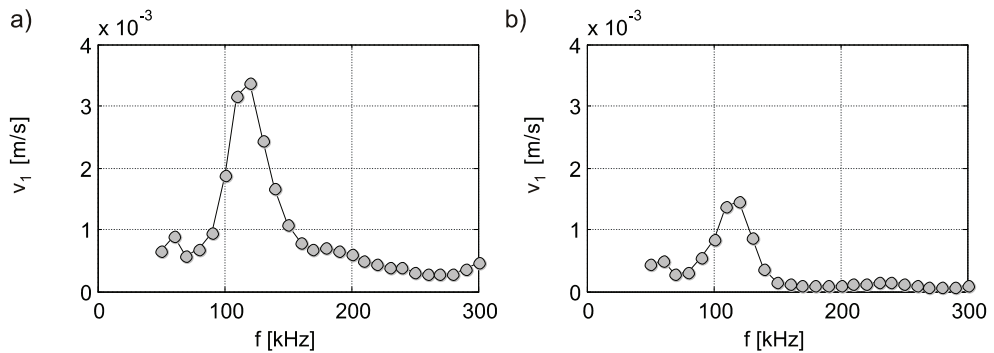


Fig. 4.11. Experimental flexural wave tuning in the intact beam for frequency range 50–300 kHz: a) maximum value of incident wave in the velocity signal $v_1(t)$; b) maximum value of first reflection signal in the velocity signal $v_1(t)$

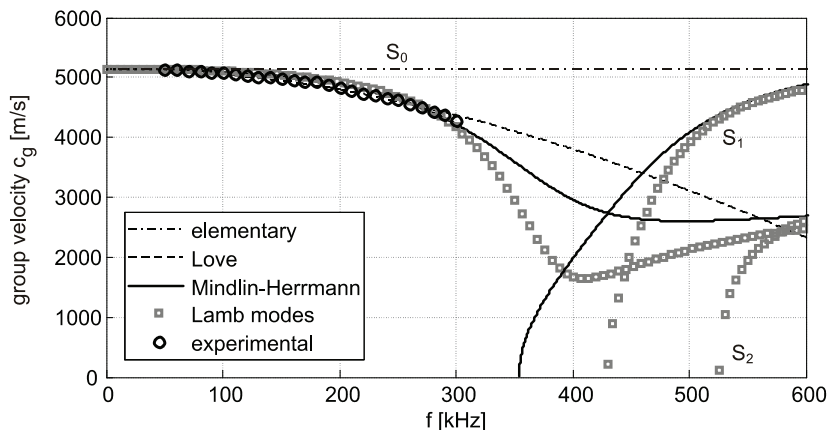


Fig. 4.12. Experimental and analytical dispersion relations for longitudinal waves in the considered rod

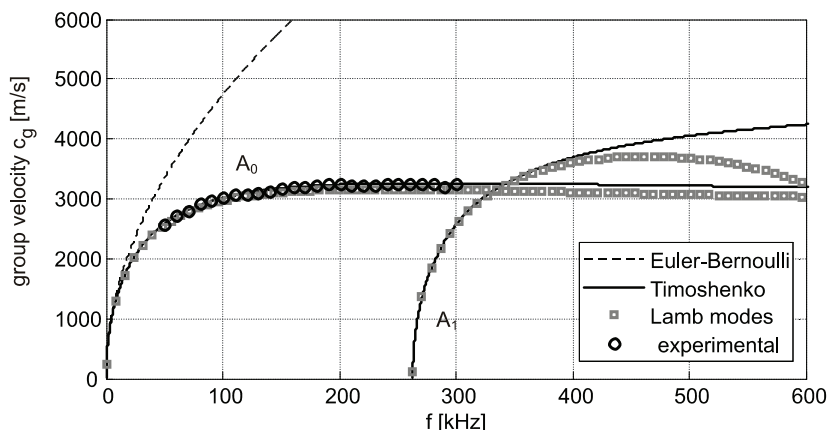


Fig. 4.13. Experimental and analytical dispersion relations for flexural waves in the considered beam

4.2. Experimental investigations on bars with discontinuities

The measurements were made on four different bars (Fig. 4.14); three of them with discontinuities of cross-section or material. The specimens were as follows (Rucka 2010a):

- bar no. 1: an intact specimen,
- bar no. 2: with a local change of the cross-section in the form of welded steel elements with dimensions $10 \text{ mm} \times 6 \text{ mm} \times 2 \text{ mm}$ on both sides of the bar (called the bar with the additional mass). The mass of additional elements equals $1.81 \times 10^{-3} \text{ kg}$, which is 0.67% of the total mass of the bar,
- bar no. 3: with a rectangular notch of dimension 2 mm in length and 1 mm in height. The depth of the notch is 16.7% of the beam height,
- bar no. 4: with a double V-groove weld of width 4 mm. The bar was cut in two parts, the edges of both pieces were chamfered doubly in two directions and welded using

TIG welding technique. The weld was grinded after welding in such a way, that the bar got the same geometry as the intact bar.

As an excitation, a twelve-peak sinusoidal signal modulated by the Hanning window was chosen. In the case of longitudinal wave propagation, the frequency of the excitation signal was 150 kHz (Fig. 4.15a). For the case of flexural waves, when the propagating wave velocity has a smaller value, the frequency of the excitation signal was chosen as 100 kHz (Fig. 4.15b).

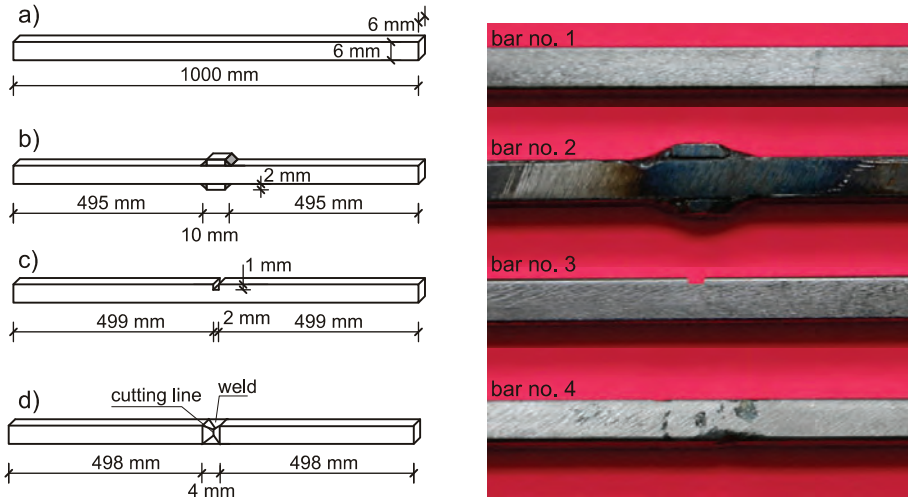


Fig. 4.14. Geometry of experimentally tested bars and close-up of structural discontinuities:
a) intact bar; b) bar with mass; c) bar with notch; d) bar with weld

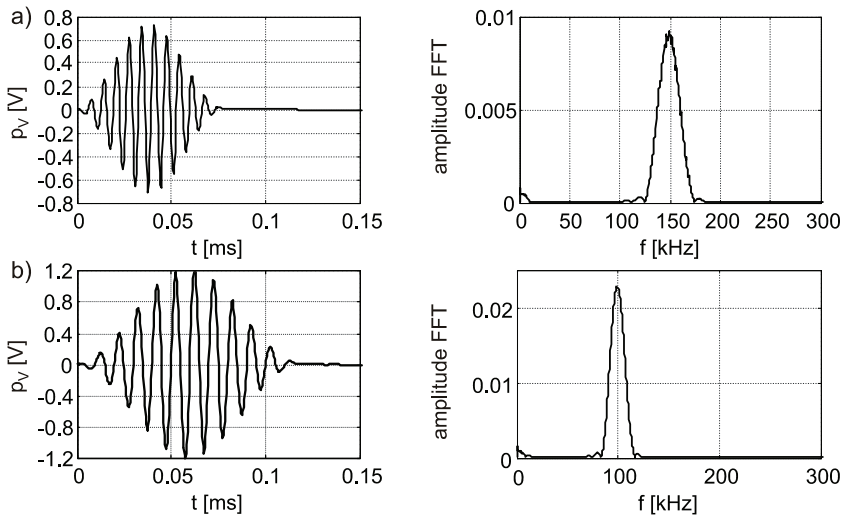


Fig. 4.15. Excitation voltage signal in time and frequency domains:
a) signal of frequency 150 kHz; b) signal of frequency 100 kHz

Figure 4.16 shows the experimental results for longitudinal wave propagation. The velocity signal $v_1(t)$ was measured on the left end of the rod, while the signal $v_2(t)$ was measured on its right end, as it is shown in Fig. 4.2a. The signal registered in the intact rod contains the first arrival and three echoes during the recorded period of 1.5 ms. For the rods with structural discontinuities, additional reflections appeared in the response signals. The greatest reflection was caused by the presence of additional mass, whereas the smallest reflection was caused by the groove weld. The discontinuities in the form of the notch and the weld caused additional reflections of an amplitude much smaller than the amplitude of reflections from the rod ends. Moreover, the amplitudes of reflections from the rod ends exponentially decreased, while the amplitudes of reflections from the notch or weld revealed a rise with the time passage (Fig. 4.16c and Fig. 4.16d). The presence of the additional mass caused different type of reflections (Fig. 4.16b), for example in $v_2(t)$ signal, the amplitude of the reflection from the mass was higher than the amplitude of the reflection from the rod end.

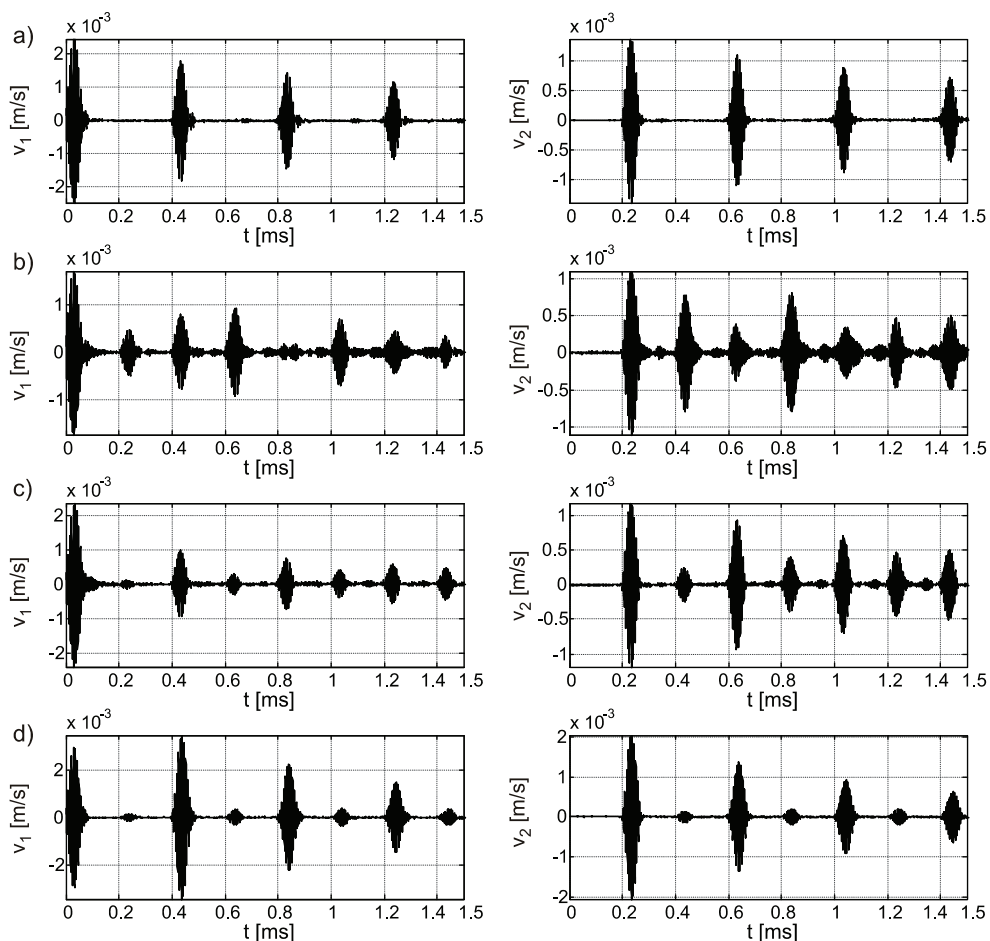


Fig. 4.16. Experimentally measured velocity signals $v_1(t)$ and $v_2(t)$ of longitudinal waves: a) intact rod; b) rod with mass; c) rod with notch; d) rod with weld

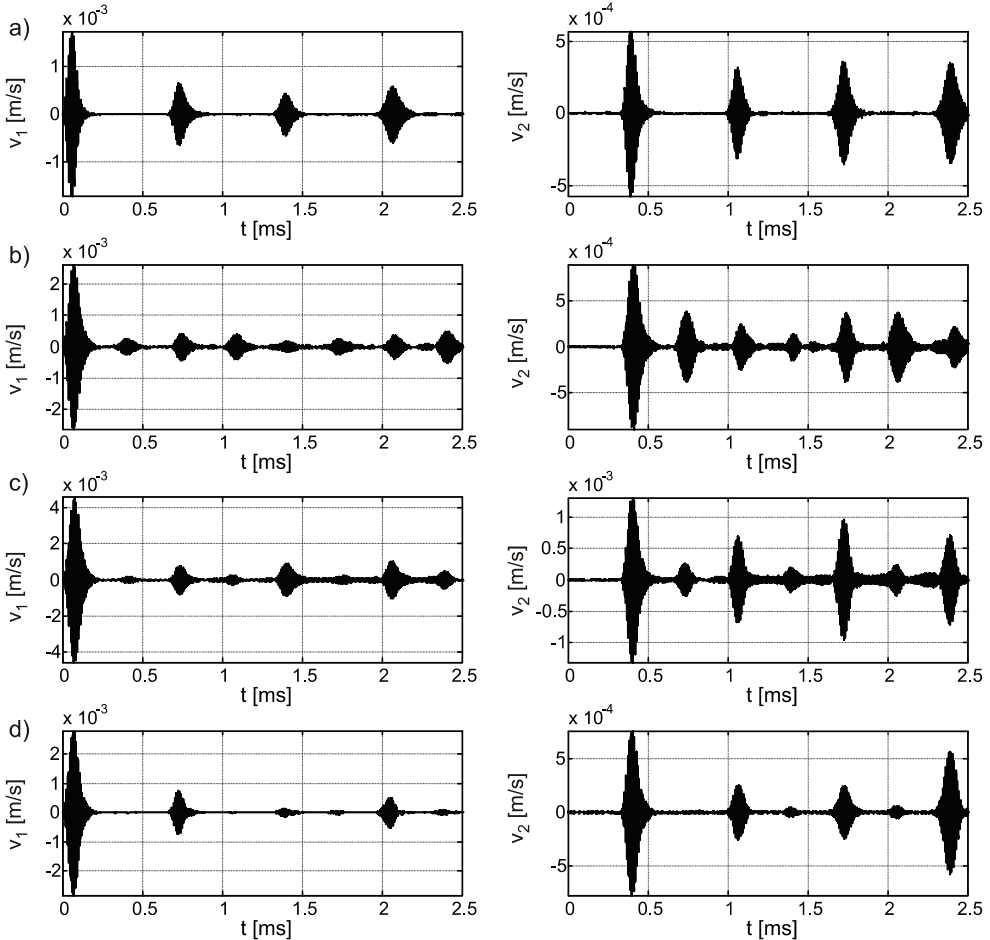


Fig. 4.17. Experimentally measured velocity signals $v_1(t)$ and $v_2(t)$ of flexural waves:
 a) intact beam; b) beam with mass; c) beam with notch; d) beam with weld

Locations of defects can be identified based on the knowledge of the rod length and the group velocity. For the considered 150 kHz excitation, the analytical value of the group velocity was 4974.17 m/s (based on the Mindlin-Hermann theory), while the experimental one was 4980.54 m/s (cf. Fig. 4.12). Considering the rod with the additional mass, the reflection from discontinuity occurred at the time instant equal to 0.2031 ms, therefore the position of the mass was identified as 506 mm. In the case of the rod with the notch, the time of reflection from the notch was 0.2 ms, which means that the defect is situated at the distance of 498 mm. Finally, for the rod with the weld, the position of the defect was identified as 503 mm, since the reflection in the $v_1(t)$ velocity signal occurred at 0.202 ms. The actual position of the defect was 500 mm. The difference between the actual position and the position identified based on the experimental signals was 0.4% to 1.2%.

The experimental velocity signals $v_1(t)$ and $v_2(t)$ for the flexural wave propagation are presented in Fig. 4.17. In the $v_1(t)$ signal for the intact beam, the incident wave and

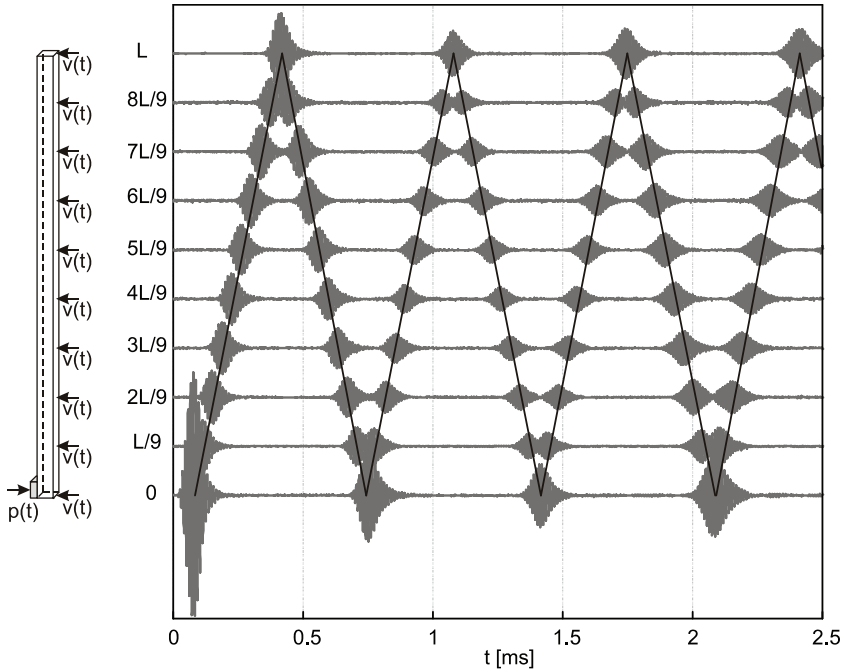


Fig. 4.18. Time-position plane of response signals measured in 10 points for the intact beam

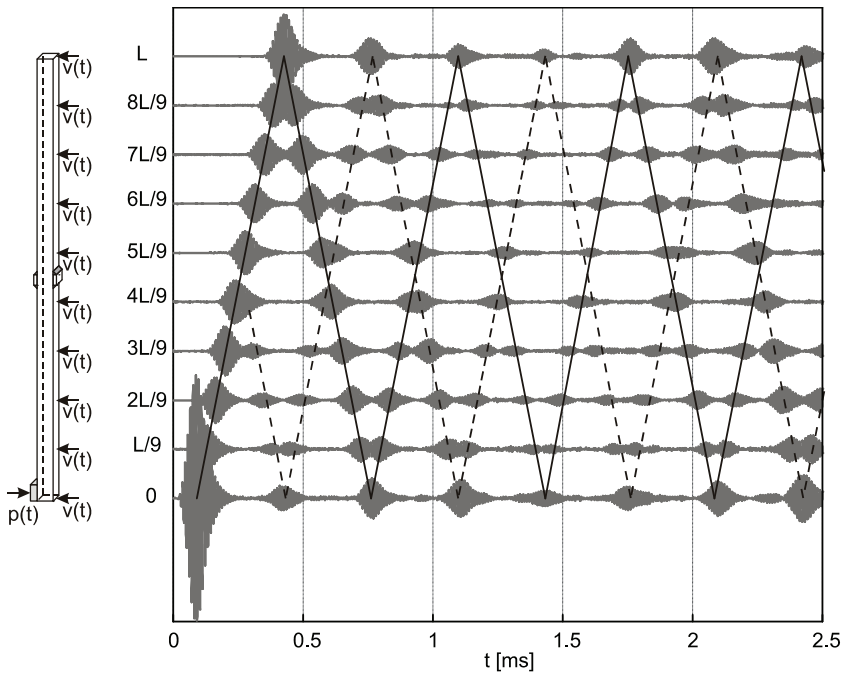


Fig. 4.19. Time-position plane of response signals measured in 10 points for the beam with mass

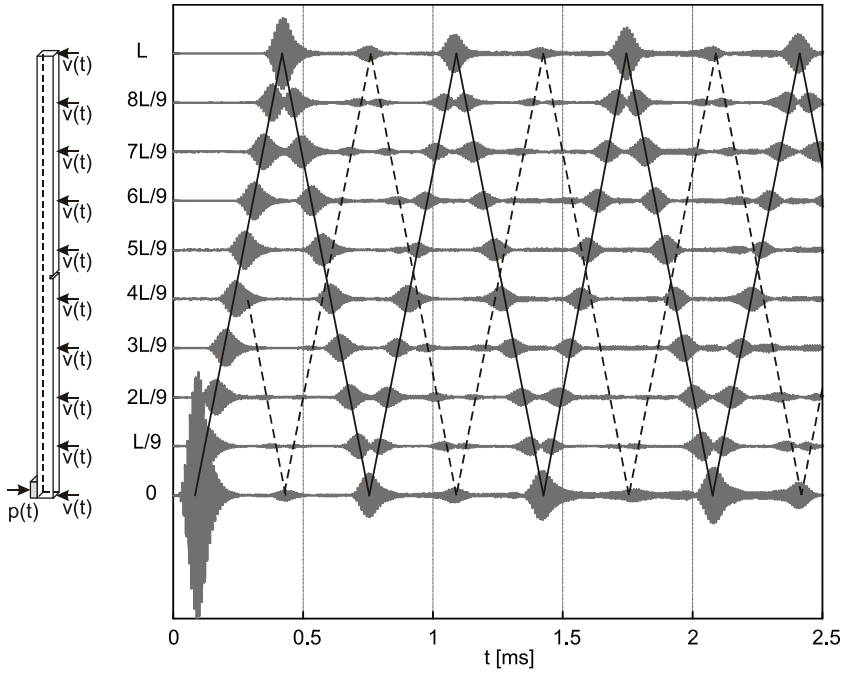


Fig. 4.20. Time-position plane of response signals measured in 10 points for the beam with notch

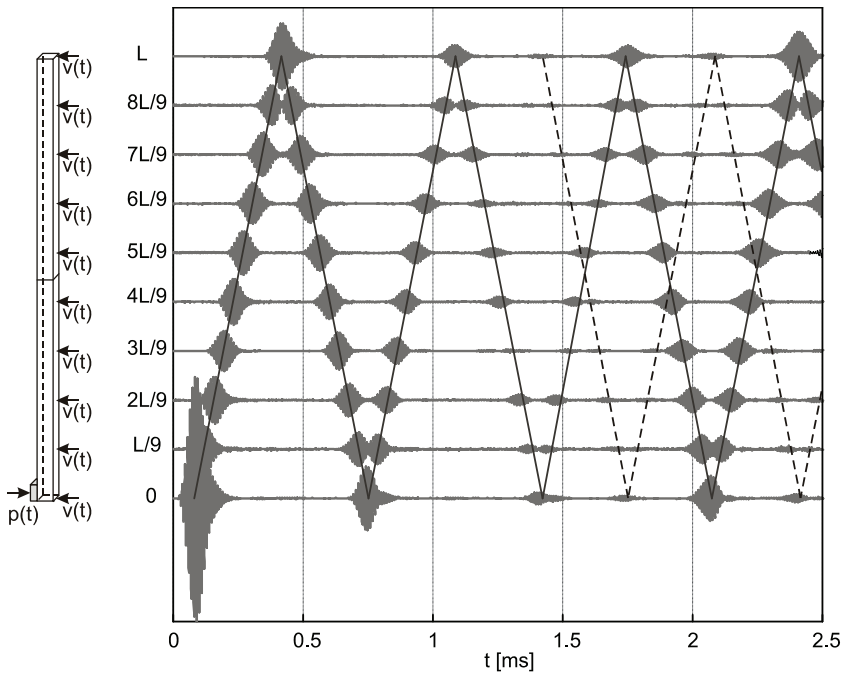


Fig. 4.21. Time-position plane of response signals measured in 10 points for the beam with weld

three reflections are visible during the recorded 2.5 ms period. Additional reflections in signals appeared for all beams with structural discontinuities. As in the case of longitudinal waves, the presence of the notch and the weld caused the reflections of an amplitude much smaller than the amplitude of reflections from the beam ends. However, for the beam with the weld, the additional reflection from the weld did not appear in the first wave passage. The reflection from the weld appeared at 1.32 ms and its amplitude was larger in every consecutive wave passage. In the beam with the mass, the amplitudes of reflections from the mass and the beam boundaries had similar values. The analytical flexural group velocity for the wave of frequency 100 kHz was 3012.06 m/s, whereas the experimental value was 3029.59 m/s (cf. Fig. 4.13). The positions of defects were identified experimentally as 506 mm, 502 mm, 502 mm, for the beam with the mass, with the notch and with the weld, respectively and the corresponding reflection times were: 0.334 ms, 0.3313 ms, 0.3316 ms.

Finally, each beam was measured in 10 equally distributed points, as it is shown in Figs. 4.18 to 4.21, to observe wave propagation in the time-position plane. As a result of such test, the interaction of waves with boundaries or potential discontinuities may be observed more precisely. Figure 4.18 illustrates flexural wave propagation in the intact beam, while Fig. 4.19, Fig. 4.20 and Fig. 4.21 give the results for the beams with the mass, the notch and the weld, respectively. The solid line indicates the centre of the wave packet reflected from boundaries, while the dashed line denotes the centre of the wave packet reflected from damage or other discontinuity.

4.3. Spectral element analysis of wave propagation in an intact bar

In this section, tests on the intact rod (described in Section 4.2) are performed. The aim of these simple tests is to experimentally validate the numerical models of wave propagation, applied later for rods and beams with structural discontinuities, as well as frame structures. Both longitudinal and flexural waves are studied. In the considered frequency range (100–150 kHz) only one longitudinal mode and one flexural mode can propagate (see Fig. 4.12 and Fig. 4.13). Modelling of longitudinal wave propagation is conducted by the spectral element method based on the elementary, Love and Mindlin-Herrmann rod theories, whereas modelling of flexural waves is conducted by the SEM based on the Timoshenko beam theory. The damping matrix is assumed as a proportional with respect to the mass matrix $\mathbf{C} = \eta_d \mathbf{M}$ with damping parameter η_d set as 1000 1/s for longitudinal waves and 2000 1/s for flexural waves. Values of damping parameters are adopted to obtain the same relationship between amplitudes of reflected signals for experimental investigations and numerical simulations. The amplitude of the excitation force signal equals 1 N. In the case of flexural waves, the wave is impacted in 3rd node from the left edge, which coincides with the actuator centre. The boundary conditions in the SEM models of the bar are established as free.

4.3.1. Guidelines for spectral element models on the example of longitudinal waves

For the analysis of wave propagation, the effective length L_e of the finite element, and the corresponding time step Δt must be able to represent accurately the travelling wave (Bathe 1996). The total time for the travel of the wave of wavelength λ past a point is:

$$t_w = \lambda / c_p . \quad (4.3)$$

To represent the travel of the wave, n_t time steps are necessary:

$$\Delta t = t_w / n_t . \quad (4.4)$$

Therefore the effective length of a finite element is defined as (Bathe 1996):

$$L_e = c_p \Delta t . \quad (4.5)$$

The number of used elements depends mainly on the wavelength of the propagating wave. The effective length of the 2-node finite element should satisfy the following equation:

$$L_e = \frac{\lambda}{n_w - 1} , \quad (4.6)$$

where n_w denotes the number of nodes per wavelength. When analysing higher order elements of evenly distributed nodes, the effective length L_e denotes the distance between any two nodes of the element. However, the GLL nodes are not evenly distributed and in higher order elements (above 3 nodes) the number of nodes n_w per wavelength depends on the spatial localization within the rod. Figure 4.22 shows two cases of higher order spectral elements with GLL nodes: one 121-node element per rod and sixteen 11-node elements. For the 121-node element, 15 nodes are situated on the first wavelength, whereas in the middle of the rod there are only about 3 nodes (Fig. 4.22a). Considering 11-node elements (Fig. 4.22b), nodes are concentrated near the element ends, and the number of nodes per wavelength varies from about 4 to 7. Therefore, in the case of spectral elements it is not possible to say about the number of nodes per wavelength, the average number of nodes can be used instead.

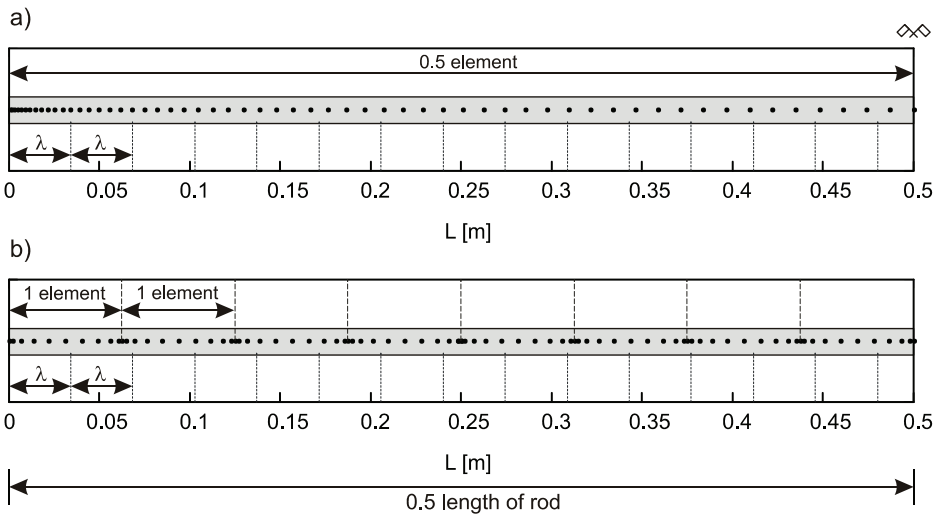


Fig. 4.22. Distribution of nodes in higher order spectral elements on half-length rod:

a) 1 element with 121 GLL nodes; b) 16 elements with 11 GLL nodes

Numerical dispersion makes the wave velocity depend on features of the numerical model, i.e. mesh size, element type, time integration step (Semblat and Brioi 2000). In general, the spatial and temporal discretizations may interact and their total dispersive errors may not be linear summation of dispersive errors due to two individual discretizations alone (Dauksher and Emery 2000). To analyse numerical errors, longitudinal wave propagation in the rod has been studied. Simulations were conducted on the rod described by the elementary theory, because such rod does not exhibit physical dispersion. Two different cases of spectral elements were considered: namely one multi-node spectral element per rod and a few 11-node spectral elements per rod. When one multi-node spectral element per rod was used, the desirable minimum number of nodes was $n = 121$, which gives about 5.1 nodes per wavelength. The resulting velocity signal for this case is presented in Fig. 4.23a. Next 11-node elements have been applied. When 12 elements with $n = 11$ nodes were used, which gives totally $N_t = 121$ nodes in the rod, the velocity signal of propagating wave was contaminated due to numerical dispersion (Fig. 4.23b), which means that there was not a sufficient number of nodes. The minimum number of nodes for the 11-node elements appeared to be $N_t = 161$ (16 elements), which gives 6.5 nodes per wavelength. Additionally, a standard FEM analysis using 2-node elements was performed. For the case of 120 elements with 2 nodes, the results are not contaminated, but they are shifted due to numerical dispersion (Fig. 4.23c). To obtain results comparable to the results for the one 121-node element, 1200 elements with 2 nodes have to be used, which leads to use about 40 nodes per wavelength. The above simulations were performed using the central difference scheme with the same time step $\Delta t = 4 \cdot 10^{-8}$ s, established according to (3.30) for the most unfavourable case, i.e. $N_t = n = 121$, $n_{el} = 1$. It can be concluded, that higher order elements were found to have a much better efficiency towards numerical dispersion than linear elements (cf. Semblat and Brioi 2000).

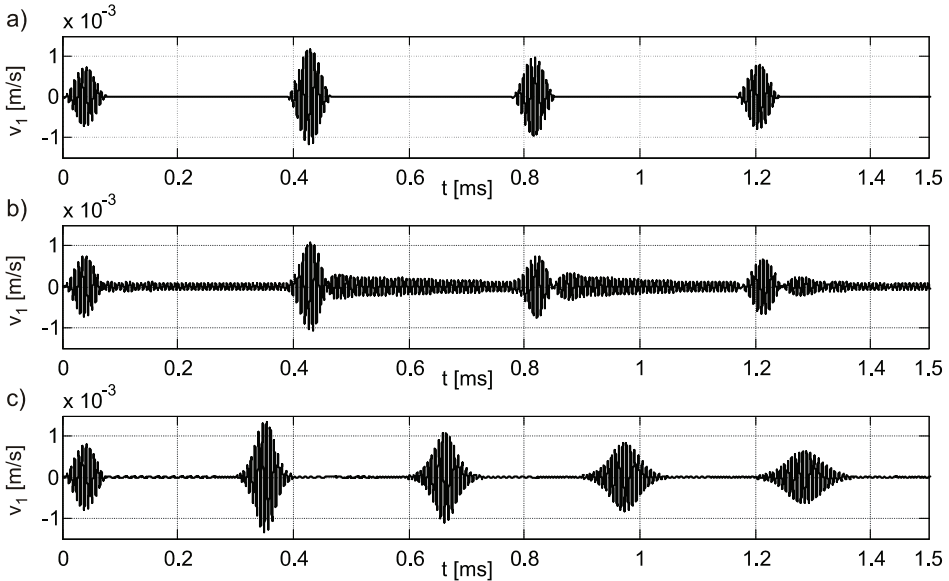


Fig. 4.23. Numerical velocity signals in elementary rod modelled by: a) 1 element with 121 GLL nodes; b) 12 elements with 11 GLL nodes; c) 120 elements with 2 nodes

Figure 4.24 presents the relationship between the number of the GLL nodes in a spectral element and the required number of nodes per wavelength. It is visible, that it reveals the exponential character, and for the elements with 7 to 121 GLL nodes, the number of nodes per wavelength becomes from 7.6 to 5.1, respectively.

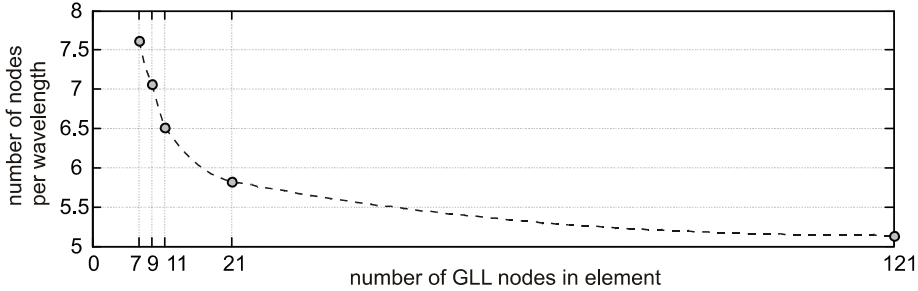


Fig. 4.24. Relationship between the number of nodes in the element and the required number of nodes per wavelength for longitudinal waves in rod based on the elementary theory

Numerical dispersion can also appear as a result of temporal discretization. In the analysis of wave propagation, if a conditionally stable algorithm is used, such as the central difference method, the numerical time step restriction for stability plays a limiting role. The applied critical time step Δt_{cr} follows from the stability criterion (3.30). Therefore, application of e.g. 16 elements with 11 GLL nodes ($\Delta t_{cr} = 3.4 \cdot 10^{-7}$ s), instead of e.g. one 121-node element ($\Delta t_{cr} = 4.2 \cdot 10^{-8}$ s) can be treated as a compromise between the multi-node spectral approach and the sufficiently large integration time step.

If an implicit unconditionally stable time integration scheme is used, the time step Δt can be assessed from the Courant condition $\Delta t \leq L_e/c_p$ (see Bathe 1996). To illustrate the numerical dispersion error connected with the temporal discretization, the numerical model of the rod with one 121-node element was analysed (Fig. 4.25). The numerical integration was performed by the Newmark method with parameters $\beta=1/4$, $\gamma=1/2$. Different time steps were applied, namely $\Delta t = 1 \cdot 10^{-8}$ s, $\Delta t = 5 \cdot 10^{-8}$ s, $\Delta t = 1 \cdot 10^{-7}$ s, $\Delta t = 5 \cdot 10^{-7}$ s, $\Delta t = 1 \cdot 10^{-6}$ s. The length of the time step calculated using Eq. (4.5) equals $\Delta t = 4.9 \cdot 10^{-8}$ s. The velocity responses for the time steps $\Delta t = 1 \cdot 10^{-8}$ s, $\Delta t = 5 \cdot 10^{-8}$ s, $\Delta t = 1 \cdot 10^{-7}$ s give similar non-dispersive results. Application of longer time steps $\Delta t = 5 \cdot 10^{-7}$ s, $\Delta t = 1 \cdot 10^{-6}$ s causes strong numerical dispersion errors.

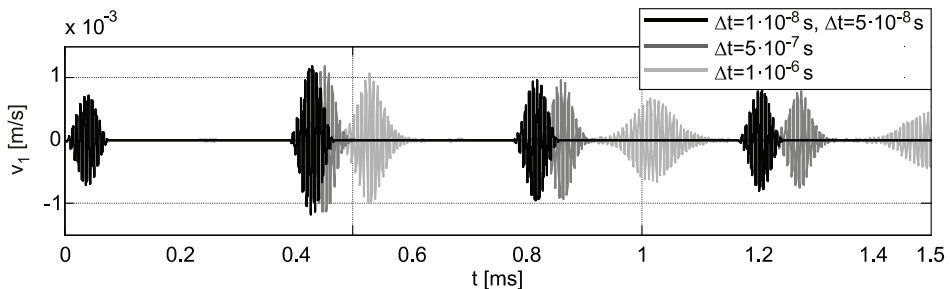


Fig. 4.25. Numerical velocity signal in elementary rod modelled by one element with 121 GLL nodes with different time steps

4.3.2. Simulations of longitudinal waves

The comparison of the experimental and numerical velocity signals for the intact rod is shown in Fig. 4.26 for the elementary, Love and Mindlin-Herrmann theories. The rod was modelled using 16 elements with 11 GLL nodes. The numerical integration was performed using the central difference method with the time step $\Delta t = 1 \cdot 10^{-7}$ s. The adjustable parameters for the Love and Mindlin-Herrmann theories were chosen to give the best fit with the experimental first mode in the frequency range 100–150 kHz and their values are: $K_L = 0.99$, $K_1^{M-H} = 1.07$, $K_2^{M-H} = 2.0$. In Fig. 4.26 amplitudes of the experimental and the numerical velocity signals were normalized to 1. In the case of the experimental signal $v_1(t)$, the normalization was carried out to the first reflection from the rod end, because the signal $v_1(t)$ was measured on the actuator. Additionally, only the signal envelopes are plotted for the sake of clarity. If the elementary rod theory is used, the experimental data are not compatible with the numerical ones. The experimental velocity signal is delayed with respect to the numerical signal. This indicates the presence of dispersion during the experiment. Considering the Love theory, it can be noted that numerical simulations are in good agreement with the experimental data. The velocity results using the Mindlin-Herrmann theory coincide with results obtained by the Love theory. The difference between two above mentioned theories is connected with the mass matrix. For the elementary theory, as well as the Mindlin-Herrmann theory the mass matrix has a diagonal structure, therefore the numerical integration using the central difference method can be efficiently conducted. Application of the Love theory results in non-diagonal mass matrix.

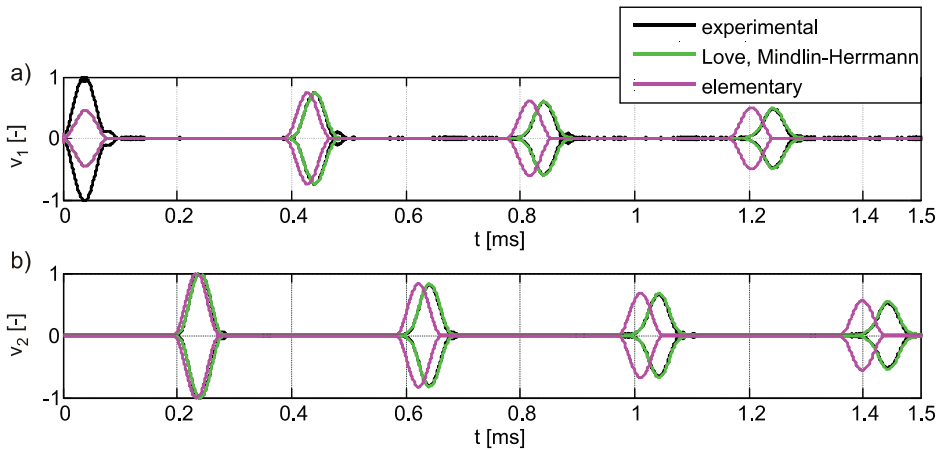


Fig. 4.26. Comparison of experimental and numerical velocity signal envelopes for the elementary, Love and Mindlin-Herrmann rod theories: a) normalized signal $v_1(t)$; b) normalized signal $v_2(t)$

4.3.3. Simulations of flexural waves

The intact specimen was modelled using 24 equal elements with 15 GLL nodes and the time step was set as $\Delta t = 1 \cdot 10^{-7}$ s. Figure 4.27 shows comparison of the $v_1(t)$ velocity signal in the beam modelled by the SEM using the Timoshenko theory and the FEM using the Euler-Bernoulli theory. The signals are highly incompatible, which indicates that in such high frequency range the Timoshenko beam theory must be used.

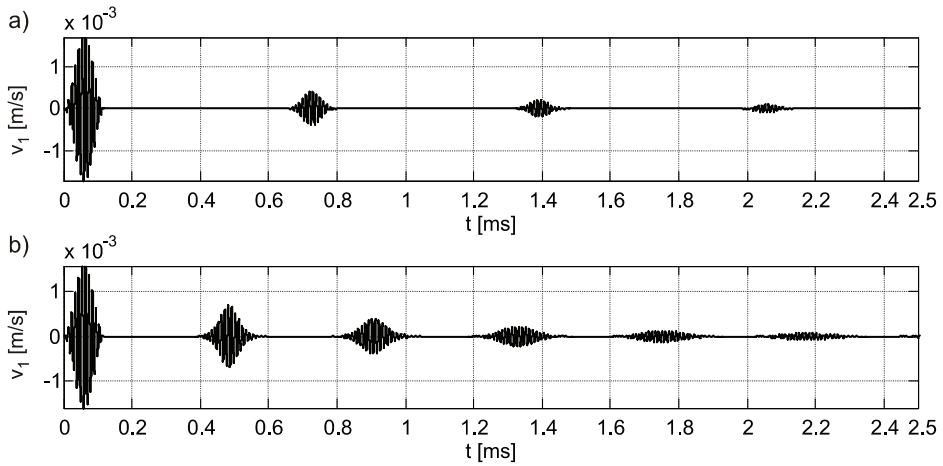


Fig. 4.27. Numerical time velocity signals in the intact beam: a) Timoshenko theory (25 elements with 15 GLL nodes); b) Euler-Bernoulli theory (400 elements with 2 nodes)

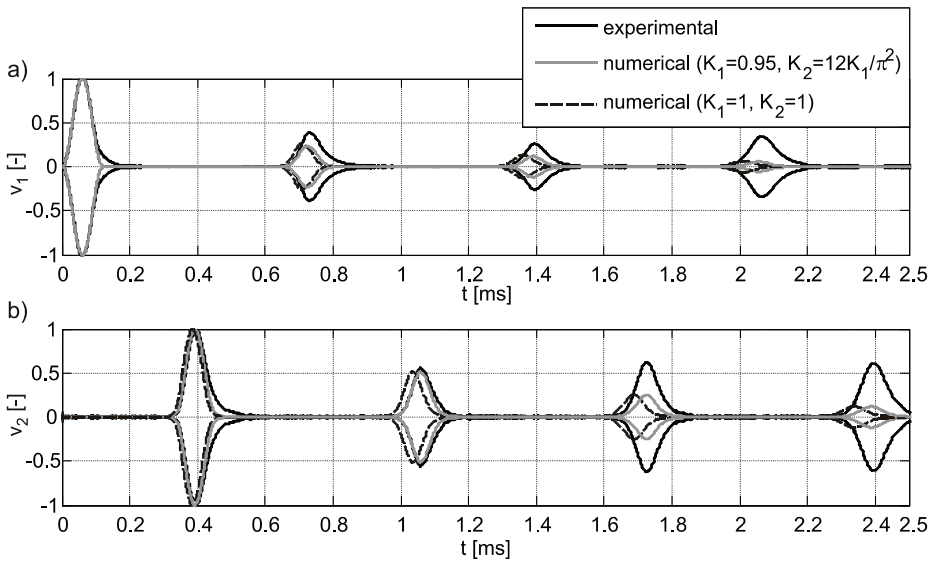


Fig. 4.28. Comparison of experimental and numerical velocity signal envelopes for the Timoshenko beam theory: a) signal $v_1(t)$; b) signal $v_2(t)$

Figure 4.28 illustrates the comparison of the experimental and numerical velocity signal for the intact beam. In the numerical simulations the spectral element based on the Timoshenko beam theory was applied with two variants of adjustable parameters, i.e. $K_1^{Tim} = 0.95$, $K_2^{Tim} = 12K_1^{Tim} / \pi^2$ and $K_1^{Tim} = 1$, $K_2^{Tim} = 1$. It can be observed that the velocity calculated from the model without adjustable parameters does not cover with the experimental signal and the adjustable parameters can compensate the approximation of displacement fields. The comparison of experimental and numerical velocity signals in the time-position plane is illustrated in Fig. 4.29. In this case the beam was modelled by 9 ele-

ments with 35 GLL nodes. It can be seen, that the numerical and the experimental waves propagate with the same speed.

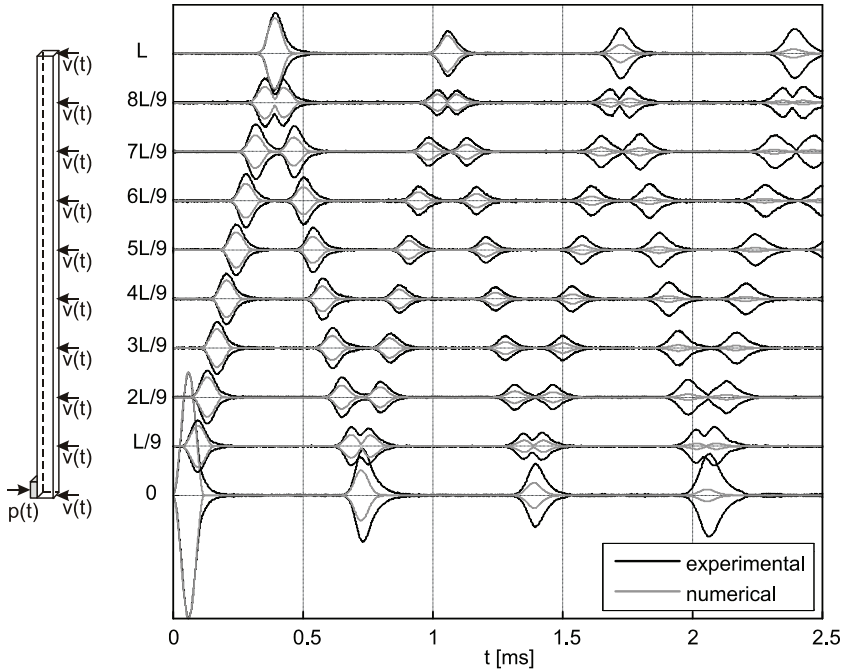


Fig. 4.29. Time-position plane of response signals measured in 10 points for the intact beam: comparison of experimental and numerical velocity responses

4.4. Spectral element analysis of wave propagation in bars with structural discontinuities

In this section, results of numerical calculations performed on the spectral element models of the previously experimentally tested bars with discontinuities are presented and the comparisons are carried out. The numerical integration was performed using the central difference method and the time step was chosen according to Eq. (3.30). Numerical simulations concerned the longitudinal and flexural wave propagation. The rods with discontinuities were modelled using 16 equal elements with 11 GLL nodes and one shorter element (with 11 GLL nodes) of different parameters in the middle of the rod. The beams with discontinuities were modelled using 24 equal elements with 15 GLL nodes and one element of different parameters with 15 GLL nodes. For the bar with the change of cross-section, the element of length 10 mm in the middle of the bar was applied and its height was enlarged to the value of 10 mm. In the case of the bar with the notch, 2 mm element with the height of 5 mm was used. Considering the bar with the weld, it was assumed that the part of the bar with the weld has worse parameters (because of heating during the welding process). Therefore the 4 mm element in the middle of the bar has the modulus of elasticity $E = 180.10$ GPa, i.e. 10% smaller than the rest of the bar.

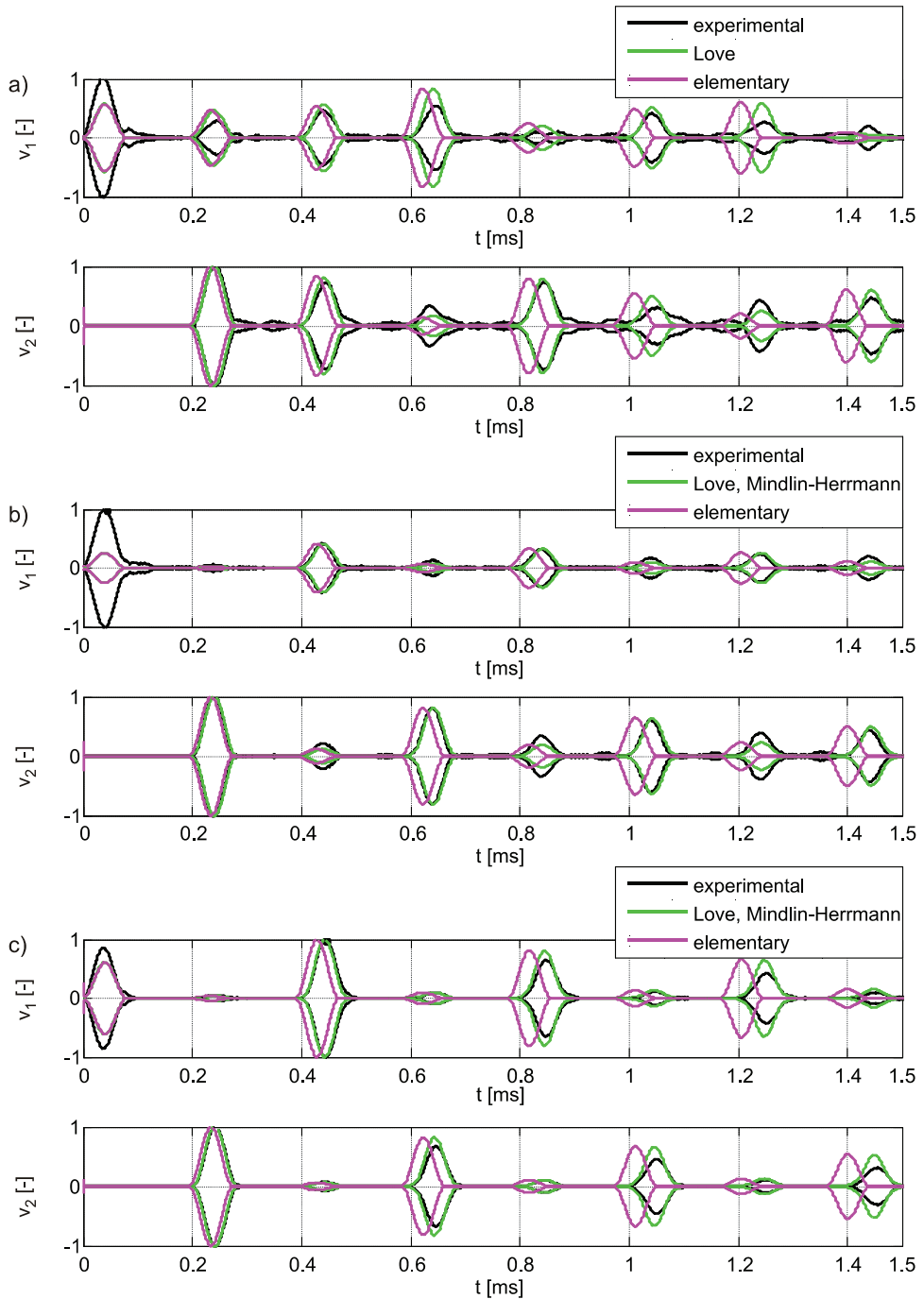


Fig. 4.30. Comparison of experimental and numerical normalized velocity signal envelopes for the elementary, Love and Mindlin-Herrmann rod theories: a) rod with mass, b) rod with notch; c) rod with weld

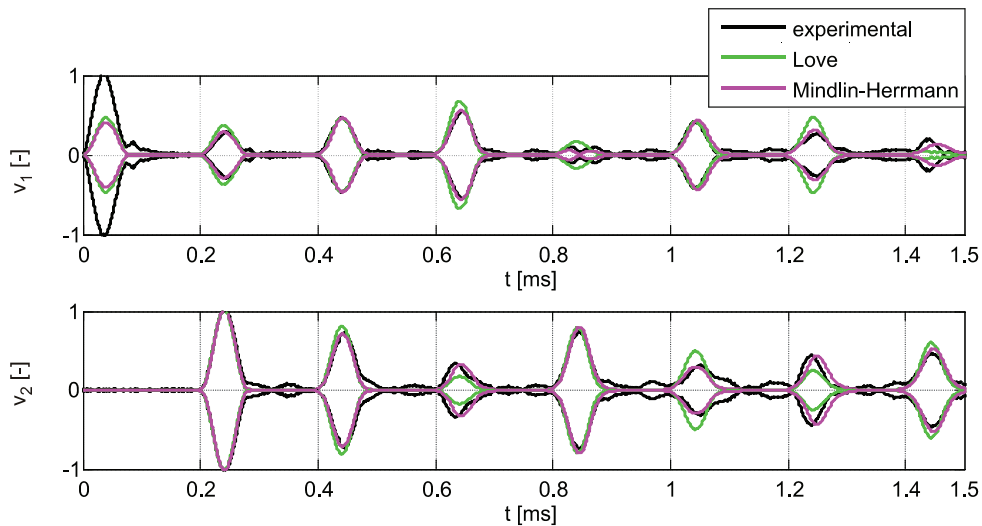


Fig. 4.31. Comparison of experimental and numerical normalized velocity signal envelopes for the Love and Mindlin-Herrmann rod theories for the rod with additional mass

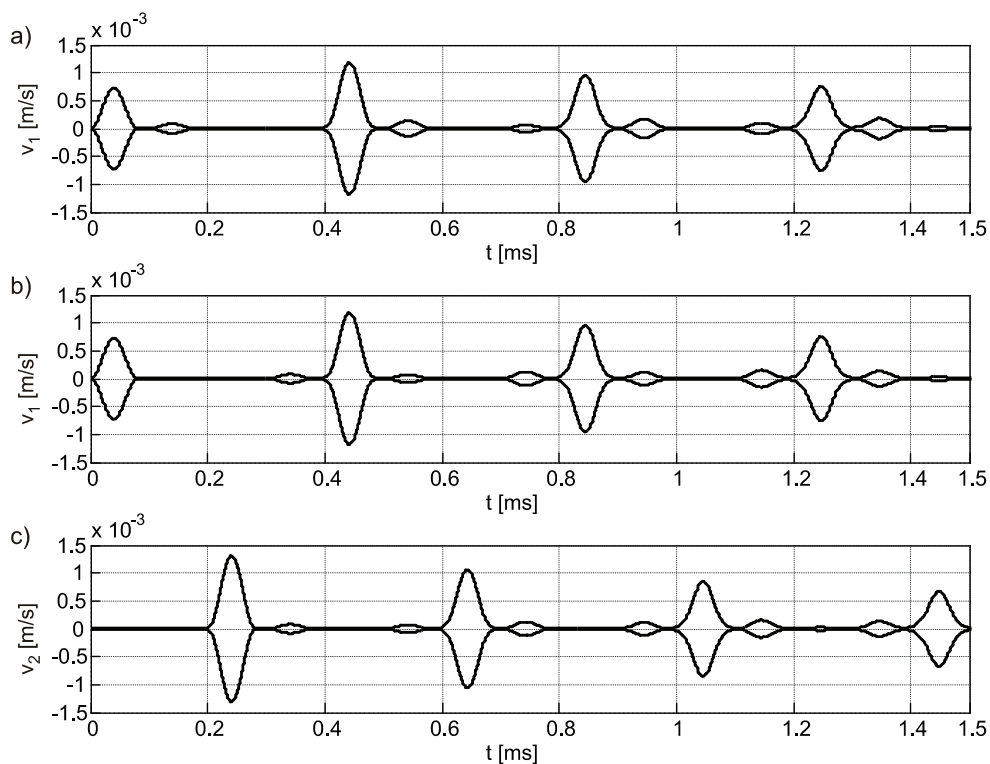


Fig. 4.32. Envelopes of numerical velocity signals $v_1(t)$ and $v_2(t)$ measured on both ends of the rod containing the notch at position L_r in the case of longitudinal wave propagation:
 a) notch at $L_r = 0.25L$; b) notch at $L_r = 0.75L$; c) notch at $L_r = 0.25L$ or $L_r = 0.75L$

The numerical results of longitudinal wave propagation are compared with the experimental data in Fig. 4.30 for the elementary, Love and Mindlin-Herrmann theories. Application of the elementary theory results in signals inconsistent with the experimental data. The experimental velocity signal is delayed with respect to the numerical signal, which is caused by physical dispersion. If the Love theory is used, the numerical simulations are generally in good agreement with the experimental data. Considering the Mindlin-Herrmann theory, the results for the rod with the notch (Fig. 4.30b) and the rod with the weld (Fig. 4.30c) cover with the results obtained using the Love theory. The discrepancy between the two above-mentioned theories appears in the case of the rod with the additional mass, as shown in Fig. 4.31. It is visible, that the Mindlin-Herrmann theory better approximates the experimental signal. This is because the rotational effects are respected independently in the mass matrix.

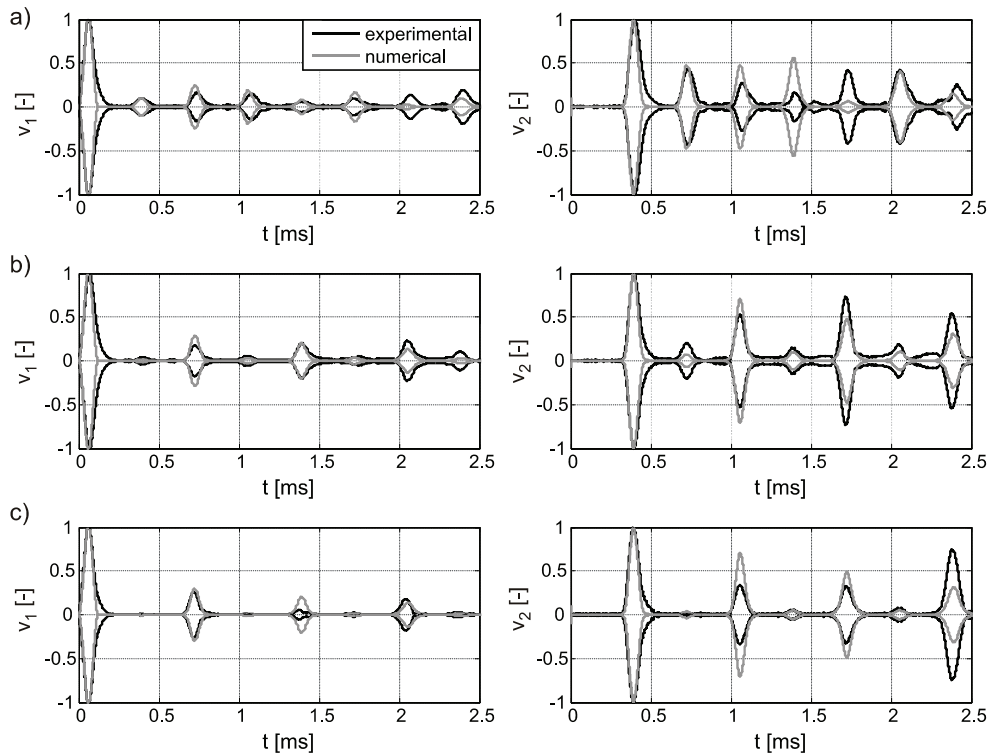


Fig. 4.33. Comparison of experimental and numerical velocity signal envelopes for the Timoshenko beam theory: a) beam with mass; b) beam with notch; c) beam with weld

For the considered specimens with singularities, additional reflections appeared in the response signal and the position of damage in the rod can easily be identified from both $v_1(t)$ and $v_2(t)$ velocity signals (Fig. 4.30). However, the situation is different when the defect does not occur in the middle of the rod. On the example of longitudinal wave propagation, two positions of damage, namely $L_r = 0.25L$ and $L_r = 0.75L$ were considered (Fig. 4.32). It can be seen, that only signal $v_1(t)$, registered at the same point as the actuator, makes an unambiguous localization of damage possible (Fig. 4.32a,

Fig. 4.32b). The velocity signal $v_2(t)$ registered at the opposite end is the same for both $L_r = 0.25L$ and $L_r = 0.75L$ damage positions (Fig. 4.32c).

In the case of flexural waves, the numerical results are compared with the experimental data in Fig. 4.33. The proposed ways of damage modelling in the beams with the notch, the mass and the weld provided velocity results compatible with the experimental signals.

4.5. Summary and conclusions

In this chapter, longitudinal and flexural wave propagation in the bar has been investigated both experimentally and numerically. Numerical simulations have been performed by the time domain spectral element method using the elementary, Love and Mindlin-Herrmann rod theories, as well as the Timoshenko beam theory. In particular, detection of damage in various forms of discontinuity of cross-section and material has been considered by analysing wave speeds and time of reflections in the registered response signals. The proposed damage models have provided numerical velocity results consistent with the experimental signals.

The results of numerical and experimental studies of guided wave propagation in bars lead to the following conclusions:

- The spectral element method appears to be more effective than the finite element method. Higher order spectral elements reveal good efficiency towards numerical dispersion due to spatial discretization. For the established number of nodes per wavelength, numerical dispersion is higher for elements with smaller number of GLL nodes.
- Numerical dispersion also appears because of temporal discretization. For a conditionally stable algorithm (here the central difference method), the numerical time step restriction for stability plays a limiting role. If an implicit unconditionally stable time integration scheme is used, the time step should be determined from the Courant condition to avoid numerical dispersion errors.
- The application of one multi-node spectral element per bar guarantees the smallest number of nodes per wavelength, but in such case the numerical time integration using the central difference method requires very small time step. The application of a few spectral elements per bar causes an increase of the number of nodes per wavelength. However, the critical time step is larger than for the case of one spectral element per bar.
- For the considered excitation frequency equal to 150 kHz, for which only one longitudinal mode could propagate in the analysed rod specimen, both the Love and Mindlin-Herrmann theories are covered, however in general the Mindlin-Herrmann theory guarantees more accurate wave propagation results in wider frequency range than the Love theory and it allows the analysis of the second mode.
- The comparison of results of the numerical simulations with the experimental ones has proved that the spectral element model based on the Love rod theory, as well as the Mindlin-Herrmann rod theory guarantees better approximation for the first longitudinal mode behaviour than the elementary theory. Therefore it is advised, that the numerical model intended as a part of the SHM system should be described in the SEM formulation based on the Love or Mindlin-Herrmann theories to obtain proper time of reflections from potential damage.
- For the elementary rod theory, the mass matrix has a diagonal structure, thus the time integration can be efficiently conducted. The application of the Love theory causes the mass matrix to lose its diagonal form. On the other hand, the Mindlin-Herrmann theory

provides the diagonal mass matrix but it requires an additional degree of freedom, which causes the size of element matrices to increase twice.

- In the analysis of flexural wave propagation based on the Timoshenko beam theory, the mass matrix is diagonal, which enables the efficient time integration. The Timoshenko beam model, with adjustable parameters selected based on the comparison with the experimental results within the frequency range of interest, provides the velocity results compatible with the experimentally measured signals.
- The experimental tuning test allows to find frequencies at which waves are strongly excited and frequencies at which waves practically cannot be excited in the considered specimen and the applied instrumentation.
- Experimental dispersion curves enable to determine the adjustable parameters for the approximate Love, Mindlin-Herrmann and Timoshenko theories. These parameters can be calculated by the method of least squares to give the best fit with the experimental modes in the considered frequency range. Numerical results obtained from the models without the adjustable parameters do not cover with experimental signals. The adjustable parameters compensate the approximation of displacement fields giving results coinciding with experimental signals.
- The excitation signal should ensure relatively narrow spectrum in the frequency domain. Application of the Hanning window provides reduction of side frequencies. Excitation of single-frequency waves is very important, especially when dealing with dispersive Lamb waves and concentration of input energy at a point on the dispersion curves in which dispersion is low can minimize the effect of dispersion.

Experimental investigations showed that for the considered bars with structural discontinuities additional reflections appeared in the guided wave response signal. The smallest reflection was caused by the groove weld, whereas the greatest was caused by the presence of the additional mass. The discontinuity in the form of the notch and the weld caused additional reflections of amplitude much smaller than the amplitude of reflections from the bar boundaries. The presence of additional mass caused a different type of reflections. The longitudinal, as well as flexural waves were successfully used to localize the discontinuity in the form of the notch and the additional mass. However, in the case of small "damage", simulated through the grooved weld, the longitudinal waves appeared to be more sensitive than the flexural waves in damage detection. When the longitudinal waves were applied, the reflection from the weld was observed during the first wave passage, while in the case of flexural waves the weld detection was possible after passage of five bar lengths. The application of flexural waves to damage detection can be enhanced through the velocity measurements in a few points and the analysis of the time-position plane.

For diagnostic purposes, in the performed experiments the velocity signals were measured at two opposite ends of the specimen (at the *start point*, on which the actuator was bonded and at the *end point*). The frequency of the applied incident wave was selected to ensure propagation of one longitudinal and one flexural mode. Damage detection in the bar was possible using longitudinal, as well as flexural waves and it was unambiguous, when the response signal was measured at the start point. The measurement of the wave propagation signal at the end point cannot provide unambiguous identification of damage position.

Chapter 5

WAVE PROPAGATION IN FRAME STRUCTURES

Complexity met in investigations of wave propagation in engineering structures suggests careful studies of simpler structural elements. Such element is for example a junction of two non-collinear rods, in particular an L-joint, i.e. a right angle joint. The L-joint can be a component of more complex engineering structures or it can represent the simplest frame structure. The analysis of wave propagation in the frame corner is of practical interest due to the mode conversion. An incident wave of one type, after reaching a junction generates propagation and reflection of waves of other types, which causes damage detection more difficult than for a simple bar.

The earliest studies (Lee and Kolsky 1972) concerned an analytical model of wave propagation at the junction of two non-collinear rods. Lee and Kolsky (1972) used the elementary theory to describe propagation of longitudinal waves and the Timoshenko theory for flexural wave propagation. In their experiments, a steel rod was bent at 15-degree intervals from 15 to 90 degrees. Strain gages were attached to the specimen and an incident pulse was created by firing a projectile, so that axial impact was achieved. Atkins and Hunter (1975) presented an analytical model of wave propagation in an L-joint. In the performed experiments, a longitudinal pulse was induced by a projectile and strains were measured by strain gauges. Liang and Chen (1998) studied theoretically reflection and transmission of the longitudinal wave around a right-angled joint of two rods. They concluded that a force applied along a horizontal rod of an L-joint causes, that the longitudinal wave nearly cannot transmit into a vertical rod. Beccu et al. (1996) studied longitudinal waves in a bent bar. Experiments were performed on a bar with a sharp and smooth bend. The bars were impacted axially by a cylindrical carbon steel piston accelerated by an air gun and strain gages were applied to monitor strains. Experimental and theoretical wave propagation through the junction of three bars was studied by Desmond (1981). Impact experiments were performed to measure stress wave responses at the junction of two collinear bars and one bar non-collinear to the first two. Doyle and Kamle (1987) analysed experimentally flexural waves for an arbitrary T-joint. An aluminium T-joint was impacted mechanically and strain gauges were used to monitor stress waves. Recently, experimental studies of wave propagation in the form of a wave packet in a damaged L-joint have been presented by Rucka (2010b). Longitudinal and flexural waves were excited by a piezoelectric actuator and a vibrometer was used to non-contact measurements of velocity signals.

Numerical simulations of wave propagation in an L-joint using the SFEM were initiated by Doyle and Farris (1990b). They developed a spectrally formulated element for wave propagation in frames based on the elementary rod and the Euler-Bernoulli beam theories. This model was examined on an L-joint consisting of two semi-infinite members. To respect dispersion, modified rod theories were formulated. Martin et al. (1994) formulated a frame element by combining the Mindlin-Herrmann rod with the Timoshenko beam in the frequency domain. Numerical simulations have been conducted on two semi-infinite rods connected with a 45 degree joint. To model longitudinal, as well as flexural wave propagation taking lateral deformations and shear deformations into consideration, the

special frame spectral element in the time domain based on the Mindlin-Herrmann rod and the Timoshenko beam theories was formulated by Rucka (2010b).

This chapter is devoted to conduct experimental and numerical analyses of longitudinal and flexural wave propagation in plane frame structures. The research is a continuation of the author's study related to wave propagation in an L-joint (Rucka 2010b). Three type of frames, namely an L-frame (a.k.a. L-joint), a T-frame (a.k.a. T-joint) and a portal frame are analysed in this chapter. Particular attention is placed on damage detection aspects. As a result, this section presents guidelines for SHM systems dedicated for the considered frames concerning the required number of actuators and measurement points essential to monitor a whole frame structure.

5.1. Experimental setup

Wave propagation experiments were performed on three types of plane frames: an L-frame, a T-frame and a portal frame. The L-frame was prepared through a welding process. It consists of two bars of cross-section $6\text{ mm} \times 6\text{ mm}$ and length $L = 995\text{ mm}$ measured in axis, as shown in Fig. 5.1. The material parameters of the bars are the same as described in Section 4.1. The bars have been chamfered at 45 degree and joined in the L-frame corner with a butt weld. Then the weld was ground to obtain the origin cross-section. Two L-frame specimens were taken into investigation: the intact L-frame and the L-frame with a notch. The rectangular notch with dimensions 2 mm in length and 1 mm in height was obtained by a precision cut. The depth of the notch was 16.7% of the rod height. The notch was introduced at the distance $L_r = 0.5L$ from the left edge of the specimen (Fig. 5.1). The second specimen was the T-frame shown in Fig. 5.2. The weld was performed at the junction of three rods. Three different specimens were prepared: the intact T-frame, the T-frame with the notch on the horizontal member and the T-frame with the notch on the vertical member. Geometry of the portal frame presents Fig. 5.3. Four specimens were taken into consideration: the intact portal frame, the portal frame with the notch on the horizontal member, the portal frame with the notch on the vertical member and the portal frame with two notches.

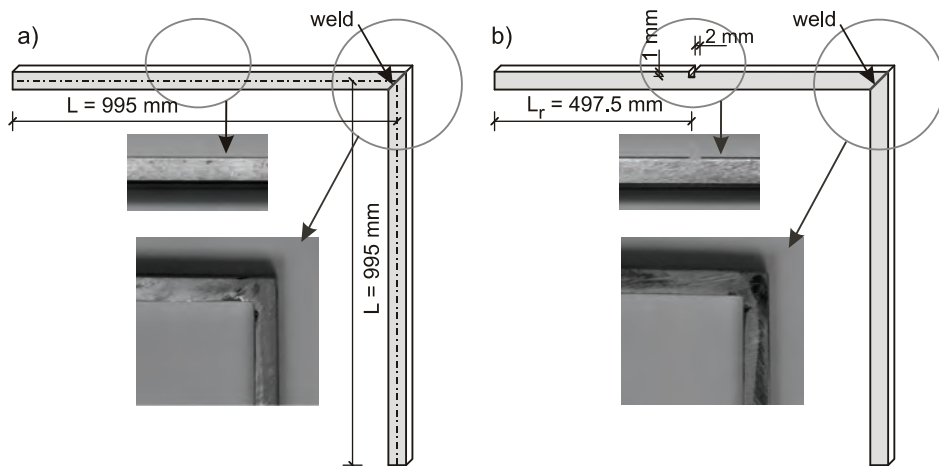


Fig. 5.1. Geometry of experimentally tested L-frame specimens:
a) intact L-frame; b) L-frame with notch

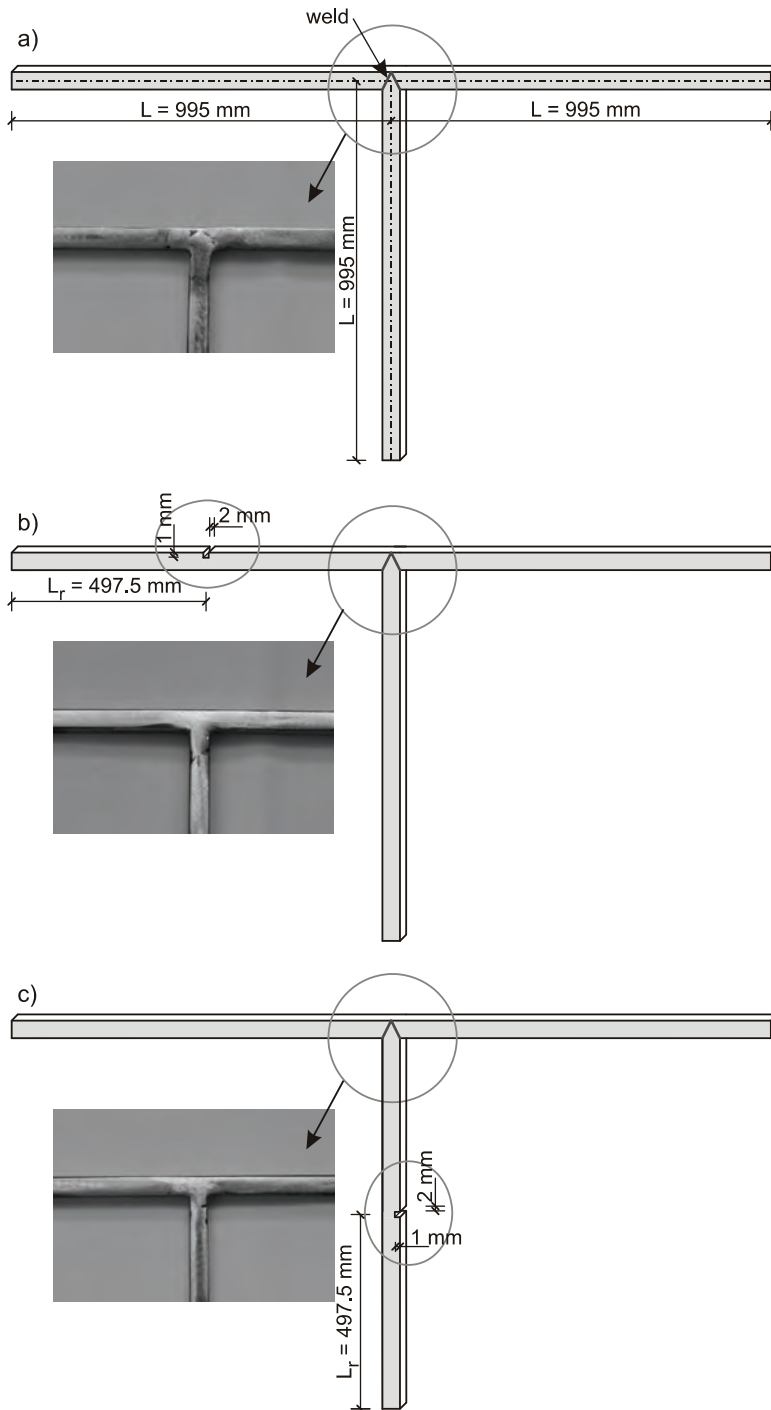


Fig. 5.2. Geometry of experimentally tested T-frame specimens: a) intact T-frame; b) T-frame with notch on horizontal member; c) T-frame with notch on vertical member

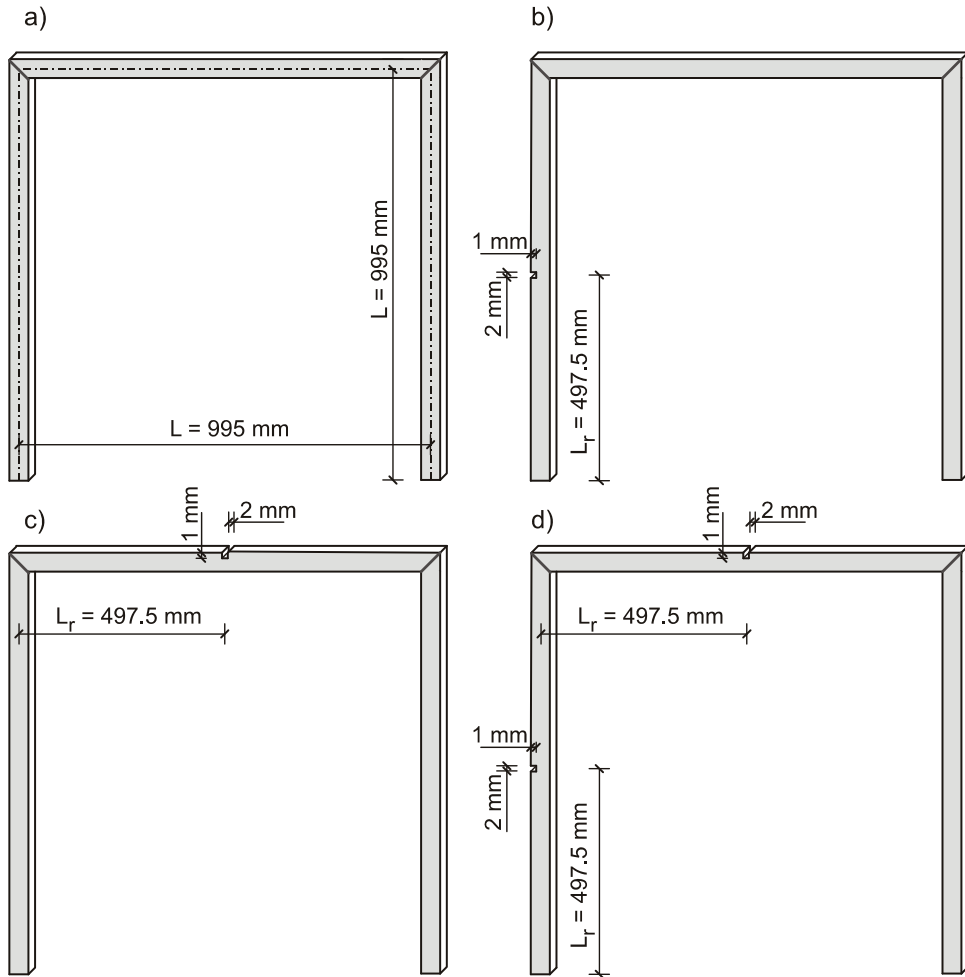


Fig. 5.3. Geometry of experimentally tested portal frame specimens: a) intact frame; b) frame with notch on vertical member; c) frame with notch on horizontal member; d) frame with two notches on vertical and horizontal members

The photos of the experimental setup are shown in Fig. 5.4. To excite ultrasonic waves the piezoelectric plate actuator Noliac CMAP11 of dimensions $5\text{ mm} \times 5\text{ mm} \times 2\text{ mm}$ was bonded at one end of the specimen. The Tektronix function generator AFG 3022 with the amplifier EC Electronics PPA 2000 created an excitation signal. Propagating velocity signals were sensed and registered by one scanning head PSV-I-400 of the Polytec Scanning Laser Vibrometer PSV-3D-400-M. As an excitation, a twelve-peak sinusoidal signal modulated by the Hanning window was chosen. In the L-frame, the T-frame and the portal frame specimens both longitudinal and flexural waves were excited and measured. In the case of longitudinal waves, the signal of frequency 120 kHz was excited, whereas in the case of flexural waves, the frequency of signal was 100 kHz. These frequencies were found to be more effective in the considered specimens and the used instrumentation. The excitation signals in time and frequency domains are shown in Fig. 5.5.

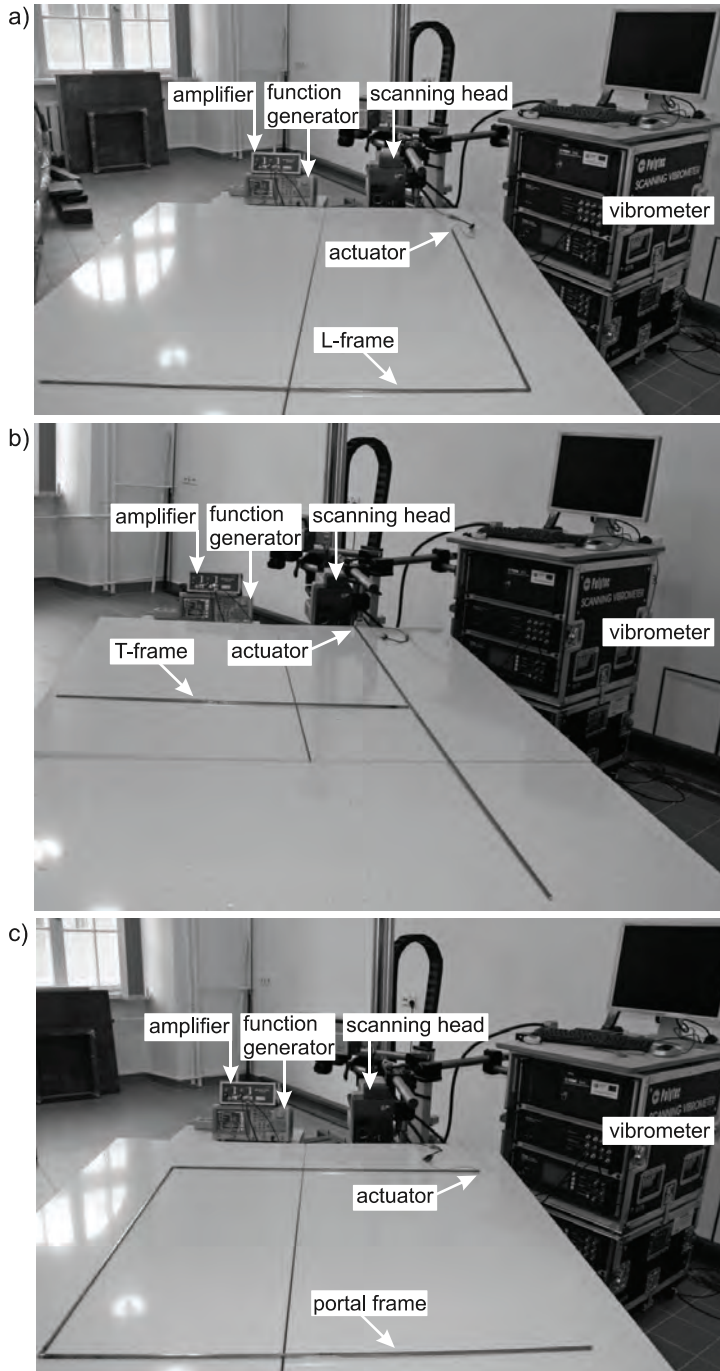


Fig. 5.4. Experimental setup for wave propagation, hardware and specimens:

a) L-frame; b) T-frame; c) portal frame

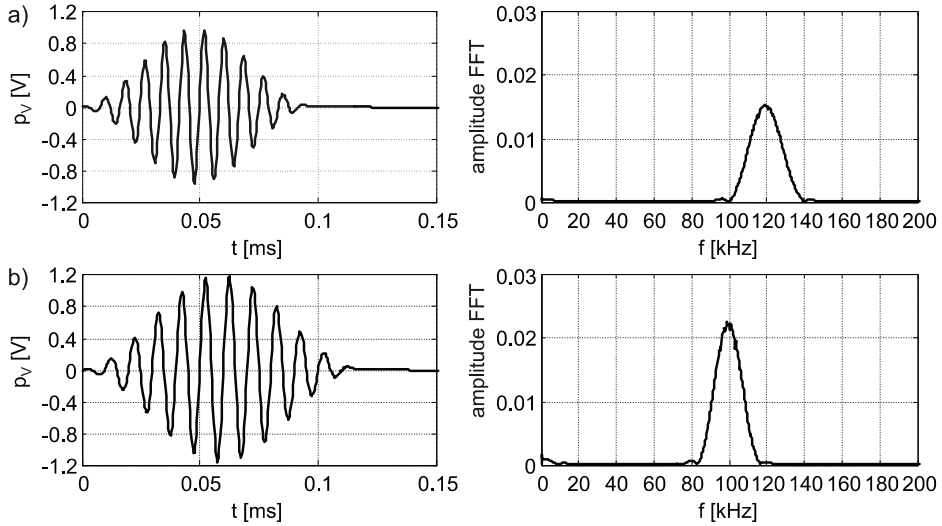


Fig. 5.5. Excitation voltage signals $p_v(t)$ in time and frequency domains for experiments on plane frames: a) signal of frequency 120 kHz; b) signal of frequency 100 kHz

5.2. Damage detection in L-frame by guided waves

Experimental and numerical investigations were performed for the intact L-frame, as well as for the L-frame with the notch (Fig. 5.1). Two positions of the notch were considered: the notch on the horizontal member and on the vertical member. A load in the form of the wave packet (Fig. 5.5) was induced in both axial and transverse directions.

5.2.1. Spectral element method model of L-frame

In the numerical simulations, the *M-H-Tim* spectral frame element was applied (cf. Section 3.2.5). The intact specimen was modelled using 24 equal elements with 15 GLL nodes (per each member), while the specimen with the notch was modelled using 24 equal elements with 15 GLL nodes and one element with 15 GLL nodes of length 2 mm with height reduced by 1 mm. For both the Mindlin-Herrmann and Timoshenko theories, the mass matrix has the diagonal structure, so the time integration using the central difference scheme can be efficiently conducted. The time step was chosen as $\Delta t = 10^{-7}$ s for the intact specimen and $\Delta t = 10^{-8}$ s for the specimen with the notch. This is so because for the specimen with the defect the largest frequency of an assembled finite element mesh is about ten times larger than for the intact specimen. For the applied mesh, the highest frequency, which affects the critical time step, is 2.93 MHz for the intact L-frame and 30.62 MHz for the L-frame with the notch.

The L-frame contains a butt weld in the corner. In this study, it is proposed to model the welded part of a bar as a part with reduced modulus of elasticity. Justification of this assumption was presented in Section 4.4 on the example of wave propagation tests on a straight bar containing a weld. Following the experiment with the straight bar, the numerical model of the L-frame with the weld was prepared. It was assumed that two elements near the corner have 10% reduced modulus of elasticity compared with the remain-

ing part of the L-frame. The length of each element was established as 2 cm, because the influence of the welding process was observed at this length. Additionally, the numerical analysis of the isotropic L-frame was performed. Figure 5.6 shows the comparison of the velocity signal $v_1(t)$ registered at node 1 (Fig. 5.7a) for the isotropic L-frame and for the L-frame with the weld. Both spectral models (for the isotropic L-frame and for the L-frame with the weld) provide comparable results. This is because the propagating waves reflect from the corner, and the reflection from the weld is masked by the reflection from the L-frame corner. Therefore, in further simulations, the SEM model of the L-frame was assumed to be isotropic, despite of the presence of the weld in its corner.

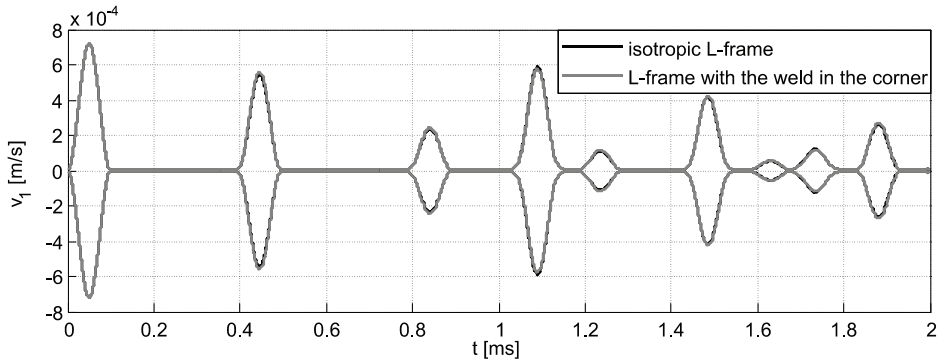


Fig. 5.6. Envelopes of numerical velocity signals for isotropic L-frame and L-frame with weld during longitudinal wave propagation

5.2.2. Longitudinal wave propagation in L-frame

The wave packet of frequency 120 kHz (Fig. 5.5a) was imposed in the longitudinal direction at node 1, whereas the velocity of vibrations was measured in both nodes 1 and 2. One L-frame specimen with damage enabled analysis of two positions of the defect. The locations of actuators and measurement points are shown in Fig. 5.7. The analytical values of group velocity were 5045.61 m/s for the longitudinal wave and 3094.71 m/s for the flexural wave, whereas the experimental values were 5044.33 m/s and 3082.48 m/s, respectively.

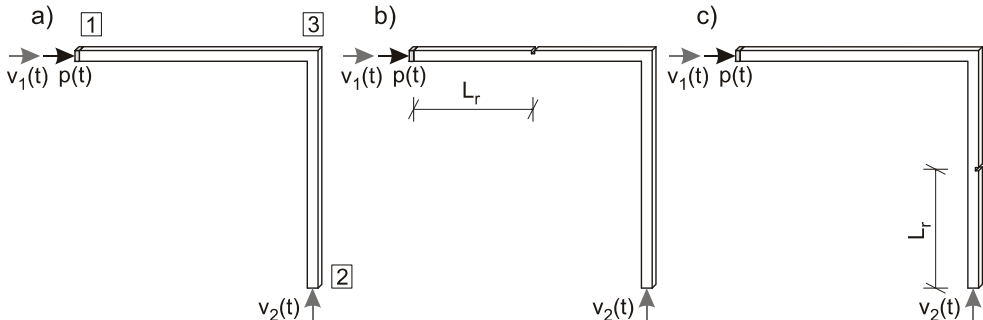


Fig. 5.7. Location of actuators and measurement points for the L-frame in the case of longitudinal wave propagation: a) intact L-frame; b) L-frame with the notch on the horizontal member; c) L-frame with the notch on the vertical member

At first, the intact frame was examined (Fig. 5.7a). The experimental and numerical signals are illustrated in Fig. 5.8. When the incident longitudinal wave reached the frame corner (node 3), both longitudinal and flexural waves propagated and reflected. In the $v_1(t)$ signal (Fig. 5.8a), the incident wave and eight reflections (R_1 to R_8) are visible during recorded 2 ms time period. The 1st, 2nd, 4th and 6th reflections were caused by propagation of the longitudinal wave only, whereas the 3rd, 5th, 7th and 8th reflections contained both longitudinal and flexural components. Similarly, in the $v_2(t)$ velocity signal, the 1st, 2nd, 4th and 6th waveforms were caused by propagation of longitudinal waves, while the 3rd, 5th, 7th and 8th waveforms appeared from both longitudinal and flexural waves. In Fig. 5.8 experimental and numerical signals in the form of signal envelopes are compared for the intact L-frame. It can be seen that the application of the numerical model based on the *M-H-Tim* spectral frame element provides the numerical data compatible with the experimental ones with respect to time of reflections.

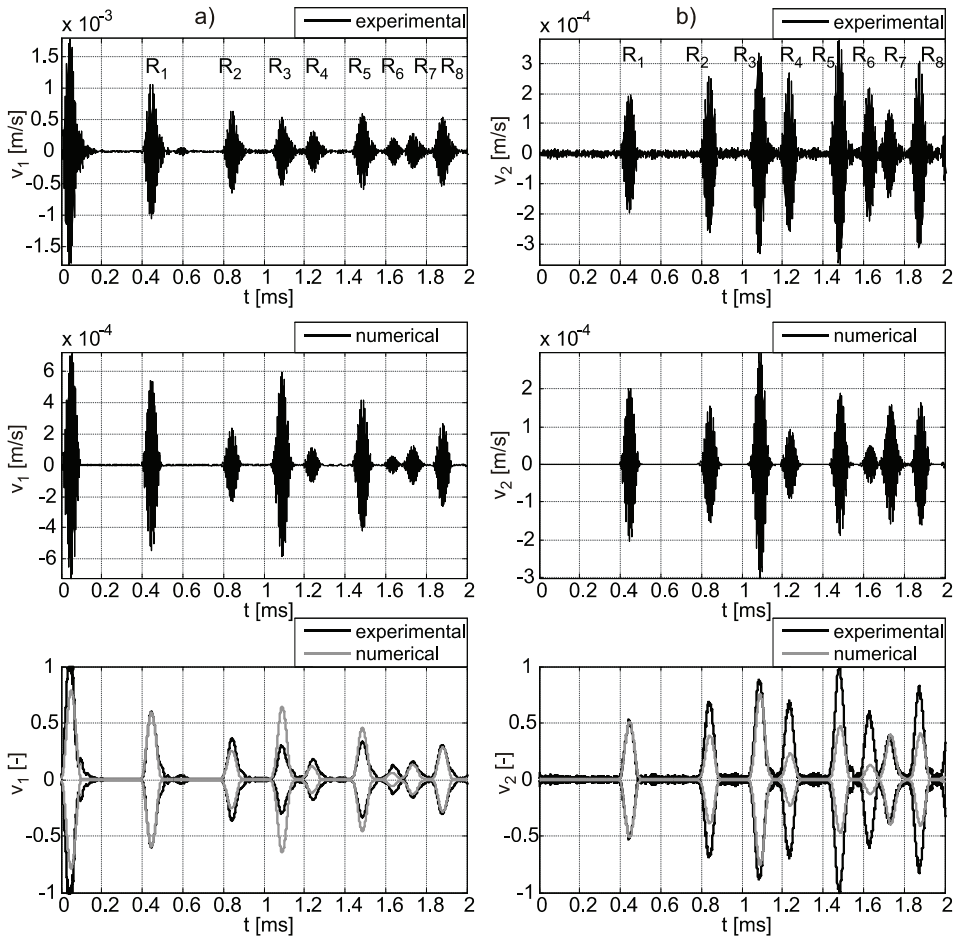


Fig. 5.8. Comparison between experimental and numerical velocity time signals for the intact L-frame in the case of longitudinal wave propagation: a) velocity signal $v_1(t)$ registered on the left end of the L-frame; b) velocity signal $v_2(t)$ registered on the right end of the L-frame

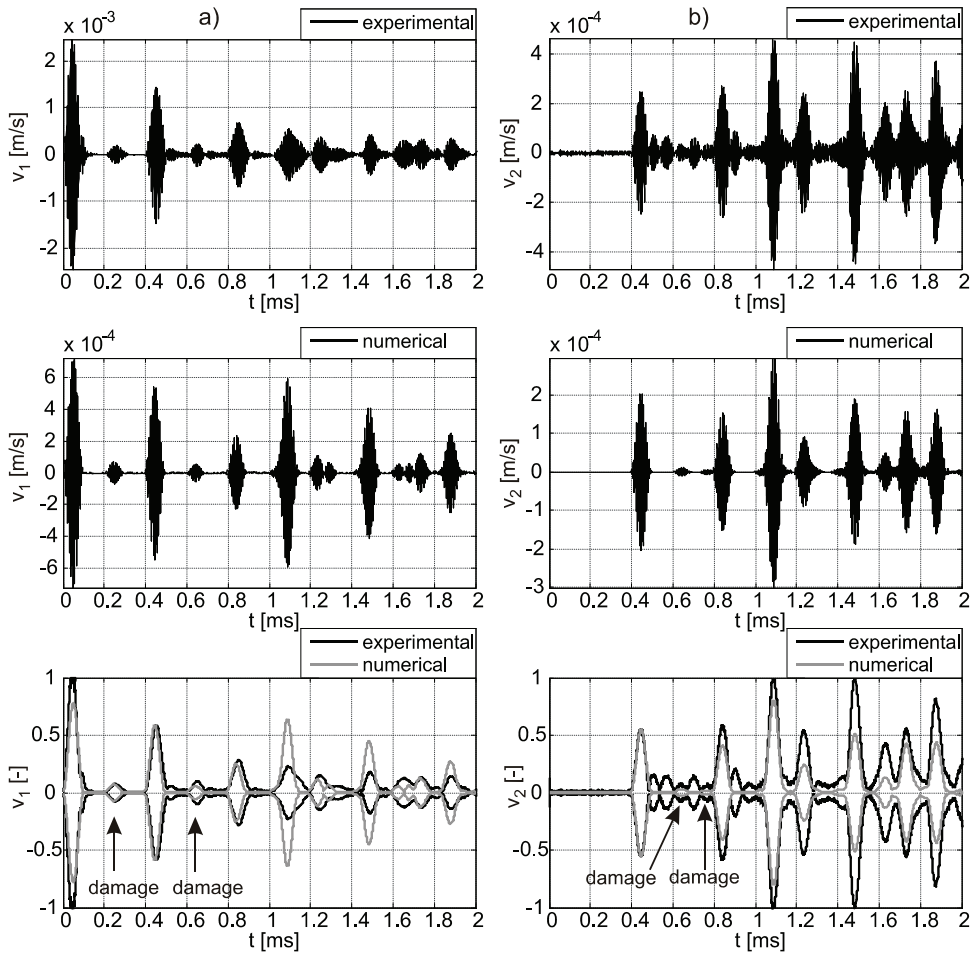


Fig. 5.9. Comparison between experimental and numerical velocity time signals for the L-frame with the notch on the horizontal member in the case of longitudinal wave propagation:

- a) velocity signal $v_1(t)$ registered on the left end of the L-frame;
- b) velocity signal $v_2(t)$ registered on the right end of the L-frame

The second example concerned the L-frame with the notch on the horizontal member (Fig. 5.7b). The numerical and experimental results for this case are compared in Fig. 5.9. The reflections from the notch, visible in both $v_1(t)$ and $v_2(t)$ velocity signals, can be identified based on the knowledge of the L-frame geometry and the group velocity of axial and flexural waves. Two distinct reflections from the notch appeared in the $v_1(t)$ signal (Fig. 5.9a) at the time instant equal to 0.2 ms and 0.6 ms. Both reflections were caused by propagation of longitudinal waves. In the $v_2(t)$ signal (Fig. 5.9b), two reflections from the notch can also be observed. The first reflection occurred at 0.6 ms as a result of propagation of the longitudinal wave. The second reflection was caused by propagation of both longitudinal and flexural waves and it occurred at the time instant equal to 0.73 ms (the longitudinal wave from node 1 to node 3, next the flexural wave from node 3 to the notch and back,

finally the longitudinal wave from node 3 to node 2). Next reflections from the notch overlapped with the reflections from the corner and from the L-frame ends, thus they cannot be easily identified. In the experimentally measured signals, the reflections from the notch can also be observed in Fig. 5.9. The reflections contained in the $v_1(t)$ signal were very distinct, but the reflections from the notch in the $v_2(t)$ experimental signal were more contaminated.

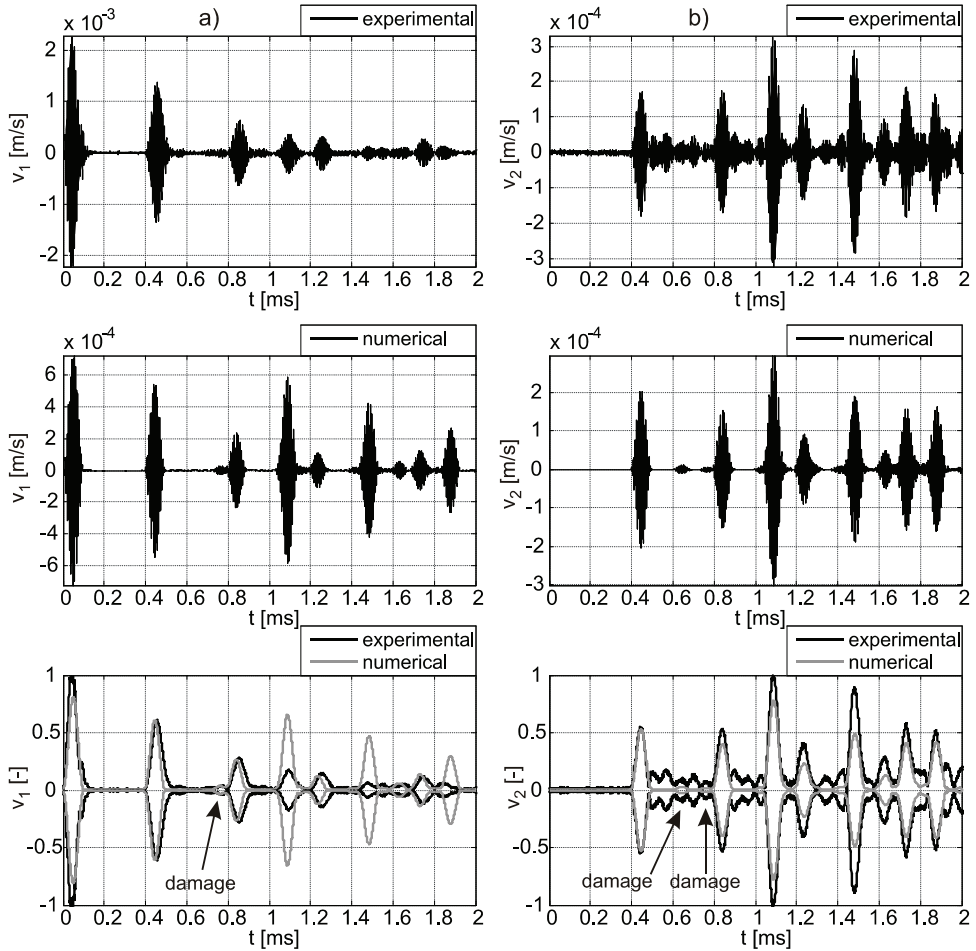


Fig. 5.10. Comparison between experimental and numerical velocity time signals for the L-frame with the notch on the vertical member in the case of longitudinal wave propagation:

- a) velocity signal $v_1(t)$ registered on the left end of the L-frame;
- b) velocity signal $v_2(t)$ registered on the right end of the L-frame

In the third example, the notch on the vertical member of the L-frame was considered (see Fig. 5.7c) and results for this case are presented in Fig. 5.10. In the $v_1(t)$ numerical signal (Fig. 5.10a), the first reflection from the notch occurred at 0.6 ms and it was caused by longitudinal wave propagation. It has very small amplitude and its usefulness in damage detection is limited because the experimental measurement of a such small waveform ap-

peared to be impossible. The second reflection from the notch in the $v_1(t)$ signal occurred at 0.73 ms and it was caused by propagation of longitudinal and flexural waves (the longitudinal wave from node 1 to the corner, then flexural to the notch and back, and finally the longitudinal wave from the corner to node 1). This component can be used for the purpose of damage detection, and it was successfully registered in the performed experiment. The numerical velocity signal $v_2(t)$ (Fig. 5.10b) was identical as in the case of the notch on the horizontal element (Fig. 5.9b). Hence, for the considered position of damage, it was impossible to indicate the precise localization of damage (i.e. whether it is on the vertical or on the horizontal element) based solely on information from the $v_2(t)$ signal.

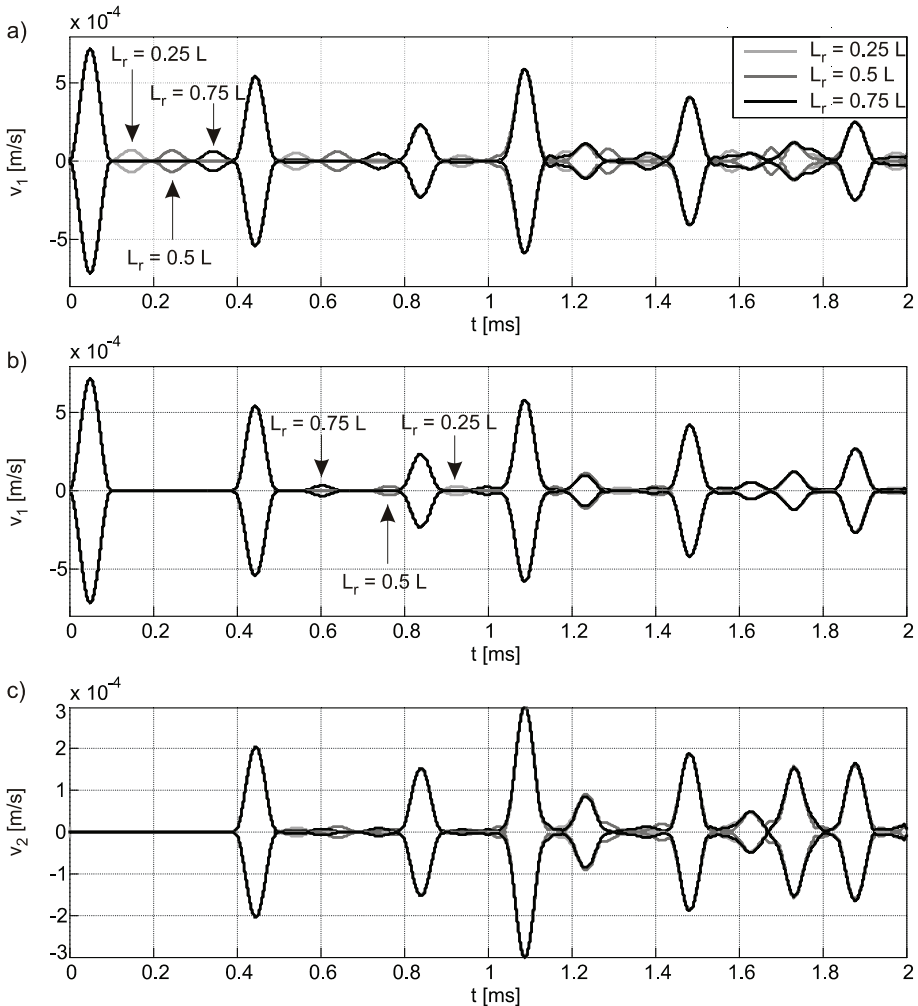


Fig. 5.11. Envelopes of numerical velocity signals for the L-frame containing the notch at different positions L_r ($L_r = 0.25L$, $L_r = 0.5L$, $L_r = 0.75L$) in the case of longitudinal wave propagation: a) L-frame with the notch on the horizontal member; b) L-frame with the notch on the vertical member; c) L-frame with the notch on the horizontal or vertical member

The last example concerned the numerical simulations for various damage positions, namely $L_r = 0.25L$, $L_r = 0.5L$ and $L_r = 0.75L$ (cf. Fig. 5.7b and c), for both the L-frame with the notch on the horizontal member and the L-frame with the notch on the vertical member. As in the case of the simple rod (cf. Section 4.4), the measurement of the velocity signal $v_2(t)$ cannot provide unambiguous identification of damage position (Fig. 5.11c). The velocity signal $v_2(t)$ was the same for both models of the L-frame, i.e. for the L-frame with the notch on the horizontal element and with the notch on the vertical element. The situation was different, when the $v_1(t)$ velocity signal was analysed. If damage was situated on the horizontal member of the L-frame (i.e. on the member, on which the actuator was bonded), the velocity signal $v_1(t)$ enabled easy localization of the notch position (Fig. 5.11a). Between incident wave and wave reflected from the L-frame corner, the single reflection from damage can be observed. However, when damage occurred on the vertical member, the reflection from damage was masked partially by the reflection from node 2. As shown in Fig. 5.11b, the localization of the notch was possible for all considered positions ($L_r = 0.25L$, $L_r = 0.5L$, $L_r = 0.75L$), but the damage placed in the neighbourhood of $L_r = 0.6L$ to $L_r = 0.7L$ would be completely masked by the reflection from node 2. This is caused by different values of the group velocities of the longitudinal (5046 m/s) and the flexural waves (3095 m/s). If the group velocity of the longitudinal wave was equalled to the group velocity of the flexural wave (here for the frequency of 312 kHz), this ambiguous situation could be eliminated. However, for the equal group velocities of the longitudinal and flexural waves, the second flexural mode appears, which makes the damage detection more difficult.

5.2.3. Flexural wave propagation in L-frame

The incident wave packet of frequency 100 kHz (Fig. 5.5b) was imposed in the transverse direction at node 1, while the velocity signals $v_1(t)$ and $v_2(t)$ were measured in both nodes 1 and 2. The arrangement of actuators and velocity measurement points is illustrated in Fig. 5.12. The intact and two damaged L-frames were taken into consideration. For the excited waves of frequency 100 kHz, the analytical group velocities were 5079.59 m/s (for longitudinal waves) and 3012.06 m/s (for flexural waves), whereas the experimental values of group velocities were 5074.33 m/s (for longitudinal waves) and 3026.59 m/s (for flexural waves).

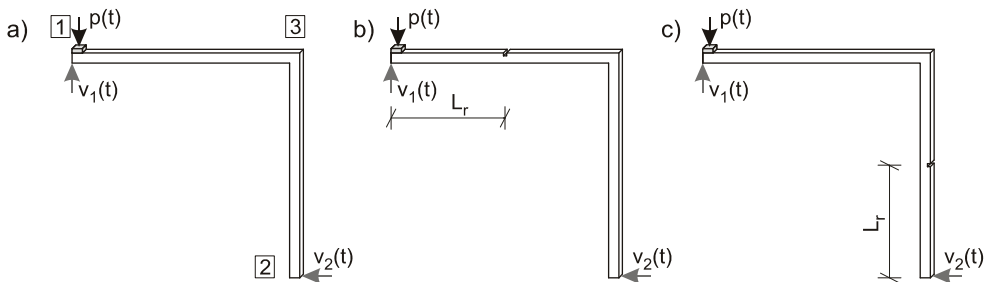


Fig. 5.12. Location of actuators and velocity measurement points for the L-frame in the case of flexural wave propagation a) intact L-frame; b) L-frame with the notch on the horizontal member; c) L-frame with the notch on the vertical member

At the beginning, the intact L-frame was investigated (Fig. 5.12a). When the incident flexural wave reached the frame corner, both flexural and longitudinal waves appeared. The results of the numerical simulations and the experiments are given in Fig. 5.13. In the $v_1(t)$ signal (Fig. 5.13a), the incident wave and six echoes (R_1 to R_6) are visible during the recorded 2 ms time period. The 1st and 3rd reflections were caused by propagation of the flexural wave, whereas the 2nd, 4th, 5th and 6th reflections contained both flexural and longitudinal components. The comparison of the numerical and experimental signals in the form of signal envelopes for the intact L-frame is illustrated in Fig. 5.13. Note that the application of the numerical model based on the *M-H-Tim* spectral frame element results in compatibility of times of reflections.

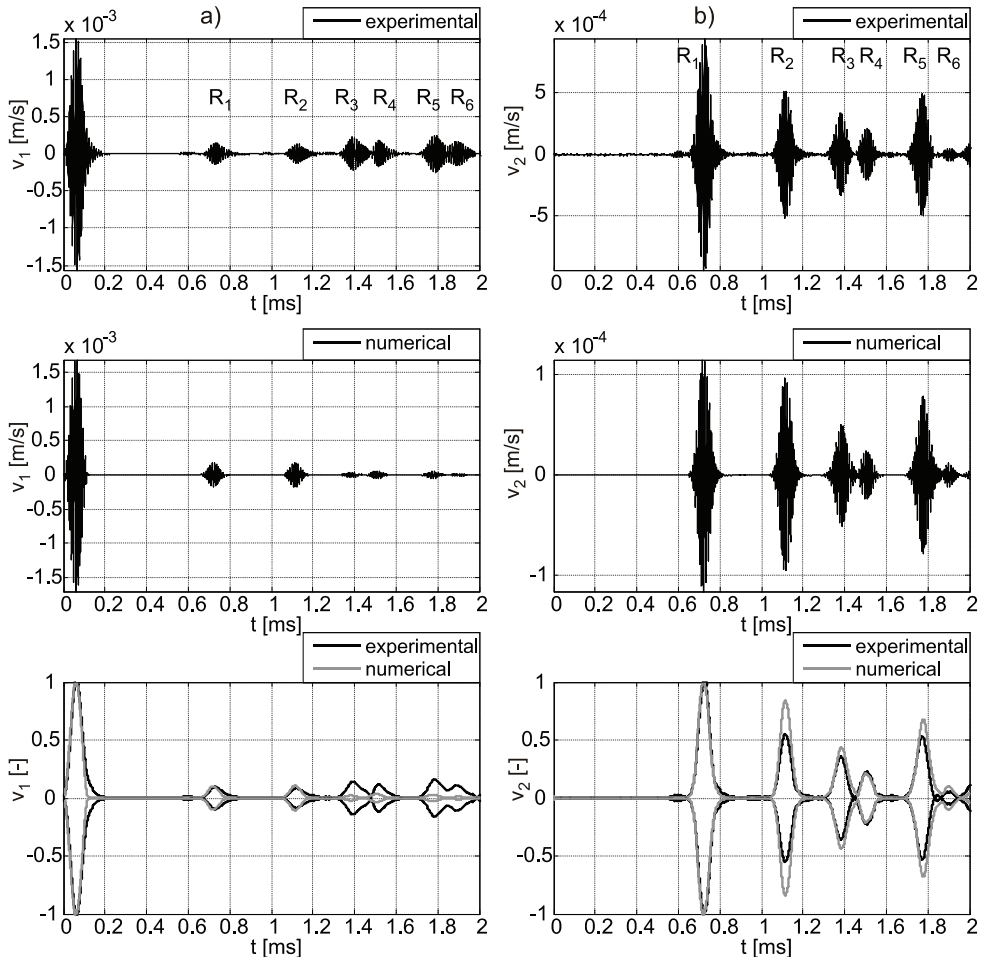


Fig. 5.13. Comparison between experimental and numerical velocity time signals for the intact L-frame in the case of flexural wave propagation: a) velocity signal $v_1(t)$ registered on the left end of the L-frame; b) velocity signal $v_2(t)$ registered on the right end of the L-frame

Next, the L-frame with the notch was tested. The numerically obtained $v_2(t)$ velocity signal for the L-frame with the notch on the horizontal member (Fig. 5.14b) was identical as for the L-frame with the notch on the vertical member (Fig. 5.15b). The reflection from damage occurred at 0.86 ms. The experimental signals $v_2(t)$ were also very similar for the frame with the notch situated on the horizontal and the vertical member. The signal $v_1(t)$ differed depending on the notch position (on the horizontal or on the vertical member). In the case of damage placed on the horizontal member, the reflection occurred at 0.33 ms, which was successfully registered in the experimental measurements (Fig. 5.14a). For damage situated on the vertical element, the velocity signal $v_1(t)$ (Fig. 5.15a) contained the reflection from damage at 0.86 ms (the flexural wave from node 1 to the corner, then the longitudinal wave to the notch and back, and finally the flexural wave to node 1).

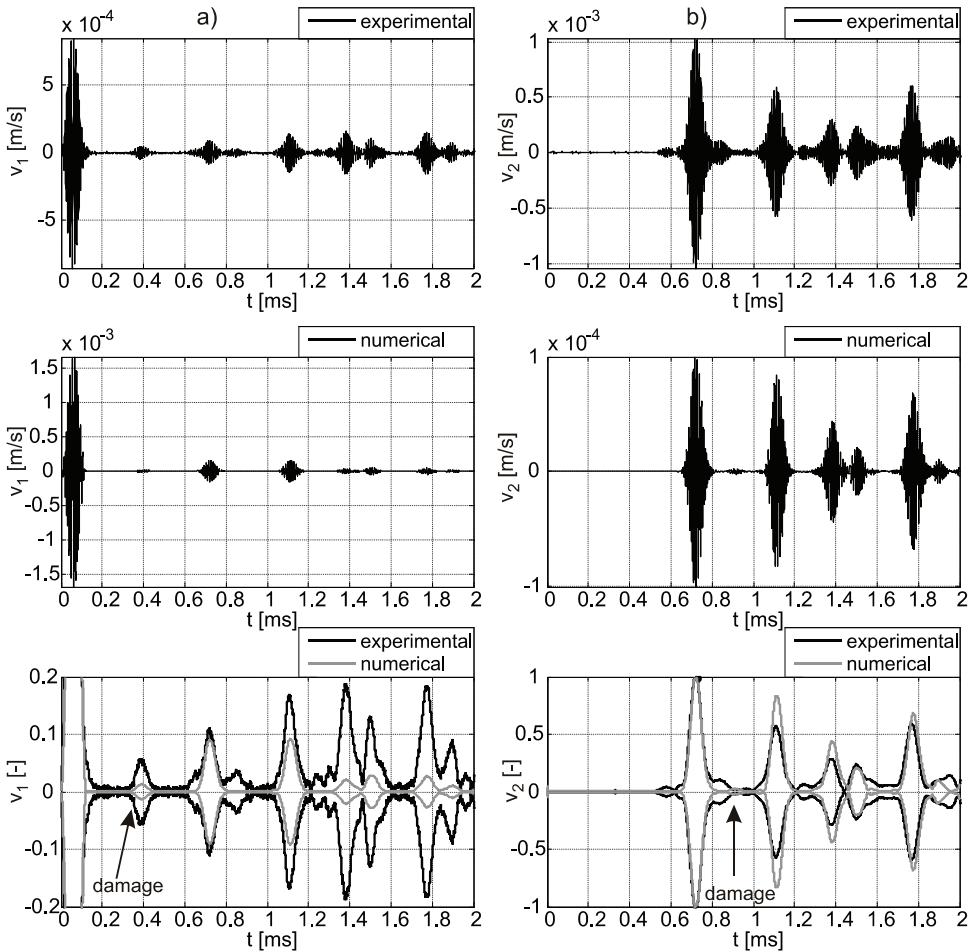


Fig. 5.14. Comparison between experimental and numerical velocity time signals for the L-frame with the notch on the horizontal member in the case of flexural wave propagation:

- a) velocity signal $v_1(t)$ registered on the left end of the L-frame;
- b) velocity signal $v_2(t)$ registered on the right end of the L-frame

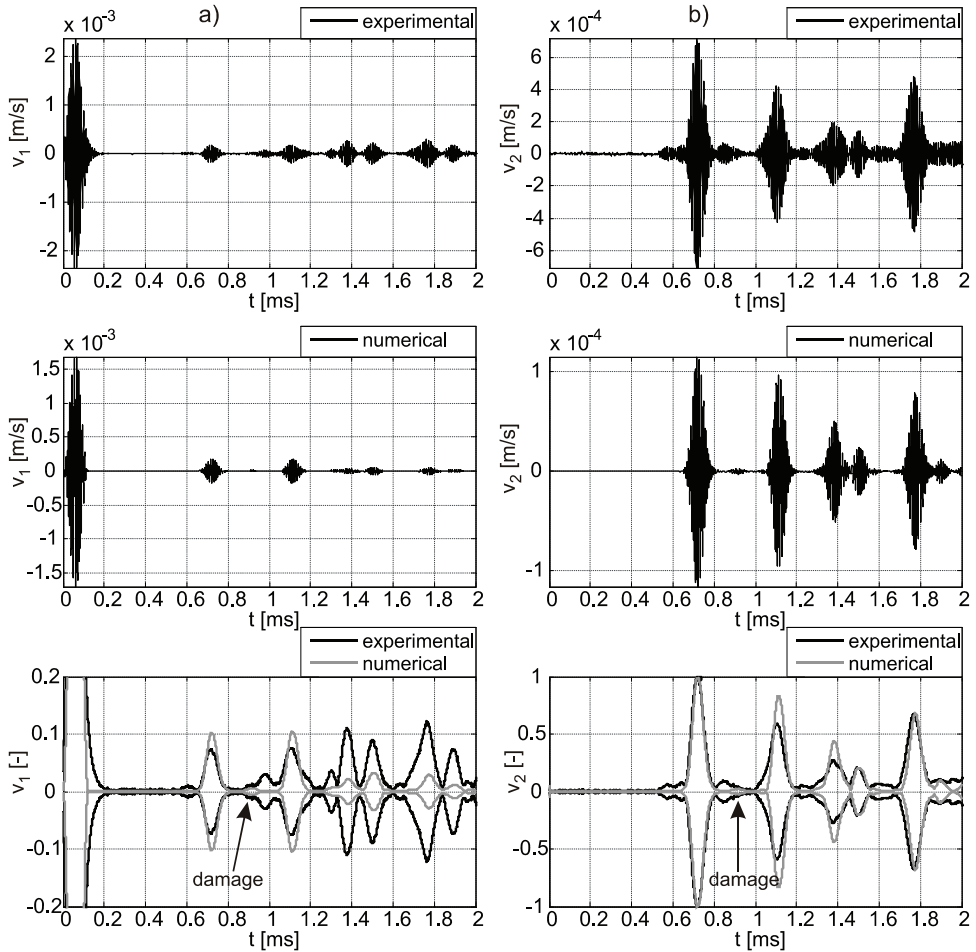


Fig. 5.15. Comparison between experimental and numerical velocity time signals for the L-frame with the notch on the vertical member in the case of flexural wave propagation:

- a) velocity signal $v_1(t)$ registered on the left end of the L-frame;
- b) velocity signal $v_2(t)$ registered on the right end of the L-frame

In the last example, the numerical simulations for three various damage positions L_r , i.e. $L_r = 0.25L$, $L_r = 0.5L$ and $L_r = 0.75L$ were investigated (cf. Fig. 5.12b and c), for both the L-frame with the notch on the horizontal member and the L-frame with the notch on the vertical member. Damage situated on the horizontal member of the L-frame (i.e. on the member, on which the actuator was bonded) can be easily identified from the $v_1(t)$ velocity signal (Fig. 5.16a) by analysis of the L-frame geometry and the velocity of the propagating flexural wave mode. For the notch situated on the vertical element of the L-frame (i.e. on the member without the actuator bonded), identification was also unambiguous for arbitrary damage position (Fig. 5.16b) until the group velocity of the longitudinal wave was larger than the group velocity of the flexural wave.

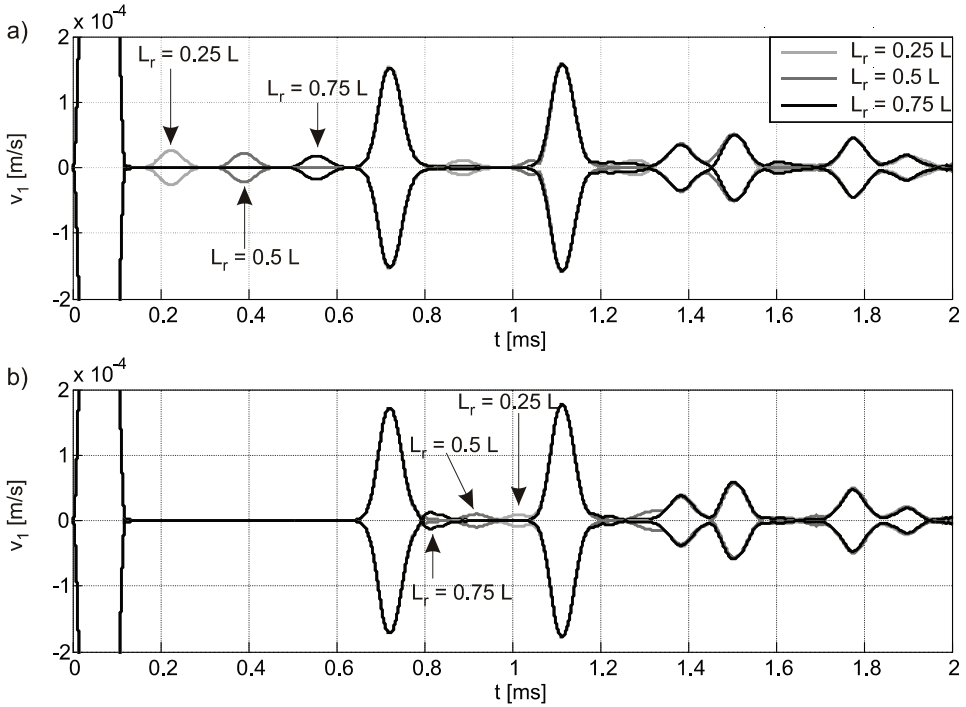


Fig. 5.16. Envelopes of numerical velocity signals $v_1(t)$ measured on the left end of the L-frame containing the notch at different positions L_r ($L_r = 0.25L$, $L_r = 0.5L$, $L_r = 0.75L$) in the case of flexural wave propagation: a) L-frame with the notch on the horizontal member; b) L-frame with the notch on the vertical member

5.3. Damage detection in T-frame by guided waves

The T-frame consists of three members: member I (between node 1 and 3) collinear to member II (between nodes 3 and 4) and member III (between nodes 2 and 3) perpendicular to them, as it is shown in Fig. 5.17. The experimental and numerical investigations were performed for the intact T-frame, as well as for the T-frame specimens with the notch (see Fig. 5.2). Two damaged T-frame specimens made analysis of three positions of the notch possible (Fig. 5.17), namely the frame with defect situated on member I, member II or member III. A load in the form of the wave packet was induced in both axial and transverse directions. In the numerical simulations, the *M-H-Tim* spectral frame element was applied. The T-type frames were modelled by the spectral element method in the same way as the L-frame (as described in Section 5.2).

5.3.1. Longitudinal wave propagation in T-frame

The wave packet of frequency 120 kHz was imposed in the longitudinal direction at node 1 and the velocity signal $v_1(t)$ was measured at the same node (Fig. 5.17). The experimental and numerical signals for the intact T-frame are illustrated in Fig. 5.18. In the velocity signal $v_1(t)$, the incident wave and eight reflections are visible during the recorded

2 ms time period. As for the L-frame, the 1st, 2nd, 4th and 6th reflections (R_1 , R_2 , R_4 , R_6) were caused by propagation of the longitudinal wave only, whereas the remaining reflections contained both longitudinal and flexural components.

For the T-frame with damage introduced on member I, two additional reflections appeared: between incident wave and reflection R_1 , as well as between reflection R_1 and reflection R_2 (Fig. 5.19). In the experimentally measured signal for this case, the first reflection from damage occurred at the time instant equal to 0.2 ms and it was more distinct than the second one, which occurred at the time instant equal to 0.6 ms. Analysing the T-frame with damage on member II, one reflection from damage can be observed in both numerical and experimental signals (Fig. 5.20). This additional reflection occurred at the time instant equal to 0.6 ms, between reflection R_1 (from the frame corner) and reflection R_2 (from nodes 2 and 4). In the last case, the notch was situated on member III and numerical and experimental results for this case are compared in Fig. 5.21. The reflection from the notch in the velocity signal $v_1(t)$ occurred at the time instant equal to 0.73 ms, and it was caused by propagation of longitudinal and flexural waves. However, this component was not quite clear in the experimental signal. Moreover, it was partially masked by reflection R_2 (from nodes 2 and 4).

Finally, the numerical simulations for various damage positions, namely $L_r = 0.25L$, $L_r = 0.5L$ and $L_r = 0.75L$ (cf. Fig. 5.17b, c and d) were conducted. For the defect situated on member I or member II, the velocity signal $v_1(t)$ enabled easy and unambiguous localization of the notch position (Fig. 5.22a and Fig. 5.22b). However, when the damage was placed on member III, perpendicular to members I and II, the reflection from damage was partially masked by reflection R_2 due to different values of the group velocities of the longitudinal and flexural waves.

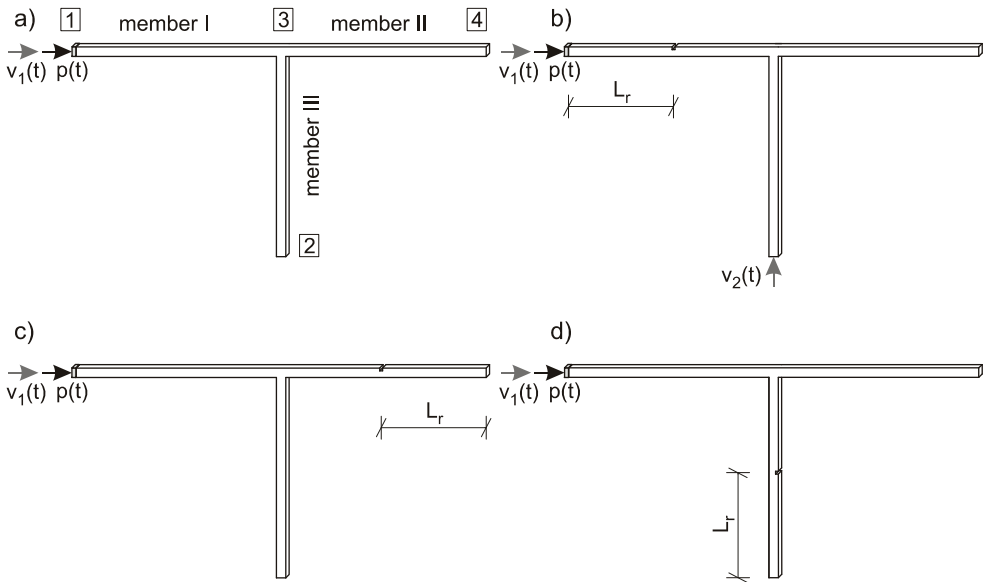


Fig. 5.17. Location of actuators and measurement points for the T-frame in the case of longitudinal waves: a) intact; b) with notch on member I; c) with notch on member II; d) with notch on member III

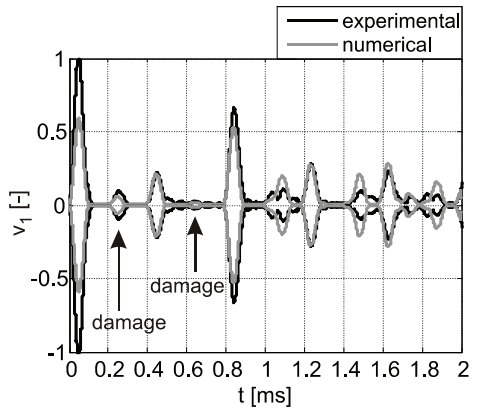
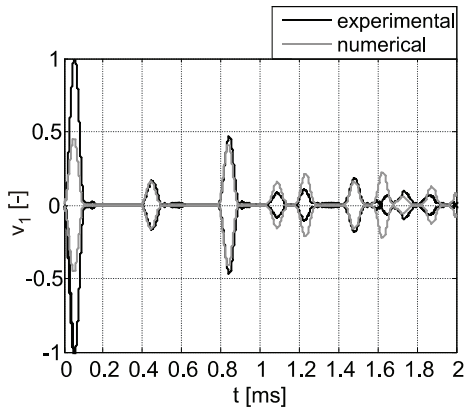
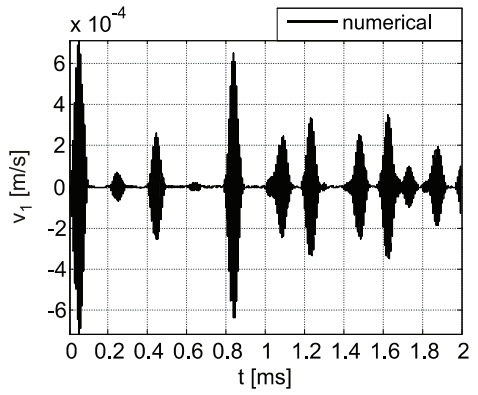
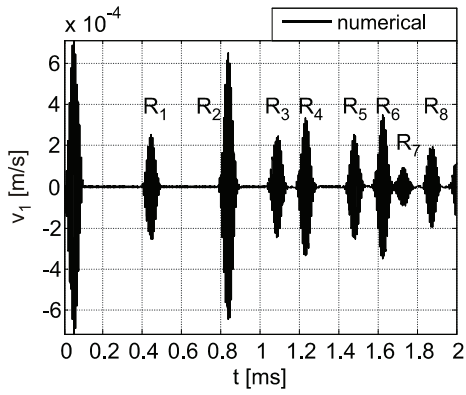
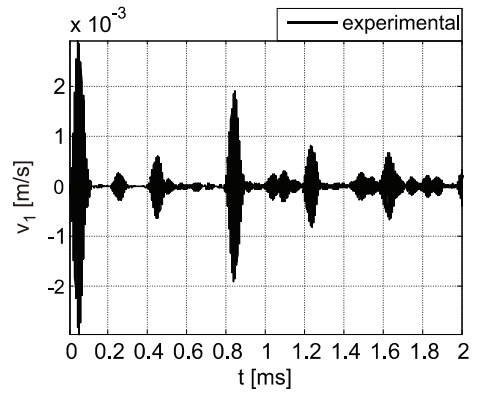
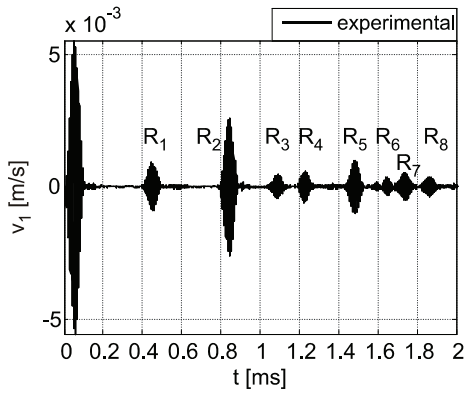


Fig. 5.18. Comparison between experimental and numerical signals for the intact T-joint during longitudinal wave propagation

Fig. 5.19. Comparison between experimental and numerical signals for the T-joint with the notch on member I during longitudinal wave propagation

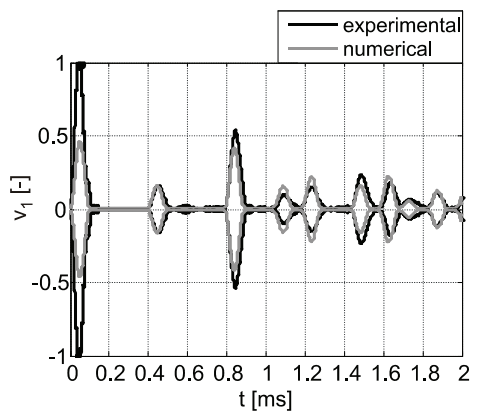
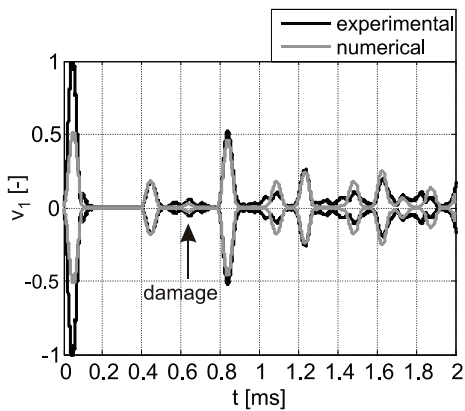
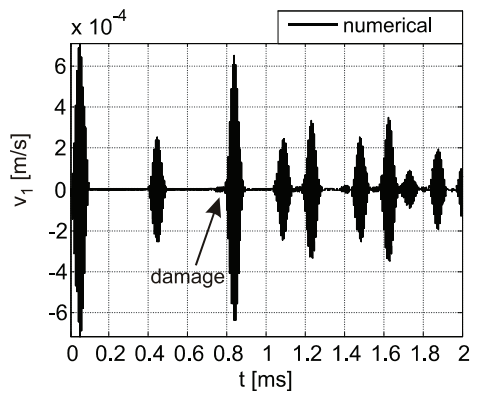
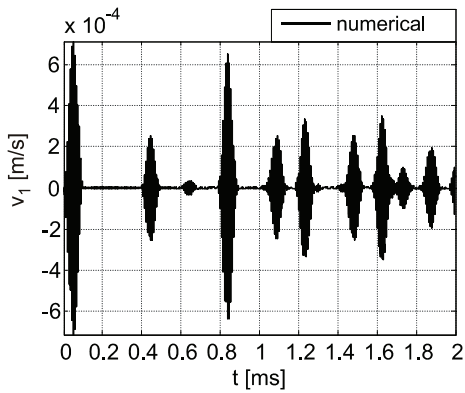
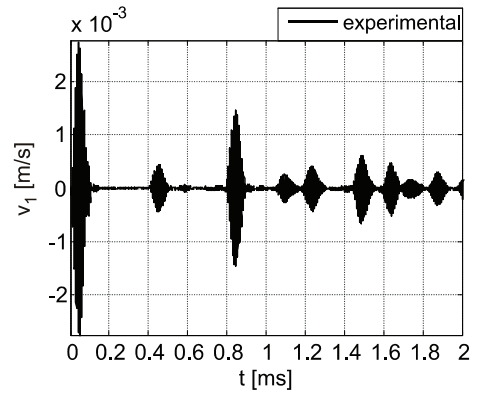
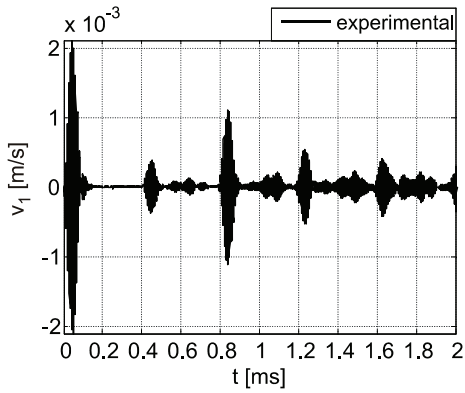


Fig. 5.20. Comparison between experimental and numerical signals for the T-joint with the notch on member II during longitudinal wave propagation

Fig. 5.21. Comparison between experimental and numerical signals for the T-joint with the notch on member III during longitudinal wave propagation

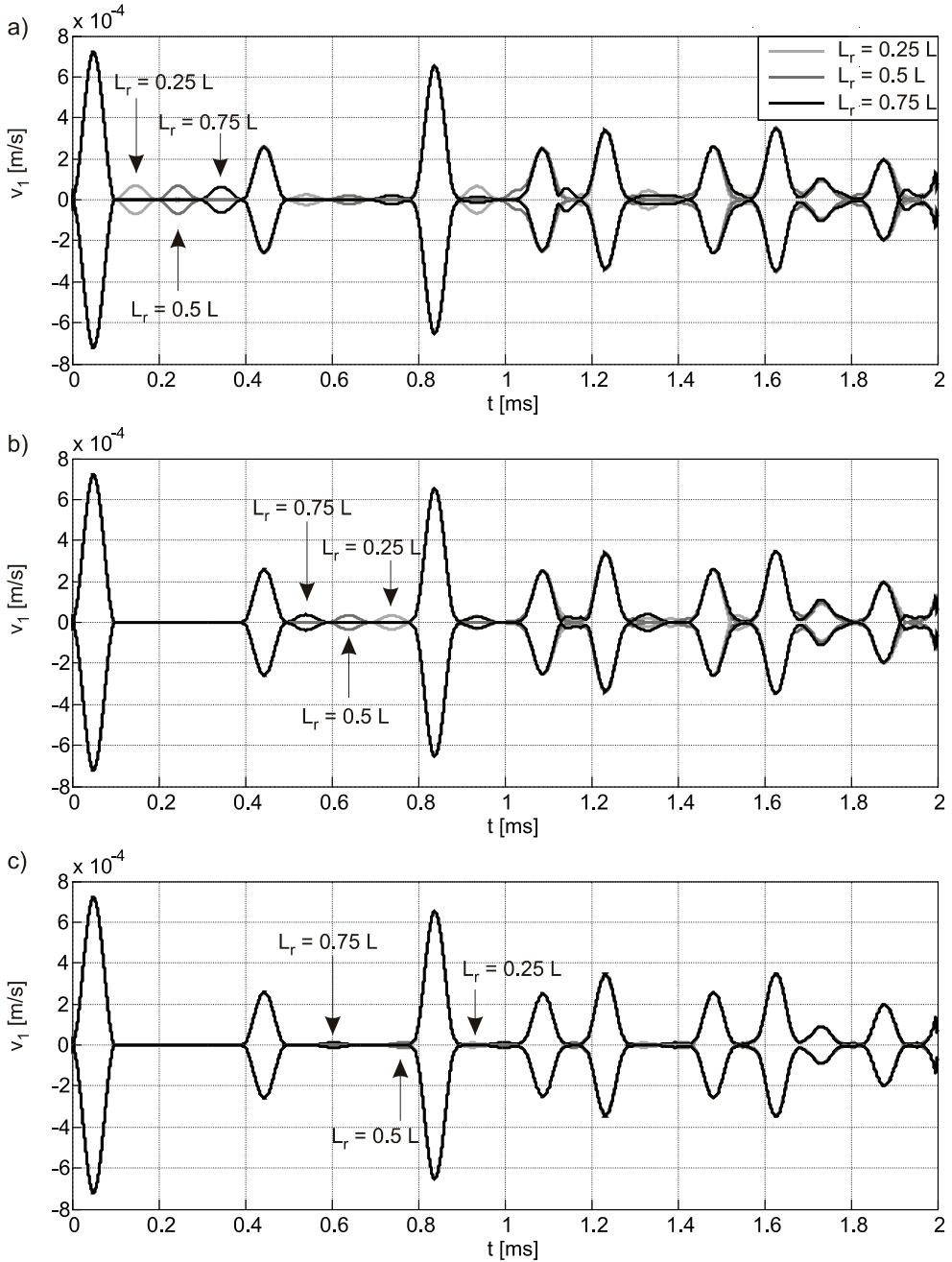


Fig. 5.22. Envelopes of numerical velocity signals of longitudinal wave propagation in T-frame for different damage positions L_r ($L_r = 0.25L$, $L_r = 0.5L$, $L_r = 0.75L$): a) T-frame with the notch on member I; b) T-frame with the notch on member II; c) T-frame with the notch on member III

5.3.1. Flexural wave propagation in T-frame

The T-frame was excited with 100 kHz burst at node 1 in the transverse direction and the velocity signal $v_1(t)$ was measured at the same node 1 (Fig. 5.23). Figure 5.24 shows the experimental and numerical results for the intact frame, as well as the comparison between them in the form of signal envelopes. In the recorded 2 ms time period, the incident wave and six echoes (R_1 to R_6) are visible in the $v_1(t)$ velocity signal.

If the notch was introduced within member I, the additional reflection appeared in both the experimental and numerical guided wave responses (Fig. 5.25), between the incident wave and reflection R_1 at the time instant equal to 0.33 ms. Figure 5.26 presents the velocity time histories for the case with damage on member II. In this case, reflection from damage occurred very close to reflection R_2 . This component had very small amplitude in the numerical signal. Moreover, it was not possible to measure such small waveform, thus its usefulness in damage detection was limited. Analysing the notch situated on member III, the reflection from damage was clear (Fig. 5.27). The reflection from damage occurred between reflections R_1 and R_2 at the time instant 0.86 ms, as a result of propagation of both longitudinal and flexural waves (the flexural wave from node 1 to node 3, then the longitudinal wave to the notch and back, and finally the flexural wave to node 1).

Figure 5.28 shows envelopes of numerical velocity signals of flexural wave propagation in the T-frame for different damage positions: $L_r = 0.25L$, $L_r = 0.5L$ and $L_r = 0.75L$ (cf. Fig. 5.23b, c and d). For the defect situated on member I or member III identification of damage position was possible based on information contained in the $v_1(t)$ velocity signal. Analysing the defect located on member II, collinear with member I, the reflection from damage was masked partially by the reflections from nodes 2, 3 and 4 due to different values of the group velocities of the longitudinal and flexural waves.

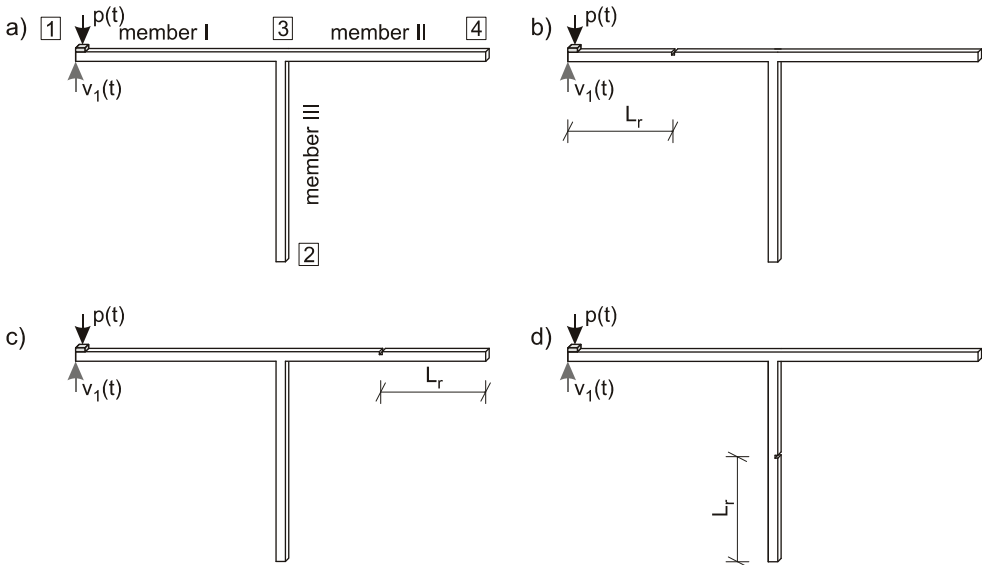


Fig. 5.23. Location of actuators and measurements points for the T-frame in the case of flexural waves: a) intact; b) with notch on member I; c) with notch on member II; d) with notch on member III

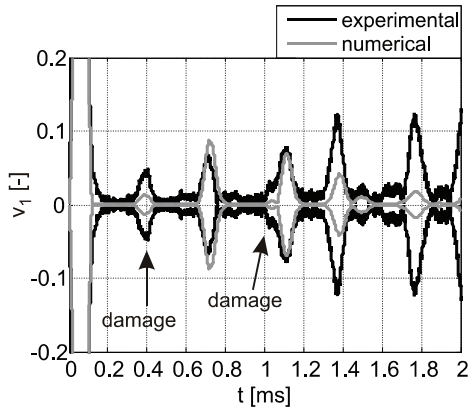
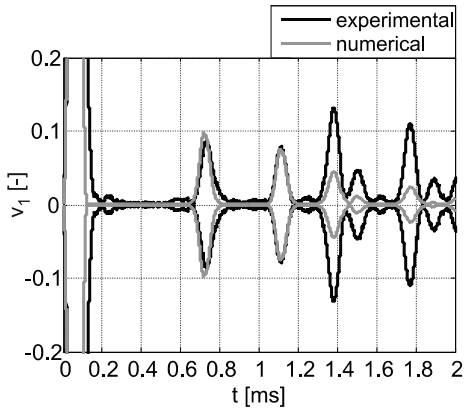
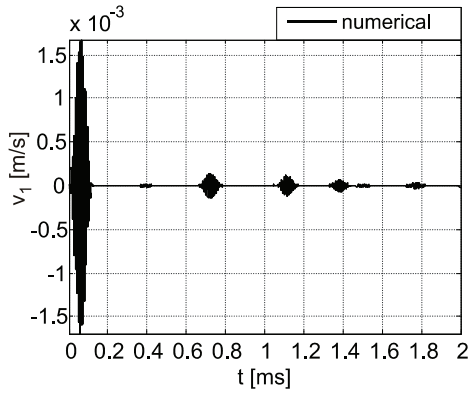
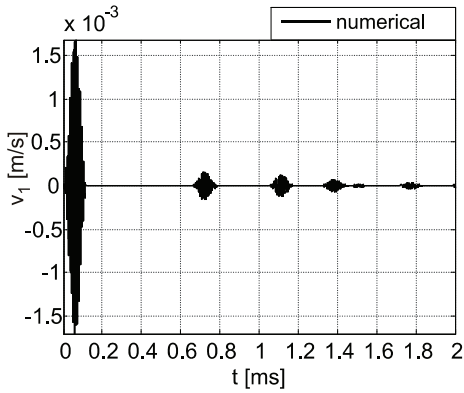
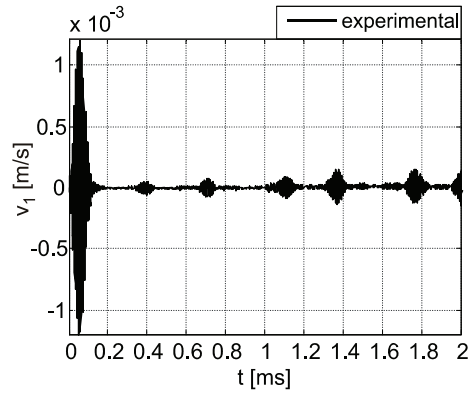
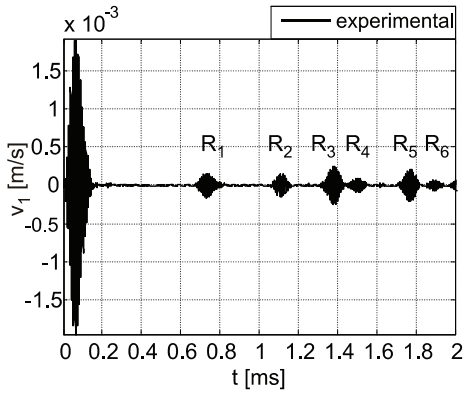


Fig. 5.24. Comparison between experimental and numerical signals for the intact T-joint during flexural wave propagation

Fig. 5.25. Comparison between experimental and numerical signals for the T-joint with the notch on member I during flexural wave propagation

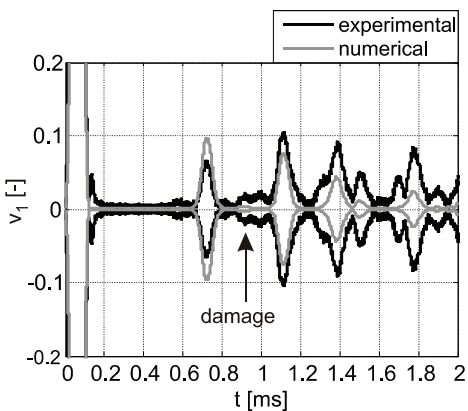
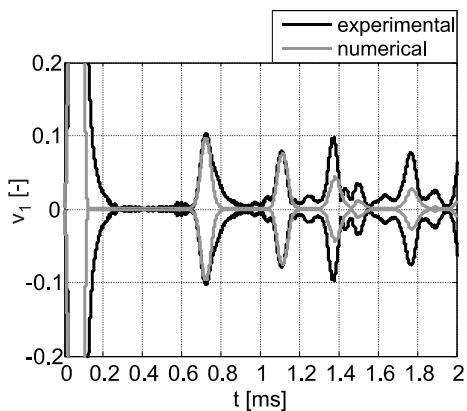
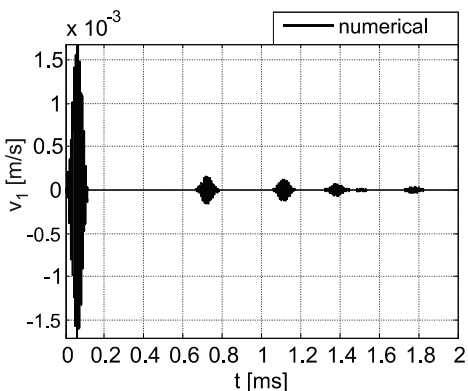
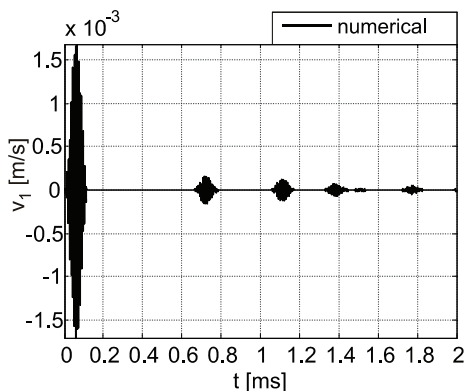
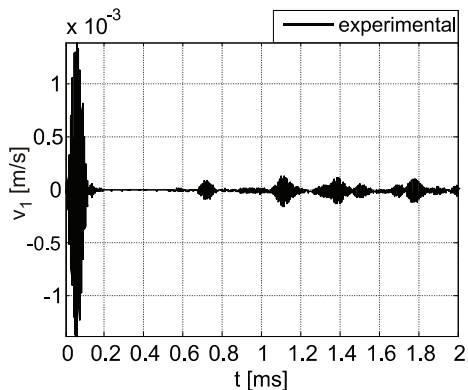
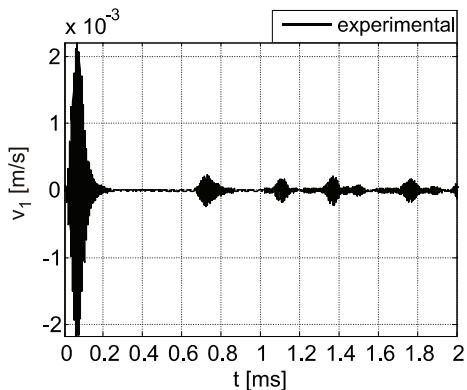


Fig. 5.26. Comparison between experimental and numerical signals for the T-joint with the notch on member II during flexural wave propagation

Fig. 5.27. Comparison between experimental and numerical signals for the T-joint with the notch on member III during flexural wave propagation

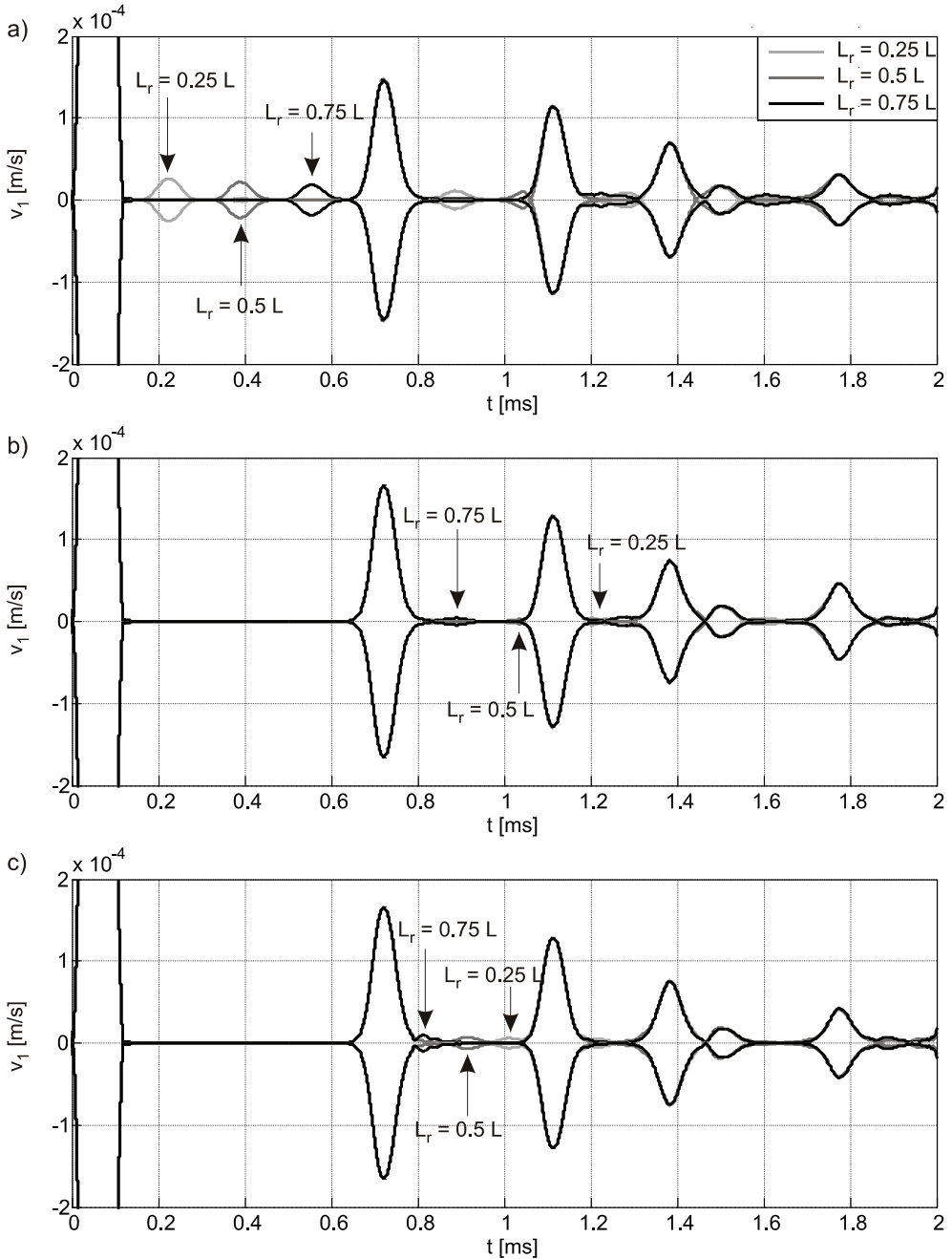


Fig. 5.28. Envelopes of numerical velocity signals of flexural wave propagation in T-frame for different damage positions L_r ($L_r = 0.25L$, $L_r = 0.5L$, $L_r = 0.75L$): a) T-frame with the notch on member I; b) T-frame with the notch on member II; c) T-frame with the notch on member III

5.4. Damage detection in portal frame by guided waves

The portal frame consists of three members: member I (between node 1 and 2), member II (between nodes 2 and 3) and member III (between nodes 3 and 4), as it is given in Fig. 5.29. The experimental and numerical investigations were conducted for the intact portal frame, as well as for the portal frame specimens with the notch (cf. Fig. 5.3). Three specimens with damage were used to consider five different cases of defect location (see Fig. 5.29): one notch on member I, II or III, as well as two notches on members I and II or on members II and III. Two forms of elastic waves were studied, namely longitudinal and flexural waves. The portal frames were modelled by the SEM in the same way as the L-frame (as described in Section 5.2). The numerical model was based on the spectral element formulation with the application of the Mindlin-Herrmann rod and the Timoshenko beam theories (*M-H-Tim* spectral frame element).

5.4.1. Longitudinal wave propagation in portal frame

The portal frame was excited in the axial direction by the wave packet of frequency 120 kHz at node 1. The velocity time history was measured at the same node 1, as it is illustrated in Fig. 5.29. The experimental and numerical signals for the intact frame are shown in Fig. 5.30. In the $v_1(t)$ signal, the first reflection R_1 was caused by propagation of

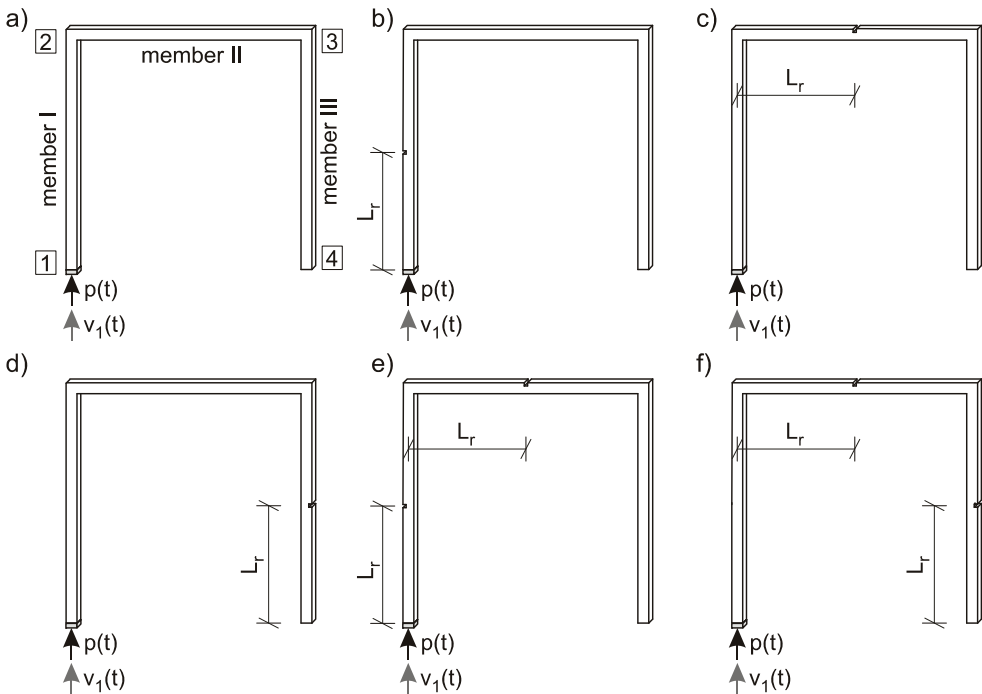


Fig. 5.29. Location of actuators and measurement points for the portal frame during longitudinal wave propagation: a) intact frame; b) frame with notch on member I; c) frame with notch on member II; d) frame with notch on member III; e) frame with notches on member I and II; f) frame with notches on member II and III

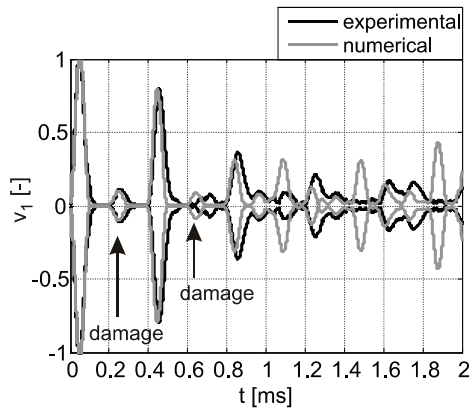
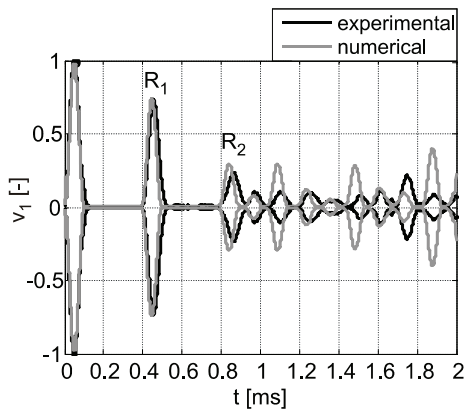
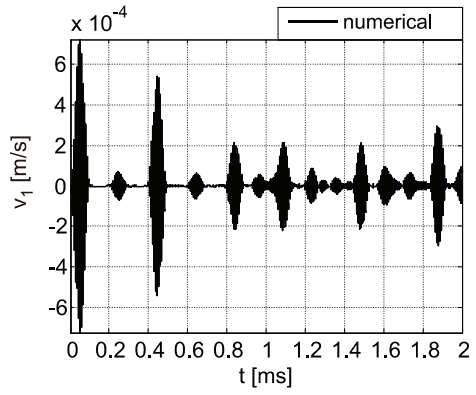
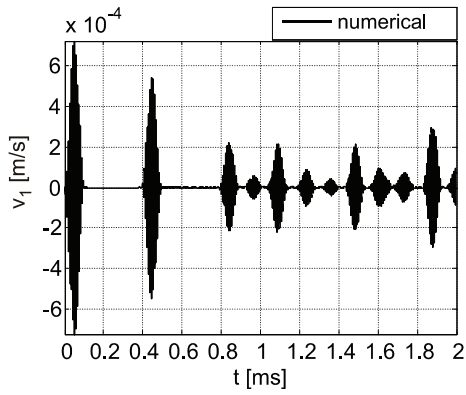
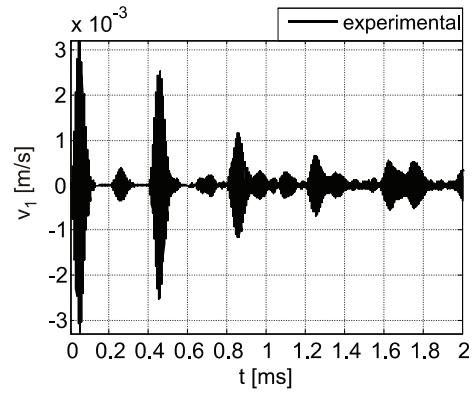
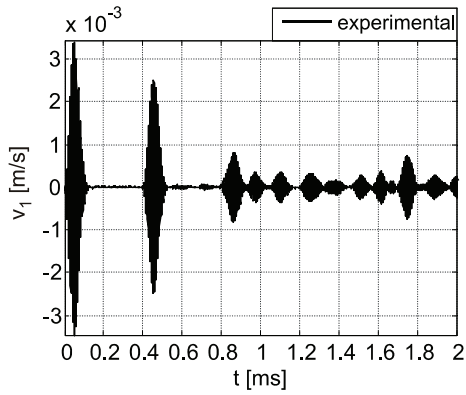


Fig. 5.30. Comparison between experimental and numerical signals for the intact portal frame during longitudinal wave propagation

Fig. 5.31. Comparison between experimental and numerical signals for the portal frame with the notch on member I during longitudinal wave propagation

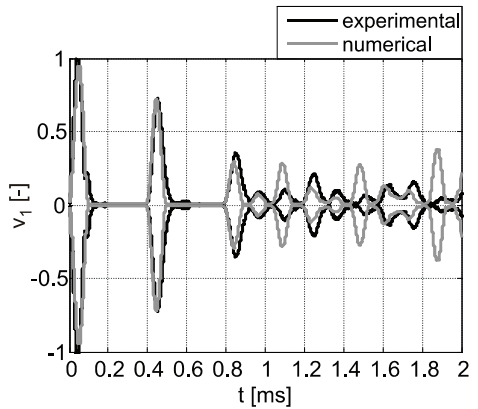
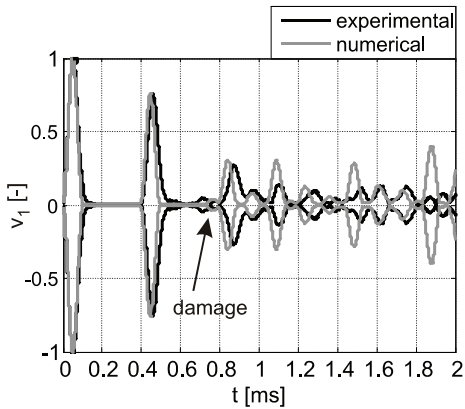
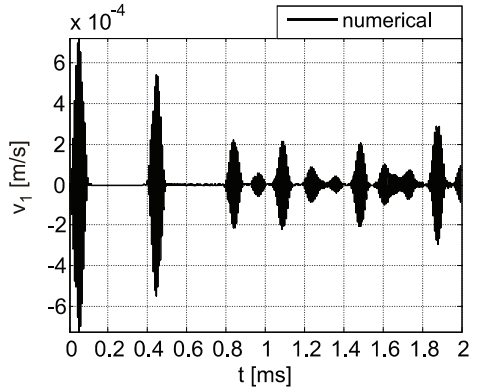
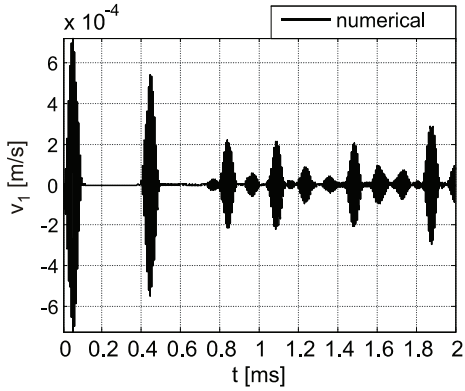
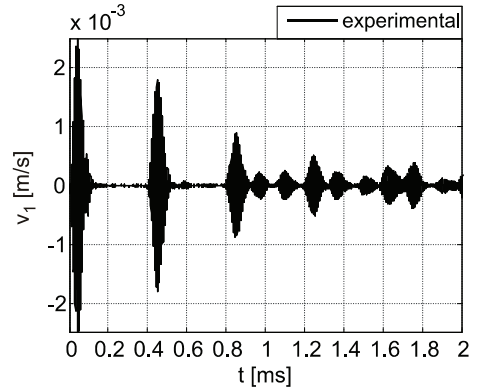
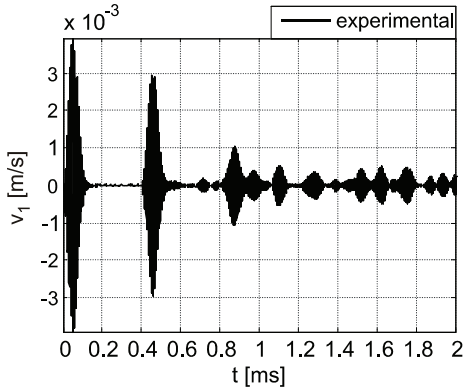


Fig. 5.32. Comparison between experimental and numerical signals for the portal frame with the notch on member II during longitudinal wave propagation

Fig. 5.33. Comparison between experimental and numerical signals for the portal frame with the notch on member III during longitudinal wave propagation

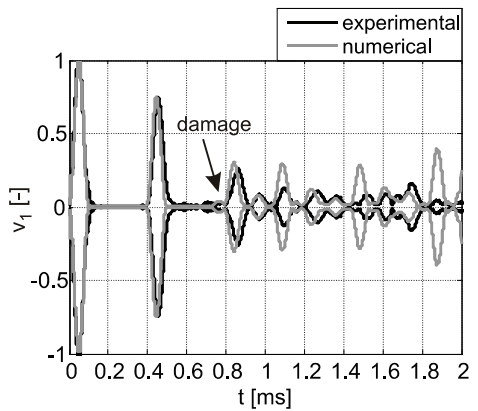
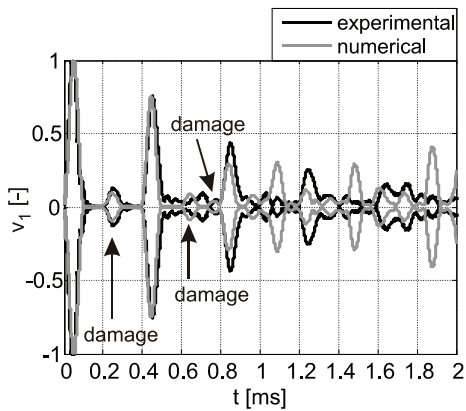
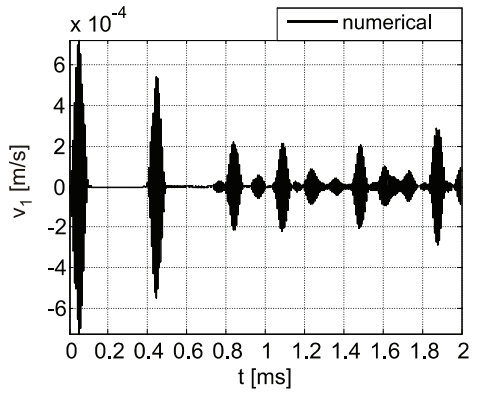
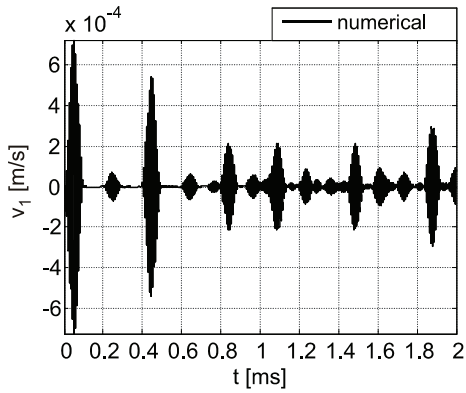
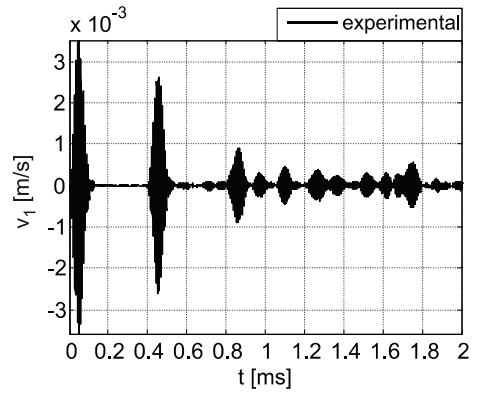
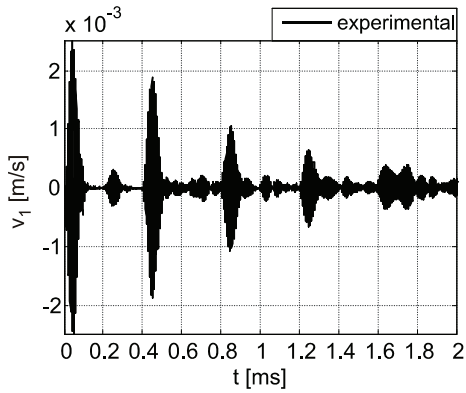


Fig. 5.34. Comparison between experimental and numerical signals for the portal frame with the notches on members I and II during longitudinal wave propagation

Fig. 5.35. Comparison between experimental and numerical signals for the portal frame with the notches on members II and III during longitudinal wave propagation

the longitudinal wave to node 2 and back. In the 2nd reflection R_2 , the wave reflected from node 3 was superposed with the wave reflected twice from node 2. The reflection of the longitudinal wave from node 4 was the 5th reflection in the $v_1(t)$ signal, and it was preceded by the reflections, which contained both longitudinal and flexural components.

The results for the portal frame with damage on member I are shown in Fig. 5.31. Two distinct additional reflections appeared in the measured and calculated signals at 0.2 ms and 0.6 ms. For the frame with damage on member II (Fig. 5.32), the additional reflection is visible at 0.73 ms, but it is very close to reflection R_2 , as in the case of the L-frame. If the notch was introduced on member III, no reflection from damage was registered in both numerical and experimental signals (Fig. 5.33) due to multiple reflections of longitudinal and flexural waves from the portal frame boundaries.

Next, two cases with double notches were considered (Fig. 5.34, Fig. 5.35). Analysing the defects on member I and member II (Fig. 5.34), three reflections from the notches appeared at 0.2 ms, 0.6 ms and 0.73 ms. Figure 5.35 shows results for the frame with notches on members II and III. In this case, results are the same as for the frame with one defect on member II, because identification of the notch on member III was impossible.

5.4.2. Flexural wave propagation in portal frame

The wave packet of frequency 100 kHz was imposed at node 1, and the velocity time history was measured at the same node (Fig. 5.36). The results for the intact portal frame

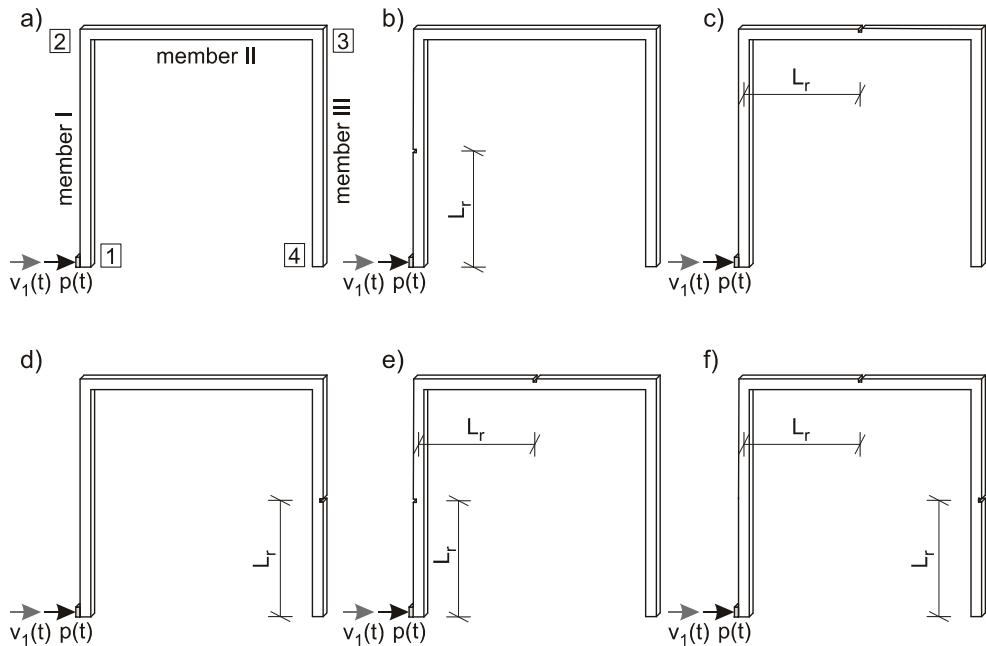


Fig. 5.36. Location of actuators and measurement points for the portal frame during flexural wave propagation: a) intact frame; b) frame with notch on member I; c) frame with notch on member II; d) frame with notch on member III; e) frame with notches on member I and II; f) frame with notches on member II and III

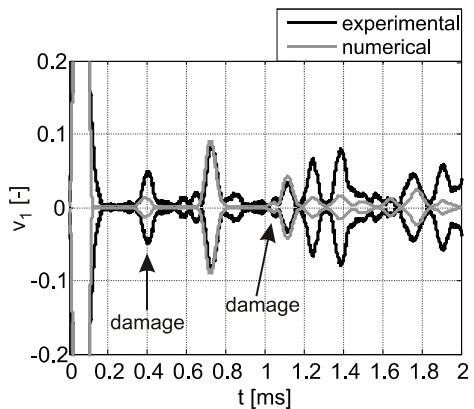
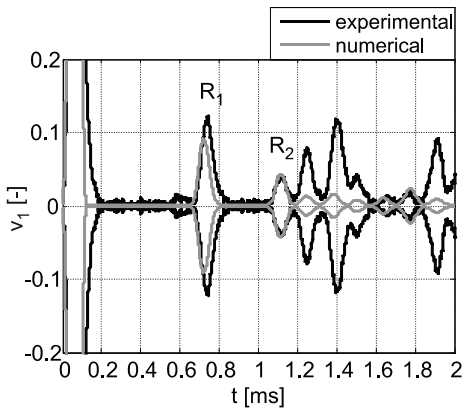
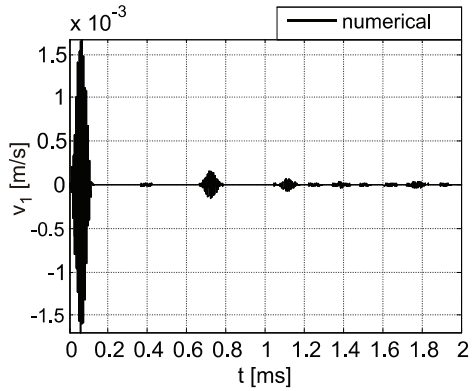
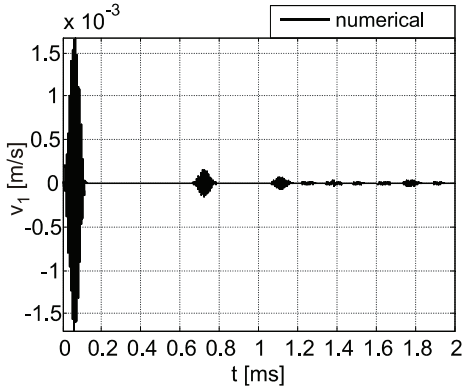
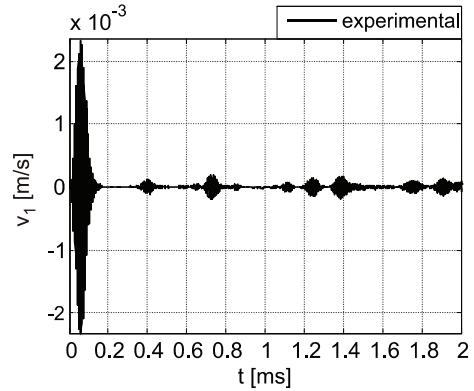
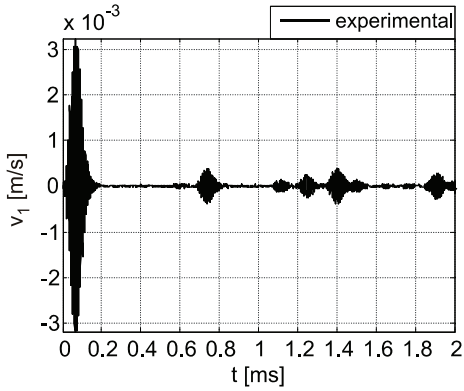


Fig. 5.37. Comparison between experimental and numerical signals for the intact portal frame during flexural wave propagation

Fig. 5.38. Comparison between experimental and numerical signals for the portal frame with the notch on member I during flexural wave propagation

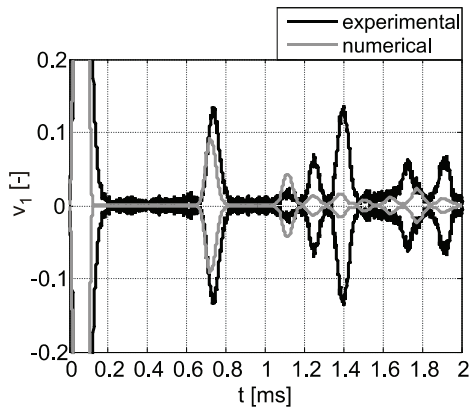
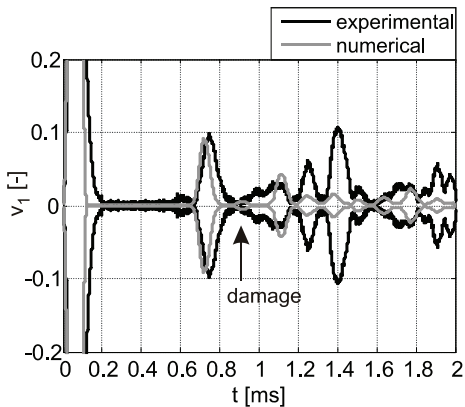
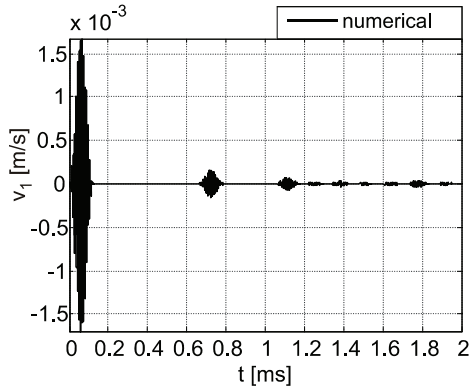
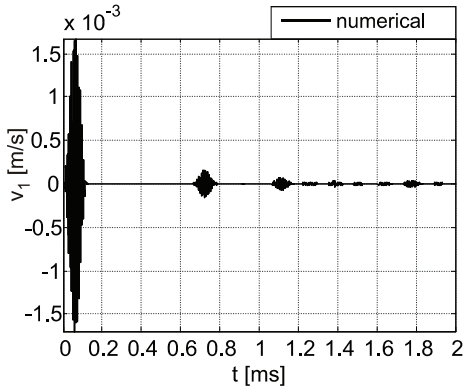
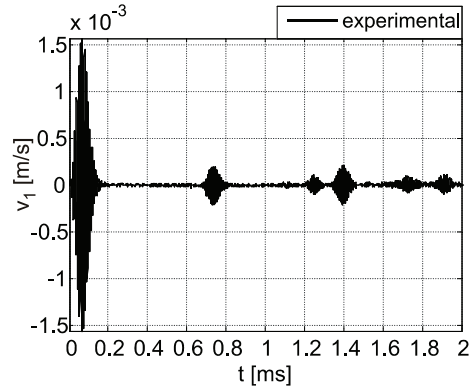
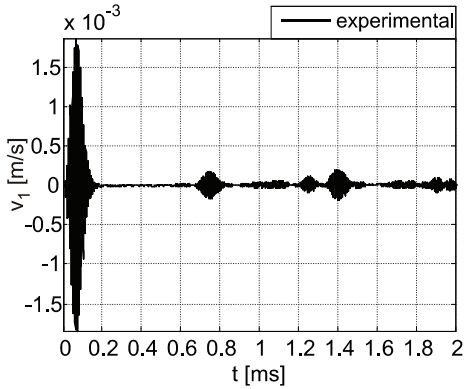


Fig. 5.39. Comparison between experimental and numerical signals for the portal frame with the notch on member II during flexural wave propagation

Fig. 5.40. Comparison between experimental and numerical signals for the portal frame with the notch on member III during flexural wave propagation

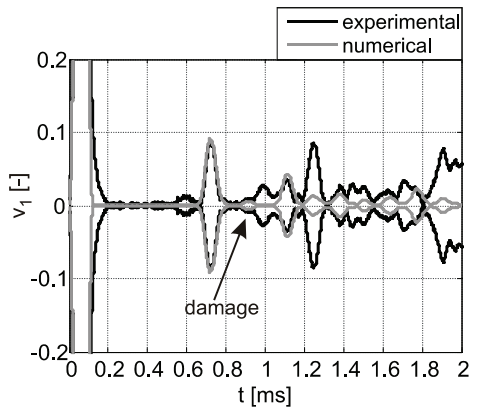
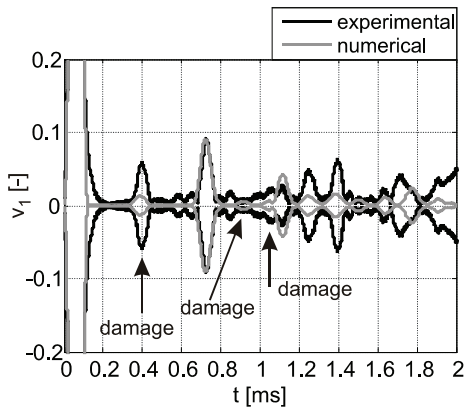
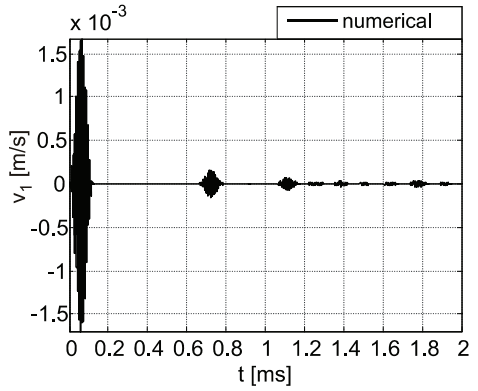
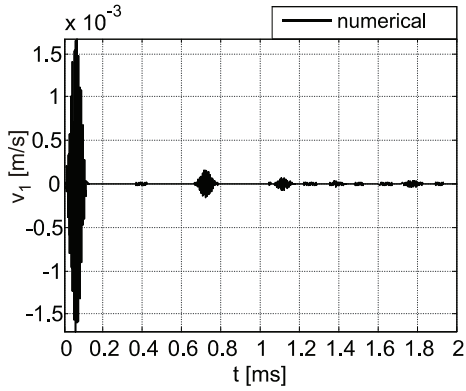
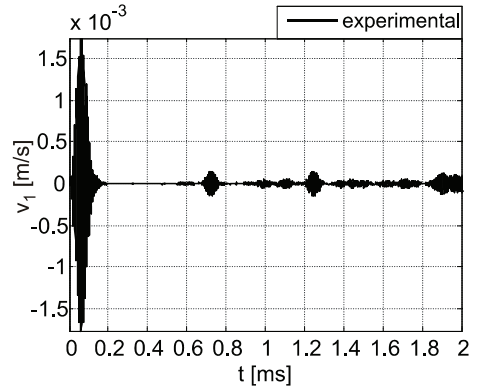
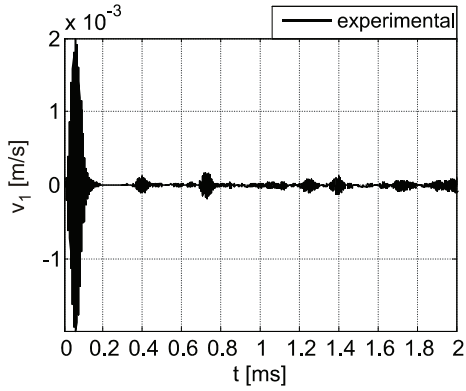


Fig. 5.41. Comparison between experimental and numerical signals for the portal frame with the notches on members I and II during flexural wave propagation

Fig. 5.42. Comparison between experimental and numerical signals for the portal frame with the notches on members II and III during flexural wave propagation

are presented in Fig. 5.37. Results for the portal frame with damage on member I are shown in Fig. 5.38. Two distinct additional reflections appeared in the measured and calculated signals at 0.33 ms and 0.99 ms. For the portal frame with damage on member II (Fig. 5.39), one additional reflection from the notch occurred at 0.86 ms. Analysing the notch introduced on member III, no reflection from damage occurred in both numerical and experimental signals (Fig. 5.40). Figures 5.41 and 5.42 illustrate two cases with double notches. For the defects on member I and member II, three reflection from notches appeared (Fig. 5.41), at 0.33 ms, 0.86 ms and 0.99 ms. Figure 5.42 shows results for the frame with notches at members II and III. In this case, results are the same as for the frame with defect on member II only, because identification of the notch on member III was impossible.

5.5. Summary and conclusions

In this chapter, longitudinal and flexural wave propagation in three types of plane frames (the L-frame, the T-frame and the portal frame) has been investigated both experimentally and numerically. In particular, detection of damage has been considered by analysing wave speeds and reflection times in the recorded guided wave signals.

Numerical simulations were performed by the spectral element method in the time domain using the *M-H-Tim* frame element based on the Mindlin-Herrmann rod combined with the Timoshenko beam. The application of the *M-H-Tim* spectral element guarantees that the mass matrix has a diagonal structure, thus time integration can be efficiently performed. The spectral model based on the Mindlin-Herrmann rod and Timoshenko beam theories guarantees excellent approximation for the first longitudinal and first flexural mode behaviour, which was proved by the comparison with the experimentally measured signals. Therefore, the numerical model of an arbitrary joint or frame structure, intended as a part of the SHM system, should be described in the SEM formulation based on the Mindlin-Herrmann rod and Timoshenko beam theories to obtain proper times of reflections from potential damage.

Experimental and numerical investigations of damage detection were performed for the intact L-frame, as well as for the L-frame with the notch. The frequency of the applied incident wave was selected to ensure propagation of one longitudinal (S_0) mode and one flexural (A_0) mode. Localization of damage in the L-frame was more difficult than for a simple bar due to the mode conversion phenomenon. In the performed experiment, the velocity time signal was measured at two opposite ends of the L-frame specimen (at the *start point*, on which the actuator was bonded and at the *end point*). As in the case of the simple bar, the measurement of the wave propagation signal at the end point cannot provide unambiguous identification of damage position. For the longitudinal, as well as flexural incident waves, damage situated on the horizontal member of the L-frame (containing the excitation point) can be easily identified by the response measurement at the start point. When damage was situated on the vertical element (after passing of the wave through the corner), the signal register in the start point cannot always provide its precise localization. For the longitudinal incident wave, there was a region, in which the reflection from damage was masked by the reflection from the L-frame ends. The location of this region depends on the group velocities of the longitudinal and flexural waves. In the case of the flexural incident wave, identification of the notch was unambiguous for arbitrary damage position until the group velocity of the longitudinal wave was larger than the group velocity of the flex-

ural wave. The results of the research on the effectiveness of the guided wave-based damage detection technique led to the conclusion, that the SHM system designed for the considered L-frame structure can be equipped with a single actuator and a single measurement point (at the same place as the actuator) since detection of damage using the flexural incident wave was possible for an arbitrary damage position.

Analysis of wave propagation in the T-frame led to the conclusion, that two actuators and two measurement points were required to unambiguous damage localization in the whole T-frame. Two actuators should be mounted at the same place, i.e. at the end of two collinear bars and the points of measurements of guided wave signals should be at the same position as the actuators. The actuators should operate interchangeably. One actuator should excite longitudinal waves, because the signal measured in the axial direction enables damage diagnosis in two collinear bars (here member I and member II). For condition monitoring of member I and member III, the second actuator should excite the flexural wave and the response in the transverse direction should be registered.

The idea of monitoring of the portal frame is similar as for the L-frame. For diagnostic purposes it is not possible to excite a wave packet solely in one point. To monitor the whole portal frame two actuators should be mounted at the base of both columns and two measurement points should be at the same positions as the actuators. One actuator and one measurement point enables condition monitoring of the whole column and half of the horizontal beam. Both longitudinal and flexural waves can be used; however, in the performed experiments longitudinal waves appeared more sensitive for considered damage. Moreover, the results for the portal frame revealed that it is possible to identify defects situated on two different members.

Chapter 6

WAVE PROPAGATION IN PLATES

Waves propagating in plates are reflected by structural boundaries or existing defects. Ultrasonic guided Lamb waves are very suitable for damage detection in plates due to the ability to be transmitted over relatively large distances and to identify both surface and internal defects. A wide range of studies has already been reported on the Lamb wave scattering from damage in the form of slots (e.g. Lee and Staszewski 2007a, 2007b), holes (e.g. Chang and Mal 1999, McKeon and Hinders 1999, Cegla et al. 2008), notches (e.g. Alleyne and Cawley 1992, Jin et al. 2005, Benmeddour et al. 2008a, 2008b, Yang et al. 2009), delaminations (e.g. Ramadas et al. 2009) or cracks (e.g. Wang and Shen 1997, Lu et al. 2006). The Lamb wave technique, complicated by the existence of at least two modes (S_0 and A_0) at any given frequency and their dispersive character, causes additional difficulties, when waves interact with asymmetric discontinuities (e.g. Benmeddour et al. 2008b). As a result of an encounter with a structural defect, the incident Lamb mode can partially convert into other modes and these modes may interact and propagate out in either direction (Jin et al. 2005).

Experimental investigations on Lamb wave propagation in plates have been performed by various researches. In general, two approaches have been applied to register Lamb waves. The first approach is directed towards non-contact techniques, based on dynamic photoelasticity (e.g. Graff 1975, Rossmannith and Fourney 1982), speckle interferometry (e.g. Lammering 2010) or laser vibrometry (e.g. Mallet et al. 2004, Staszewski et al. 2004, 2007, Rucka 2010c). Another approach depends on using transducers on the plate surface (e.g. Alleyne and Cawley 1992, Wang et al. 2004, Wang et al. 2008, Benmeddour et al. 2008a, 2008b, Lu et al. 2008, Ramadas et al. 2009). Conventional ultrasonic transducers are rather bulky and expensive, thus recently piezoelectric ceramic transducers (PZT) have been commonly used, since they are small, lightweight, unobtrusive and inexpensive, and can be produced in different geometries (Giurgiutiu 2008). The ultrasonic or PZT transducers can act as both actuators (transmitting transducers) and sensors (receiving transducers), and if a receiving transducer is bonded at a remote point of a structure, the received signal contains information about the integrity of the line between them (Alleyne and Cawley 1992). Two methods can be used for damage detection: the pitch-catch method and the pulse-echo method. In the *pulse-echo method*, a transmitter and a receiver are situated at the same location and defects are detected in the form of additional echoes in a signal. In the *pitch-catch method*, a transmitter and receiver are placed at different positions, and changes in Lamb waves travelling through a damaged area are used as defect indicators (Giurgiutiu 2008). In particular, several embedded PZT transducers can be arranged in distributed sensor networks (e.g. Wang and Chang 2005, Lu et al. 2006), guided wave transducer arrays (e.g. Wilcox 2003, Kudela et al. 2008), or phased arrays that are a group of sensors located at distinct spatial locations in which relative phases of the sensor signals are varied in such way, that the effective propagation pattern is reinforced in the desired direction (e.g. Giurgiutiu and Bao 2004, Yu and Giurgiutiu 2007, 2008, Ostachowicz et al. 2009).

Numerical simulations of Lamb waves in plates performed in this chapter, have been conducted by the SEM. In earlier studies, Žak et al. (2006a, 2006b) presented an analysis of

in-plane waves by the SEM, based on the plane stress theory resulting in non-dispersive waves. They analysed an aluminium plate of thickness 1 mm and an excitation signal of frequency 100 kHz. Within such frequency-thickness ratio, the S_0 mode is practically dispersionless and the plane stress theory provides appropriate results. However, for many civil engineering structures, for example for steel bridge plate girders, plates are thicker and dispersion occurs. To solve this problem, Peng et al. (2009) proposed a 3-D spectral element, which makes the analysis of dispersive waves possible. Such 3-D model is very useful in analysing structures of complicated geometries. However, for dispersive wave propagation in plates, an alternative solution could be a 2-D plate model, which results in a substantial reduction of computational time in comparison with a 3-D model. Such SEM plate model should be based on higher order plate theories, in order to characterize propagation of ultrasonic waves over considerable range of frequencies. For flexural waves, the spectral element based on the Mindlin plate theory was developed by Kudela et al. (2007b) and Chróścielewski et al. (2010). However, in these works only numerical results were reported and a correction parameter for the Mindlin theory was not considered. Some experimental results of flexural wave propagation were presented by Rucka (2010c). To analyse in-plane waves, the higher order Kane-Mindlin extensional plate theory can be used (Kane and Mindlin 1956). The Kane-Mindlin theory includes the out-of-plane stress component and retains the simplicity of the 2-D model. In earlier research, the Kane-Mindlin theory was used in analytical studies of static and dynamic fracture problems of cracked plates (e.g. Jin and Batra 1997a, 1997b, Kotousov and Wang 2002, Kotousov 2007). Wang and Chang (2005) presented a study of waves scattering by a cylindrical inhomogeneity and compared analytical solutions based on the Kane-Mindlin theory with experiments performed on a plate with an added mass. McKeon and Hinders (1999) utilized the Kane-Mindlin theory to derive analytical solutions for the scattering of Lamb waves from a circular inclusion. Rucka (2011) developed the time domain spectral element based on the Kane-Mindlin theory and proved its efficiency on the example of in-plane waves in a plate measured in 17 points.

In this chapter, results of experimental and numerical analyses of Lamb waves propagating in a 5 mm-thick steel plate in the frequency range of 50–300 kHz are presented. Within such thickness-frequency ratio, S_0 and A_0 Lamb modes reveal dispersive character. The chapter resumes the author's studies of damage detection in plates by in-plane waves (Rucka 2011). Results presented in this chapter are broadened to complete analysis of in-plane and flexural (out-of-plane) waves interaction with defects located at three different positions and two different angles. Damage detection is considered by analysing velocity data in the form of A-scans, B-scans and C-scans. Finally, an application of in-plane and flexural waves for damage detection is discussed.

6.1. In-plane wave propagation in plate

6.1.1. Experimental setup

Wave propagation experiments were performed on a steel plate of length $L = 1000$ mm, width $b = 1000$ mm and thickness $h = 5$ mm (Fig. 6.1). The experimentally determined mass density ρ is equal to 7872 kg/m³. The modulus of elasticity E and the Poisson's ratio ν were also determined experimentally in a force-displacement test using two strain gauges attached to the specimen of cross-section 20 mm \times 5 mm in both longitudinal and transverse directions, and their values are: $E = 205.35$ GPa, $\nu = 0.28$. The plate

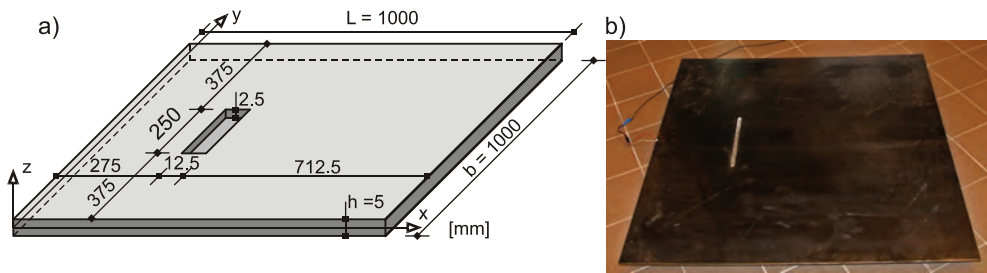


Fig. 6.1. Steel plate: a) geometry; b) photograph of plate with damage

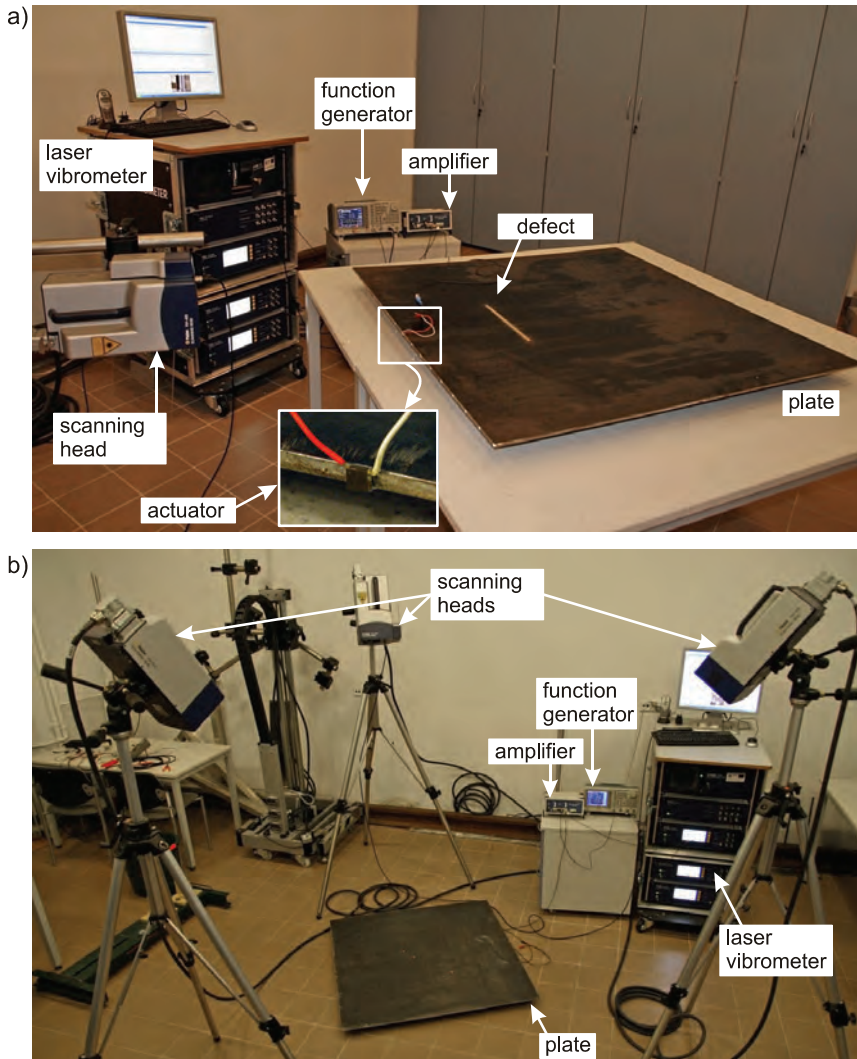


Fig. 6.2. Instrumentation for measurements of in-plane waves in the steel plate: a) experiment #1 with the use of one scanning head; b) experiment #2 with the use of three scanning heads

was placed on four concrete blocks and all plate edges were free. The supporting blocks had no influence on the registered signals. Two plates were taken into investigation: the pristine plate and the plate with damage. In the damaged plate, the plate thickness was changed abruptly to 2.5 mm on the area of 250 mm×12.5 mm. Such rectangular notch, obtained by machine cutting, was introduced at the position given in Fig. 6.1a. This is an academic approach defect, but it can represent corrosion damage, which often occurs in civil engineering structures subjected to environmental conditions.

The experimental setup is presented in Fig. 6.2. The ultrasonic in-plane waves were generated by the piezoelectric actuator Noliac CMAP11 bonded at the edge of the plate, at position $x = 0$, $y = 500$ mm. Buckwheat honey coupling was used for the actuator. A tone burst $p_V(t)$, in the form of a five-peak sine of frequency 250 kHz modulated with the Hanning window (Fig. 6.3), was delivered to the PZT actuator by means of the arbitrary function generator Tektronix AFG 3022 with the amplifier EC Electronics PPA 2000. Lamb waves are typically excited by two transducers mounted on the upper and lower surface of the plate. If in-phase shear-stress boundary excitation signals are applied on both actuators, a pure symmetric mode is excited. To excite a pure antisymmetric mode, out-of-phase shear stress excitation signals are applied on both actuators. A PZT actuator mounted at one side of the plate surface, excited by a shear stress signal, generates both S_0 and A_0 modes simultaneously. In this study, the PZT actuators utilized the thickness-wise expansion effect were used and the actuator bonded to the cross-section of the plate enabled to excite mainly the fundamental S_0 mode and the influence of the A_0 mode was insignificant. Velocity signals $v(t)$ (velocity components parallel to the x axis) were recorded by the scanning laser vibrometer Polytec PSV-3D-400-M. In order to improve the signal-to-noise ratio, 500 averages in time were utilized.

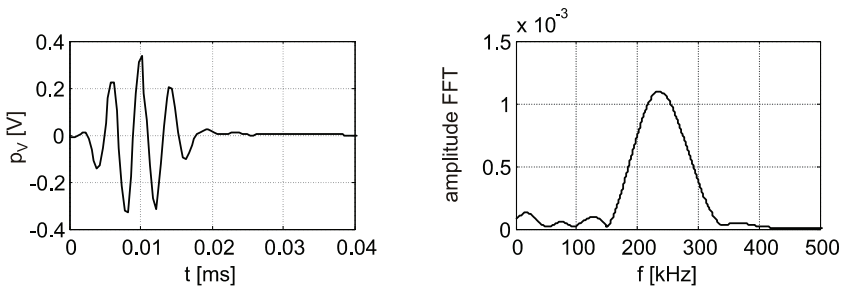


Fig. 6.3. A 250-kHz 5-count Hanning windowed burst in time and frequency domains

Two instrumentation setups were considered. In the first (experiment #1), velocity signals were registered in evenly distributed points along the edge of the plate (Fig. 6.2a) by one scanning head of the vibrometer. The scanning head was shifted along the specimen from one point to another to register in-plane velocity component perpendicular to the plate edge. In this test, the pristine and damaged plates were measured. In the second instrumentation setup (experiment #2), three scanning heads were used and the signals were measured on the plate surface. This test was performed on the plate with defect. Measurements were made on the intact surface, i.e. defect was underside of the object during test (Fig. 6.2b). The velocity signals were measured along line #1 and line #2, as indicated in Fig. 6.4. The one plate specimen with defect enabled analysis of three different locations of damage: damage #1 (Fig. 6.4b), damage #2 (Fig. 6.4c) and damage #3 (Fig. 6.4d).

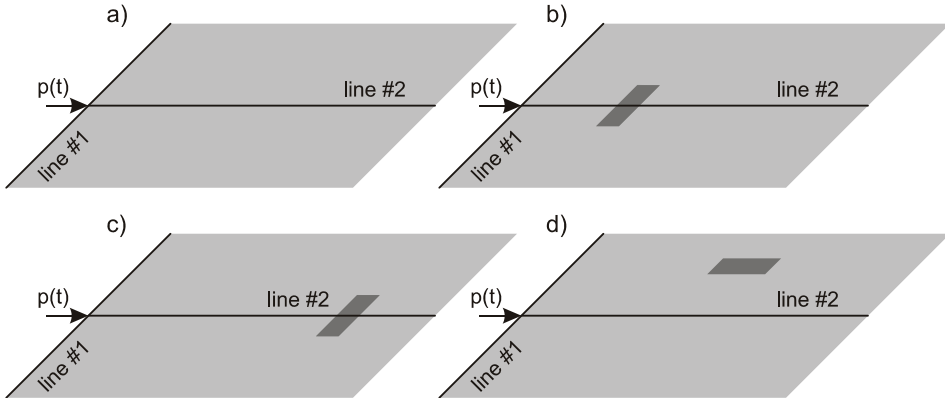


Fig. 6.4. Measurement lines for different damage locations in the plate for in-plane wave propagation: a) pristine plate; b) plate with damage #1; c) plate with damage #2; d) plate with damage #3

6.1.2. Dispersion curves

Group velocity dispersion curves were experimentally determined for the pristine plate. Velocity signals were measured on the plate edge (at $x = 0$, $y = 500$ mm) for frequencies varying from 50 to 300 kHz with the increment of 10 kHz. Figure 6.5 presents examples of registered signals for frequencies 120, 200 and 250 kHz. The force applied normal to the plate edge results in propagation of both in-plane waves, namely an extensional wave and the shear horizontal wave. Since the measurements were made on the plate edge, a strong Rayleigh wave was also observed. In the measured signals, the first reflection is the

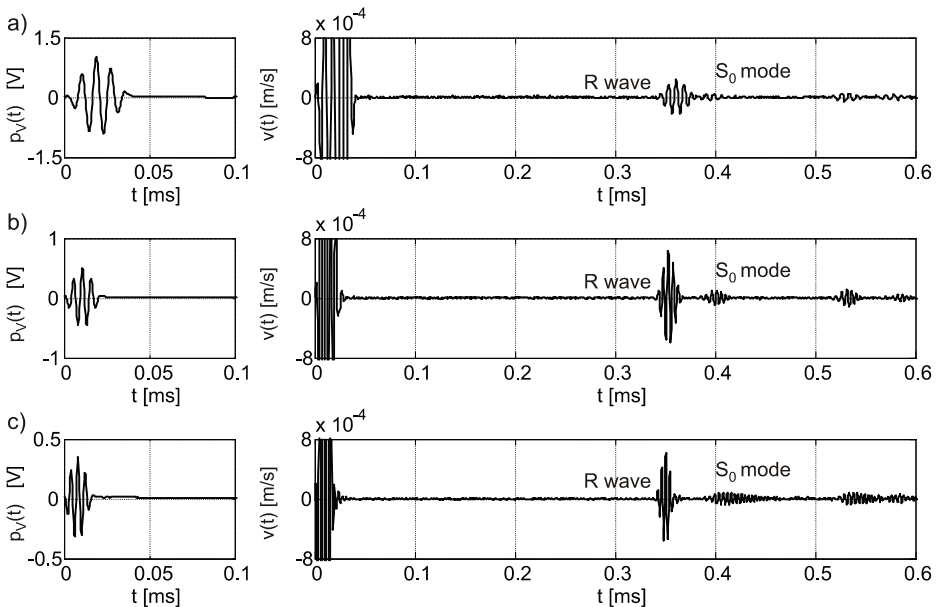


Fig. 6.5. Time history of experimentally measured in-plane waves in the pristine plate for determination of dispersion curves: a) 120 kHz; b) 200 kHz; c) 250 kHz

non-dispersive Rayleigh wave, while the second reflection is the first symmetric S_0 mode. Figure 6.5 reveals dispersive behaviour of the measured S_0 mode. The S_1 mode was not excited in the experiment. The SH_0 mode was not directly registered on the plate edge. Based on the time-of-flight, group velocities of the S_0 mode and the R wave were determined. Then the velocity of the SH wave was determined through the relation (2.3).

To identify the optimal range of excitation frequencies, experimental in-plane wave tuning for the pristine plate was conducted (Fig. 6.6). During this test, the measurements for all frequencies were made with the same gain level set on the amplifier. The signals on the amplifier output, as well as velocity signals were collected for frequencies from 50 to 300 kHz in steps of 10 kHz. With the increase of frequency, the voltage signal on the amplifier decreased, but at the same time, the R wave and the S_0 mode amplitudes increased. Both the R wave and the S_0 mode reached similar strength around 180–250 kHz. The amplitudes of the S_0 mode in Fig. 6.6d were plotted in the frequency range 120–300 kHz, because for smaller frequencies the S_0 mode coincided with the Rayleigh wave. Thereby the response for the R wave in Fig. 6.6c is a combination of the R wave and the S_0 mode below frequency of 110 kHz.

Figure 6.7 shows the experimental and analytical dispersion curves for the 5 mm plate. For the plane stress theory two modes exist: the fundamental extensional mode, which approximates the S_0 mode only at low frequencies, and the shear horizontal mode which is the SH_0 mode (non-dispersive for isotropic body). The Kane-Mindlin theory captures three modes: the SH_0 mode, as well as the first and second extensional

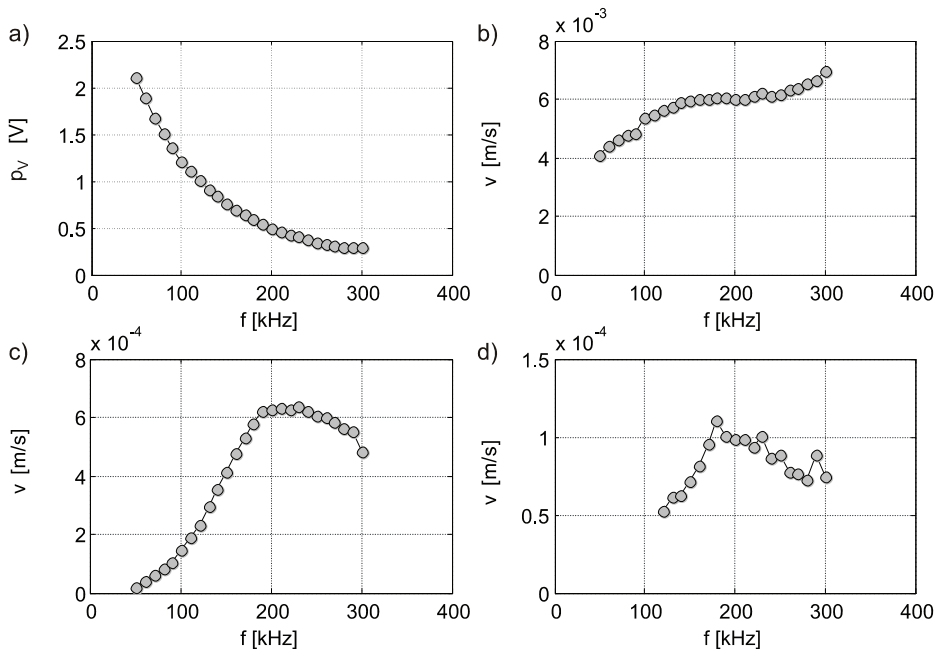


Fig. 6.6. Experimental in-plane wave tuning in the pristine plate for frequency range 50–300 kHz: a) maximum value of voltage excitation signal; b) maximum value of incident wave in velocity signal; c) maximum value of first reflection (R wave) in velocity signal; d) maximum value of second reflection (S_0 mode) in velocity signal

modes, which correctly approximate the dispersion behaviour of the S_0 and S_1 Lamb modes. The parameter κ_{KM} in the Kane-Mindlin theory was chosen as 0.73 to give the best fit to the experimentally measured group velocity of the S_0 mode for the frequency range 120–300 kHz. It can be noted in Fig. 6.7 that the Kane-Mindlin analytical dispersion curve for the S_0 mode agrees with the experimental results; moreover, it agrees with the exact Lamb mode in the selected frequency range 120–300 kHz.

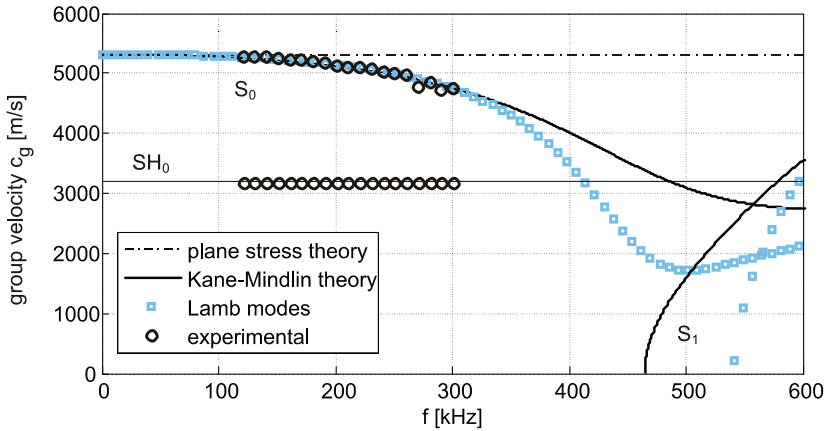


Fig. 6.7. Experimental and analytical dispersion relation for in-plane waves for 5 mm steel plate

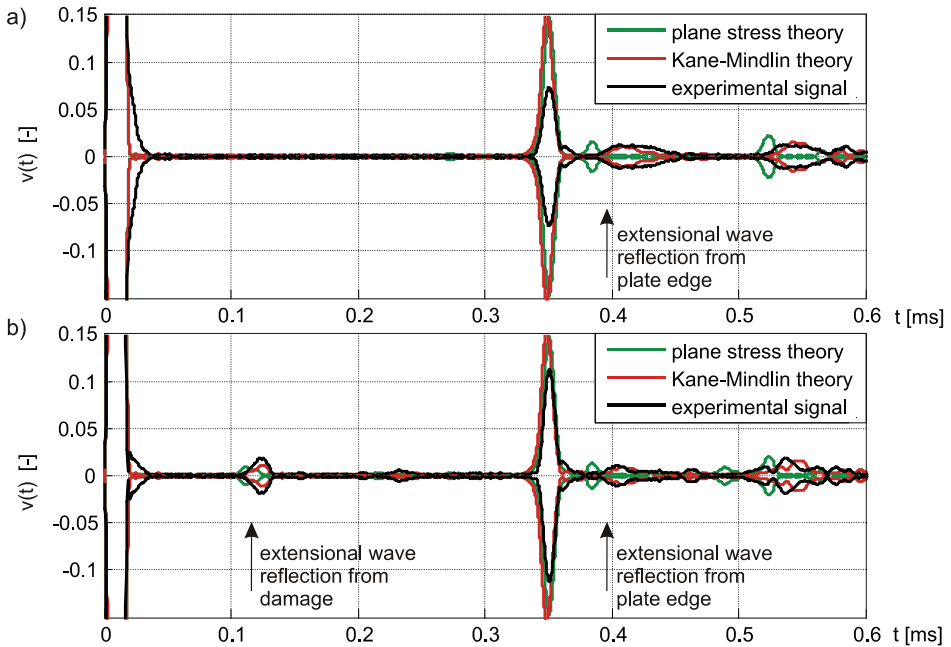


Fig. 6.8. Propagation of in-plane wave of frequency 250 kHz – comparison between experimental and numerical velocity response signals: a) pristine plate; b) plate with damage

6.1.3. Numerical model

Modelling of in-plane wave propagation in plates was performed by the time domain spectral element method. The plate was meshed to 80×80 2-D spectral finite elements, each element with $9 \times 9 = 81$ GLL nodes. The boundary conditions were free on all edges. The defect was modelled using 20 elements with height reduced by 2.5 mm. The highest excitation frequency used in numerical simulations was 250 kHz, and for this frequency the applied mesh guaranteed 8.6 nodes per the shortest wavelength. Damping was not considered in this model. Temporal integration was performed using the Newmark scheme with the time step $\Delta t = 5 \cdot 10^{-8}$ s. This algorithm uses accelerations as the primary variables and takes advantage of the diagonal structure of the mass matrix (cf. Section 3.1.4.2).

In Fig. 6.8, experimental signals for in-plane wave propagation are compared with numerical results for the plane stress and Kane-Mindlin theories. The amplitudes of the experimental and numerical signals were normalized to 1, and only signal envelopes were plotted for clarity. The velocity signal $v(t)$ was measured on the plate edge at position $x = 0$, $y = 500$ mm (see Fig. 6.1). If the plane stress theory is used, experimental data are not compatible with the numerical ones. It is visible in Fig. 6.8 that reflections (from defect or from plate edge) of extensional waves in the numerical signal are delayed with reference to the experimental signal. Considering the Kane-Mindlin plate theory, it can be noted that the numerical simulations are in good agreement with the experimental data and this theory guarantees better approximation for the S_0 mode than the plane stress theory.

6.1.4. Damage detection in plate by in-plane waves

In experiment #1, velocity responses were measured in 17 nodes evenly distributed on the left edge of the plate (along line #1 in Fig. 6.4) from $x = 0$, $y = 0$ m to $x = 0$, $y = 1$ m. As a reference state, the pristine plate was firstly examined. Experimental and numerical velocity signals in the time and spatial domains are given in Fig. 6.9. They consist of particular *A-scans*, i.e. waveform data plotted as a function of time, registered in consecutive points. Fronts of the R wave and the S_0 mode were registered on the plate edge.

The second example concerned the plate with damage #1 (Fig. 6.10). In both the numerical and experimental results, the fronts of the S_0 mode reflected from damage were visible. Two fronts of the S_0 mode were caused by the 1st and 2nd reflection from damage and they are marked by solid lines in Fig. 6.10. The first reflection in the numerical signal occurred at time $t = 0.1149$ ms and knowing the plate geometry and the group velocity of the S_0 mode (4973.17 m/s) the location of the defect can be identified as 286 mm. In the case of experimental signal, reflection occurred at $t = 0.1141$ ms and the velocity of the S_0 mode was 5009.78 m/s, thus the identified position of damage was 286 mm. Two additional fronts of wave, marked with dashed line in Fig. 6.10, were caused by the S_0 mode diffraction from defect ends. This S_0 mode arose from a mode conversion upon interaction of the SH_0 mode with defect. The fronts of diffracted waves enabled to estimate the defect length. Moreover, in the experimental signals an additional reflection appeared. It was the R wave reflected by damage (dotted line in Fig. 6.10b). This reflection was identified as coming from imperfect work of the equipment (electromagnetic coupling in the cabling). The amplifier created additional wave packet (of amplitude about 0.01 of the incident wave) at the moment of arriving the S_0 mode reflected from defect. This wave packet induced propagation of new R wave, which provided the additional indicator of damage existence.

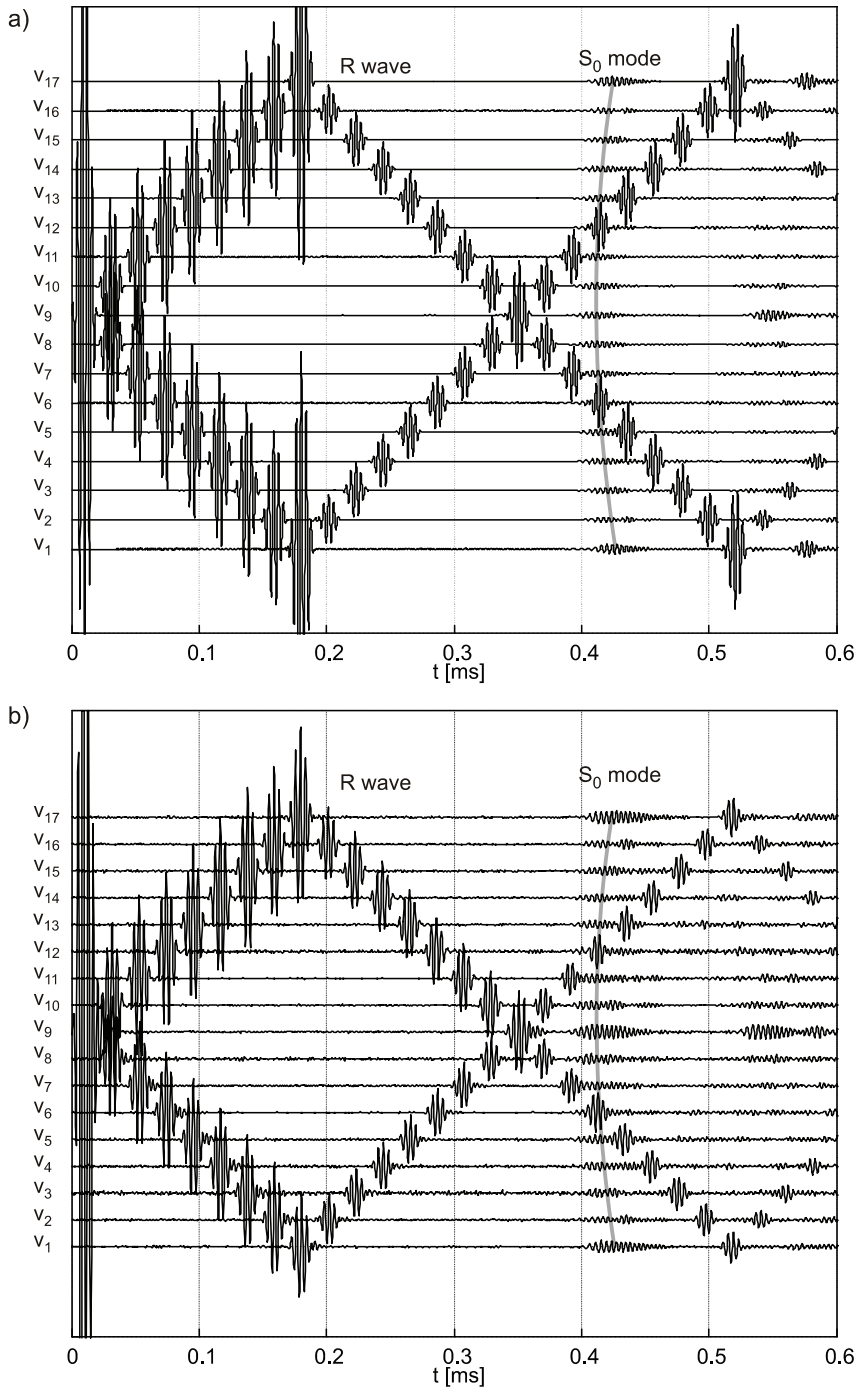


Fig. 6.9. Set of time signals collected at 17 points evenly distributed along the plate edge during propagation of in-plane waves of frequency 250 kHz in the pristine plate: a) spectral element method simulations based on the Kane-Mindlin theory; b) experimental results

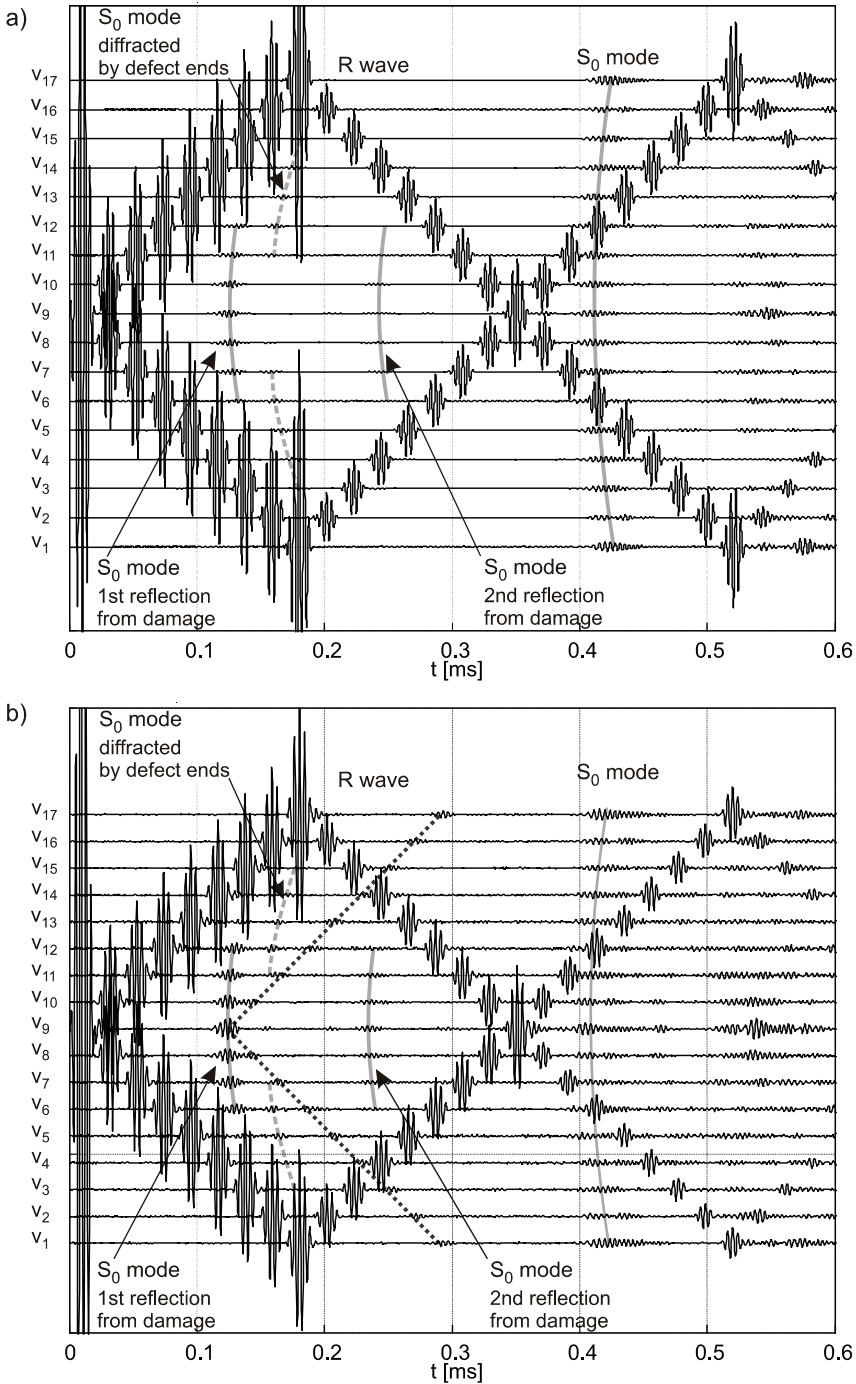


Fig. 6.10. Set of time signals collected at 17 points evenly distributed along the plate edge during propagation of in-plane waves of frequency 250 kHz in the plate with damage #1: a) spectral element method simulations based on the Kane-Mindlin theory; b) experimental results

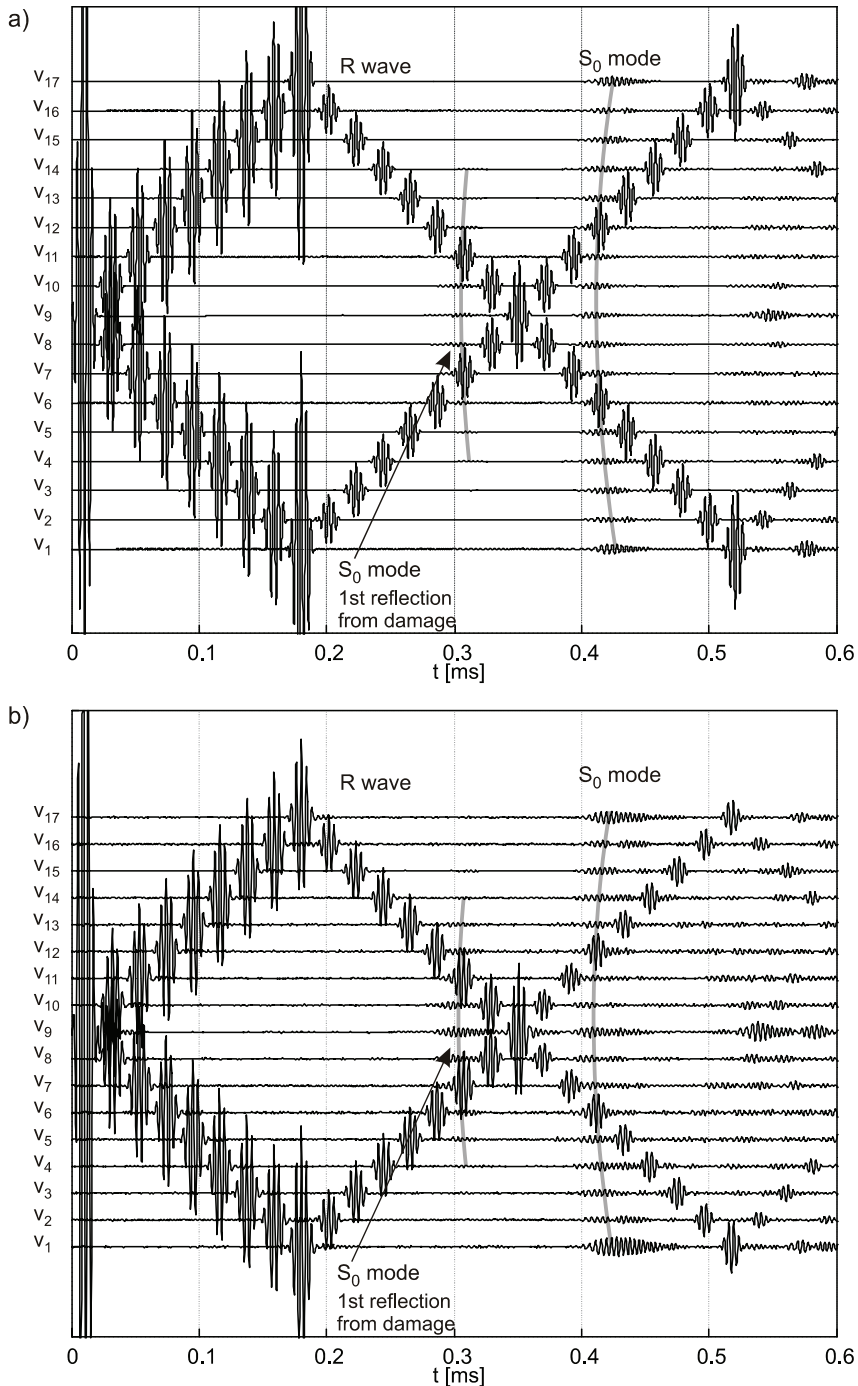


Figure 6.11 shows propagation of in-plane waves in the plate with damage #2. Both numerical and experimental results revealed the existence of the reflection from the defect. The front of the S_0 mode reflected from damage was partially covered with the R wave, but the identification of damage was still possible. The reflection in the numerical signal occurred at time $t = 0.2936$ ms and the position of the defect was identified as 730 mm. For the experimental signal, the reflection occurred at time $t = 0.2902$ ms, so the identified position of damage was 727 mm.

In experiment #2, velocity responses were measured in 161 evenly distributed points along each of lines #1 and #2 (see. Fig. 6.4). Lines #1 and #2 were situated on the plate surface and their lengths were insignificantly shorter than the plate length. Moreover, line #1 was shifted from the left edge of the plate at about 2.5 cm thus in the numerical simulations the velocity signals were calculated at the distance of 2.5 cm from the plate edge. The measurements were performed for the plate with damage #1, #2 and #3. Numerical and experimental results are presented in Fig. 6.12 to Fig. 6.18 in the forms of so called *B-scans*, which present data in the form of a time-position scan (a cross-sectional view).

In Fig. 6.12, numerical results for the pristine plate are shown. The horizontal axis represents time while the vertical one gives the distance along the plate width (or length). The amplitudes of waves are displayed as the grey scale values. In the presented B-scans, the S_0 and SH_0 modes, the R waves, as well as the head waves (a.k.a. PS waves) can be found.

Numerical and experimental B-scans for the plate with damage #1 are presented in Fig. 6.13 and Fig. 6.14, respectively. Observation of the time-position plane enabled to identify both the position and the extent of damage. Fronts of the S_0 mode caused by the 1st and 2nd reflection from damage, as well as diffraction from the defect ends are visible in Fig. 6.13a for line #1 based on the numerical data. This scan provided the estimation of the defect length. Figure 6.13b shows the numerical scan data for line #2. In this case, the plot provided information on the distance of damage from the plate edge. Based on the experimental data (Fig. 6.14), it was possible to identify both damage position and its size, but the velocity signals did not exactly cover with the numerical ones. This was caused by the presence of the A_0 mode in the experiment. The appearance of small amplitude A_0 mode caused, that the waves diffracted on the defect ends cannot be clearly observed.

Figures 6.15 and 6.16 give the B-scans for the plate with damage #2 for numerical and experimental data, respectively. Both the extent and position of the defect can be detected from the numerical, as well as the experimental signals. In the experimental results, the influence of the A_0 mode was insignificant in comparison with the test on the plate with damage #1. This was caused by slightly different mounting of the actuator. Therefore it is visible, that the excitation of pure S_0 mode depends on the quality of actuator mounting.

Numerical and experimental B-scans for the plate with defect #3 are illustrated in Fig. 6.17 and Fig. 6.18, respectively. The defect #3 was situated perpendicularly to the plate left edge. Detection of such defect was more difficult than of the defects parallel to left plate edge (defect #1 and defect #2). The extent of the defect can be superficially assessed from the B-scan along line #2 and its position can be calculated from the B-scan along line #1, knowing the time of the reflection and the group velocity. Moreover, the B-scan along line #1 showed, that the defect occurs on the upper half of the plate.

Finally, C-scans were analysed based on the numerical velocity signals. The *C-scan* provides a two-dimensional xy plane view at selected time instants. Velocity components parallel to the x axis are illustrated in Fig. 6.19 to 6.22. Results for the pristine plate are given in Fig. 6.19 at the time instants $t = 0.12; 0.2; 0.25; 0.4$ ms. The force applied normal to

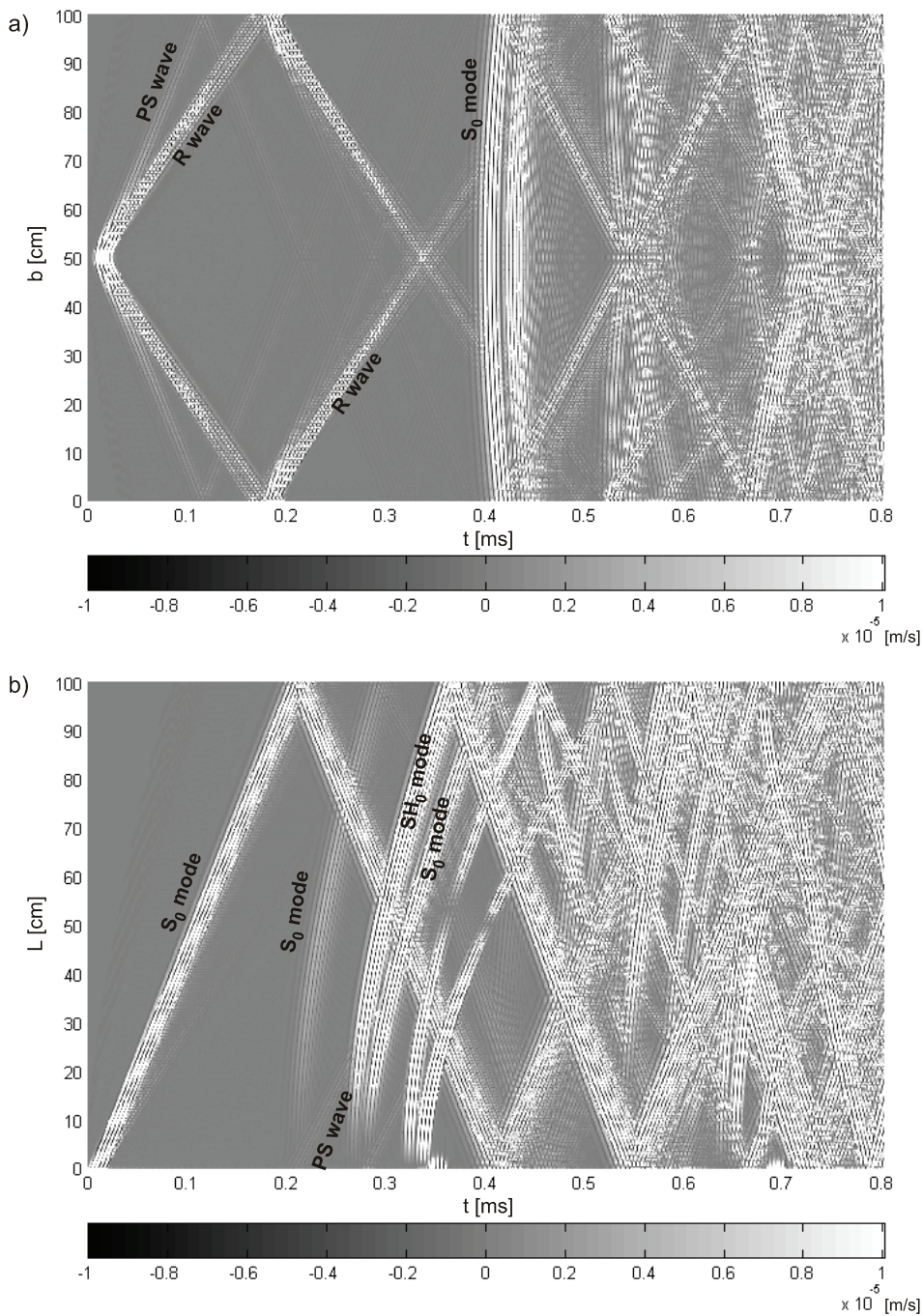


Fig. 6.12. B-scans of numerical in-plane waves in the pristine plate: a) line #1; b) line #2

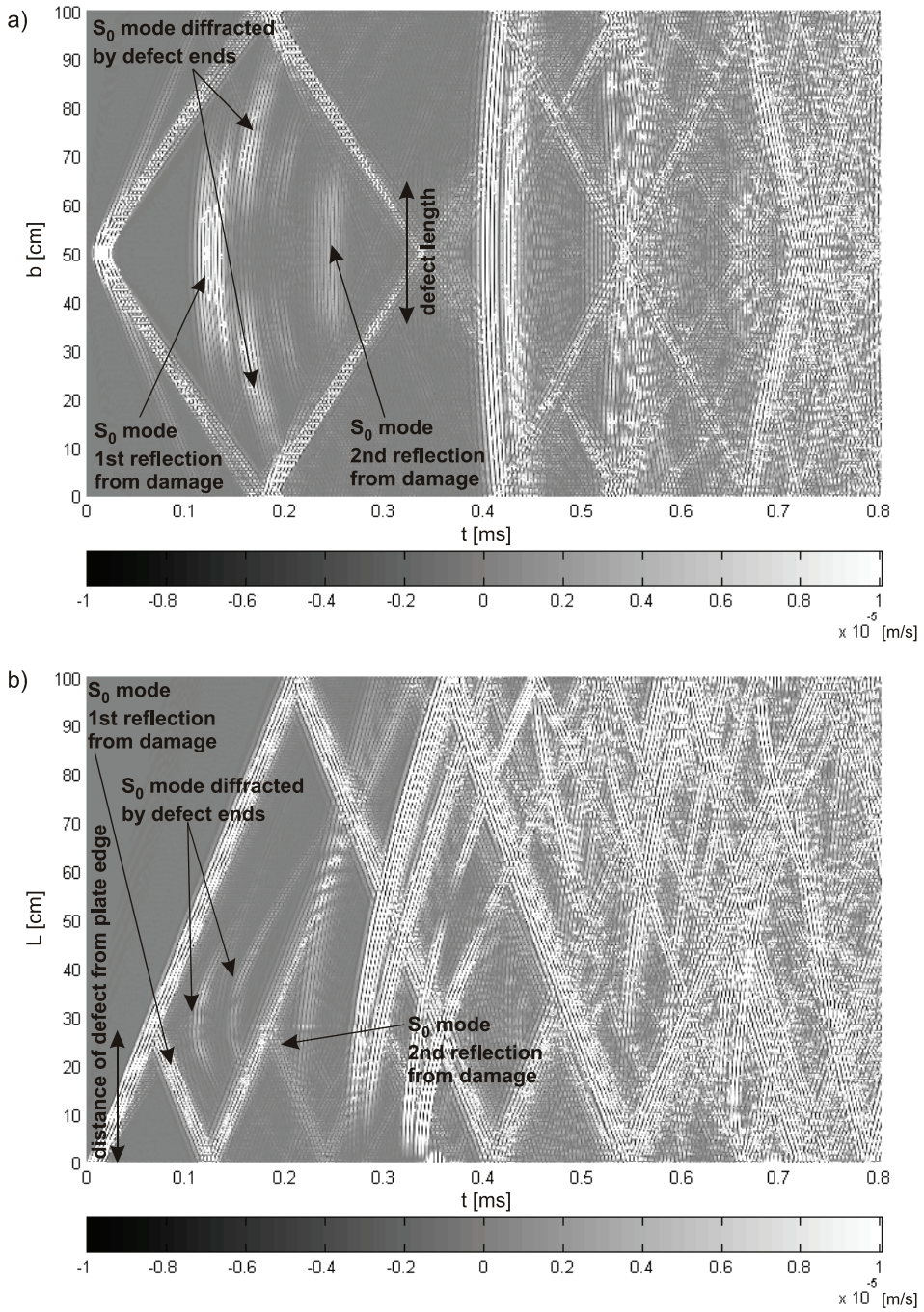


Fig. 6.13. B-scans of numerical in-plane waves in the plate with damage #1: a) line #1; b) line #2

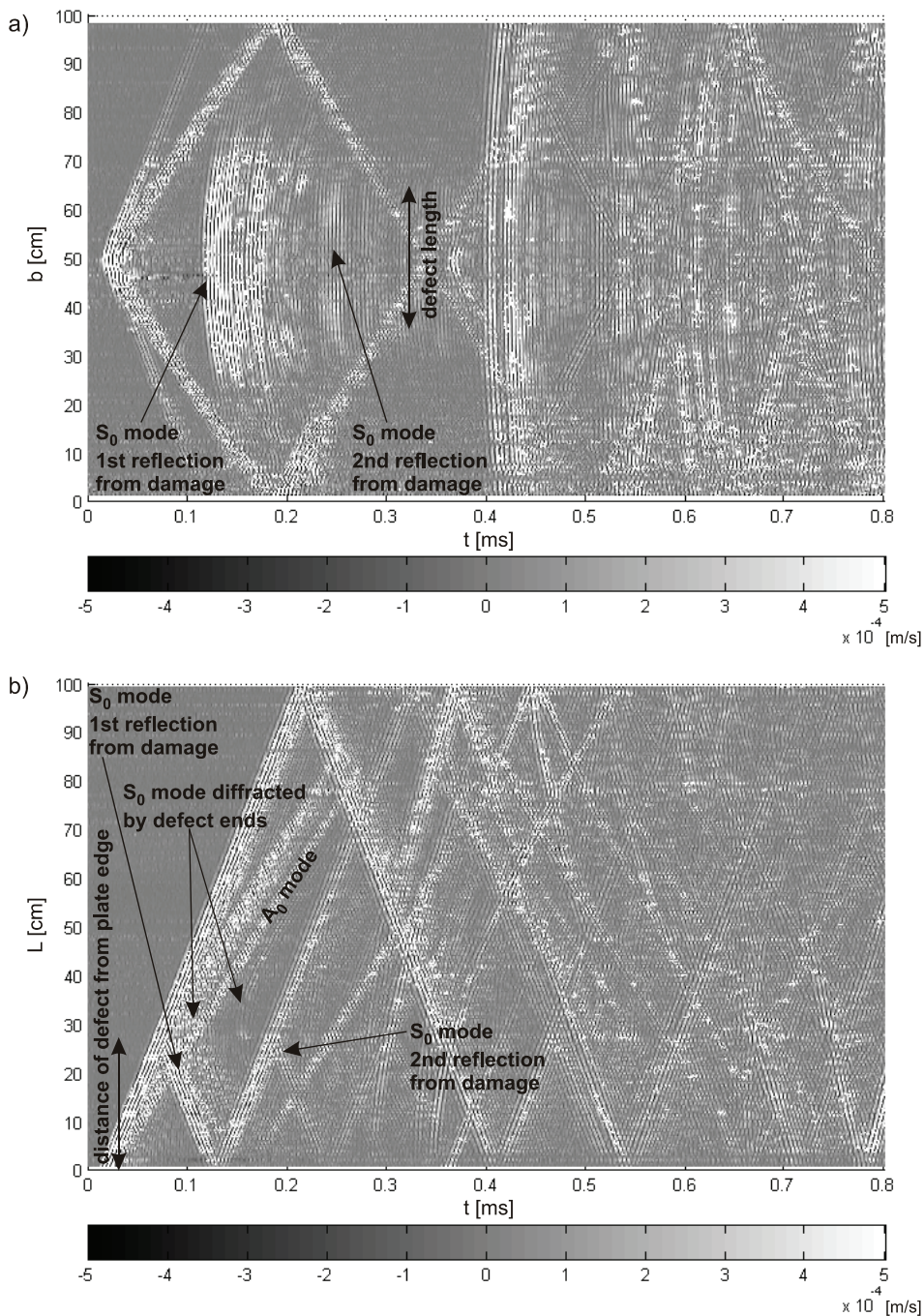


Fig. 6.14. B-scans of experimental in-plane waves in the plate with damage #1: a) line #1; b) line #2

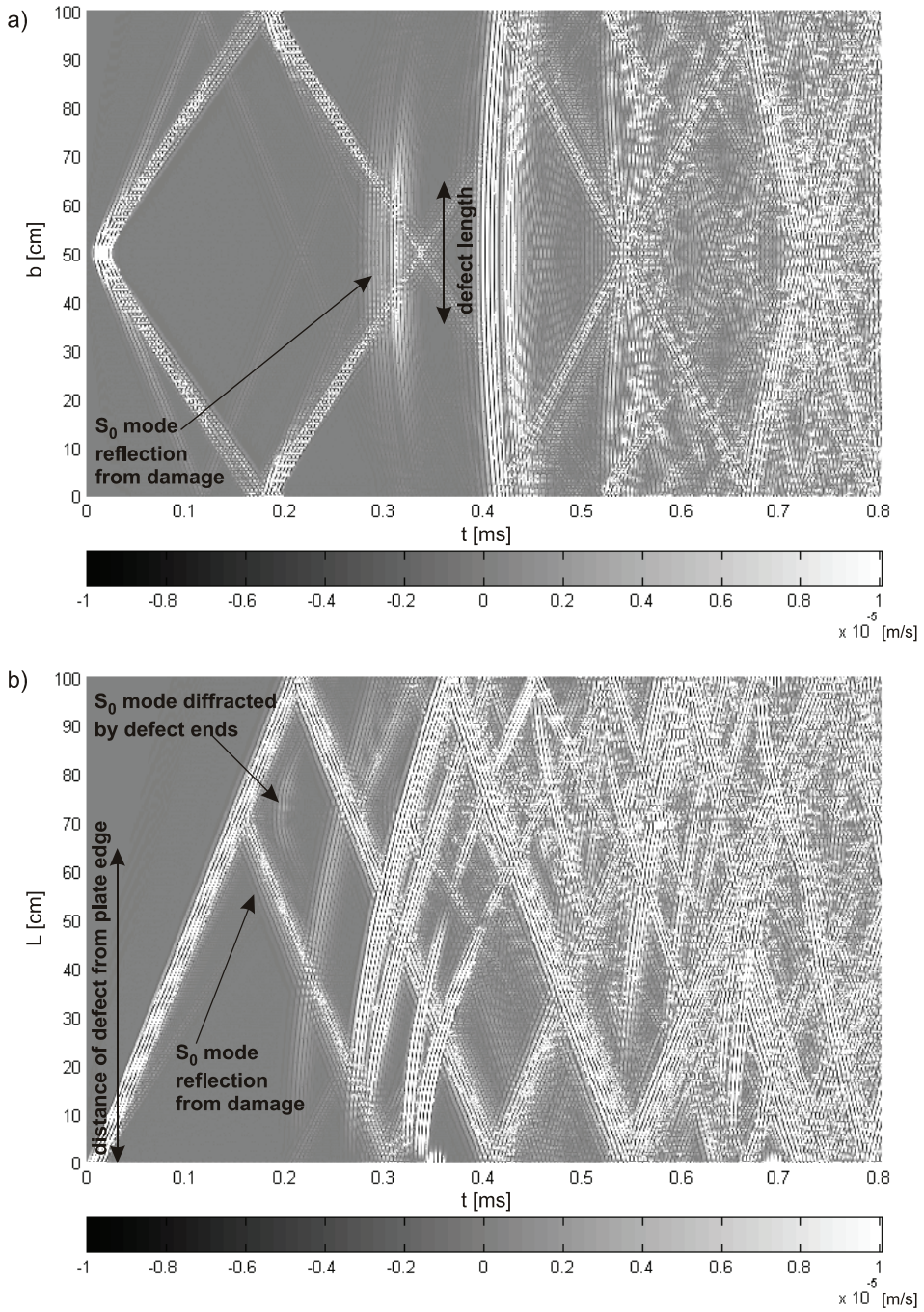


Fig. 6.15. B-scans of numerical in-plane waves in the plate with damage #2: a) line #1; b) line #2

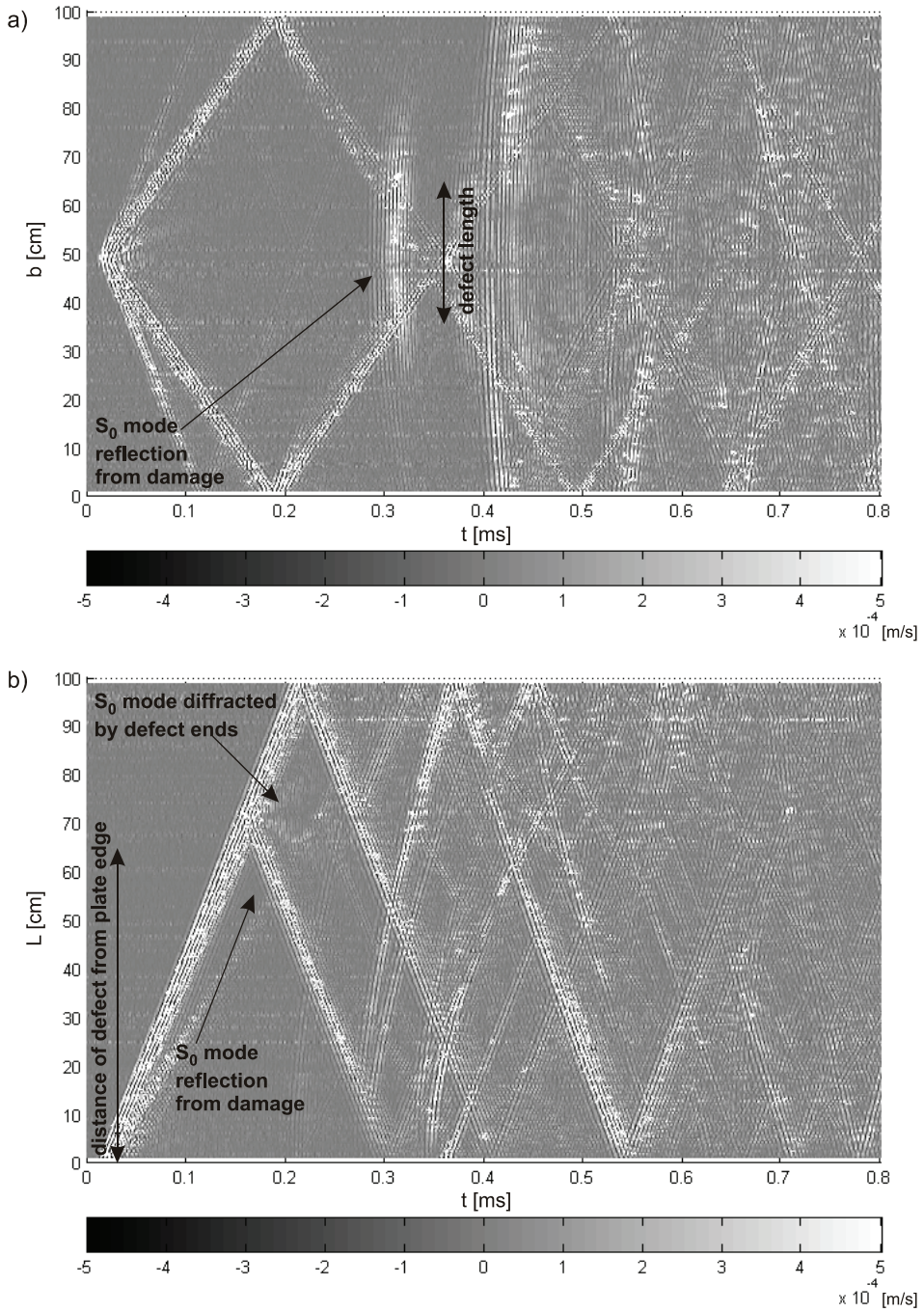


Fig. 6.16. B-scans of experimental in-plane waves in the plate with damage #2: a) line #1; b) line #2

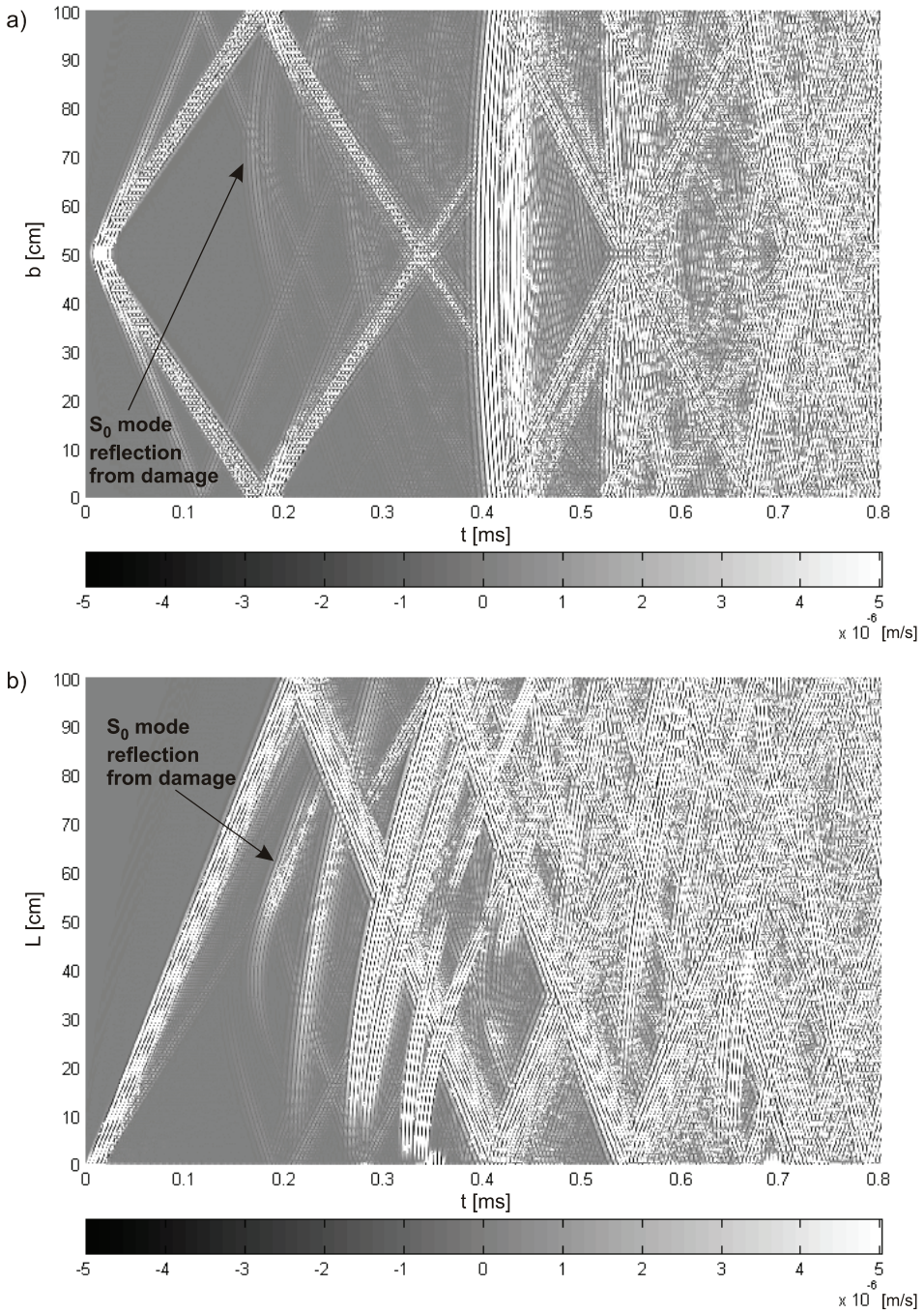


Fig. 6.17. B-scans of numerical in-plane waves in the plate with damage #3: a) line #1; b) line #2

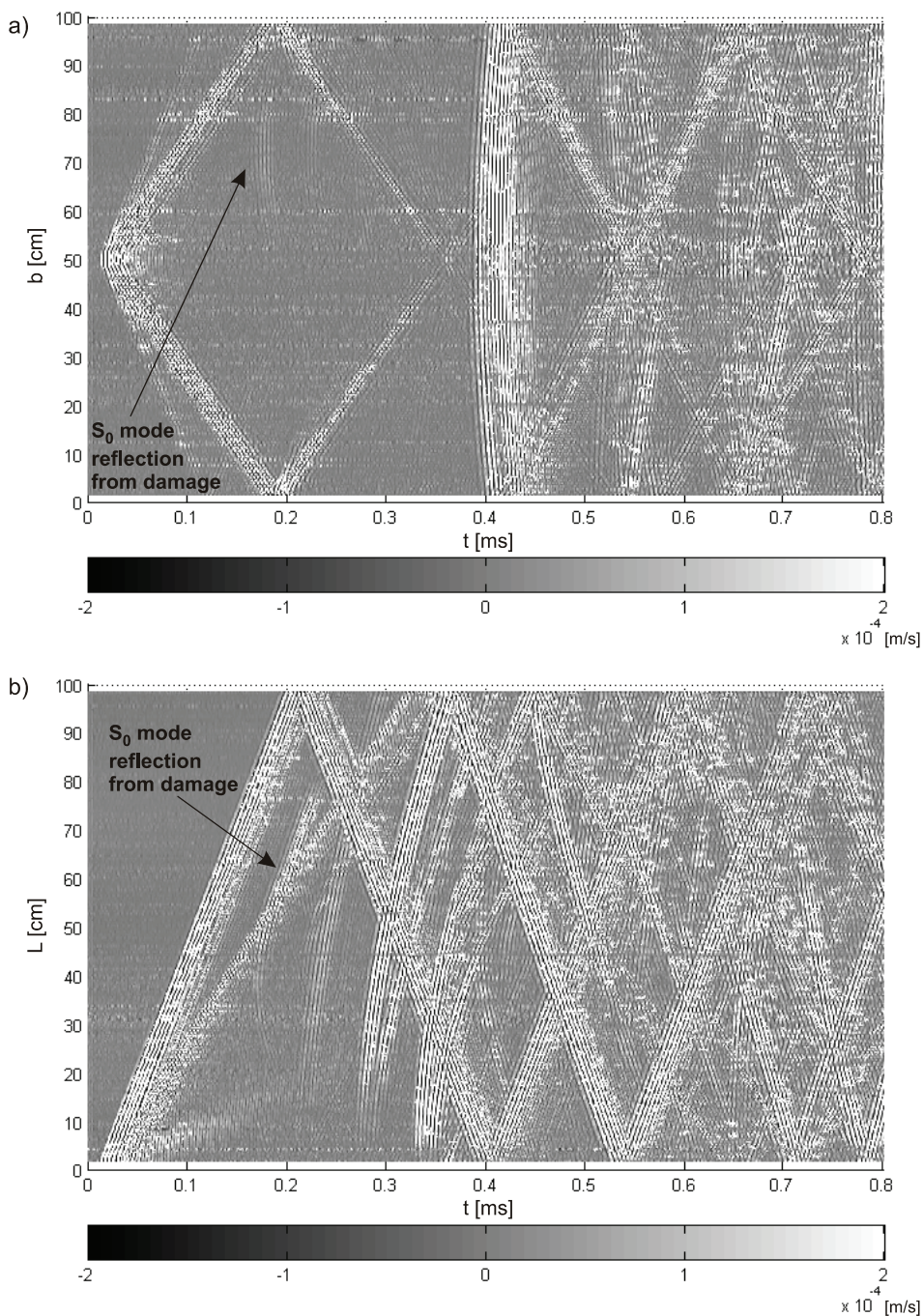


Fig. 6.18. B-scans of experimental in-plane waves in the plate with damage #3: a) line #1; b) line #2

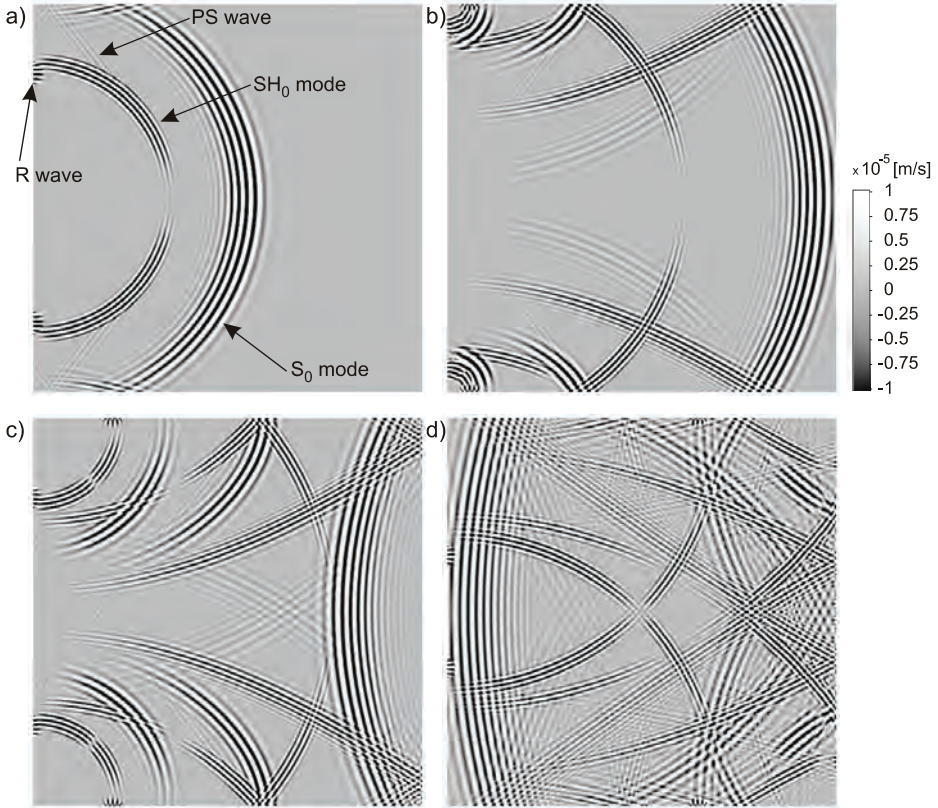


Fig. 6.19. C-scans of numerical in-plane waves in the pristine plate registered at selected time instants: a) $t = 0.12$ ms; b) $t = 0.2$ ms; c) $t = 0.25$ ms; d) $t = 0.4$ ms

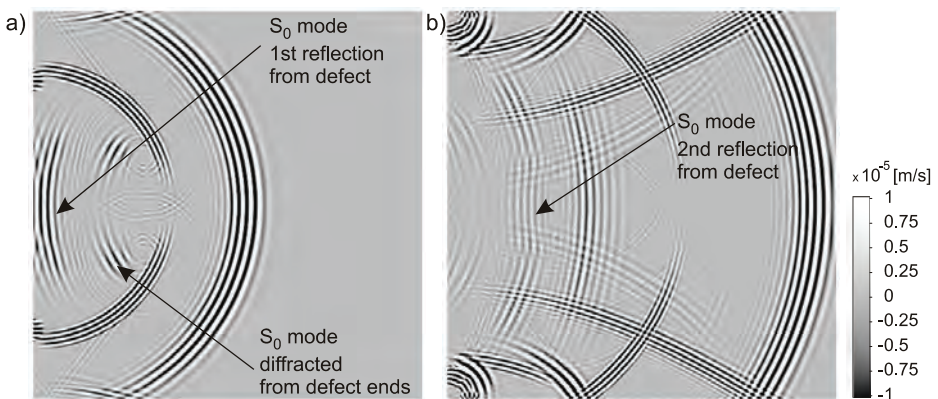


Fig. 6.20. C-scans of numerical in-plane waves in the plate with damage #1 registered at selected time instants: a) $t = 0.12$ ms; b) $t = 0.2$ ms

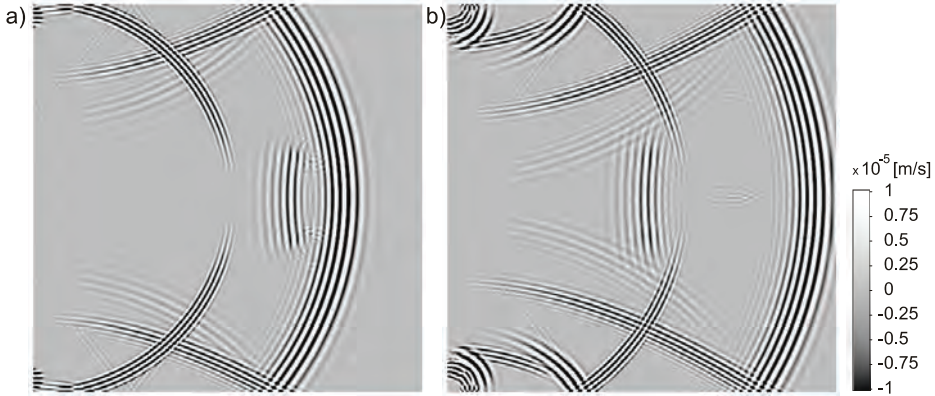


Fig. 6.21. C-scans of numerical in-plane waves in the plate with damage #2 registered at selected time instants: a) $t = 0.17$ ms; b) $t = 0.2$ ms

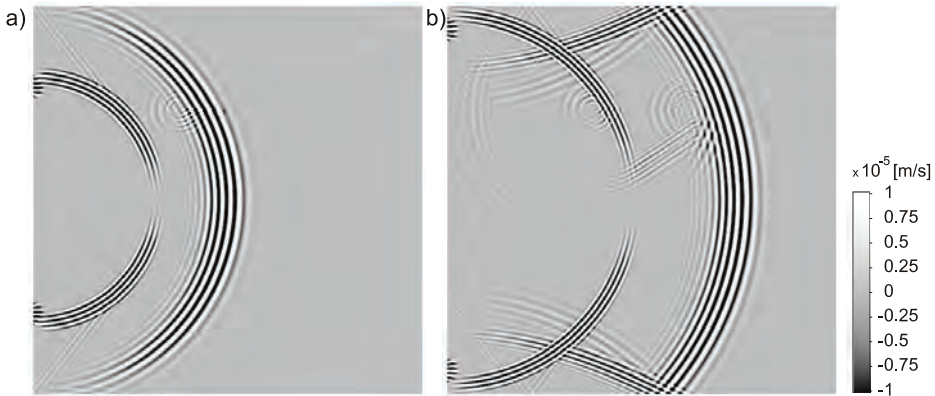


Fig. 6.22. C-scans of numerical in-plane waves in the plate with damage #3 registered at selected time instants: a) $t = 0.11$ ms; b) $t = 0.16$ ms

the plate edge results in propagation of cylindrical fronted S_0 and SH_0 modes, as indicated in Fig. 6.19. The straight-crested PS wave is the von Schmidt head wave, arising from the reflection of a grazing incidence P wave (Graff 1975). Moreover, the Rayleigh wave is visible. The R wave is not separated clearly from the SH wave due to the early stage of the wave development (Fig. 6.19a). Lamb wave interaction with defect #1 is shown in Fig. 6.20. The defect is indicated at position corresponding to its actual location. At time $t = 0.12$ ms (Fig. 6.20a) the S_0 mode 1st reflection from damage approaches the plate left edge. It is also visible, that the SH_0 mode after interaction with damage is converted into the S_0 mode, which is then diffracted by the defect ends. The second reflection of the S_0 mode from damage is visible at $t = 0.2$ ms (Fig. 6.20b). The C-scans for the plate with damage #2 are presented in Fig. 6.21. Based on the C-scan at $t = 0.17$ ms both position and extent of damage can be identified. Figure 6.22 shows the numerical results for the plate with damage #3. The C-scan at $t = 0.11$ ms shows interaction of the S_0 mode with damage. At the time instant $t = 0.16$ ms interaction of the S_0 and SH_0 mode with the defect is visible. Diffraction of waves on the defect ends indicates the defect length.

6.2. Flexural wave propagation in plate

6.2.1. Experimental setup

Two plate specimens were used in the experiments of propagation of flexural (out-of-plane) waves: the pristine plate and the plate with damage. The geometry and material properties of plates were the same as described in Section 6.1.1. The experimental setup (Fig. 6.23) consisted of the arbitrary function generator Tektronix AFG 3022, the amplifier

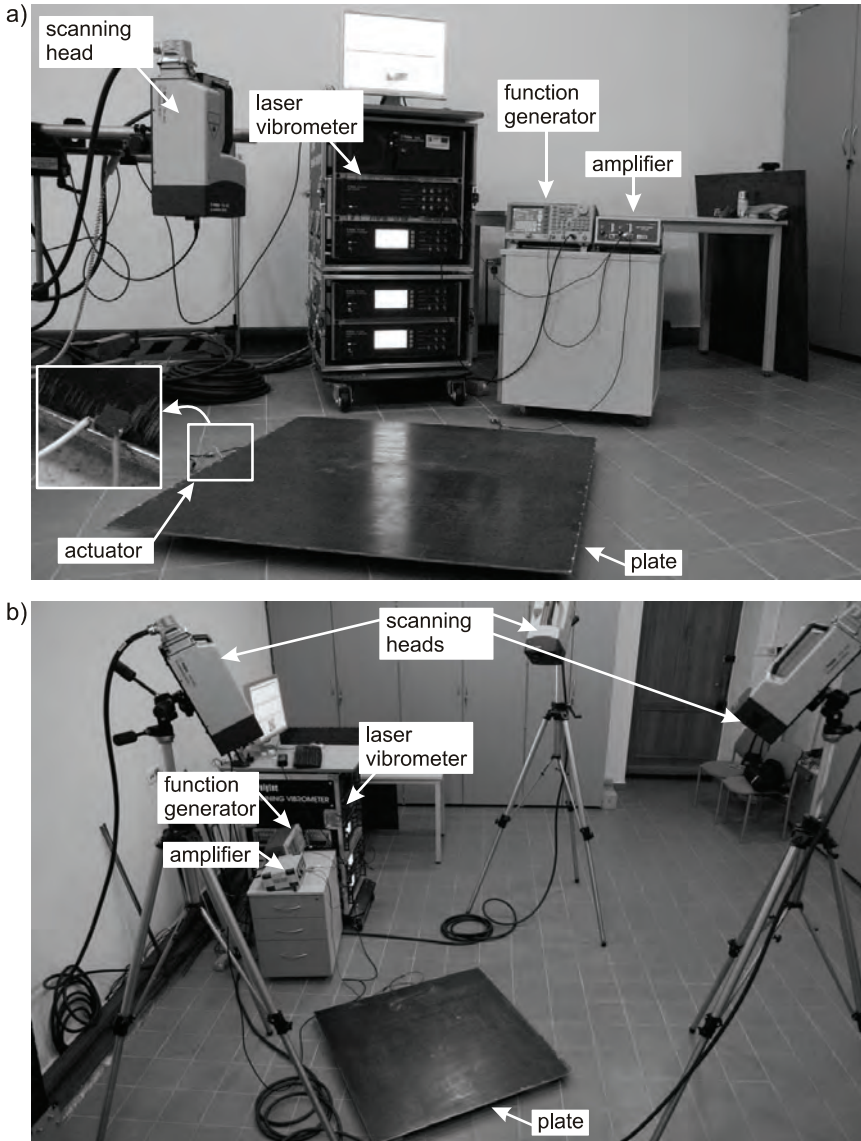


Fig. 6.23. Instrumentation for measurements of flexural waves in the steel plate: a) experiment #1 with the use of one scanning head; b) experiment #2 with the use of three scanning heads

EC Electronics PPA 2000 and the scanning laser vibrometer Polytec PSV-3D-400-M. A burst signal in the form of a five-peak sine of frequency of 200 kHz modulated with the Hanning window (Fig. 6.24) was applied to the actuator Noliac CMAP11 bonded at the plate surface, at $x = 0$, $y = 500$ mm (Fig. 6.23a), to excite flexural waves. The PZT actuator, utilizing the thickness-wise expansion effect, bonded to the plate surface, generated mainly the fundamental A_0 mode and the influence of the S_0 mode was insignificant. Velocity signals were averaged 500 times in the time domain to improve the signal-to-noise ratio.

Two instrumentation setups were considered. In the first experimental setup (experiment #1), velocity signals were registered by one scanning head of the vibrometer in 17 evenly distributed points along the edge of both the pristine and damaged plates (Fig. 6.23a). The scanning head was shifted along the specimen from one point to another to register out-of-plane velocity component perpendicular to the plate surface. In the second instrumentation setup (experiment #2), three scanning heads were used for measurements of the plate with damage. The velocity signals (out-of-plane velocity components) were measured in 161 points distributed along each of lines #1 and line #2 (Fig. 6.25). One plate with defect enabled analysis of three different locations of damage: damage #1 (Fig. 6.25b), damage #2 (Fig. 6.25c) and damage #3 (Fig. 6.25d). Finally, C-scans were performed. The plate was scanned in $65 \times 65 = 4225$ points (Fig. 6.26). During all tests with flexural wave propagation, signals were measured on the intact surface, i.e. defect was underside of the object during test.

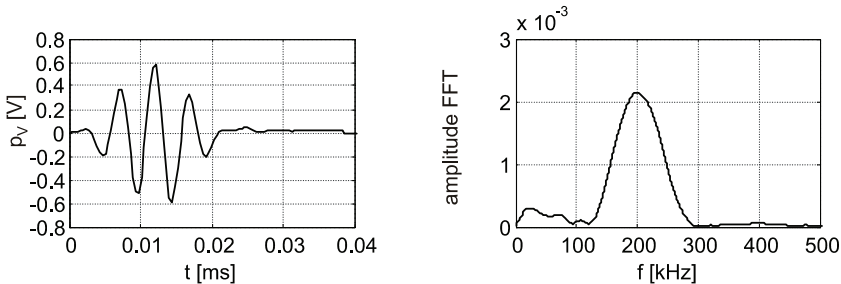


Fig. 6.24. A 200-kHz 5-count Hanning windowed burst in time and frequency domains

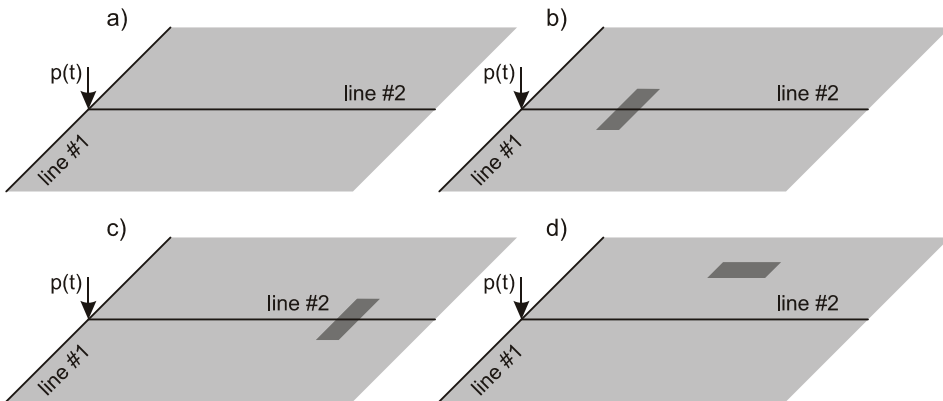


Fig. 6.25. Measurement lines for different damage location in the plate for flexural wave propagation: a) pristine plate; b) plate with damage #1; c) plate with damage #2; d) plate with damage #3

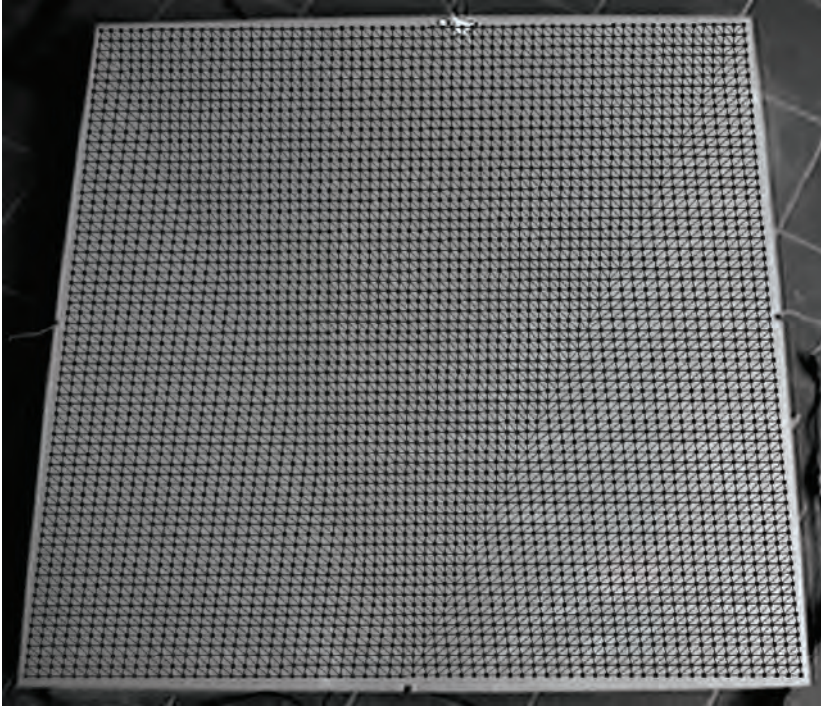


Fig. 6.26. Damaged plate with the indicated scanned area consisted of $65 \times 65 = 4225$ points

6.2.2. Dispersion curves

Group velocity dispersion curves were experimentally determined for the pristine plate. Velocity signals were measured on the plate surface, at position $x = 0$, $y = 500$ mm. The frequency of the wave packet was swept from 50 to 300 kHz in steps of 10 kHz. The examples of the registered signals are shown in Fig. 6.27 for frequencies 120, 200 and 250 kHz. In the experimental signal, the incident wave and two reflections of the A_0 mode are visible during 0.8 ms time period. The difference in the time-of-flight can be observed in the signals of frequency 120 kHz and 200 kHz, which indicates influence of dispersion. However, there is no significant difference in the time-of-flight in the signals of frequency 200 kHz and 250 kHz because this frequency range lies in the non-dispersive region.

The experimental flexural wave tuning for the pristine plate is shown in Fig. 6.28. The experimental results showed that a strong excitation of the A_0 mode was observed around the frequency range 200–250 kHz. The experimental and analytical dispersion curves for the considered 5 mm thick steel plate are given in Fig. 6.29. For the Mindlin plate theory, two flexural modes exist (A_0 and A_1 modes) and one shear horizontal mode (SH_2 mode). However, in the measured frequency range only the A_0 mode was observed. The parameter κ in the Mindlin theory was chosen to give the best fit to experimentally measured wave group velocity for the frequency range 50–300 kHz. It was determined by the method of least squares and its value was set as 0.94. Figure 6.29 shows that the Mindlin analytical dispersion curve for the A_0 mode agrees with the experimental results; moreover, it covers with the exact A_0 Lamb mode.

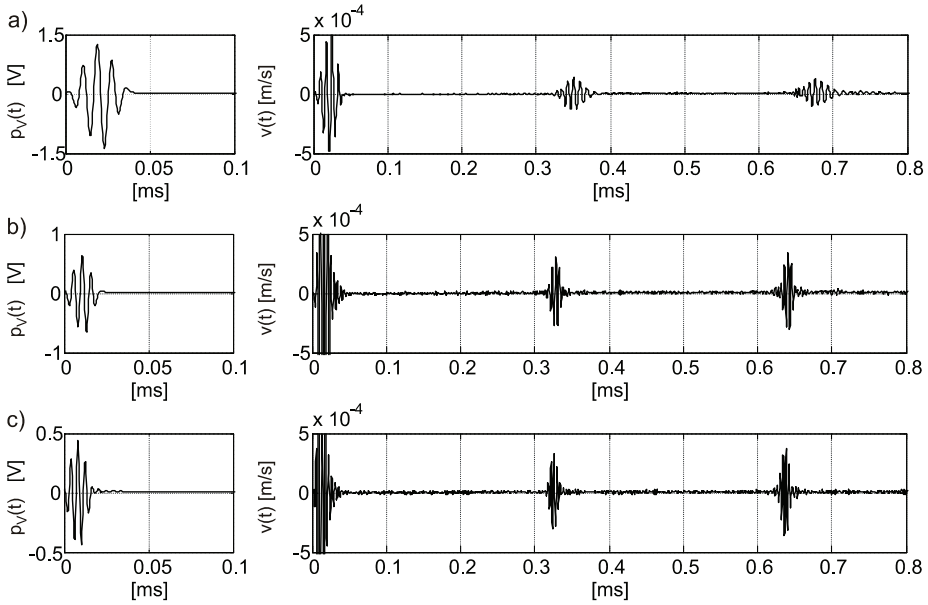


Fig. 6.27. Time history of experimentally measured flexural waves in the pristine plate for determination of dispersion curves: a) 120 kHz; b) 200 kHz; c) 250 kHz

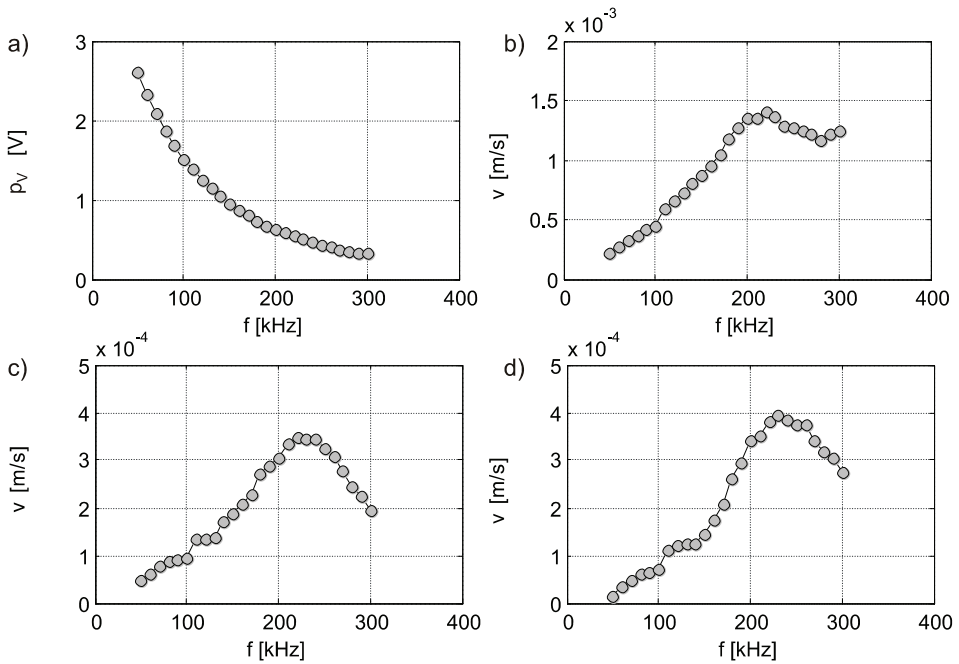


Fig. 6.28. Experimental flexural wave tuning in a pristine plate for frequency range 50–300 kHz: a) maximum value of excitation voltage signal; b) maximum value of incident wave in velocity signal; c) maximum value of first reflection in velocity signal; d) maximum value of second reflection in velocity signal

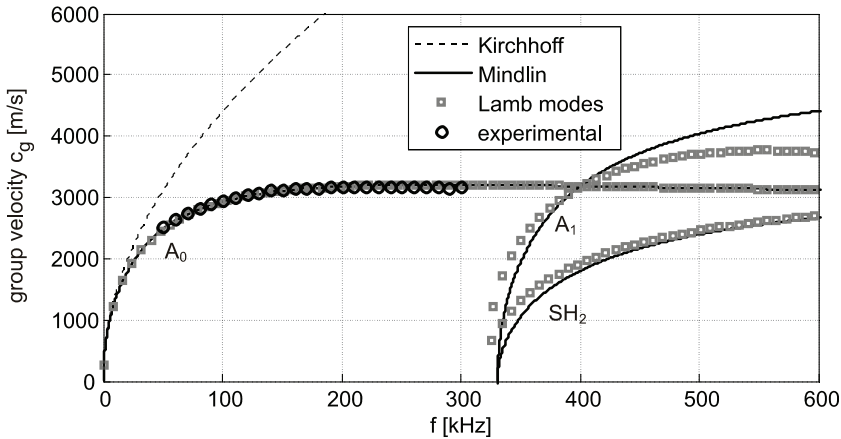


Fig. 6.29. Experimental and analytical dispersion relation for flexural waves for 5 mm steel plate

6.2.3. Numerical model

Modelling of flexural wave propagation in the plate was performed by the time domain spectral element method with the use of the Mindlin bending plate theory. The plate was meshed in the same way, as described in Section 6.1.3. For the highest excitation frequency used in numerical simulations (200 kHz) the applied mesh (80×80 2-D spectral finite elements, each element with $9 \times 9 = 81$ GLL nodes) guaranteed 8.5 nodes per the shortest wavelength.

6.2.4. Damage detection in plate by flexural waves

In experiment #1, velocity responses were measured in nodes 1 to 17 evenly distributed on the plate surface along line #1, shown in Fig. 6.25. The first example used the pristine plate. Figure 6.30 shows comparison of numerical and experimental time velocity signals (out-of-plane velocity components) in the time and spatial domains. The flexural wave (A_0 mode) propagates along the plate left vertical edge (linear wavefront visible in Fig. 6.30), as well as it propagates through the plate and reflects from the plate right vertical edge (circular wavefront depicted in Fig. 6.30).

For the plates with damage #1 and damage #2, additional circular wavefront appeared in the collected time signals in Fig. 6.31 and Fig. 6.32, respectively. In the case of plate with damage #1, the wavefront caused by the reflection from damage in the numerical signal occurred at the time instant equal to $t = 0.1728$ ms. The group velocity of the flexural wave was equal to 3176.62 m/s, therefore the identified damage position was 274 mm. Similarly, making use of the experimental signals, the position of the defect can be identified as 270 mm since time of the additional reflection was 0.173 ms and the group velocity was 3164.4 m/s. Considering the plate with damage #2, the reflection in the numerical signal occurred at the time instant equal to 0.4472 ms, and knowing the group velocity of the flexural wave, location of the defect can be identified as 710 mm. In the case of the experimental signal, reflection occurred at the time instant equal to 0.448 ms, therefore the identified position of damage was 709 mm.

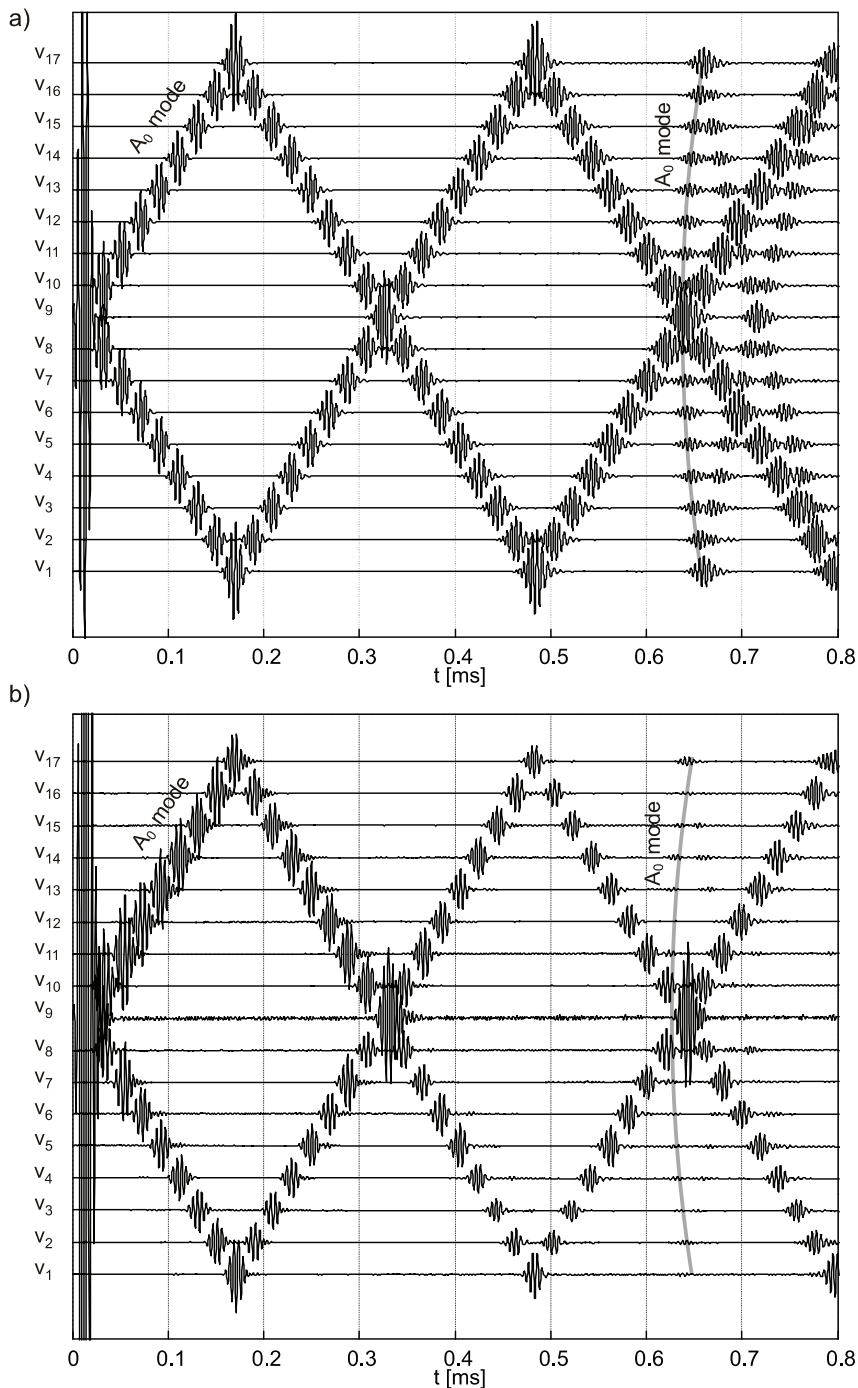


Fig. 6.30. Set of time signals collected at 17 points evenly distributed along line #1 during propagation of flexural wave of frequency 250 kHz in the pristine plate: a) spectral element method simulations based on the Mindlin theory; b) experimental results

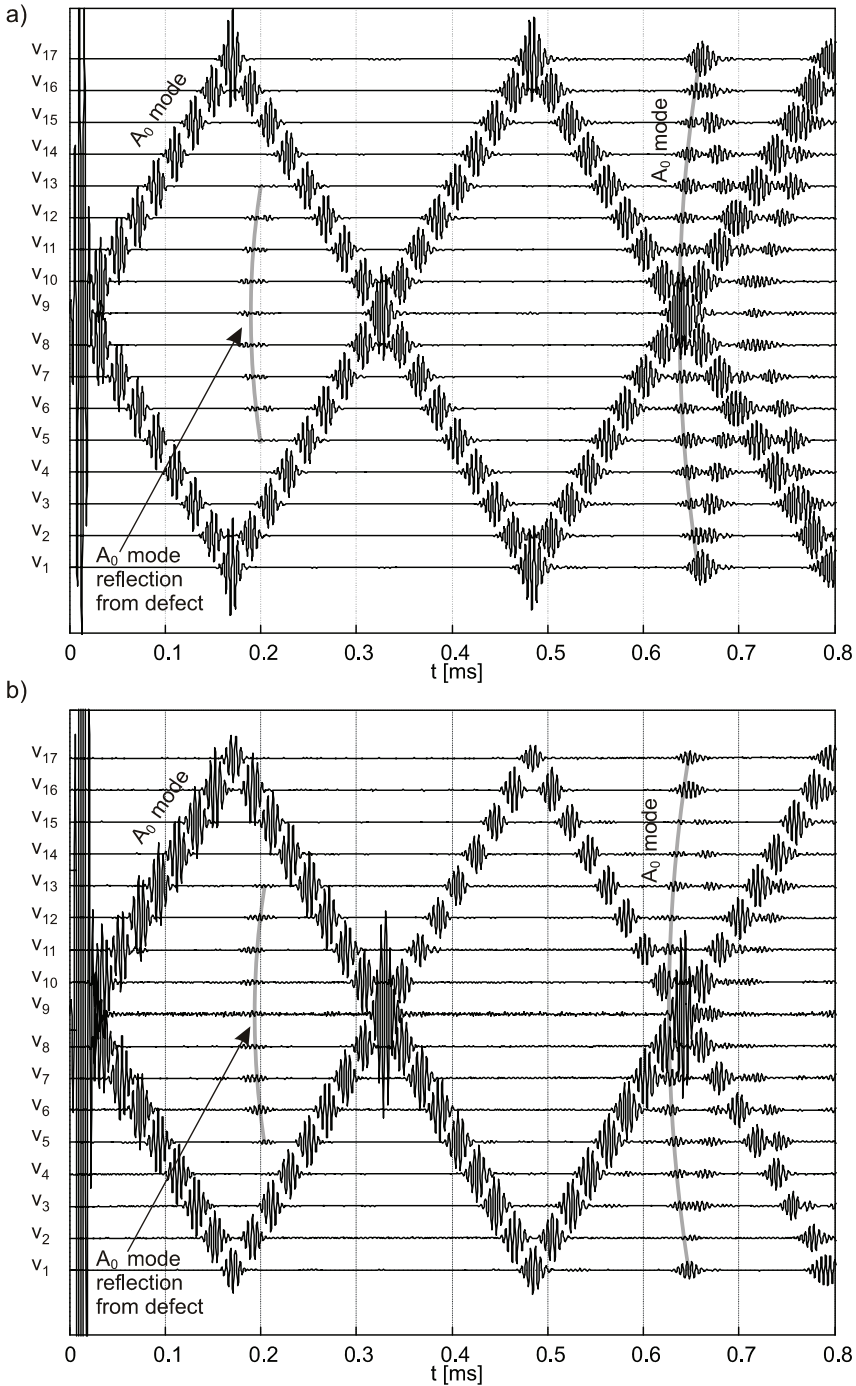


Fig. 6.31. Set of time signals collected at 17 points evenly distributed along line #1 during propagation of flexural wave of frequency 250 kHz in the plate with damage #1: a) spectral element method simulations based on the Mindlin theory; b) experimental results

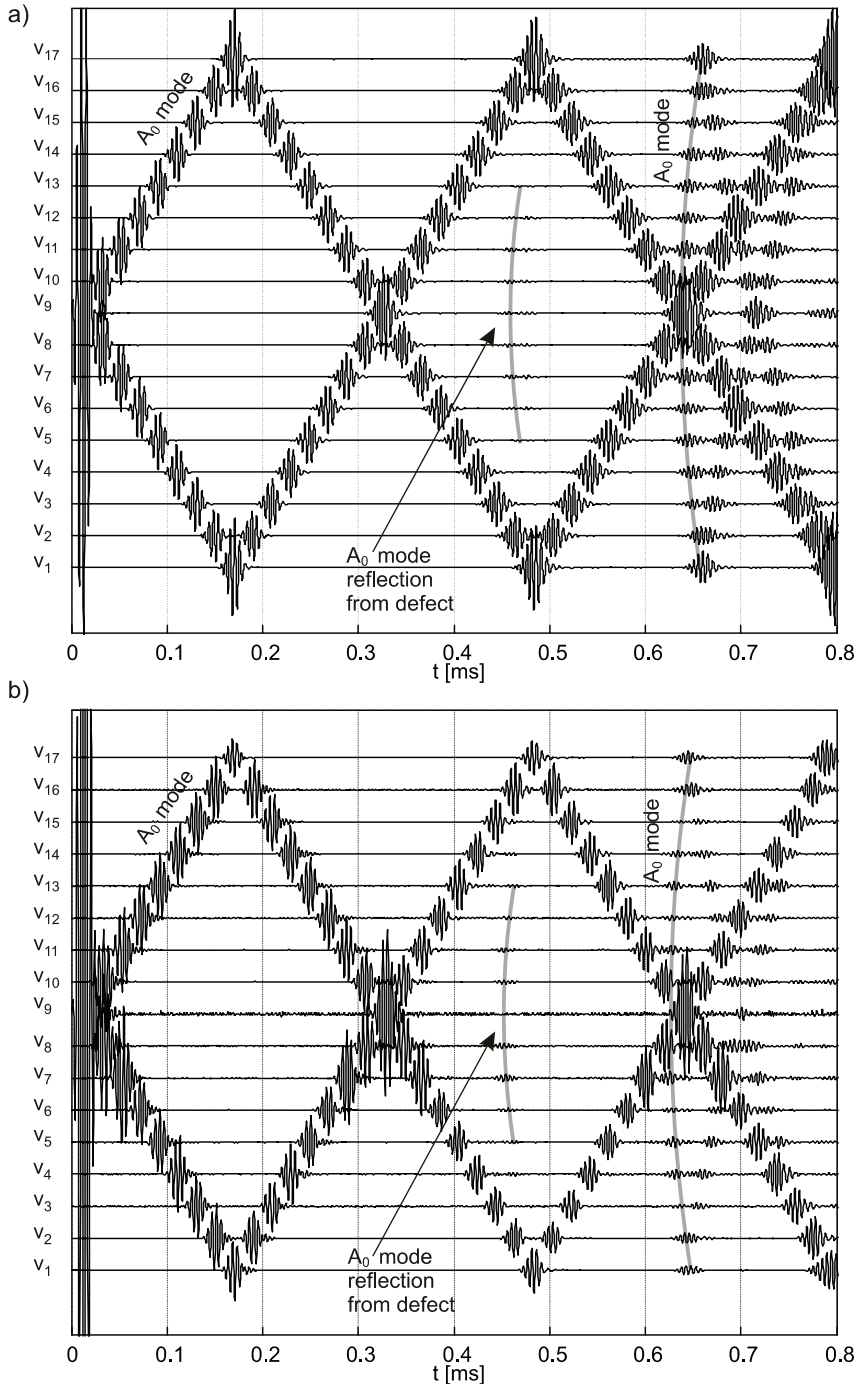


Fig. 6.32. Set of time signals collected at 17 points evenly distributed along line #1 during propagation of flexural wave of frequency 250 kHz in the plate with damage #2: a) spectral element method simulations based on the Mindlin theory; b) experimental results

In experiment #2, the B-scans were performed by measurements of time velocity signals in 161 evenly distributed points along each of lines #1 and #2 (Fig. 6.25), situated on the plate surface. The length of the lines was insignificantly shorter than the plate length and the line #1 was shifted from the left edge of the plate by about 2.5 cm. The measurements were performed for the plate with damage #1, #2 and #3. Numerical and experimental results in the form of the B-scans are shown in Fig. 6.33 to Fig. 6.39. In Fig. 6.33, the numerical results for the pristine plate are presented. The numerical and experimental B-scans for the plate with damage #1 are illustrated in Fig. 6.34 and Fig. 6.35, respectively. Figure 6.34a shows the numerical scan data for line #1. The additional wavefront appeared as a result of the A_0 mode reflection from damage and this plot provided information about the extent of the defect. The B-scan for line #2 (Fig. 6.34b) revealed the reflection of the A_0 mode from the defect, providing estimation of its position from the plate edge. In the experimental results, a small influence of the S_0 mode can be observed. The reflection of the A_0 mode from damage was preceded by the reflection of the S_0 mode (Fig. 6.35a). However, both localization and extent of damage can clearly be detect.

Figures 6.36 and 6.37 show the B-scans for the plate with damage #2 for the numerical and experimental data, respectively. The reflection of the A_0 mode in the B-scan along line #1 indicated the extent of damage, whereas the reflection of the A_0 mode in the B-scan along line #2 pointed its position with reference to the plate left edge. In the B-scans based on the experimental data, a small influence of the S_0 mode can be observed (Fig. 6.37).

The numerical and experimental B-scans for the plate with defect #3 are illustrated in Fig. 6.38 and Fig. 6.39. In the B-scan along line #1 based on the numerical signals, the reflection from defect is visible. Moreover, in the wavefront of the A_0 mode reflected from the right vertical edge, the influence of damage can be observed as a local decrease in the signal amplitude, as a result of passing the wavefront through the long “crack” (Fig. 6.38a). Analysing experimental signals (Fig. 6.39a), the area of signals with decreased amplitude is clearly visible, but the reflection of the A_0 mode is hardly visible. The B-scans along the line #2 (Fig. 6.38b, Fig. 6.39b) show the influence of damage in an insignificant range.

The last test in experiment #2 concerned performing C-scans based on numerical and experimental signals. The comparison of the numerical and experimental results for the plate with damage #1 is given in Fig. 6.40, at the selected time instants. At the first time instant, $t = 0.11$ ms, the A_0 mode interaction with damage is visible. The C-scan at the next time instant, $t = 0.15$ ms, reveals both reflected and diffracted waves, and finally at $t = 0.23$ ms, the wave reflected from damage can be observed after reflection from the left vertical plate edge. In the C-scans based on the experimental measurements, the reflection from damage can also be observed, but observation of smaller amplitude diffracted waves is impossible due to excessive noise. The C-scans for the plate with damage #2 are presented in Fig. 6.41. At time $t = 0.26$ ms the interaction of the A_0 mode with the defect occurs, and at the consecutive time instants the wave reflected from damage come back to the plate edge. Both the numerical and experimental scans made the identification of damage position and its size possible. Figure 6.42 shows the numerical results for the plate with damage #3. At time $t = 0.17$ ms, the A_0 mode interacts with the left end of damage, resulting in the additional reflection. The interaction of propagating wave with the right end of the defect can be observed at $t = 0.26$ ms. The C-scan based on the numerical time signals enables to detect the position and the extent of the defect. In the experimental C-scans, no reflection from damage can be observed because the influence of measurement noise is larger than the influence of the reflection from defect.

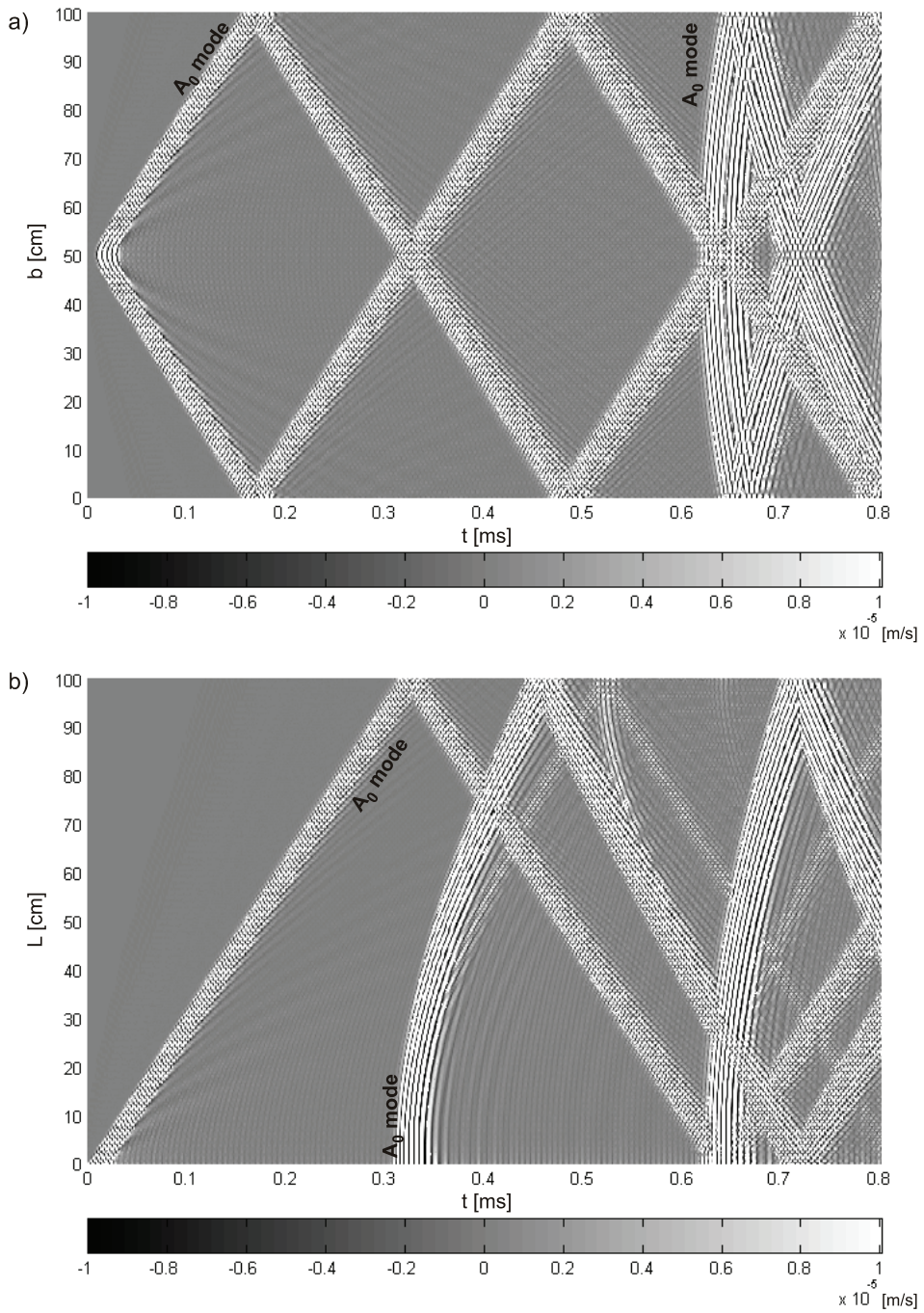


Fig. 6.33. B-scans of numerical flexural waves in the pristine plate: a) line #1; b) line #2

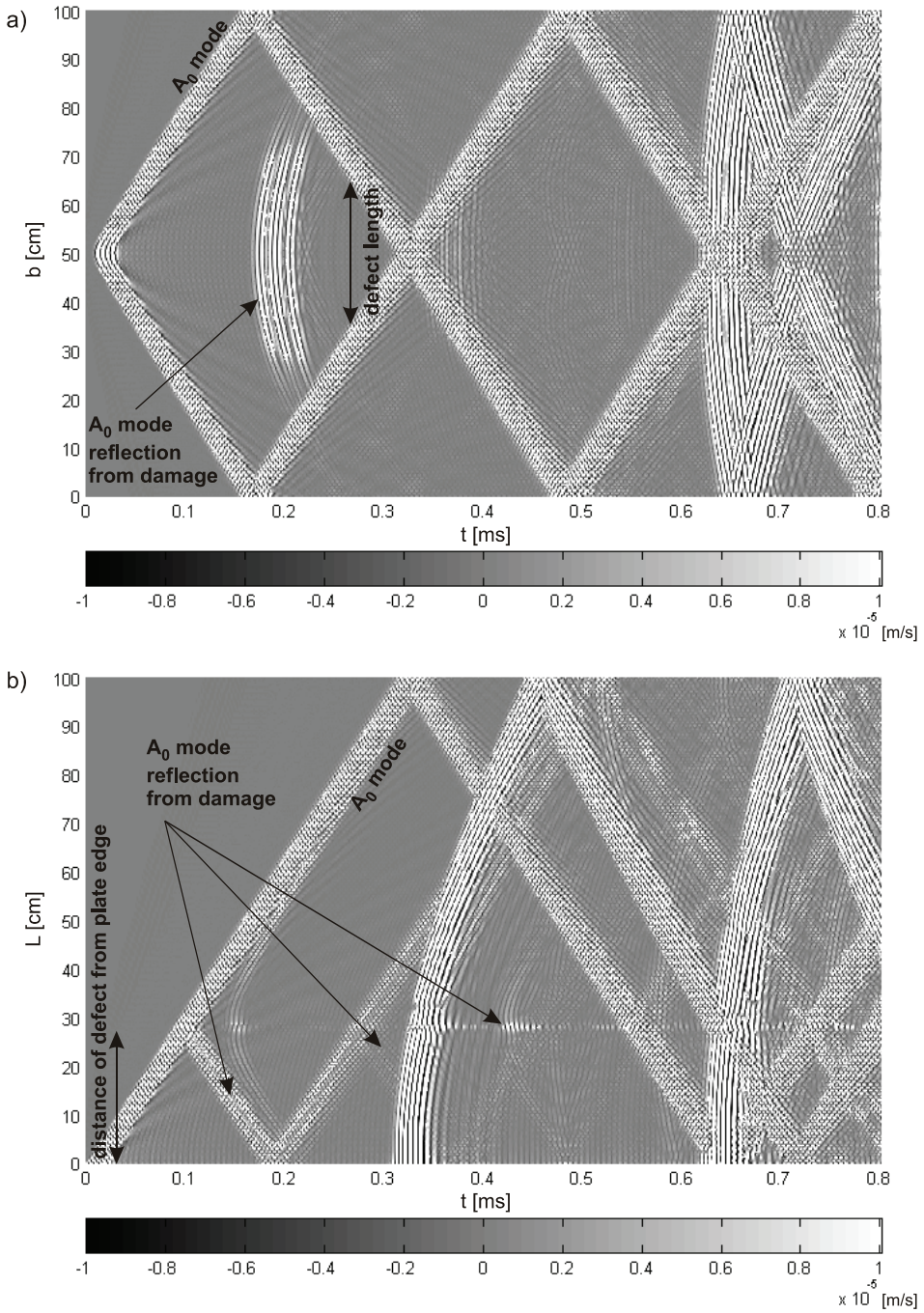


Fig. 6.34. B-scans of numerical flexural waves in the plate with damage #1: a) line #1; b) line #2

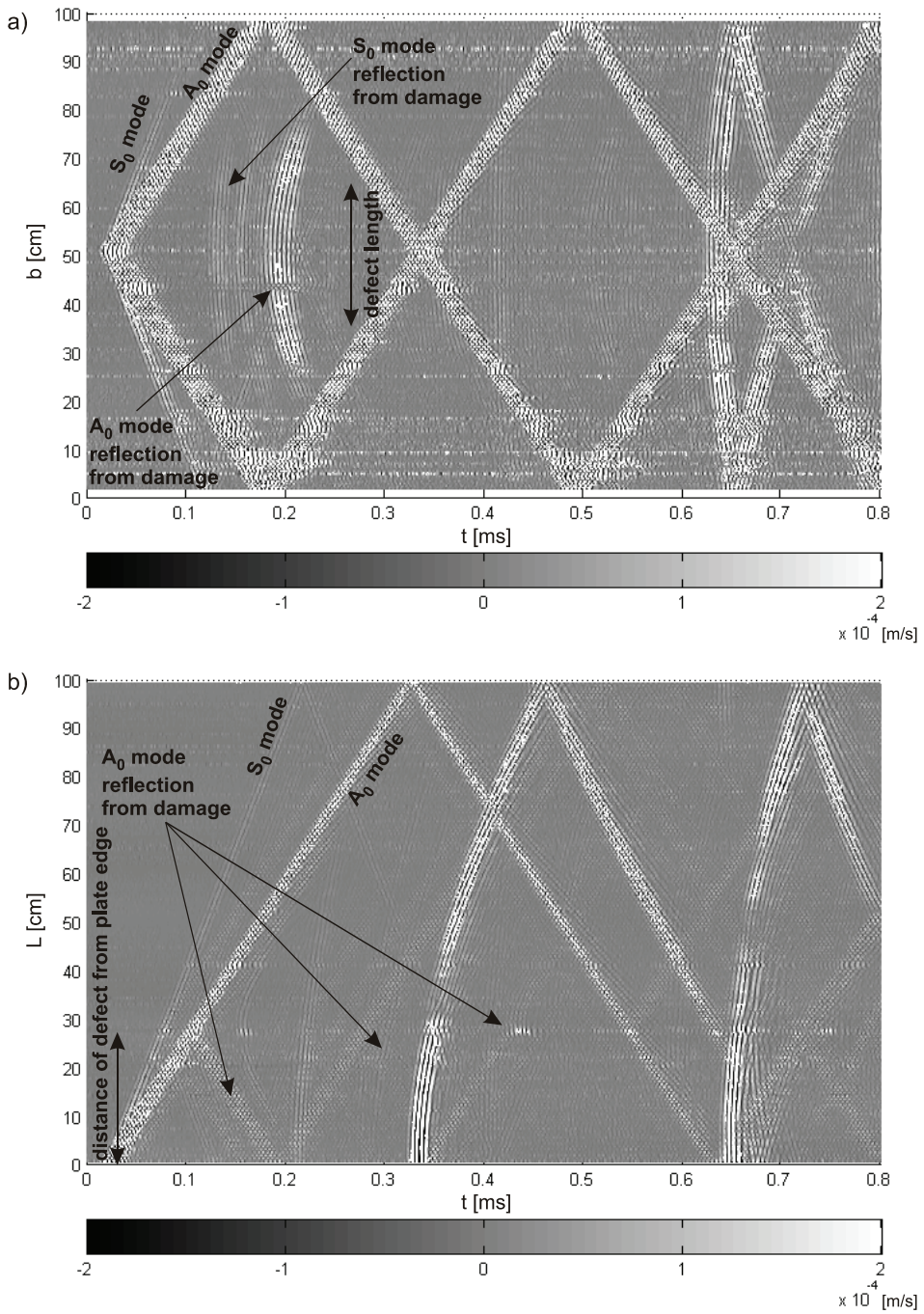


Fig. 6.35. B-scans of experimental flexural waves in the plate with damage #1: a) line #1; b) line #2

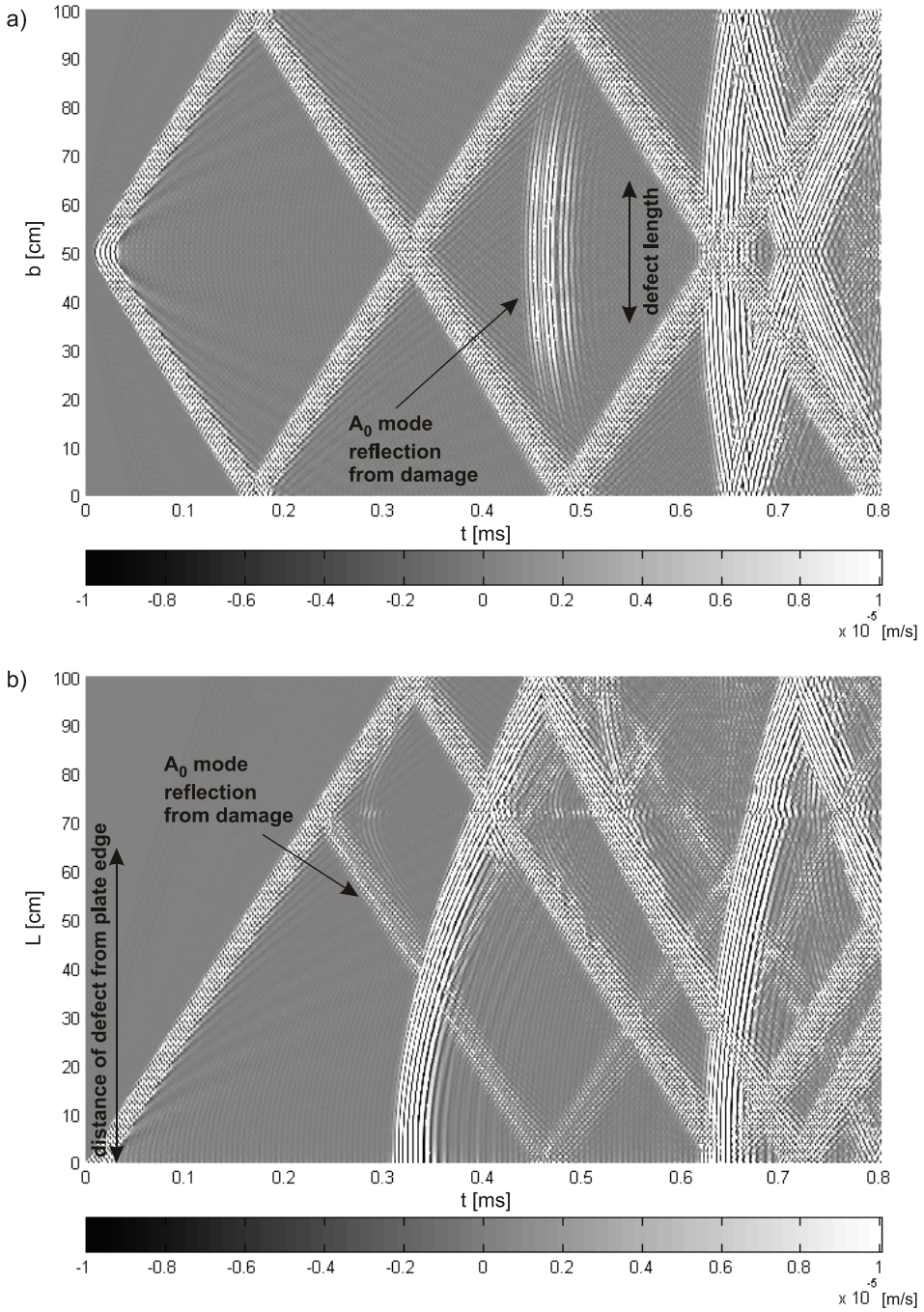


Fig. 6.36. B-scans of numerical flexural waves in the plate with damage #2: a) line #1; b) line #2

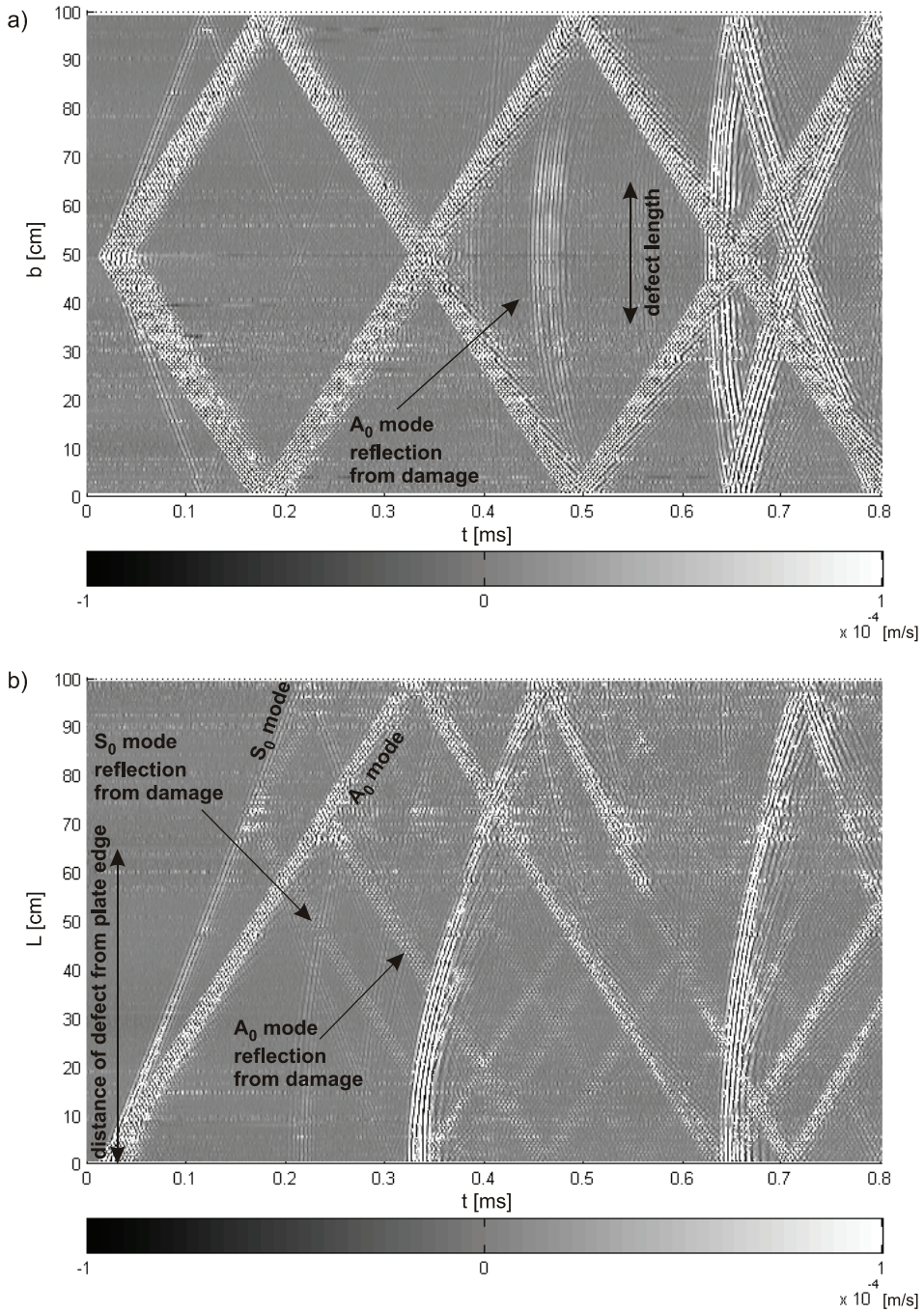


Fig. 6.37. B-scans of experimental flexural waves in the plate with damage #2: a) line #1; b) line #2

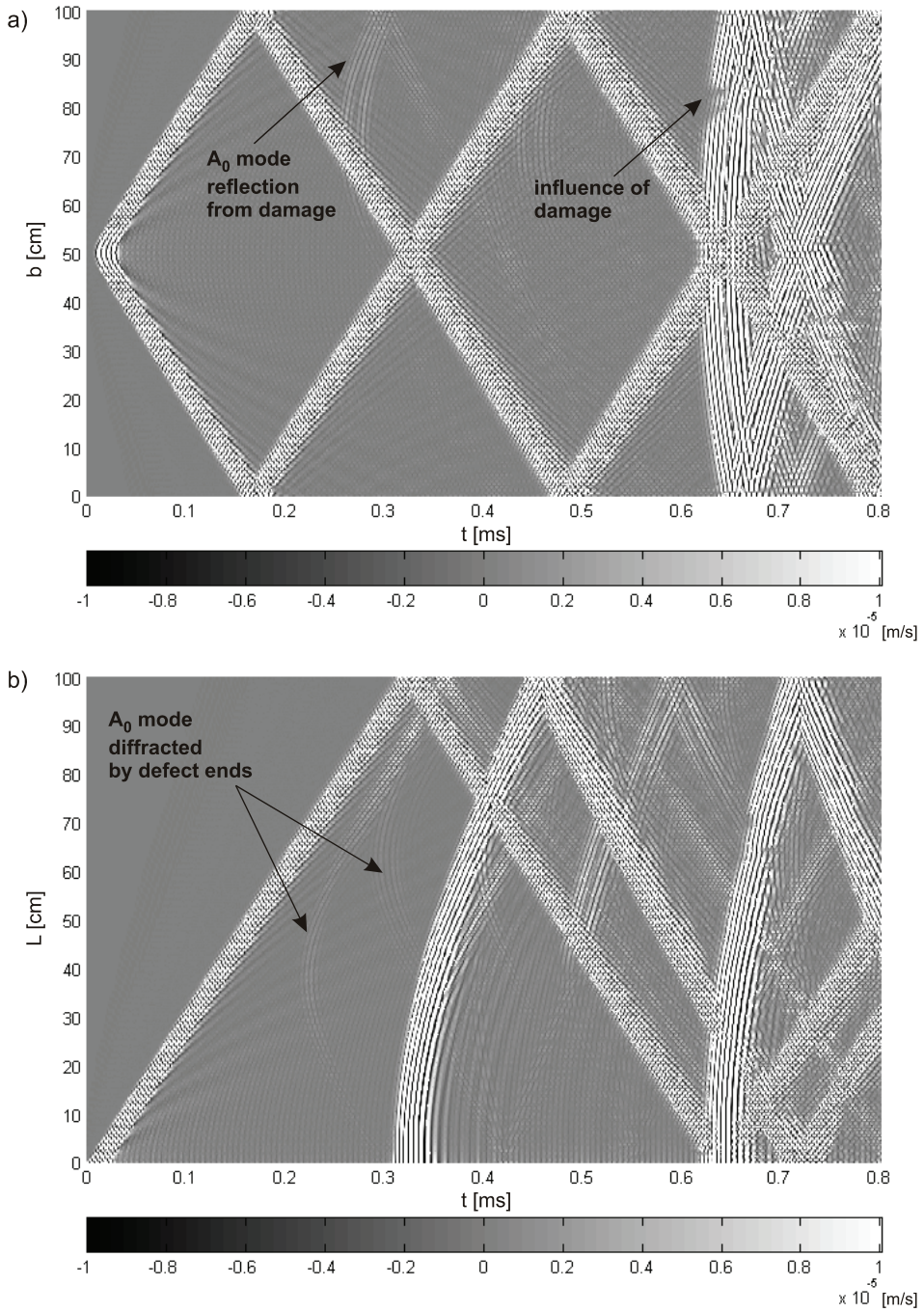


Fig. 6.38. B-scans of numerical flexural waves in the plate with damage #3: a) line #1; b) line #2

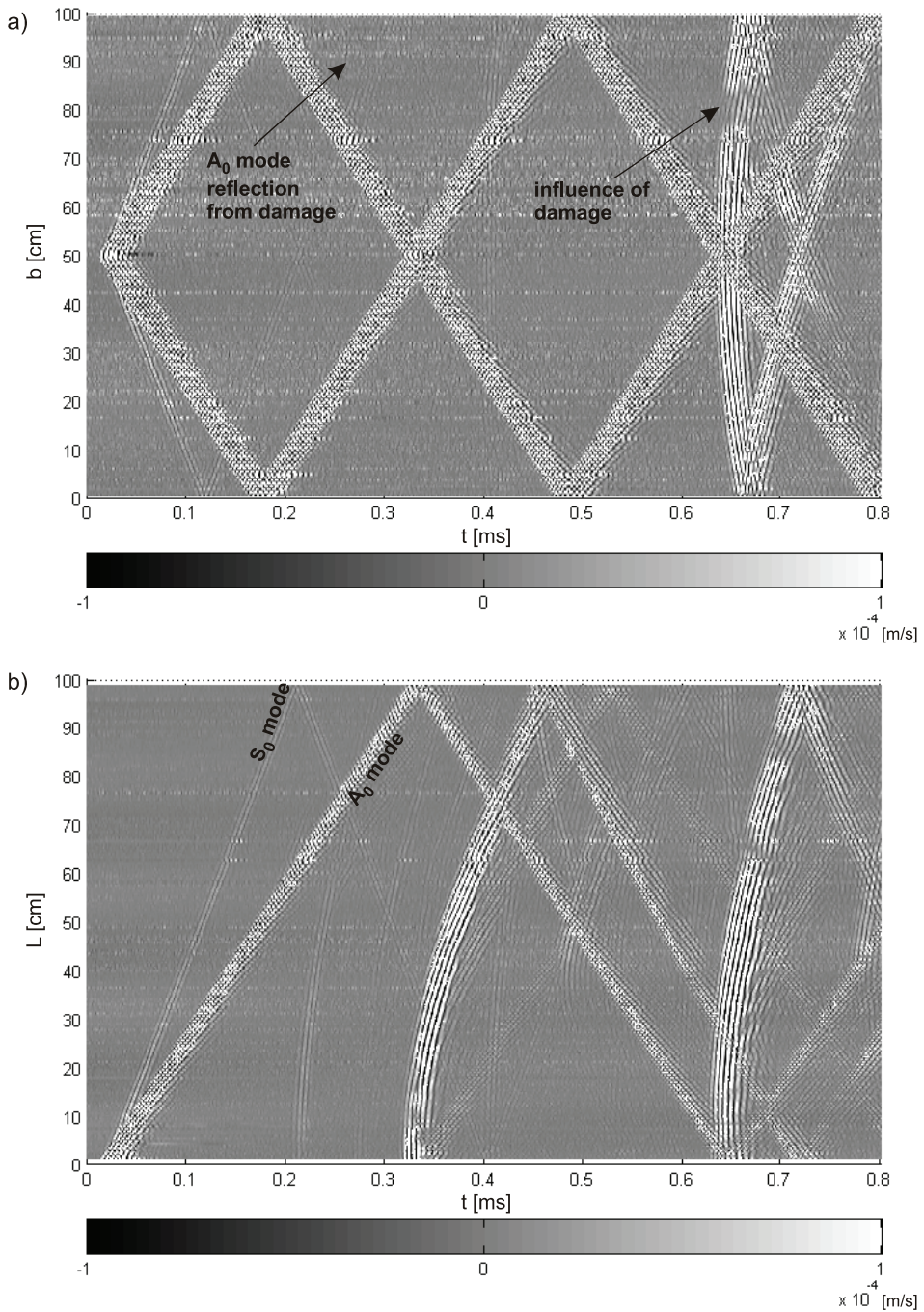


Fig. 6.39. B-scans of experimental flexural waves in the plate with damage #3: a) line #1; b) line #2

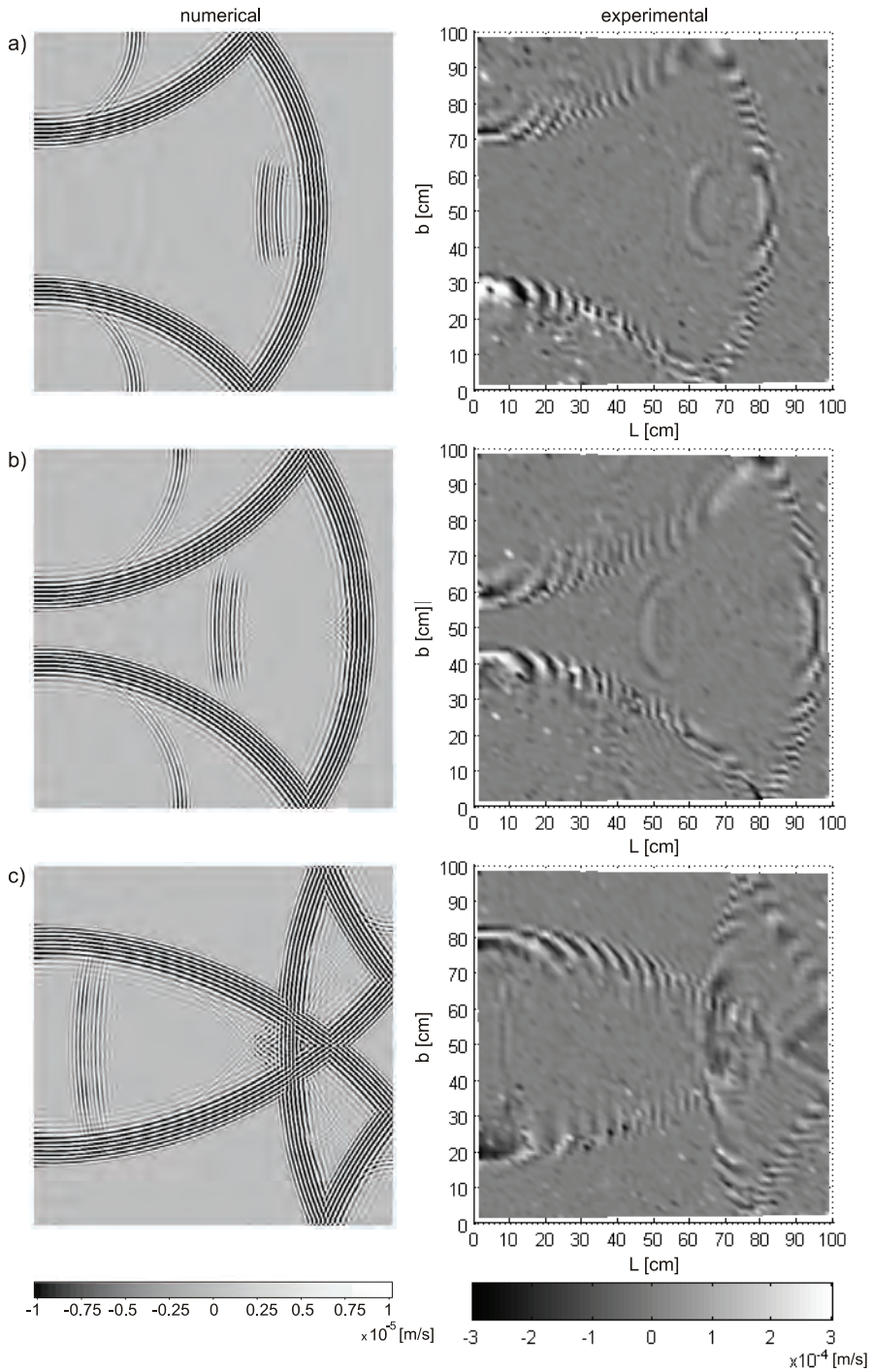


Fig. 6.41. Comparison of experimental and numerical C-scans of flexural wave propagation data in the plate with damage #2: a) $t = 0.26$ ms; b) $t = 0.30$ ms; c) $t = 0.42$ ms

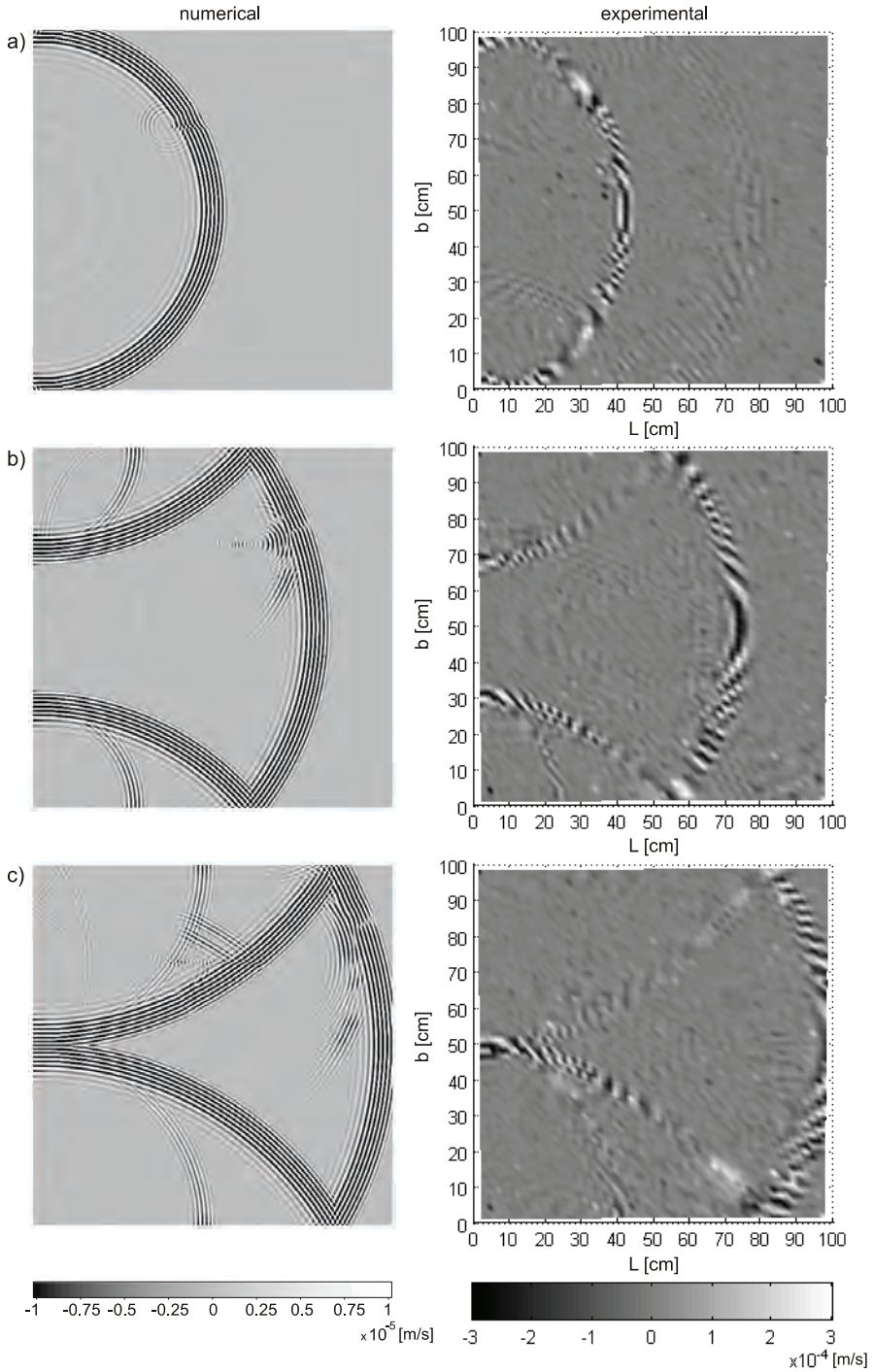


Fig. 6.42. Comparison of experimental and numerical C-scans of flexural wave propagation data in the plate with damage #3: a) $t = 0.17$ ms; b) $t = 0.26$ ms; c) $t = 0.32$ ms

6.3. Summary and conclusions

In this chapter, numerical and experimental studies of Lamb wave propagation in the steel plate have been presented. Detection of damage in the form of rectangular surface notch has been considered by analysing velocity signals in the form of A-scans, B-scans and C-scans. The interaction of Lamb waves with the defect located at three different positions and two different angles has been investigated.

The numerical analyses were performed by the spectral element method based on higher order theories: the Kane-Mindlin plate theory for in-plane waves and the Mindlin plate theory for flexural waves. The higher order Kane-Mindlin and Mindlin theories provided a very accurate description of dispersive behaviour of the first mode of longitudinal and flexural waves, which was proved by the comparison with the experimentally measured signals. The approximate Kane-Mindlin and Mindlin theories were valid over the frequency range of interest in the performed experimental investigations.

In the presented numerical and experimental examples, both symmetric and antisymmetric Lamb modes were excited by a single actuator. A single point excitation located on the plate edge results in weak wave directivity, i.e. a wave propagates in all directions through a half-plane and along the plate edge. Therefore, information obtained by the pulse-echo method cannot provide an angle at which a defect is located. To overcome this problem, measurements along selected lines containing the excitation point were conducted. In such a way from single time-traces (A-scans), time-space maps (B-scans) can be performed. Two lines perpendicular to each other, along which the B-scans were performed, enabled identification of the distance of the defect from the plate edge, as well as estimation of the defect extent for both in-plane and flexural waves. In the experimental results, some influence of another mode (the A_0 mode in the case of excitation of the S_0 mode, and the S_0 in the case of excitation of the A_0 mode) was observed. However, defect identification was still possible. In the case of damage situated perpendicularly to the plate edge, the axial waves appeared that were more sensitive to such direction of the defect. Monitoring of structure responses along selected lines appeared to be a good solution for damage detection in plates.

A further improvement of guided wave-based damage localization presented in this chapter was obtained by a C-scan method, which provided a two-dimensional plane view at the selected time instants. The numerical C-scans showed the interaction of both in-plane and flexural waves with defects and enabled precise damage localisation. However, the experimental measurements, performed for the flexural waves, were successful only for defects situated parallel to the plate edge. Damage detection in the plate with the defect perpendicular to the plate edge based on the C-scan was impossible because the influence of measurement noise was larger than the influence of the reflection from the defect.

Chapter 7

FINAL REMARKS

The presented study has been devoted to a computational method for wave propagation modelling and an application of ultrasonic guided waves to damage detection and localization. A special attention has been paid to modelling of dispersion effects and the experimental verification of developed numerical models.

The first part of the study describes elastic wave propagation in structural elements. Several models of rods, beams and plates have been derived. Since damage detection should be based on a single wave propagation mode, an effort has been made on the development of an approximate description of wave motions providing the first mode behaviour compatible with exact Lamb modes. The necessity of using higher order theories (the Mindlin-Herrmann theory for rods, the Timoshenko theory for beams, the Kane-Mindlin theory for extensional plates and the Mindlin theory for bending plates) when analysing ultrasonic frequency ranges has been demonstrated. It has been found that the approximated higher order theories can adequately account for dispersive behaviour of the lowest symmetric and antisymmetric modes over substantial range of frequencies.

In the next part of the work, the spectral element method has been described. The time domain spectral element method combines the generality and the geometrical flexibility of the standard finite element method with the accuracy of spectral methods. In this study, the spatial discretization is based on high-degree Legendre interpolants spread over Gauss-Legendre-Lobatto nodes and the spatial integration is performed using the Gauss-Legendre-Lobatto quadrature. Such numerical strategy provides the exponential accuracy and a reduction of the computational cost because a mass matrix becomes exactly diagonal by construction as a result of the Gauss-Lobatto-Legendre integration rule. In the presented study, a systematic construction of the numerical Legendre spectral element models for the considered higher order theories for rods, beams, frames, as well as extensional and bending plates has been carried out.

A substantial part of the work contains experimental and numerical analyses of wave propagation in bars, frames and plates. As an excitation, a sinusoidal wave packet modulated by the Hanning window has been chosen to concentrate input energy. In the experimental investigations, structural elements have been excited by means of the PZT actuator and the propagating wave signals have been detected and recorded by the scanning laser vibrometer. For each tested structure, the experimental wave tuning has been performed, which allowed to identify the optimal frequency range of excitation. The experimental dispersion curves have been obtained for the considered frequency range 50–300 kHz to determine adjustable parameters for the approximate theories applied in the numerical models.

Numerical simulations of wave propagation have shown that the spectral element method appears to be more effective than the finite element method with regard to the required number of nodes per wavelength and better efficiency towards numerical dispersion. For the established number of nodes per wavelength, numerical dispersion due to spatial discretization is higher for elements with smaller number of GLL nodes. Numerical simulations conducted for longitudinal waves in a simple bar have indicated, that application of

one multi-node spectral element per bar guarantees the smallest number of nodes per wavelength, but in such case, the numerical time integration scheme using a conditionally stable algorithm (here the central difference method) requires very small time step. The application of a few spectral elements per bar causes an increase of the number of nodes per wavelength. However, the critical time step is larger than for the case of one spectral element per bar. Therefore, the spectral element with about 7 to 21 GLL nodes can be regarded as a compromise between the spectral accuracy and the relatively large time step. The effectiveness of the proposed spectral element models has been experimentally confirmed. The model based on the Mindlin-Herrmann rod and Timoshenko beam theories guarantees reasonable approximation for the S_0 and A_0 modes behaviour, which has been proved by the comparison with the experimentally measured signals. Similarly, the Kane-Mindlin theory for extensional plate waves and the Mindlin theory for flexural plate waves provide a very accurate description of dispersive behaviour of the first mode of longitudinal and flexural waves. Therefore, the numerical model of an arbitrary frame or plate structure intended as a part of the structural health monitoring system should be described in the SEM formulation based on the higher order theories to obtain proper times of reflections from potential damage.

In the presented study, detection of damage in various forms of discontinuity of cross-section and material has been considered by analysing wave speeds and reflection times in the recorded response signals. For the bar and frame structures, damage has been simulated as the rectangular notch, the grooved weld and the additional mass. For the plate, the rectangular surface defect has been obtained by a one-sided reduction of the plate thickness. In the performed experimental examples, both S_0 and A_0 modes have been excited by a single actuator. Detection of damage has been considered by analysing velocity data in the form of A-scans, B-scans and C-scans. Making use of the A-scan, damage detection in the bars has been unambiguous, when the response signal was measured at the start point (i.e. at the point at which the actuator was bonded). The experimental investigations have shown that for considered bars with structural discontinuities both longitudinal and flexural waves can detect the defect in the form of the notch of 16.7% depth of the bar height, as well as the defect in the form of the additional mass. However, in the case of "small damage", simulated through the grooved weld, the longitudinal waves appeared to be more sensitive than the flexural waves in damage detection. Therefore, the application of flexural waves to damage detection can be enhanced through the response measurements in a few points and the analysis of the time-position plane (B-scan). As a result of such test, the interaction of waves with boundaries or potential discontinuities may be observed more precisely.

The next group of experimental and numerical examples for damage detection have been plane frames, namely the L-frame, the T-frame and the portal frame. During wave propagation in frames, a mode conversion is observed. An incident wave of one type, after reaching a junction generates propagation and reflection of waves of other types, which causes damage detection to be more difficult than for a simple bar. Damage in the form of a single or doubled notch has been introduced at an arbitrary frame member. The results of experimental and numerical analyses have led to the conclusion, that the SHM system designed for the L-frame structure can be equipped with a single actuator and a single measurement point (at the same place as the actuator) since detection of damage using the flexural incident wave has been possible for an arbitrary damage position. In the case of the T-frame, two actuators and two measurement points have been required to unambiguous damage localization in the whole T-frame. Two actuators should be mounted at the same

place, i.e. at the end of two collinear bars and the points of measurements of response signals should be at the same position as the actuators. The actuators should operate interchangeably. One actuator should excite and measure the longitudinal waves, while the second actuator should excite and measure the flexural waves. The idea of monitoring of the portal frame is similar as for the L-frame. For diagnostic purposes it is not possible to excite a wave packet solely in one point. To monitor the whole portal frame two actuators should be mounted at the base of both columns and two measurement points should be at the same positions as the actuators. One actuator and one measurement point have enabled condition monitoring of the whole column and half of the horizontal beam. Both longitudinal and flexural waves can be used; however, in the performed experiments longitudinal waves have appeared to be more sensitive for the considered defects.

For the plates, the interaction of Lamb waves with the defect located at three different positions and two different angles has been investigated. Both S_0 and A_0 modes represented in the form of B-scans have been able to detect defects situated parallel to the plate edge. However, in the case of damage situated perpendicularly to the plate edge, the S_0 mode has appeared more sensitive to such direction of the defect than the A_0 mode. The monitoring of selected lines has appeared to be a good solution for damage detection in plates. An improvement of guided wave-based damage location has been obtained by C-scans. The numerical C-scans have shown the interaction of both S_0 and A_0 modes with defects and have enabled excellent damage localisation. However, the experimental measurements, performed for the flexural waves, have been successful only for defects situated parallel to the plate edge. Damage detection in the plate with the defect perpendicular to the plate edge based on the C-scan has been impossible because the influence of measurement noise has been larger than the influence of the reflection from the defect.

The presented researches are continued within the confines of the grant of the European Union and Polish Ministry of Science and Higher Education no. POIG.01.01.02-10-106/09-00 (2010–2013). They are focused on the analysis of wave propagation in concrete structures. The main challenge is to design the SHM system based on ultrasonic waves for the real concrete structure that can handle all the complication included with material, geometry and environmental conditions.

ACKNOWLEDGEMENTS

I would like to express sincere gratitude to Prof. Jacek Chróścielewski and Prof. Krzysztof Wilde for their unwavering support, constant encouragement and valuable comments.

I am thankful to Prof. Wojciech Gilewski and Prof. Tomasz Mikulski for very thorough reviews of the manuscript and constructive suggestions that have substantially improved my work.

Words of thanks are directed to Dr Wojciech Witkowski for the help in some pre- and post-processing of numerical data. I am also indebted to Mr. Krzysztof Genc and Mr. Tomasz Rutkowski for their help in preparing experimental models. The final English language correction was made by Ms. Anna Kucharska-Raczunas.

This work was partially supported by grant no. POIG 01.01.02-10-106/09-00.

REFERENCES

- [1] Achenbach J. D.: *Wave Propagation in Elastic Solids*. Amsterdam: North-Holland Publishing Company 1975.
- [2] Adams D. E.: *Health Monitoring of Structural Materials and Components. Methods with applications*. Chichester: John Wiley & Sons 2007.
- [3] Alleyne D. N., Cawley P.: The interaction of Lamb waves with defects. *IEEE Transaction on Ultrasonics, Ferroelectrics, and Frequency Control* 39, 1992, 381–397.
- [4] Atkins K. J., Hunter S. C.: The propagation of longitudinal elastic waves around right-angled corners in rods of square cross section. *The Quarterly Journal of Mechanics and Applied Mathematics* 28, 1975, 245–260.
- [5] Babuška I., Suri M.: The p - and h - p versions of the finite element method, an overview. *Computer Methods in Applied Mechanics and Engineering* 80, 1990, 5–26.
- [6] Bartoli I., Lanza di Scalea F., Fateh M., Viola E.: Modeling guided wave propagation with application to the long-range defect detection in railroad tracks. *NDT&E International* 38, 2005, 325–334.
- [7] Bathe K. J.: *Finite Element Procedures*. Upper Saddle River, New Jersey: Prentice Hall 1996.
- [8] Beccu R., Wu C. M., Lundberg B.: Reflection and transmission of the energy of transient elastic extensional waves in a bent bar. *Journal of Sound and Vibration* 191, 1996, 261–27.
- [9] Benmeddour F., Grondel S., Assaad J., Moulin E.: Study of the fundamental Lamb modes interaction with symmetrical notches. *NDT&E International* 41, 2008a, 1–9.
- [10] Benmeddour F., Grondel S., Assaad J., Moulin E.: Study of the fundamental Lamb modes interaction with asymmetrical discontinuities. *NDT&E International* 41, 2008b, 330–340.
- [11] Boyd J. P.: *Chebyshev and Fourier Spectral Methods*, 2nd ed. Mineola, New York: Dover Publications 2000.
- [12] Brunarski L., Runkiewicz L.: *Podstawy i przykłady stosowania metod nieniszczących w badaniach konstrukcji z betonu*. Warszawa: Wydawnictwa ITB 1983.
- [13] Campion S. D., Jarvis J. L.: An investigation of the implementation of the p -version finite element method. *Finite Elements in Analysis and Design* 23, 1996, 1–21.
- [14] Canuto C., Hussaini M. Y., Quarteroni A., Zang T. A.: *Spectral Methods in Fluid Dynamics*. Berlin Heidelberg: Springer-Verlag 1998.
- [15] Cawley P., Alleyne D.: The use of Lamb waves for the long range inspection of large structures. *Ultrasonics* 34, 1996, 287–290.
- [16] Cegla F. B., Rohde A., Veid M.: Analytical prediction and experimental measurement for mode conversion and scattering of plate waves at non-symmetric circular bind holes in isotropic plates. *Wave Motion* 45, 2008, 162–177.
- [17] Chakraborty A., Gopalakrishnan S.: A spectrally formulated plate element for wave propagation analysis in anisotropic material. *Computer Methods in Applied Mechanics and Engineering* 194, 2005, 4425–4446.
- [18] Chakraborty A., Gopalakrishnan S.: A spectral finite element model for wave propagation analysis in laminated composite plate. *Journal of Vibration and Acoustics, Trans. ASME* 128, 2006, 477–488.
- [19] Chakraborty A., Mahapatra D. R., Gopalakrishnan S.: Finite element analysis of free vibration and wave propagation in asymmetric composite beams with structural discontinuities. *Composite Structures* 55, 2002, 23–36.
- [20] Chang Z., Mal A.: Scattering of Lamb waves from a rivet hole with edge cracks. *Mechanics of Materials* 31, 1999, 197–204.
- [21] Chopra A. K.: *Dynamics of Structures*. Upper Saddle River, New Jersey: Prentice Hall 2001.

- [22] Chróścielewski J., Rucka M., Wilde K., Witkowski W.: Formulation of spectral truss element for guided waves damage detection in spatial steel trusses. *Archives of Civil Engineering* 55, 2009, 43–63.
- [23] Chróścielewski J., Rucka M., Wilde K., Witkowski W.: Zastosowanie metody elementów spektralnych do modelowania zjawisk propagacji fal sprężystych dla celów diagnostyki. W: *56 Konferencja Naukowa Komitetu Inżynierii Lądowej i Wodnej PAN oraz Komitetu Nauki PZITB. Problemy Naukowo-Badawcze Budownictwa*. Kielce: Wydawnictwo Politechniki Świętokrzyskiej, 2010, 821–828.
- [24] Chróścielewski J., Rucka M., Wilde K., Witkowski W.: Modelowanie propagacji fal sprężystych w tarczy typu T w kontekście możliwości diagnostycznych. *Biuletyn WAT* 1, 2011 (in press).
- [25] Clark M. R., McCann D. M., Forde M. C.: Application of infrared thermography to the non-destructive testing of concrete and masonry bridges. *NDT&E International* 36, 2003, 265–275.
- [26] Cook R. D., Malkus D. S., Plesha M. E.: *Concepts and Applications of Finite Element Analysis*, 3rd ed. New York: John Wiley & Sons 1989.
- [27] Dalton R. P., Cawley P., Lowe M. J. S.: The potential of guided waves for monitoring large areas of metallic aircraft fuselage structures. *Journal of Nondestructive Evaluation* 20, 2001, 29–46.
- [28] Dauksher W., Emery A. F.: Accuracy in modelling the acoustic wave equation with Chebyshev spectral finite elements. *Finite Elements in Analysis and Design* 26, 1997, 115–128.
- [29] Dauksher W., Emery A. F.: An evaluation of the cost effectiveness of Chebyshev spectral and p -finite element solutions to the scalar wave equation. *International Journal for Numerical Methods in Engineering* 45, 1999, 1099–1113.
- [30] Dauksher W., Emery A. F.: The solution of elastostatic and elastodynamic problems with Chebyshev spectral finite elements. *Computer Methods in Applied Mechanics and Engineering* 188, 2000, 217–233.
- [31] Demma A., Cawley P., Lowe M., Roosenbrand A. G., Pavlakovic B.: The reflection of guided waves from notches in pipes: a guide for interpreting corrosion measurements. *NDT&E International* 37, 2004, 167–180.
- [32] Desmond T. P.: Theoretical and experimental investigation of stress waves at a junction of three bars. *Journal of Applied Mechanics, Trans. ASME* 48, 1981, 148–154.
- [33] Dimarogonas A. D.: Vibration of cracked structures: a state of the art review. *Engineering Fracture Mechanics* 55, 1996, 831–857.
- [34] Doebling S. W., Farrar C. R., Prime M. B.: A summary review of vibration-based damage identification methods. *The Shock and Vibration Digest* 30, 1998, 91–105.
- [35] Doyle J. F.: A spectrally formulated finite element for longitudinal wave propagation. *The International Journal of Analytical and Experimental Modal Analysis* 3, 1988, 1–5.
- [36] Doyle J. F.: *Wave Propagation in Structures: Spectral Analysis Using Fast Discrete Fourier Transforms*, 2nd ed. New York: Springer-Verlag 1997.
- [37] Doyle J. F., Farris T. N.: A spectrally formulated finite element for flexural wave propagation in beams. *International Journal of Analytical and Experimental Modal Analysis* 5, 1990a, 99–107.
- [38] Doyle J. F., Farris T. N.: A spectrally formulated element for wave propagation in 3-D frame structures. *The International Journal of Analytical and Experimental Modal Analysis* 5, 1990b, 223–227.
- [39] Doyle J. F., Kamle S.: An experimental study of the reflection and transmission of flexural waves at discontinuities. *Journal of Applied Mechanics, Trans. ASME* 52, 1985, 669–673.
- [40] Doyle J. F., Kamle S.: An experimental study of the reflection and transmission of flexural waves at an arbitrary T-joint. *Journal of Applied Mechanics, Trans. ASME* 54, 1987, 136–140.
- [41] Firestone F. A., Ling D.S.: Method and means for generating and utilizing vibrational waves in plates. U.S. patent no. 2536128, 1951.
- [42] Fung Y. C.: *Foundations of solid mechanics*. Englewood Cliffs: Prentice Hall 1965.
- [43] Gao J., Yang J., Cui L.-J., Cheng J.-C., Qian M.-L.: Modeling laser-generated guided waves in bonded plates by the finite element method. *Ultrasonics* 44, 2006, 985–989.

- [44] Ghose B., Kankane D. K.: Estimation of location of defects in propellant grain by X-ray radiography. *NDT&E International* 41, 2008, 125–128.
- [45] Giurgiutiu V.: *Structural Health Monitoring with Piezoelectric Wafer Active Sensors*. Amsterdam: Academic Press 2008.
- [46] Giurgiutiu V., Bao J. J.: Embedded-ultrasonics structural radar for in situ structural health monitoring of thin-walled structures. *Structural Health Monitoring* 3, 2004, 121–140.
- [47] Giurgiutiu V., Zagrai A., Bao J.: Damage identification in aging aircraft structures with piezoelectric wafer active sensors. *Journal of Intelligent Material Systems and Structures* 15, 2004, 673–687.
- [48] Gopalakrishnan S.: A deep rod finite element for structural dynamics and wave propagation problems. *International Journal for Numerical Methods in Engineering* 48, 2000, 731–744.
- [49] Gopalakrishnan S., Doyle J. F.: Spectral super-element for wave propagation in structures with local non-uniformities. *Computer Methods in Applied Mechanics and Engineering* 121, 1995, 77–90.
- [50] Gopalakrishnan S., Chakraborty A., Mahapatra D.R.: *Spectral Finite Element Method. Wave Propagation, Diagnostics and Control in Anisotropic and Inhomogeneous Structures*. London: Springer-Verlag 2008.
- [51] Gopalakrishnan S., Martin M., Doyle J. F.: A matrix methodology for spectral analysis of wave propagation in multiple connected Timoshenko beams. *Journal of Sound and Vibration* 158, 1992, 11–24.
- [52] Graff K.F.: *Wave Motion in Elastic Solids*. Oxford: Clarendon Press 1975.
- [53] Grigsby T. N., Tajchman E. J.: Properties of Lamb waves relevant to the ultrasonic inspection of plates. *IRE Transactions on Ultrasonics Engineering* 8, 1961, 26–33.
- [54] Gros X. E.: An eddy current approach to the detection of damage caused by low-energy impacts on carbon fibre reinforced materials. *Materials & Design* 16, 1995, 167–173.
- [55] Hagedorn P., DasGupta A.: *Vibrations and Waves in Continuous Mechanical Systems*. Chichester: John Wiley & Sons 2007.
- [56] Hilderbrand F. B.: *Introduction to Numerical Analysis*. New York: McGraw-Hill Book Company 1956.
- [57] Hill R., Forsyth S. A., Macey P.: Finite element modelling of ultrasound, with reference to transducers and AE waves. *Ultrasonics* 42, 2004, 253–258.
- [58] Hola J., Schabowicz K.: New technique of nondestructive assessment of concrete strength using artificial intelligence. *NDT&E International* 38, 2005, 251–259.
- [59] Hola J., Sadowski Ł., Schabowicz K.: Nondestructive evaluation of the concrete floor quality using impulse response method and impact-echo method. *e-Journal of Nondestructive Testing & Ultrasonics* 14(3), 2009.
- [60] Huber M. T.: *Teoria sprężystości. Tom II*. Kraków: Polska Akademia Umiejętności 1950.
- [61] Hughes T. J. R.: *The Finite Element Method: Linear Static and Dynamic Finite Element Analysis*. Mineola, New York: Dover Publications 2000.
- [62] Igawa H., Komatsu K., Yamaguchi I., Kasai T.: Wave propagation analysis of frame structures using the spectral element method. *Journal of Sound and Vibration* 227, 2004, 1071–1081.
- [63] Jin J., Quek S. T., Wang Q.: Wave boundary element to study Lamb wave propagation in plates. *Journal of Sound and Vibration* 288, 2005, 195–213.
- [64] Jin Z. H., Batra R. C.: A crack at the interface between a Kane-Mindlin plate and a rigid substrate. *Engineering Fracture Mechanics* 57, 1997a, 343–354.
- [65] Jin Z. H., Batra R. C.: Dynamic fracture of a Kane-Mindlin plate. *Theoretical and Applied Fracture Mechanics* 26, 1997b, 199–209.
- [66] Kaliski S.: *Drgania i fale*. Warszawa: Państwowe Wydawnictwo Naukowe 1986.
- [67] Kane T. R., Mindlin R. D.: High-frequency extensional vibrations of plates. *Journal of Applied Mechanics, Trans. ASME* 23, 1956, 277–283.
- [68] Kawecki J., Stypuła K.: Use of dynamic measurements in diagnostics of buildings situated near the area of road works. In: *Proc. of the International Conference on Experimental Vibration Analysis for Civil Engineering Structures – EVACES'09*, Kraków 2009, 649–654.

- [69] Kishore N. N., Sridhar I., Iyengar N. G. R.: Finite element modelling of the scattering of ultrasonic waves by isolated flaws. *NDT&E International* 33, 2000, 297–305.
- [70] Knitter-Piątkowska A., Pozorski Z., Garstecki A.: Application of discrete wavelet transformation in damage detection. Part I: Static and dynamic experiments. *Computer Assisted Mechanics and Engineering Sciences (CAMES)* 13, 2006, 21–38.
- [71] Kokot S., Zembaty Z.: Damage reconstruction of 3D frames using genetic algorithms with Levenberg-Marquardt local search. *Soil Dynamics and Earthquake Engineering* 29, 2008, 311–323.
- [72] Kokot S., Zembaty Z.: Vibration based stiffness reconstruction of beams and frames by observing their rotations under harmonic excitations - Numerical analysis. *Engineering Structures* 31, 2009, 1581–1588.
- [73] Kolsky H.: *Stress Waves in Solids*. London: Oxford University Press 1953.
- [74] Komatitsch D., Vilotte J.-P.: The spectral element method: an efficient tool to simulate the seismic response of 2D and 3D geological structures. *Bulletin of the Seismological Society of America* 88, 1998, 368–392.
- [75] Komatitsch D., Martin R., Tromp J., Taylor M. A., Wingate B. A.: Wave propagation in 2-D elastic media using a spectral element method with triangles and quadrangles. *Journal of Computational Acoustics* 9, 2001, 703–718.
- [76] Komatitsch D., Vilotte J.-P., Vai R., Castillo-Covarrubias J. M., Sánchez-Sesma F. J.: The spectral element method for elastic wave equations—application to 2D and 3D seismic problems. *International Journal for Numerical Methods in Engineering* 45, 1999, 1139–1164.
- [77] Kosiński W.: *Wstęp do teorii osobliwości pola i analizy fal*. Warszawa-Poznań: Państwowe Wydawnictwo Naukowe 1981.
- [78] Kotousov A.: Fracture in plates of finite thickness. *International Journal of Solids and Structures* 44, 2007, 8259–8273.
- [79] Kotousov A., Wang C. H.: Three-dimensional stress constraint in an elastic plate with a notch. *International Journal of Solids and Structures* 39, 2002, 4311–4326.
- [80] Krawczuk M., Grabowska J., Palacz M.: Longitudinal wave propagation. Part I—Comparison of rod theories. *Journal of Sound and Vibration* 295, 2006a, 461–478.
- [81] Krawczuk M., Grabowska J., Palacz M.: Longitudinal wave propagation. Part II—Analysis of crack influence. *Journal of Sound and Vibration* 295, 2006b, 479–490.
- [82] Krawczuk M., Palacz M., Ostachowicz W.: The dynamic analysis of a cracked Timoshenko beam by the spectral element method. *Journal of Sound and Vibration* 264, 2003, 1139–1153.
- [83] Krawczuk M., Palacz M., Ostachowicz W.: Wave propagation in plate structures for crack detection. *Finite Elements in Analysis and Design* 40, 2004, 991–1004.
- [84] Kudela P., Krawczuk M., Ostachowicz W.: Wave propagation modelling in 1D structures using spectral finite elements. *Journal of Sound and Vibration* 300, 2007a, 88–100.
- [85] Kudela P., Ostachowicz W., Żak A.: Damage detection in composite plates with embedded PZT transducers. *Mechanical Systems and Signal Processing* 22, 2008, 1327–1335.
- [86] Kudela P., Żak A., Krawczuk M., Ostachowicz W.: Modelling of wave propagation in composite plates using the time domain spectral element method. *Journal of Sound and Vibration* 302, 2007b, 728–745.
- [87] Kuźniar K., Waszczyszyn Z.: Neural analysis of vibration problems of real flat buildings and data pre-processing. *Engineering Structures* 24, 2002, 1327–1335.
- [88] Lamb H.: On waves in elastic plate. *Proceedings of the Royal Society of London. Series A*. London, 93, 1917, 114–128.
- [89] Lammering R.: Observation of piezoelectrically induced Lamb wave propagation in thin plates by use of speckle interferometry. *Experimental Mechanics* 50, 2010, 377–387.
- [90] Lashkia V.: Defect detection in X-ray images using fuzzy reasoning. *Image and Vision Computing* 19, 2001, 261–269.
- [91] Lee B. C., Staszewski W. J.: Lamb wave propagation modelling for damage detection: I: Two-dimensional analysis. *Smart Materials and Structures* 16, 2007a, 249–259.
- [92] Lee B. C., Staszewski W. J.: Lamb wave propagation modelling for damage detection: II: Damage monitoring strategy. *Smart Materials and Structures* 16, 2007b, 260–274.

- [93] Lee C. M., Rose J. L., Cho Y.: A guided wave approach to defect detection under shelling in rail. *NDT&E International* 42, 2009, 174–180.
- [94] Lee J. P., Kolsky H.: The generation of stress pulses at the junction of two non-collinear rods. *Journal of Applied Mechanics, Trans. ASME* 39, 1972, 809–813.
- [95] Liang M.-T., Chen C.-J.: Investigation of longitudinal elastic wave at right-angle joint of two rods. *Journal of Marine Science and Technology* 6, 1998, 45–53.
- [96] Lin Y., Chang C., Kuo S.-F., Liou H.-C.: A simple device for detecting impact time in impact-echo testing of concrete. *NDT&E International* 37, 2004, 1–8.
- [97] Liu G. R., Quek S. S.: *The Finite Element Method: A Practical Course*. Oxford: Butterworth-Heinemann 2003.
- [98] Love A. E. H.: *Treatise of The Mathematical Theory of Elasticity*, 3rd ed. Cambridge University Press 1920.
- [99] Lowe M. J. S., Alleyne D. N., Cawley P.: Defect detection in pipes using guided waves. *Ultrasonics* 36, 1998, 147–154.
- [100] Lu Y., Ye L., Su Z.: Crack identification in aluminium plates using Lamb wave signals of a PZT sensor network. *Smart Materials and Structures* 15, 2006, 839–849.
- [101] Lu Y., Wang X., Tang J., Ding Y.: Damage detection using piezoelectric transducers and the Lamb wave approach: II. Robust and quantitative decision making. *Smart Materials and Structures* 17, 2008, doi:10.1088/0964-1726/17/2/025034.
- [102] Mahapatra D. R., Gopalakrishnan S.: A spectral finite element model for analysis of axial-flexural-shear coupled wave propagation in laminated composite beams. *Composite Structures* 59, 2003, 67–88.
- [103] Mahapatra D. R., Gopalakrishnan S.: Spectral finite analysis of coupled wave propagation in composite beams with multiple delaminations and strip inclusions. *International Journal of Solids and Structures* 41, 2004, 1173–1208.
- [104] Mahapatra D. R., Gopalakrishnan S., Sankar T. S.: Spectral-element-based solutions for wave propagation analysis of multiply connected unsymmetric laminated composite beams. *Journal of Sound and Vibration* 237, 2000, 819–836.
- [105] Maia N. M. M., Silva J. M. M.: *Theoretical and Experimental Modal Analysis*. Baldock, Hertfordshire: Research Studies Press 1997.
- [106] Mallet L., Lee B. C., Staszewski W. J., Scarpa F.: Structural health monitoring using scanning laser vibrometry: II: Lamb waves for damage detection. *Smart Materials and Structures* 13 2004, 261–269.
- [107] Martin M., Gopalakrishnan S., Doyle J. F.: Wave propagation in multiply connected deep waveguides. *Journal of Sound and Vibration* 174, 1994, 521–538.
- [108] McKeon J. C. P., Hinders M. K.: Lamb wave scattering from a through hole. *Journal of Sound and Vibration* 224, 1999, 843–862.
- [109] Mendrok K., Uhl T.: The application of modal filters for damage detection. *Smart Structures and Systems* 6, 2010, 115–133.
- [110] Miklowitz J., Calif P.: The propagation of compressional waves in a dispersive elastic rod. Part I-Results from the theory. *Journal of Applied Mechanics, Trans. ASME* 24, 1957a, 231–239.
- [111] Miklowitz J., Nisewanger C. R., Calif P.: The propagation of compressional waves in a dispersive elastic rod. Part II-Experimental results and comparison with theory. *Journal of Applied Mechanics, Trans. ASME* 24, 1957b, 240–244.
- [112] Mindlin R. D.: Influence of rotatory inertia and shear on flexural motions of isotropic, elastic plates. *Journal of Applied Mechanics, Trans. ASME* 18, 1951, 31–38.
- [113] Mindlin R. D., Herrmann G.: A one-dimensional theory of compressional waves in an elastic rod. *Proceedings of First U.S. National Congress of Applied Mechanics* 1952, 187–191.
- [114] Mitra M., Gopalakrishnan S.: Spectrally formulated wavelet finite element for wave propagation and impact force identification in connected 1-D waveguides. *International Journal of Solids and Structures* 42, 2005, 4695–4721.
- [115] Mitra M., Gopalakrishnan S.: Wavelet based spectral finite element for analysis of coupled wave propagation in higher order composite beams. *Composite Structures* 73, 2006, 263–277.

- [116] Moser F., Jacobs L. J., Qu J.: Modeling elastic wave propagation in waveguides with the finite element method. *NDT&E International* 32, 1999, 225–234.
- [117] Newmark N. N. A method of computation for structural dynamics. *Journal of Engineering Mechanics Division, Proc. ASCE* 85, 1959, 67–94.
- [118] Nowacki W.: *Teoria sprężystości*. Warszawa: Państwowe Wydawnictwo Naukowe 1970.
- [119] Nowacki W.: *Dynamika budowli*. Warszawa: Arkady 1972.
- [120] Ostachowicz W.: Damage detection of structures using spectral finite element method. *Computers & Structures* 86, 2008, 454–462.
- [121] Ostachowicz W., Kudela P., Malinowski P., Wandowski T.: Damage localization in plate-like structures based on PZT sensors. *Mechanical Systems and Signal Processing* 23, 2009, 1805–1829.
- [122] Palacz M., Krawczuk M.: Analysis of longitudinal wave propagation in a cracked rod by the spectral element method. *Computers & Structures* 80, 2002, 1809–1816.
- [123] Palacz M., Krawczuk M., Ostachowicz W.: Detection of additional mass in rods: experimental and numerical investigations. *Archives of Applied Mechanics* 74, 2005a, 820–826.
- [124] Palacz M., Krawczuk M., Ostachowicz W.: The spectral finite element model for analysis of flexural-shear coupled wave propagation. Part 1: Laminated multilayer composite beam. *Composite Structures* 68, 2005b, 37–44.
- [125] Palacz M., Krawczuk M., Ostachowicz W.: The spectral finite element model for analysis of flexural-shear coupled wave propagation. Part 2: Delaminated multilayer composite beam. *Composite Structures* 68, 2005c, 45–51.
- [126] Patera T.: A spectral element method for fluid dynamics: laminar flow in a channel expansion. *Journal of Computational Physics* 54, 1984, 468–488.
- [127] Peng H., Meng G., Li F.: Modeling of wave propagation in plate structures using three-dimensional spectral element method for damage detection. *Journal of Sound and Vibration* 320, 2009, 942–954.
- [128] Pozrikidis C.: *Introduction to Finite and Spectral Element Methods using MATLAB®*. Chapman & Hall/CRC 2005.
- [129] Rahman Z., Ohba H., Yoshioka T., Yamamoto T.: Incipient damage detection and its propagation monitoring of rolling contact fatigue by acoustic emission. *Tribology International* 42, 2009, 807–815.
- [130] Ramadas C., Balasubramaniam K., Joshi M., Krishnamurthy C. V.: Interaction of the primary anti-symmetric Lamb mode (A0) with symmetric delaminations: numerical and experimental studies. *Smart Materials and Structures* 18, 2009, doi: 10.1088/0964-1726/18/8/085011.
- [131] Rayleigh L.: On waves propagated along the plane surface of an elastic solid. *Proceedings of the London Mathematical Society* 17, 1885, 4–11.
- [132] Reddy J. N.: *Energy Principles and Variational Methods in Applied Mechanics*, 2nd ed. John Wiley & Sons 2002.
- [133] Ren W.-X., Roeck G. D.: Structural damage identification using modal data. I: Simulation verification. *Journal of Structural Engineering ASCE* 128, 2002a, 87–95.
- [134] Ren W.-X., Roeck G. D.: Structural damage identification using modal data. II: Test verification. *Journal of Structural Engineering ASCE* 128, 2002b, 96–104.
- [135] Rogers L. M.: Crack detection using acoustic emission methods – fundamentals and applications. *Key Engineering Materials* 293–294, 2005, 33–46.
- [136] Rose J. L.: *Ultrasonic Waves in Solid Media*. Cambridge: Cambridge University Press 1999.
- [137] Rose J. L., Cho Y., Avioli M. J.: Next generation guided wave health monitoring for long range inspection of pipes. *Journal of Loss Prevention in the Process Industries* 22, 2009, 1010–1015.
- [138] Rose J. L., Avioli M. J., Mudge P., Sanderson R.: Guided wave inspection potential defects in rail. *NDT&E International* 37, 2004, 153–161.
- [139] Rossmannith H. P., Fournery W. L.: Fracture initiation and stress wave diffraction at cracked interfaces in layered media: I. Brittle/brittle transition. *Rock Mechanics* 14, 1982, 209–233.
- [140] Rucka M., Wilde K.: Application of continuous wavelet transform in vibration based damage detection method for beam and plates. *Journal of Sound and Vibration* 297, 2006, 536–550.

- [141] Rucka M., Wilde K.: *Application of Wavelet Analysis in Damage Detection and Localization*. Gdańsk: Wydawnictwo Politechniki Gdańskiej 2007.
- [142] Rucka M., Wilde K.: Non-destructive diagnostics of concrete cantilever beam and slab by impact echo method. *Diagnostyka* 3, 2010, 63–68.
- [143] Rucka M.: Experimental and numerical studies of guided wave damage detection in bars with structural discontinuities. *Archive of Applied Mechanics* 80, 2010a, 1371–1390.
- [144] Rucka M.: Experimental and numerical study on damage detection in an L-joint using guided wave propagation. *Journal of Sound and Vibration* 329, 2010b, 1760–1779.
- [145] Rucka M.: Diagnostyka konstrukcji ramowych i płytowych za pomocą fal sprężystych. W: *56 Konferencja Naukowa Komitetu Inżynierii Lądowej i Wodnej PAN oraz Komitetu Nauki PZITB. Problemy Naukowo-Badawcze Budownictwa*. Kielce: Wydawnictwo Politechniki Świętokrzyskiej, 2010c, 851–858.
- [146] Rucka M.: Modelling of in-plane wave propagation in a plate using spectral element method and Kane-Mindlin theory with application to damage detection. *Archive of Applied Mechanics* 2011, doi: 10.1007/s00419-011-0524-1 (in press)
- [147] Runkiewicz L.: *Diagnostyka i wzmacnianie konstrukcji żelbetowych*. Kielce: Wydawnictwo Politechniki Świętokrzyskiej 1999.
- [148] Salawu O. S.: Detection of structural damage through changes in frequency: a review. *Engineering Structures* 19, 1997, 718–723.
- [149] Semblat J. F., Briost J. J.: Efficiency of higher order finite elements for analysis of seismic wave propagation. *Journal of Sound and Vibration* 231, 2000, 460–467.
- [150] Sprague M. A., Geers T. L.: Legendre spectral finite elements for structural dynamics analysis. *Communications in Numerical Methods in Engineering* 24, 2008, 1953–1965.
- [151] Sridhar R., Chakraborty A., Gopalakrishnan S.: Wave propagation analysis in anisotropic and inhomogeneous uncracked and cracked structures using pseudospectral finite element method. *International Journal of Solids and Structures* 43, 2006, 4997–5031.
- [152] Staszewski W. J., Lee B. C., Mallet L., Scarpa F.: Structural health monitoring using scanning laser vibrometry: I: Lamb wave sensing. *Smart Materials and Structures* 13, 2004, 251–260.
- [153] Staszewski W. J., Lee B. C., Traynor R.: Fatigue crack detection in metallic structures with Lamb waves and 3D laser vibrometry. *Smart Materials and Structures* 18, 2007, 727–739.
- [154] Stein E., de Borst R., Hughes T. J. R.: *Encyclopedia of Computational Mechanics. Vol. I: Fundamentals*. Chichester: John Wiley & Sons 2004.
- [155] Su Z., Ye L., Bu X.: A damage identification technique for CF/EP composite laminates using distributed piezoelectric transducers. *Composite Structures* 57, 2002, 465–471.
- [156] Su Z., Ye L., Lu Y.: Guided Lamb waves for identification of damage in composite structures: a review. *Journal of Sound and Vibration* 295, 2009, 753–780.
- [157] Szabó B. A.: The p - and h - p versions of the finite element method in solid mechanics. *Computer methods in Applied Mechanics and Engineering* 80, 1990, 185–195.
- [158] Świercz A., Kotakowski P., Holnicki-Szulc J.: Damage identification in skeletal structures using the virtual distortion method in frequency domain. *Mechanical Systems and Signal Processing* 22, 2008, 1826–1839.
- [159] Thompson R. B., Alers G. A., Tension M. A.: Application of direct electromagnetic lamb wave generation to gas pipeline inspection. *Ultrasonic Symposium*, 1972, 91–94.
- [160] Timoshenko S., Goodier J. N.: *Teoria sprężystości*. Warszawa: Wydawnictwo Arkady 1962.
- [161] Tomaszewska A.: Influence of statistical errors on damage detection based on structural flexibility and mode shape curvature. *Computers and Structures* 88, 2010, 154–164.
- [162] Tromp J., Komatitsch D., Liu Q.: Spectral-element and adjoint methods in seismology. *Communications in Computational Physics* 3, 2008, 1–32.
- [163] Uhl T.: Identification of modal parameters for nonstationary mechanical systems. *Archive of Applied Mechanics* 74, 2005, 878–889.
- [164] Victorov I. A.: *Rayleigh and Lamb Waves. Physical Theory and Applications*. New York: Plenum Press 1967.
- [165] Wang C. H., Chang F.-K.: Scattering of plate waves by a cylindrical inhomogeneity. *Journal of Sound and Vibration* 282, 2005, 429–451.

- [166] Wang C. H., Rose J. T., Chang F.-K.: A synthetic time-reversal imaging method for structural health monitoring. *Smart Materials and Structures* 13, 2004, 415–423.
- [167] Wang L., Shen J.: Scattering of elastic waves by a crack in an isotropic plate. *Ultrasonics* 35, 1997, 451–457.
- [168] Wang X., Lu Y., Tang J.: Damage detection using piezoelectric transducers and the Lamb wave approach: I. System analysis. *Smart Materials and Structures* 17, 2008, doi:10.1088/0964–1726/17/2/025033.
- [169] Waszczyszyn Z., Ziemiański L.: Neural networks in mechanics of structures and materials – new results and prospects of applications. *Computers & Structures* 79, 2001, 2261–2276.
- [170] Weaver W., Johnston P. R.: *Structural Dynamics by Finite Elements*. Englewood Cliffs, New Jersey: Prentice-Hall 1987.
- [171] Wilcox P. D.: Omni-directional guided wave transducer arrays for the rapid inspection of large areas of plate structures. *IEEE Transactions on Ultrasonics, Ferroelectrics, and Frequency Control* 50, 2003, 699–709.
- [172] Wilcox P., Lowe M., Cawley P.: The effect of dispersion on long-range inspection using ultrasonic guided waves. *NDT&E International* 34, 2001, 1–9.
- [173] Wilde K.: *Modal Diagnostics of Civil Engineering Structures*. Gdańsk: Wydawnictwo Politechniki Gdańskiej 2008.
- [174] Wilde K., Rucka M., Chrościelewski J., Witkowski W. i inni: *Wielopoziomowy system detekcji uszkodzeń w dużych obiektach infrastrukturalnych*. Ministerstwo Nauki i Szkolnictwa Wyższego. Raport końcowy z projektu badawczego N506 065 31/3149, 2006-2006, Gdańsk 2009.
- [175] Witkowski W., Rucka M., Chrościelewski J., Wilde K.: Wave propagation analysis in spatial frames using spectral Timoshenko beam elements in the context of damage detection. *Archives of Civil Engineering* 55, 2009, 367–402.
- [176] Worlton D. C.: Experimental confirmation of Lamb waves at megacycle frequencies. *Journal of Applied Physics* 32, 1961, 967–971.
- [177] Yang Y., Cascante G., Polak M. A.: Depth detection of surface-breathing crack in concrete plates using fundamental Lamb modes. *NDT&E International* 42, 2009, 501–512.
- [178] Yeih W., Huang R.: Detection of the corrosion damage in reinforced concrete members by ultrasonic testing. *Cement and Concrete Research* 28, 1998, 1071–1083.
- [179] Yu L., Giurgiutiu V.: In-situ optimized PWAS phased arrays for Lamb wave structural health monitoring. *Journal of Mechanics of Materials and Structures* 2, 2007, 459–488.
- [180] Yu L., Giurgiutiu V.: In situ 2-D piezoelectric wafer active sensors array for guided wave damage detection. *Ultrasonics* 48, 2008, 117–134.
- [181] Zienkiewicz O. C., Taylor R. L.: *The Finite Element Method, 5th ed. Volume 1: The Basis*. Oxford: Butterworth-Heinemann 2000a.
- [182] Zienkiewicz O. C., Taylor R. L.: *The Finite Element Method, 5th ed. Volume 2: Solid Mechanics*. Oxford: Butterworth-Heinemann 2000b.
- [183] Zienkiewicz O. C., Zhu J. Z., Gong N. G.: Effective and practical h - p -version adaptive analysis procedures for the finite element method. *International Journal for Numerical Methods in Engineering* 28, 1989, 879–891.
- [184] Ziopaja K., Pozorski Z., Garstecki A.: Application of discrete wavelet transformation in damage detection. Part II: Heat transfer experiments. *Computer Assisted Mechanics and Engineering Sciences (CAMES)* 13, 2006, 39–51.
- [185] Żak A., Krawczuk M., Ostachowicz W.: Propagation of in-plane wave in an isotropic panel with a crack. *Finite Elements in Analysis and Design* 42, 2006a, 929–941.
- [186] Żak A., Krawczuk M., Ostachowicz W.: Propagation of in-plane elastic waves in a composite panel. *Finite Elements in Analysis and Design* 43, 2006b, 145–154.

GUIDED WAVE PROPAGATION IN STRUCTURES MODELLING, EXPERIMENTAL STUDIES AND APPLICATION TO DAMAGE DETECTION

Engineering structures undergo gradual destruction in the course of time as a result of static and dynamic loading, temperature, humidity, wind or corrosive factors. Since damage in structural elements may lead to improper operation of any engineering object, various damage detection techniques have been investigated to improve reliability and safety of structures. The guided wave-based damage detection methods have been dynamically developed over last years, because guided waves are very suitable for inspecting large structures due to their ability of propagation over long distances with a little amplitude loss.

The purpose of this study is to conduct detailed experimental and numerical investigations on ultrasonic guided wave propagation in steel structures. The particular aims are: (a) modelling of wave propagation phenomenon in structural elements including dispersion effects; (b) developing of numerical models for wave propagation; (c) systematic experimental verification of the developed numerical models; (d) application of the guided wave-based technique to damage detection.

The first part of the work describes wave propagation in structural elements. The governing equations for several models of rods, beams and plates providing approximated description of wave motion are derived. Verification of the models is conducted by comparing dispersion relations with exact Lamb modes. The study indicates necessity of using higher order theories (the Mindlin-Herrmann rod theory, the Timoshenko beam, the Kane-Mindlin theory of extensional plates and the Mindlin theory of bending plates) when analysing waves of ultrasonic frequencies because the higher order theories can adequately account for dispersive behaviour of the lowest symmetric and antisymmetric modes.

The next part of the work describes the spectral element method. The spatial discretization is based on high-degree Legendre interpolants spread over Gauss-Legendre-Lobatto (GLL) nodes and the spatial integration is performed using the GLL quadrature. Such numerical strategy provides the exponential accuracy and a reduction of the computational cost because a mass matrix is exactly diagonal by construction as a result of the GLL integration rule. Special spectral elements based on the considered higher order theories are formulated, in particular the frame spectral element based on the Mindlin-Herrmann rod and Timoshenko beam theories, as well as the extensional plate element based on the Kane-Mindlin theory and the bending plate element based on the Mindlin theory.

A substantial part of the study contains experimental and numerical analyses of wave propagation in rods, beams, frames and plates. In the experimental investigations, structural elements are excited by means of the piezoelectric actuator and propagating velocity signals are detected and recorded by the laser vibrometer. Experimental dispersion curves are obtained for the considered frequency range 50–300 kHz to determine adjustable parameters for the approximate theories applied in the numerical models. The effectiveness of the proposed spectral element models has been experimentally confirmed. The model based on the Mindlin-Herrmann rod and Timoshenko beam theories guarantees reasonable approximation for the first longitudinal and flexural modes behaviour, which has been proved by the comparison with the experimentally measured signals. Similarly, the Kane-Mindlin theory for extensional plate waves and the Mindlin theory for flexural plate waves provide a very accurate description of dispersive behaviour of the first mode of longitudinal and flexural waves. The results of the analyses show that the numerical model of an arbitrary frame or plate structure intended as a part of the SHM system should be described in the SEM formulation based on the higher order theories to obtain proper times of reflections from potential damage.

Finally, an application of ultrasonic guided waves to damage detection is presented. Detection of damage in various forms of discontinuity of cross-section and material is considered by analysing guided wave response signals in the form of A-scans, B-scans and C-scans. As a result, the study discusses in detail the possibility of detection of damage in rods, beams, frames and plates and it compares the usefulness of longitudinal and flexural waves in nondestructive damage detection.

PROPAGACJA FAL PROWADZONYCH W KONSTRUKCJACH MODELOWANIE, BADANIA EKSPERYMENTALNE ORAZ ZASTOSOWANIE DO WYKRYWANIA USZKODZEŃ

Konstrukcje inżynierskie podlegają naturalnym procesom zużycia wraz z upływem czasu. Aby zapewnić bezpieczeństwo ich użytkowania, konieczne jest wczesne wykrycie oraz wskazanie lokalizacji potencjalnych uszkodzeń. Niezwykle istotną tematyką staje się zatem diagnostyka i monitorowanie stanu technicznego obiektów infrastruktury. Rozwój aparatury pomiarowej, jak również technologii przetwarzania sygnałów umożliwia budowę urządzeń i systemów do precyzyjnej diagnostyki elementów konstrukcji inżynierskich. Jedną z metod diagnostyki konstrukcji jest technika wykorzystująca propagację fal sprężystych. Moduł diagnostyczny bazujący na propagacji fal ultradźwiękowych może być wykorzystywany w sposób ciągły. Ultradźwiękowe fale prowadzone charakteryzują się zdolnością propagowania na znaczne odległości z nieznacznym spadkiem amplitudy. W metodach propagacji fal sprężystych konstrukcja wzbudzana jest za pomocą impulsu lub paczki falkowej, zaś położenie uszkodzenia identyfikowane jest na podstawie analizy odbić w zarejestrowanych sygnałach czasowych propagującej fali.

Celem niniejszej pracy są eksperymentalne i numeryczne analizy propagacji prowadzonych fal sprężystych w stalowych konstrukcjach prętowych, belkowych, ramowych, tarczowych i płytowych. W szczególności praca poświęcona jest: (a) modelowaniu propagacji fal z uwzględnieniem zjawiska dyspersji; (b) budowie modeli obliczeniowych w formalizmie metody elementów spektralnych; (c) eksperymentalnej weryfikacji zaproponowanych modeli; (d) zastosowaniu technik propagacji fal prowadzonych do wykrywania uszkodzeń.

Praca składa się z siedmiu rozdziałów:

W **rozdziale 1** opisano metody monitoringu technicznego, dokonano przeglądu literatury dotyczącej detekcji uszkodzeń za pomocą ultradźwiękowych fal sprężystych oraz przedstawiono cel i zakres pracy.

W **rozdziale 2** wyprowadzono równania propagacji fal w prętach, belkach, tarczach i płytach. Przedstawione w dalszej części pracy wyniki pokazały, iż w modelowaniu propagacji fal szczególnie ważny jest wybór teorii opisującej ruch. Klasyczne teorie, jak elementarna teoria prętów rozciąganych, teoria belek Eulera-Bernoulliego, płaskiego stanu naprężenia, czy też teoria płyt zginanych Kirchhoffa, nie umożliwiają dokładnego modelowania zjawisk falowych. Do precyzyjnego opisu propagacji fal wymagane jest uwzględnienie zjawiska dyspersji oraz efektów ścinania i bezwładności obrotowej, co umożliwiają teorie wyższych rzędów. Na podstawie porównania krzywych dyspersji dla rozważanych teorii ze ścisłymi rozwiązaniami fal Lamba oraz z wynikami eksperymentalnymi wykazano, iż przybliżone teorie wyższego rzędu (teoria pręta Mindlina-Herrmana, teoria belki Timoshenki, teoria tarczy Kane-Mindlina oraz teoria płyty Mindlina) umożliwiają poprawny opis zjawiska propagacji fal sprężystych, szczególnie w odniesieniu do najniższych postaci drgań: symetrycznej (S_0) i antysymetrycznej (A_0).

Rozdział 3 poświęcono metodzie elementów spektralnych sformułowanej w dziedzinie czasu. Metoda ta jest rozwinięciem klasycznej metody elementów skończonych. W metodzie elementów spektralnych stosuje się w każdym z przestrzennych kierunków aproksymacji elementy wielowęzłowe z rozkładem węzłów w punktach Gaussa-Lobatto-Legendre'a oraz z interpolacją Lagrange'a. Podejście to ma dwie znaczące zalety w analizie dynamicznej w zakresie wysokich częstotliwości. Po pierwsze wymagana liczba węzłów zmniejsza się do ok. 5-10 na długość fali (podczas gdy przy zastosowaniu elementów dwuwęzłowych liczba ta osiąga wartość 20 do 40). Drugą zaletą jest uzyskanie diagonalnej macierzy mas w wyniku całkowania numerycznego kwadraturą Gaussa-Lobatto-Legendre'a, co powoduje znaczące przyspieszenie całkowania w czasie. W rozdziale 3 przedstawiono wyprowadzenia macierzy elementów spektralnych, w szczególności elementu ramowego na podstawie teorii prętowej Mindlina-Herrmana oraz belki Timoshenki, a także elementu tarczowego na podstawie teorii Kane-Mindlina i elementu płytowego na podstawie teorii Mindlina.

Numeryczne i eksperymentalne analizy propagacji fal podłużnych i giętych w prętach oraz belkach przeprowadzono w **rozdziale 4**. W wykonanych badaniach doświadczalnych do wzbudzenia fal użyto wzbudnika piezoelektrycznego, natomiast sygnał propagującej fali rejestrowany był bezstykowo za pomocą wibrometru laserowego. Efektywność zaproponowanych numerycznych modeli spektralnych została potwierdzona na podstawie porównania z eksperymentalnymi krzywymi dyspersji. W rozdziale przedstawiono także dyskusję na temat doboru liczby węzłów w elementach wielowęzłowych oraz doboru fali wzbudzającej. Zaprezentowano eksperymentalne i numeryczne wyniki propagacji fal w prętach i belkach bez uszkodzeń oraz z uszkodzeniami. Detekcja uszkodzeń w formie nieciągłości materiału bądź pola przekroju analizowana była na podstawie prędkości i czasów odbicia zarejestrowanych sygnałów propagujących fal.

Rozdział 5 zawiera eksperymentalne i numeryczne wyniki propagacji fal w ramach płaskich typu L, T oraz w ramie portalowej. Badano wpływ zjawiska konwersji postaci drgań przez węzły ramy na możliwość wykrywania uszkodzeń. Na podstawie analizy różnych położeń i liczby uszkodzeń określono wskazówki dotyczące liczby i położenia wzbudników oraz punktów odbioru sygnałów czasowych, tak by monitoring obejmował całą analizowaną konstrukcję.

W **rozdziale 6** przedstawiono wyniki eksperymentalnych i numerycznych badań propagacji fal w tarczach i płytach z uszkodzeniem w formie powierzchniowej zmiany grubości. Badano trzy różne położenia uszkodzenia. Identyfikacja położenia uszkodzenia została wykonana na podstawie sygnałów prędkości fali w formie obrazowań typu A (zobrazowanie wielkości amplitudy sygnału w funkcji czasu), B (zobrazowanie wielkości amplitud w funkcji czasu i położenia) oraz C (dwuwymiarowy obraz konstrukcji w wybranej chwili czasowej).

Uwagi końcowe oraz kierunki dalszych prac zawarto w **rozdziale 7**.

Appednix A

WAVE SOLUTIONS IN ELASTIC CONTINUA

The present appendix shows the wave solutions in isotropic elastic continua using the theory of elasticity. The exact solutions are obtained for waves propagated in unbounded continua, as well as for waves propagated in elastic continua with boundaries: Rayleigh surface waves in solids with a free surface, shear horizontal plate waves and Lamb plate waves. For more details, see books by Achenbach (1975), Giurgiutiu (2008), Graff (1975), Huber (1950), Nowacki (1970, 1972), Rose (1999), Timoshenko and Goodier (1962).

A.1. Waves in infinite media

Two types of uncoupled waves, *dilatational waves* (a.k.a. primary, pressure, compressional, extensional, irrotational, axial, longitudinal, P waves) and *distortional waves* (a.k.a. secondary, shear, rotational, transverse, S waves) can propagate in isotropic infinite continuum. In the absence of body forces, the Navier's governing equations in the vector notation are given by (e.g. Graff 1975, Huber 1950, Nowacki 1970, Timoshenko and Goodier 1962):

$$(\Lambda + G)\nabla\nabla \cdot \mathbf{u} + G\nabla^2\mathbf{u} = \rho\ddot{\mathbf{u}}, \quad (\text{A.1})$$

where Λ , G are Lamé constants of elasticity, ρ is mass density and $\mathbf{u} = u_x\mathbf{i} + u_y\mathbf{j} + u_z\mathbf{k}$ is a vector of displacements. The del operator ∇ and the Laplace operator ∇^2 are:

$$\nabla = \frac{\partial}{\partial x}\mathbf{i} + \frac{\partial}{\partial y}\mathbf{j} + \frac{\partial}{\partial z}\mathbf{k}, \quad \nabla^2 = \nabla \cdot \nabla = \frac{\partial^2}{\partial x^2} + \frac{\partial^2}{\partial y^2} + \frac{\partial^2}{\partial z^2}. \quad (\text{A.2})$$

To calculate the dilatational waves, the vector operation of divergence is performed on the Eq. (A.1):

$$(\Lambda + G)\nabla \cdot (\nabla\nabla \cdot \mathbf{u}) + G\nabla \cdot (\nabla^2\mathbf{u}) = \rho\nabla \cdot \ddot{\mathbf{u}}. \quad (\text{A.3})$$

Defining the dilatation Δ as:

$$\Delta = \nabla \cdot \mathbf{u} = \varepsilon_{xx} + \varepsilon_{yy} + \varepsilon_{zz}, \quad (\text{A.4})$$

and substituting the above result to Eq. (A.3), one can obtain the dilatational wave equation:

$$(\Lambda + 2G)\nabla^2\Delta = \rho\ddot{\Delta}, \quad (\text{A.5})$$

$$\nabla^2\Delta = \frac{1}{c_p^2}\ddot{\Delta}, \quad (\text{A.6})$$

which indicates that a change in the volume (dilatational disturbance), involving no rotation, propagates with the pressure wave speed c_p :

$$c_p = \sqrt{\frac{\Lambda + 2G}{\rho}} = \sqrt{\frac{E(1-\nu)}{\rho(1+\nu)(1-2\nu)}}. \quad (\text{A.7})$$

To calculate the rotational waves, the operation of curl on the Eq. (A.1) is performed:

$$(\Lambda + G)\nabla \times (\nabla \nabla \cdot \mathbf{u}) + G\nabla \times (\nabla^2 \mathbf{u}) = \rho \nabla \times \ddot{\mathbf{u}}. \quad (\text{A.8})$$

If the rotation vector is defined as:

$$\boldsymbol{\omega} = \frac{\nabla \times \mathbf{u}}{2}, \quad (\text{A.9})$$

the distortional wave equation can be obtained as:

$$G\nabla^2 \boldsymbol{\omega} = \rho \ddot{\boldsymbol{\omega}}, \quad (\text{A.10})$$

$$\nabla^2 \boldsymbol{\omega} = \frac{1}{c_s^2} \ddot{\boldsymbol{\omega}}, \quad (\text{A.11})$$

which indicates, that rotational waves (distortional disturbance), involving no volume changes, propagate with the shear wave speed c_s :

$$c_s = \sqrt{\frac{G}{\rho}} = \sqrt{\frac{E}{2\rho(1+\nu)}}. \quad (\text{A.12})$$

Another possibility to determine wave speeds is the application of wave potentials (see e.g. Achenbach 1975, Fung 1965, Graff 1975, Rose 1999). The vector of displacements $\mathbf{u} = u_x \mathbf{i} + u_y \mathbf{j} + u_z \mathbf{k}$ can be expressed via the Helmholtz decomposition as the gradient of a scalar potential Φ and a zero-divergence vector potential $\mathbf{H} = H_x \mathbf{i} + H_y \mathbf{j} + H_z \mathbf{k}$:

$$\mathbf{u} = \nabla \Phi + \nabla \times \mathbf{H}, \quad \nabla \cdot \mathbf{H} = 0. \quad (\text{A.13})$$

or using indicial notation:

$$u_i = \Phi_{,i} + e_{ijk} H_{k,j}, \quad H_{i,i} = 0, \quad i, j, k = x, y, z. \quad (\text{A.14})$$

By substituting Eq. (A.13) into Eq. (A.1), the Navier's equation of motion can be expressed by potential functions:

$$(\Lambda + G)\nabla \nabla \cdot (\nabla \Phi + \nabla \times \mathbf{H}) + G\nabla^2 (\nabla \Phi + \nabla \times \mathbf{H}) = \rho(\nabla \ddot{\Phi} + \nabla \times \ddot{\mathbf{H}}), \quad (\text{A.15})$$

$$\nabla [(\Lambda + 2G)\nabla^2 \Phi - \rho \ddot{\Phi}] + \nabla \times [G\nabla^2 \mathbf{H} - \rho \ddot{\mathbf{H}}] = 0. \quad (\text{A.16})$$

The Eq. (A.16) is satisfied, if both terms vanish. As the result, the wave equation is decomposed as two simplified wave equations:

$$c_p^2 \nabla^2 \Phi = \ddot{\Phi}, \quad (\text{A.17})$$

$$c_s^2 \nabla^2 \mathbf{H} = \ddot{\mathbf{H}}. \quad (\text{A.18})$$

A.2. Z-invariant 3-D waves

In this section, z -invariant wave propagation is presented. This case will be later used in studies of Rayleigh surface waves, as well as shear horizontal plate waves and Lamb plate waves. Consider 3-D waves that are invariant in one direction along the wavefront. The horizontal plane is denoted as Oxz , and the vertical plane as Oxy . The wavefront is assumed as parallel to the z axis and the wave disturbance is invariant along the z axis, which means that all the functions involved in the analysis do not depend on z , and their derivatives with respect to z are zero, i.e. (Giurgiutiu 2008):

$$\frac{\partial}{\partial z} = 0, \quad \nabla = \frac{\partial}{\partial x} \mathbf{i} + \frac{\partial}{\partial y} \mathbf{j}. \quad (\text{A.19})$$

The potentials Φ , H_x , H_y and H_z satisfy the wave equations:

$$\begin{aligned} c_p^2 \nabla^2 \Phi &= \ddot{\Phi}, \\ c_s^2 \nabla^2 H_x &= \ddot{H}_x, \\ c_s^2 \nabla^2 H_y &= \ddot{H}_y, \\ c_s^2 \nabla^2 H_z &= \ddot{H}_z, \end{aligned} \quad (\text{A.20})$$

and the zero-divergence condition:

$$\frac{\partial H_x}{\partial x} + \frac{\partial H_y}{\partial y} = 0. \quad (\text{A.21})$$

For the z -invariant case, the components of the displacement vector are as follows:

$$u_x = \frac{\partial \Phi}{\partial x} + \frac{\partial H_z}{\partial y}, \quad u_y = \frac{\partial \Phi}{\partial y} - \frac{\partial H_z}{\partial x}, \quad u_z = \frac{\partial H_y}{\partial x} - \frac{\partial H_x}{\partial y}. \quad (\text{A.22})$$

Therefore it is possible to partition the solution into two parts. The first solution, a shear horizontal wave (SH wave), is described in terms of potentials H_x and H_y , and it accepts the u_z displacement only. The second solution is the combination of a pressure wave (P wave) and a shear vertical wave (SV wave). It accepts u_x and u_y displacements and it is described by potentials Φ and H_z (Giurgiutiu 2008).

For the elastic media the stress-displacements relations are (see e.g. Timoshenko and Goodier 1962):

$$\begin{aligned} \sigma_{xx} &= (\Lambda + 2G) \frac{\partial u_x}{\partial x} + \Lambda \frac{\partial u_y}{\partial y} + \Lambda \frac{\partial u_z}{\partial z}, & \sigma_{xy} &= G \left(\frac{\partial u_x}{\partial y} + \frac{\partial u_y}{\partial x} \right), \\ \sigma_{yy} &= \Lambda \frac{\partial u_x}{\partial x} + (\Lambda + 2G) \frac{\partial u_y}{\partial y} + \Lambda \frac{\partial u_z}{\partial z}, & \sigma_{yz} &= G \left(\frac{\partial u_y}{\partial z} + \frac{\partial u_z}{\partial y} \right), \\ \sigma_{zz} &= \Lambda \frac{\partial u_x}{\partial x} + \Lambda \frac{\partial u_y}{\partial y} + (\Lambda + 2G) \frac{\partial u_z}{\partial z}, & \sigma_{zx} &= G \left(\frac{\partial u_z}{\partial x} + \frac{\partial u_x}{\partial z} \right). \end{aligned} \quad (\text{A.23})$$

Considering the *SH wave solution*, the wave motion is contained in the horizontal plane Oxz :

$$u_x = u_y = 0, \quad u_z \neq 0. \quad (\text{A.24})$$

Substitution of Eqs. (A.22) and (A.24) into (A.23) yields stress components for the SH waves:

$$\begin{aligned} \sigma_{yz} &= G \left(-\frac{\partial^2 H_x}{\partial y^2} + \frac{\partial^2 H_y}{\partial x \partial y} \right), \\ \sigma_{zx} &= G \left(-\frac{\partial^2 H_x}{\partial x \partial y} + \frac{\partial^2 H_y}{\partial x^2} \right). \end{aligned} \quad (\text{A.25})$$

Considering the *P+SV wave solution*, the wave motion is contained in the vertical plane *Oxy*:

$$u_x \neq 0, \quad u_y \neq 0, \quad u_z = 0. \quad (\text{A.26})$$

Substitution of Eqs. (A.22) and (A.26) into (A.23) yields stress components for the P waves and the SV waves:

$$\begin{aligned} \sigma_{xx} &= (\Lambda + 2G) \left(\frac{\partial^2 \Phi}{\partial x^2} + \frac{\partial^2 \Phi}{\partial y^2} \right) - 2G \left(\frac{\partial^2 \Phi}{\partial y^2} - \frac{\partial^2 H_z}{\partial x \partial y} \right) = \\ &= \Lambda \left(\frac{\partial^2 \Phi}{\partial x^2} + \frac{\partial^2 \Phi}{\partial y^2} \right) + 2G \left(\frac{\partial^2 \Phi}{\partial x^2} + \frac{\partial^2 H_z}{\partial x \partial y} \right), \\ \sigma_{yy} &= (\Lambda + 2G) \left(\frac{\partial^2 \Phi}{\partial x^2} + \frac{\partial^2 \Phi}{\partial y^2} \right) - 2G \left(\frac{\partial^2 \Phi}{\partial x^2} + \frac{\partial^2 H_z}{\partial x \partial y} \right) = \\ &= \Lambda \left(\frac{\partial^2 \Phi}{\partial x^2} + \frac{\partial^2 \Phi}{\partial y^2} \right) + 2G \left(\frac{\partial^2 \Phi}{\partial y^2} - \frac{\partial^2 H_z}{\partial x \partial y} \right), \\ \sigma_{zz} &= \Lambda \left(\frac{\partial^2 \Phi}{\partial x^2} + \frac{\partial^2 \Phi}{\partial y^2} \right), \\ \sigma_{xy} &= G \left(2 \frac{\partial^2 \Phi}{\partial x \partial y} - \frac{\partial^2 H_z}{\partial x^2} + \frac{\partial^2 H_z}{\partial y^2} \right). \end{aligned} \quad (\text{A.27})$$

A.3. Rayleigh surface waves

Rayleigh waves propagate in solids containing a free surface (cf. Victorov 1967, Nowacki 1972). The propagation occurs very close to the surface with a little penetration in the depth (cf. Fig. 2.2). Rayleigh waves are analysed under the *z*-invariant assumption (cf. Section A.2), i.e. $\partial/\partial z = 0$. The particle wave motion, having elliptical trajectories, is contained in the vertical plane, hence the P+SV wave solution from Section A.2 is applied:

$$u_x \neq 0, \quad u_y \neq 0, \quad u_z = 0, \quad (\text{A.28})$$

and only the Φ and H_z potentials are required to describe Rayleigh wave motion:

$$c_p^2 \nabla^2 \Phi = \ddot{\Phi}, \quad c_s^2 \nabla^2 H_z = \ddot{H}_z. \quad (\text{A.29})$$

For Rayleigh wave propagation in the x direction with speed c and wavenumber k , the potentials Φ and H_z can be written as:

$$\Phi(x, y, t) = f(y)e^{i(kx - \omega t)}, \quad H_z(x, y, t) = h(y)e^{i(kx - \omega t)}. \quad (\text{A.30})$$

Substitution of Eqs. (A.30) into Eqs. (A.29) yields:

$$f''(y) - \alpha^2 f(y) = 0, \quad h''(y) - \beta^2 h(y) = 0, \quad (\text{A.31})$$

where:

$$\alpha^2 = k^2 - \frac{\omega^2}{c_P^2}, \quad \beta^2 = k^2 - \frac{\omega^2}{c_S^2}. \quad (\text{A.32})$$

Solutions of Eqs. (A.31) are:

$$f(y) = A_1 e^{\alpha y} + A_2 e^{-\alpha y}, \quad h(y) = B_1 e^{\beta y} + B_2 e^{-\beta y}. \quad (\text{A.33})$$

Substitution of Eqs. (A.33) into Eqs. (A.30), after discarding the impractical part of the solution which does not attenuate yields (Giurgiutiu 2008, Rose 1999):

$$\Phi(x, y, t) = A e^{-\alpha y} e^{i(kx - \omega t)}, \quad H_z(x, y, t) = B e^{-\beta y} e^{i(kx - \omega t)}. \quad (\text{A.34})$$

The boundary conditions for Rayleigh waves correspond to a tractions-free half-plane surface (Giurgiutiu 2008):

$$\sigma_{yy}(y=0) = 0, \quad \sigma_{xy}(y=0) = 0. \quad (\text{A.35})$$

Substitution of (A.34) into (A.27)₂ and (A.27)₄ yields:

$$\sigma_{yy} = \left[(\Lambda + 2G)(\alpha^2 - k^2)A e^{-\alpha y} + 2Gk^2 A e^{-\alpha y} + 2G\beta ik B e^{-\beta y} \right] e^{i(kx - \omega t)}, \quad (\text{A.36})$$

$$\sigma_{xy} = G \left[-2\alpha ik A e^{-\alpha y} + (k^2 + \beta^2) B e^{-\beta y} \right] e^{i(kx - \omega t)}. \quad (\text{A.37})$$

Substitution of P wave and S wave speeds (A.7) and (A.12) into Eq. (A.32) gives:

$$(\alpha^2 - k^2)(\Lambda + 2G) = -\rho\omega^2, \quad G\beta^2 = Gk^2 - \rho\omega^2, \quad (\text{A.38})$$

and therefore Eq. (A.36) can be simplified to:

$$\begin{aligned} \sigma_{yy} &= \left[(2Gk^2 - \rho\omega^2)A e^{-\alpha y} + 2G\beta ik B e^{-\beta y} \right] e^{i(kx - \omega t)} = \\ &= G \left[(\beta^2 + k^2)A e^{-\alpha y} + 2\beta ik B e^{-\beta y} \right] e^{i(kx - \omega t)}. \end{aligned} \quad (\text{A.39})$$

Substitution of Eqs. (A.39) and (A.37) into the boundary conditions (A.35) leads to the equations:

$$\begin{aligned} (\beta^2 + k^2)A + 2\beta ik B &= 0, \\ -2\alpha ik A + (\beta^2 + k^2)B &= 0. \end{aligned} \quad (\text{A.40})$$

It has the nontrivial solution if the determinant vanishes:

$$\begin{vmatrix} \beta^2 + k^2 & 2\beta ik \\ -2\alpha ik & \beta^2 + k^2 \end{vmatrix} = 0, \quad (\text{A.41})$$

which gives the following characteristic equation:

$$(\beta^2 + k^2)^2 - 4\alpha\beta k^2 = 0. \quad (\text{A.42})$$

The above can be rewritten into:

$$\left(2 - \frac{c^2}{c_S^2}\right)^2 = 4\left(1 - \frac{c^2}{c_P^2}\right)^{1/2} \left(1 - \frac{c^2}{c_S^2}\right)^{1/2}, \quad (\text{A.43})$$

$$\left(\frac{c^2}{c_S^2}\right)^3 - 8\left(\frac{c^2}{c_S^2}\right)^2 + 24\left(\frac{c^2}{c_S^2}\right) - 16 - 16\left(\frac{c^2}{c_P^2}\right) + 16\left(\frac{c_S^2}{c_P^2}\right) = 0. \quad (\text{A.44})$$

Defining the ratio of the wave speeds ϑ as

$$\vartheta^2 = \frac{c_P^2}{c_S^2} = \frac{\Lambda + 2G}{G} = \frac{2(1-\nu)}{1-2\nu}, \quad (\text{A.45})$$

the Eq. (A.44) can be expressed by:

$$\left(\frac{c^2}{c_S^2}\right)^3 - 8\left(\frac{c^2}{c_S^2}\right)^2 + (24 - 16\vartheta^2)\left(\frac{c^2}{c_S^2}\right) - 16(1 - \vartheta^2) = 0. \quad (\text{A.46})$$

The Eq. (A.46) is cubic in c^2 / c_S^2 , but for practical conditions only one real root is accepted, the Rayleigh wave speed c_R , depending on the shear wave speed c_S . A common approximation for the Rayleigh wave speed is (cf. Doyle 1997):

$$c_R(\nu) = c_S \left(\frac{0.87 + 1.12\nu}{1 + \nu} \right). \quad (\text{A.47})$$

A.4. Shear horizontal plate waves

Shear horizontal waves are characterized by a particle motion along the z axis (in the horizontal plane) and wave propagation along the x axis (cf. Fig. 2.4). The particle motion has only the u_z component given by (Giurgiutiu 2008):

$$u_z(x, y, t) = h(y)e^{i(kx - \omega t)}, \quad (\text{A.48})$$

where $h(y)$ represents a standing wave across the plate thickness and $e^{i(kx - \omega t)}$ represents a wave propagating in the x direction. The displacement u_z satisfies the wave equation:

$$\nabla^2 u_z = \frac{1}{c_S^2} \ddot{u}_z. \quad (\text{A.49})$$

Since the problem is z -invariant, the Eq. (A.49) can be rewritten as:

$$\left(\frac{\partial^2}{\partial x^2} + \frac{\partial^2}{\partial y^2} \right) u_z = \frac{1}{c_s^2} \ddot{u}_z. \quad (\text{A.50})$$

Substituting Eq. (A.48) into Eq. (A.50) results in:

$$h''(y) + \eta^2 h(y) = 0, \quad (\text{A.51})$$

where:

$$\eta^2 = \frac{\omega^2}{c_s^2} - k^2. \quad (\text{A.52})$$

The solution of the above equation has the general form:

$$h(y) = C_1 \sin \eta y + C_2 \cos \eta y. \quad (\text{A.53})$$

The general form of the displacement is therefore given by:

$$u_z(x, y, t) = (C_1 \sin \eta y + C_2 \cos \eta y) e^{i(kx - \omega t)}. \quad (\text{A.54})$$

The boundary conditions define the upper and lower plate surfaces to be free of tractions:

$$\sigma_{yz}(x, \pm d, t) = 0, \quad (\text{A.55})$$

where the shear stress σ_{yz} is:

$$\sigma_{yz} = G \frac{\partial u_z}{\partial y}. \quad (\text{A.56})$$

Substitution of Eq. (A.54) into Eq. (A.56) yields:

$$\sigma_{yz} = G\eta (C_1 \cos \eta y - C_2 \sin \eta y) e^{i(kx - \omega t)}. \quad (\text{A.57})$$

After imposing boundary conditions (A.55) one can obtain:

$$\begin{aligned} C_1 \cos \eta d - C_2 \sin \eta d &= 0, \\ C_1 \cos \eta d + C_2 \sin \eta d &= 0. \end{aligned} \quad (\text{A.58})$$

The system of linear equations has nontrivial solution, if the determinant is zero, which results in the following characteristic equation:

$$\cos \eta d \sin \eta d = 0. \quad (\text{A.59})$$

The solution of $\sin \eta d = 0$ leads to symmetric modes ($\text{SH}_0, \text{SH}_2, \text{SH}_4, \dots$):

$$\eta d = 0, \pi, 2\pi, \dots, \frac{n\pi}{2}, \quad n = 0, 2, 4, \dots, \quad (\text{A.60})$$

while the solution of $\cos \eta d = 0$ leads to antisymmetric modes ($\text{SH}_1, \text{SH}_3, \text{SH}_5, \dots$):

$$\eta d = \frac{\pi}{2}, \frac{3\pi}{2}, \frac{5\pi}{2}, \dots, \frac{n\pi}{2}, \quad n = 1, 3, 5, \dots \quad (\text{A.61})$$

Recalling Eq. (A.52):

$$\eta^2 = \frac{\omega^2}{c_s^2} - k^2 = \frac{\omega^2}{c_s^2} - \frac{\omega^2}{c^2}, \quad (\text{A.62})$$

the dispersion relation can be written as:

$$c = c_s \left(\sqrt{1 - (\eta d)^2 \left(\frac{c_s}{\omega d} \right)^2} \right)^{-1}, \quad (\text{A.63})$$

or in terms of group velocity:

$$c_g = \frac{d\omega}{dk} = \frac{c_s^2}{c} \quad (\text{A.64})$$

$$c_g(\omega) = c_s \sqrt{1 - (\eta d)^2 \left(\frac{c_s}{\omega d} \right)^2}. \quad (\text{A.65})$$

A.5. Lamb plate waves

Lamb waves are waves of plain strain that propagates between two parallel free surfaces (e.g. Graff 1975, Nowacki 1972, Rose 1999, Victorov 1967). They arise as a result of simultaneous operation of P waves and SV waves, through their multiple reflections on plate surfaces and through their constructive and destructive interference. Lamb waves (see Fig. 2.3) consist of a pattern of standing waves in the y direction (Lamb wave modes) behaving like travelling waves in the x direction (Giurgiutiu 2008). The derivation of Lamb waves is based on the z -invariant problem (cf. Section A.2) in terms of the Φ and H_z potentials (P+SV wave solution), which satisfy the wave equations:

$$\frac{\partial^2 \Phi}{\partial x^2} + \frac{\partial^2 \Phi}{\partial y^2} = \frac{1}{c_p^2} \ddot{\Phi}, \quad \frac{\partial^2 H_z}{\partial x^2} + \frac{\partial^2 H_z}{\partial y^2} = \frac{1}{c_s^2} \ddot{H}_z. \quad (\text{A.66})$$

The displacements and stresses can be expressed in terms of potentials as:

$$u_x = \frac{\partial \Phi}{\partial x} + \frac{\partial H_z}{\partial y}, \quad u_y = \frac{\partial \Phi}{\partial y} - \frac{\partial H_z}{\partial x}, \quad u_z = 0, \quad (\text{A.67})$$

$$\sigma_{xy} = G \left(2 \frac{\partial^2 \Phi}{\partial x \partial y} - \frac{\partial^2 H_z}{\partial x^2} + \frac{\partial^2 H_z}{\partial y^2} \right), \quad (\text{A.68})$$

$$\sigma_{yy} = \Lambda \left(\frac{\partial^2 \Phi}{\partial x^2} + \frac{\partial^2 \Phi}{\partial y^2} \right) + 2G \left(\frac{\partial^2 \Phi}{\partial y^2} - \frac{\partial^2 H_z}{\partial x \partial y} \right).$$

The potentials Φ and H_z can be written as:

$$\begin{aligned} \Phi(x, y, t) &= \phi(y) e^{i(kx - \omega t)}, \\ H_z(x, y, t) &= \psi(y) e^{i(kx - \omega t)}. \end{aligned} \quad (\text{A.69})$$

Substitution of Eqs. (A.69) into Eqs. (A.66) yields:

$$\phi''(y) + p_L^2 \phi(y) = 0, \quad \psi''(y) + q_L^2 \psi(y) = 0, \quad (\text{A.70})$$

where:

$$p_L^2 = \frac{\omega^2}{c_p^2} - k^2, \quad q_L^2 = \frac{\omega^2}{c_s^2} - k^2. \quad (\text{A.71})$$

Solutions of Eqs. (A.70) are given by:

$$\begin{aligned} \phi &= A_1 \sin p_L y + A_2 \cos p_L y, \\ \psi &= B_1 \sin q_L y + B_2 \cos q_L y. \end{aligned} \quad (\text{A.72})$$

Substitution of Eqs. (A.72) into Eqs. (A.69) yields:

$$\begin{aligned} \Phi(x, y, t) &= (A_1 \sin p_L y + A_2 \cos p_L y) e^{i(kx - \omega t)}, \\ H_z(x, y, t) &= (B_1 \sin q_L y + B_2 \cos q_L y) e^{i(kx - \omega t)}. \end{aligned} \quad (\text{A.73})$$

Hence, the displacement and stresses can be rewritten as:

$$u_x = \phi ik + \frac{\partial \psi}{\partial y}, \quad u_y = \frac{\partial \phi}{\partial y} - ik \psi, \quad (\text{A.74})$$

$$\begin{aligned} \sigma_{xy} &= G \left(2ik \frac{\partial \phi}{\partial y} + \psi k^2 + \frac{\partial^2 \psi}{\partial y^2} \right), \\ \sigma_{yy} &= \Lambda \left(-k^2 \phi + \frac{\partial^2 \phi}{\partial y^2} \right) + 2G \left(\frac{\partial^2 \phi}{\partial y^2} - ik \frac{\partial \psi}{\partial y} \right). \end{aligned} \quad (\text{A.75})$$

At this stage, the problem can be split into symmetric and antisymmetric solutions. The guided Lamb waves can exist as symmetric (S_0, S_1, S_2, \dots) and antisymmetric (A_0, A_1, A_2, \dots) modes. At the lowest frequencies two basic modes S_0 and A_0 simultaneously exist. With the increase of frequency, larger numbers of Lamb modes appear and in general, infinite number of modes is associated with a guided Lamb wave problem.

Symmetric solution. Eqs. (A.72), (A.74) and (A.75) can be simplified to:

$$\begin{aligned} \phi &= A_2 \cos p_L y, \\ \psi &= B_1 \sin q_L y, \\ u_x &= A_2 ik \cos p_L y + q_L B_1 \cos q_L y, \\ u_y &= -p_L A_2 \sin p_L y - B_1 ik \sin q_L y, \\ \sigma_{xy} &= G \left[-2p_L A_2 ik \sin p_L y + B_1 (k^2 - q_L^2) \sin q_L y \right], \\ \sigma_{yy} &= G \left[A_2 (k^2 - q_L^2) \cos p_L y - 2q_L B_1 ik \cos q_L y \right]. \end{aligned} \quad (\text{A.76})$$

The symmetric solution of the Lamb wave problem assumes that displacements and stresses are symmetric about the mid-plane (Giurgiutiu 2008):

$$\begin{aligned} u_x(x, -d) &= u_x(x, d), & \sigma_{xy}(x, -d) &= -\sigma_{xy}(x, d), \\ u_y(x, -d) &= -u_y(x, d), & \sigma_{yy}(x, -d) &= \sigma_{yy}(x, d), \end{aligned} \quad (\text{A.77})$$

and the symmetric boundary conditions are:

$$\begin{aligned} \sigma_{xy}(x, -d) &= -\sigma_{xy}(x, d) = 0, \\ \sigma_{yy}(x, -d) &= \sigma_{yy}(x, d) = 0. \end{aligned} \quad (\text{A.78})$$

Upon substitution, the linear system of equations can be obtained:

$$\begin{aligned} -2p_L A_2 ik \sin p_L d + B_1(k^2 - q_L^2) \sin q_L d &= 0, \\ A_2(k^2 - q_L^2) \cos p_L d - 2q_L B_1 ik \cos q_L d &= 0, \end{aligned} \quad (\text{A.79})$$

which has a solution, if the determinant is zero, i.e.:

$$4p_L q_L k^2 \sin p_L d \cos q_L d + (k^2 - q_L^2)^2 \sin q_L d \cos p_L d = 0. \quad (\text{A.80})$$

The above is the Rayleigh-Lamb equation for symmetric modes, which can be rewritten as:

$$\frac{-4p_L q_L k^2}{(k^2 - q_L^2)^2} = \frac{\tan q_L d}{\tan p_L d}. \quad (\text{A.81})$$

The Rayleigh-Lamb frequency equations can be used to determine the velocities at which wave of particular frequency f propagates within a plate of thickness $h = 2d$. It is visible from the Rayleigh-Lamb frequency equations, that the wave speed depends on the frequency, therefore Lamb waves are dispersive.

Antisymmetric solution. Eqs. (A.72), (A.74) and (A.75) can be simplified to:

$$\begin{aligned} \phi &= A_1 \sin p_L y, \\ \psi &= B_2 \cos q_L y, \\ u_x &= A_1 ik \sin p_L y - q_L B_2 \sin q_L y, \\ u_y &= p_L A_1 \cos p_L y - B_2 ik \cos q_L y, \\ \sigma_{xy} &= G \left[2p_L A_1 ik \cos p_L y + B_2(k^2 - q_L^2) \cos q_L y \right], \\ \sigma_{yy} &= G \left[A_1(k^2 - q_L^2) \sin p_L y + 2q_L B_2 ik \sin q_L y \right]. \end{aligned} \quad (\text{A.82})$$

The antisymmetric solution of the Lamb wave problem assumes that displacements and stresses are antisymmetric about the mid-plane (Giurgiutiu 2008):

$$\begin{aligned} u_x(x, -d) &= -u_x(x, d), & \sigma_{xy}(x, -d) &= \sigma_{xy}(x, d), \\ u_y(x, -d) &= u_y(x, d), & \sigma_{yy}(x, -d) &= -\sigma_{yy}(x, d), \end{aligned} \quad (\text{A.83})$$

and the antisymmetric boundary conditions are:

$$\begin{aligned} \sigma_{xy}(x, -d) &= \sigma_{xy}(x, d) = 0, \\ \sigma_{yy}(x, -d) &= -\sigma_{yy}(x, d) = 0. \end{aligned} \quad (\text{A.84})$$

Upon substitution, the linear system of equations can be obtained:

$$\begin{aligned} 2p_L A_1 i k \cos p_L d + B_2 (k^2 - q_L^2) \cos q_L d &= 0, \\ A_1 (k^2 - q_L^2) \sin p_L d + 2q_L B_1 i k \sin q_L d &= 0, \end{aligned} \quad (\text{A.85})$$

which has a solution, if the determinant is zero, i.e.:

$$4p_L q_L k^2 \sin q_L d \cos p_L d + (k^2 - q_L^2)^2 \sin p_L d \cos q_L d = 0. \quad (\text{A.86})$$

The above is the Rayleigh-Lamb equation for antisymmetric modes, which can be rewritten as:

$$\frac{(k^2 - q_L^2)^2}{-4p_L q_L k^2} = \frac{\tan q_L d}{\tan p_L d}. \quad (\text{A.87})$$

WYDAWNICTWO POLITECHNIKI GDAŃSKIEJ

Wydanie I. Ark. wyd. 12,3, ark. druku 11,5, 106/624

Druk i oprawa: *EXPOL* P. Rybiński, J. Dąbek, Sp. Jawna
ul. Brzeska 4, 87-800 Włocławek, tel. 054 232 37 23